COSMOLOGICAL MODELS OF DARK ENERGY: THEORY AND OBSERVATIONS

OLGA AVSAJANISHVILI

A dissertation submitted to the graduate division of
the Faculty of Natural Sciences and Medicine of
Ilia State University in partial fulfillment of
the requirements for the academic degree of
Doctor Philosophy in Physics

Doctoral Program in Physics and Astronomy

Supervisor: Prof. Tina Kahniashvili

ILIA STATE UNIVERSITY
Tbilisi, 2019

კოსმოლოგიური ფარული ენერგიის მოდელები: თეორია და დაკვირვებები

ოლღა ავსაჯანიშვილი

სადისერტაციო ნაშრომი წარდგენილია ილიას სახელმწიფო უნივერსიტეტის
საბუნებისმეტყველო მეცნიერებებისა და მედიცინის ფაკულტეტზე
ფიზიკის დოქტორის აკადემიური ხარისხის მინიჭების მოთხოვნების შესაბამისად

ფიზიკისა და ასტრონომიის სადოქტორო პროგრამა

სამეცნიერო ხელმძღვანელი: პროფესორი თინათინ კახნიაშვილი

ილიას სახელმწიფო უნივერსიტეტი

თბილისი, 2019

Declaration /განაცხადი

As the author of the represented dissertation, I state that the given work is my original, and does not contain any published material, presented for defence by other authors, that are not cited or acknowledged according to accepted standards.

როგორც წარდგენილი სადისერტაციო ნაშრომის ავტორი, ვაცხადებ, რომ ნაშრომი წარმოადგენს ჩემს ორიგინალურ ნამუშევარს და არ შეიცავს სხვა ავტორების მიერ აქამდე გამოქვეყნებულ, გამოსაქვეყნებლად მიღებულ ან დასაცავად წარდგენილ მასალებს, რომლებიც ნაშრომში არ არის მოხსენიებული ან ციტირებული სათანადო წესების შესაბამისად.

Signature /ხელმოწერა: **Olga Avsajanishvili**

Date /თარიღი: **20.05.2019**

აბსტრაქტი

თანამედროვე კოსმოლოგიური დაკვირვებები გვიჩვენებენ, რომ სამყარო ფართოვდება აჩქარებულად. ამ აჩქარების მიზეზის დადგენა თანამედროვე კოსმოლოგიის ერთ-ერთი უდიდესი გამოცანაა. არსებობს პრობლემის ახსნის ორი გზა. პირველი გზა გულისხმობს, რომ სამყაროში არსებობს ე.წ. ფარული ენერგია (უარყოფითი წნევის ფარული სითხე), ხოლო მეორე გზის მიხედვით შესაძლებელია ფარდობითობის ზოგადი თეორიის დარღვევა დიდ მასშტაბებზე. ფარული ენერგიის უმარტივესი მოდელი გულისხმობს ვაკუუმის ენერგიის კონცეფციას, რომელიც აღიწერება ლამბდა კონსტანტით. ეს მოდელი, რომელსაც ეწოდება ლამბდა ცივი ფარული მასის მოდელი (Lambda Cold Dark Matter ΛCDM), წარმოადგენს სტანდარტულ კოსმოლოგიურ მოდელს. ΛCDM მოდელის თეორიული წინასწარმეტყველებები გასაოცრად კარგად ემთხვევიან დაკვირვებით მონაცემებს, თუმცა არსებობს რამდენიმე ამოუხსნელი ამოცანაც (მათ შორისაა, მაგალითად, საწყისი პირობების არაბუნებრივად ზუსტი შერჩევის პრობლემა). ΛCDM მოდელის ძირითად ალტერნატივას წარმოადგენს დინამიური სკალარული ველის მოდელი, ანუ ϕCDM მოდელი. ამ მოდელებში სივრცულად ერთგვაროვანი კოსმოლოგიური სკალარული ველი მიილევა პოტენციალის მინიმუმისაკენ. ამ მოდელებში არ დგება პარამეტრების დამთხვევის პრობლემა, რაც უფრო ბუნებრივად ხსნის დაკვირვებული ფარული ენერგიის სიმკვრივის სიმცირეს. სამყაროს გაფართოების გვიანი ეპოქის აჩქარების ალტერნატიული მიდგომა დაფუძვნებულია დაშვებაზე, რომ გრავიტაციის თეორია იცვლება კოსმოლოგიურ მასშტაბებზე. ამ ნაშრომში ჩვენ Ratra-Peebles-ის პოტენციალით შევისწავლეთ სკალარული ველის მოდელებში მატერიის შეშფოთების ფონური გავრცელება და ზრდის ტემპი. ზრდის ტემპისა და ბარიონულ-აკუსტიკური რხევების პიკის პოზიციების ბოლოდროინდელი გაზომვებით ჩვენ შევიმუშავეთ ამ პოტენციალის მოდელის პარამეტრი α და მატერიის სიმკვრივის პარამეტრი $\Omega_{\rm m}$. ასევე შევისწავლეთ სკალარული ველის მოდელები და მათი შესაძლო განსხვავება საბაზისო მოდელებისგან. ამ მიზნით, დაკვირვებითი მონაცემები, როგორიცაა გაფართოების სიჩქარე, კუთხური მანძილი და ზრდის ტემპის გაზომვები გამოვიყენეთ შემომავალი ფარული ენერგიის DESI-ს დაკვირვებიდან. ამ მოდელების ΛCDM მოდელთან შესადარებლად ჩავატარეთ ბაიესის სტატისტიკური ანალიზი და ვიპოვეთ, რომ ბაიესის კოეფიციენტები დიდი ალბათობით ადასტურებენ ΛCDM მოდელს. ჩვენ ვიკვლევთ რამდენად კარგად შეუძლია შევალიე-პოლარსკი-ლენდერის (CPL) პარამეტრიზაციას სხვადასხვა

სკალარული ველის მოდელების მიახლოება. ვადგენთ სკალარული ველის მოდელის ადგილს CPL პარამეტრიზაციის ფაზურ სივრცეში. ცვლადი მასის ნეიტრინოს მოდელში ვიკვლევთ ფერმიონული ველისა და სკალარული ველის ურთიერთქმედებას რატრა-პიბლსის პოტენციალის გამოყენებით. გამოყვანილია განტოლება, რომელიც აღწერს სამყაროს ევოლუციას ნეიტრინოების სკალარულ ველთან ურთიერთქმედების მომენტამდე (ე.წ. კრიტიკულ წერტილამდე) და კრიტიკული წერტილიდან დღევანდელ ეპოქამდე. გამოთვლილია სკალარული მამარავლის მნიშვნელობა კრიტიკულ წერტილში, ნეიტრინოს მასა კრიტიკულ წერტილში და ნეიტრინოს მასა დღევანდელ ეპოქაში, რომელიც დამოკიდებულია რატრა-პიბლსის პოტენციალის α პარამეტრზე.
ძირითადი საძიებო სიტყვები: ფარული ენერგია, კოსმოლოგიური მუდმივა, სკალარული ველი, მსხვილ მასშტაბოვანი სტრუქტურა, მატერიის ზრდის შეშფოთებები, ნეიტრინო, ბაიესის სტატისტიკა, MCMC მონაცემთა ანალიზი.

Abstract

The standard Lambda Cold Dark Matter (ΛCDM) cosmological model assumes that the General Relativity is a correct theory of gravity on the cosmological spatial and temporal scales, and the acceleration of the universe is due to dark energy or the cosmological constant Λ. Dark energy exerts the negative pressure on space, *i.e.*, it has the property of "antigravity" and, thus, causes the accelerated expansion of the universe. The energy density of the cosmological constant does not depend on time and has recently become dominant (in particular, the energy density associated with the cosmological constant is about 69% of the total energy density of the universe today). In addition, around 26% of the total energy density in the universe is presented in the form of cold dark matter. Thereby, within the framework of the standard ΛCDM model, about 95% of the universe energy density content today is presented in the dark (invisible) form (dark energy and dark matter) with unknown nature, and only 5% is presented in the form of the radiation and the ordinary matter (baryons, leptons). The theoretical predictions of the ΛCDM model are in a good agreement with the current observations, but there are several unresolved problems associated with this model. The so-called cosmological constant problem (an extremely small value of the cosmological constant when compared to the theoretical estimate of the vacuum energy density), and the so-called problem of the coincidence (order of) of the dark energy density and the dark matter energy density. To overcome these difficulties, the dynamical dark energy models have been proposed. In these models, dark energy is presented in the form of the dynamical scalar field, in which the density of dark energy varies over time. In this thesis, we studied the various scalar field models. In particular, we investigated the evolution of the background expansion and the growth rate of the matter density fluctuations in the scalar field ϕCDM Ratra-Peebles model. We constrained the model parameter α and the matter density parameter Ω_{m} using the recent measurements of the growth rate of the matter density fluctuations and the baryon acoustic oscillation peak positions. In addition, we studied a number of the ϕCDM scalar field models in order to distinguish these models from each other and from the baseline ΛCDM model, using the predicted data for the future Dark Energy Spectroscopic Instrument (DESI) observations. For this purpose, we carried out the statistical Bayesian analysis, such as Bayes coefficients, as well as Akaike and Bayesian information criteria. We found that the results of the Bayesian analysis provide the compelling evidence in favor of the ΛCDM model. We also conducted the MCMC anal-

ysis and obtained the constraints on the parameters of the scalar field models, comparing the observational data for: the universe expansion rate, the angular diameter distance and the growth rate function, with the corresponding data generated for the ΛCDM model. We investigated how well the Chevallier-Polarsky-Linder (CPL) parametrization approximates the various scalar field models. We determined the location of scalar field model in the phase space of the CPL parameters. In the Mass Varying Neutrino model, we investigated the interaction of the fermion field and the scalar field with the Ratra-Peebles potential. We obtained the equations describing the dynamics of the universe: up to the moment of the neutrinos interaction with the scalar field (up to the so-called *critical point*) and from the critical point up to the present epoch. We calculated the value of the scale factor and the value of the sum of neutrino masses at the critical point, as well as the value of the sum of neutrino masses at the present epoch depending on the value of the model parameter α of the Ratra-Peebles potential.

Key words: dark energy, cosmological constant, scalar field, large-scale structure, growth rate of the matter density fluctuations, neutrinos, Bayesian statistics, Monte Carlo Markov Chains (MCMC) analysis.

Acknowledgments

I would like to express the gratitude towards my supervisor Tina Kahniashvili. I highly appreciate her leadership, assistance and very serious attitude to writing papers. Tina stimulated me to self-development, to independent research and to deepen knowledge in cosmology. I am very thankful to my co-supervisor Lado Samushia. As a guide, he has got me acquainted with the world of the Baiesian statistics and Markov Chain Monte Carlo analysis. He taught me to write computer codes in data analysis field. We discussed a lot of problems, conducted with creating the computer codes and understanding some phenomena in cosmology. I would like to thank my collaborator Natalia Arhipova. My first steps in cosmology were related with this kind and smart woman. We derived the equations, wrote the computer codes and discussed the results obtained. I am grateful to Gennady Chitov for guidance and helpful discussions on Mass Varying Neutrino model. I would like to appreciate with great pleasure and to express my gratitude to Vasil Kukhianidze, Luka Poniatowski and Alexander Tevzadze for their help and support. I could always rely on the comprehensive answer from them at any moment I needed concerning any problematic question. I am very grateful to Bharat Ratra for useful discussions, help and guidance. I also want to thank my collaborator Yiwen Huang. I would like to thank Sayan Mandal and Bijit Bsingha for helpful discussions on Mass Varying Neutrino model. I want to thank Maya Todua for assistance and support. I would like with great pleasure to express my gratitude and respect to Mzia Barateli. This amazing and kind woman supported and helped me in hard moments. I would like to appreciate with great pleasure Bidzina Chargeishvili for helpful comments. I am very grateful to my daughter Maria for helpful comments and creating the pictures on page 37. I would like with great pleasure to thank Erwin for moral support and inspiration in my work. I would like to thank Ilia State University, where this work was done. I would like to express my gratitude to Katholieke University of Leuven, Belgium as well as Kansas State University Physics department for hospitality, where the part of this thesis was done.

This work was supported in part by the following grants: Shota Rustaveli Georgian NSF (FR/339/6-350/14 and PhD_F_17_196), the CRDF-SRNSF-GRDF Georgia Women's Research Fellowship Program (WRF-14-22), the Swiss NSF SCOPES (IZ 7370-152581), the SOLSPANET FP7-PEOPLE-2010-IRSES, 269299 EC FP7-PEOPLE-2010-IRSES project 269299.

Dedication

To the memory of my beloved parents.

List of Figures

2.1 The spatial distribution of the galaxies in the Two-degree-Field (2dF) Galaxy Redshift Survey. The escape velocities (redshifts) are plotted in the radial direction, the polar angle is a right ascension. This distribution is obtained for 200 000 galaxies using 350 000 spectra. (Figure from Ref. (Colless et al. (2003))) 14

2.2 The Hubble diagram, which is based on the observations of the remote Cepheids from Hubble Space Telescope. The solid line corresponds to the Hubble's law with $H_0 = 75$ km c^{-1} Mpc^{-1}. (Figure from Ref. (Freedman et al. (2001))) . . 16

2.3 Hubble expansion. (Figure from https://www.nature.com) 19

2.4 Left panel: the flat curve of the spiral galaxy NGC 3198 rotation (upper curve), which is a combination of the visible matter rotation (curve "disk") and dark matter (curve "halo"). (Figure from Ref. (Begeman et al. (1991))) Right panel: the evolution of the Newton's potential, Φ, and the relative density contrast for: dark matter, $\delta_{\rm DM}$, the baryons, $\delta_{\rm B}$, and the photons, δ_γ. $t_{\rm eq}$ is the transition from the radiation domination epoch to the matter domination epoch; $t_{\rm rec}$ is the beginning of the recombination epoch; t_Λ is the transition from the decelerated to accelerated expansion of the universe. (Figure from Ref. (Rubakov (2014))) 31

2.5 Left panel: the three-dimensional Cartesian coordinates. Right panel: the spherical coordinates. (Figure from Ref. (Dubrovin et al. (1979))) 34

2.6 Left panel: two-dimensional Minkovski diagram. Right panel: three-dimensional light cone. 37

2.7 The examples of closed, flat and open two-dimensional spaces. (Figure from http://www.astro.cornell.edu/academics/courses/astro201/) 42

2.8 The evolution of the scale factor, $a(t)$, for the different signs of the curvature parameter, K. (Figure from https://wmap.gsfc.nasa.gov/universe/) 44

3.1 Illustration of the parallax effect. (Figure from Ref. (Schneider (2006))) . . . 50
3.2 Illustration of the relativistic Doppler shift. (Figure from Ref. (Carroll & Ostlie (2007))) . . . 52

4.1 Left panel: B-band light curves for the different SNeIa from the Calan-Tolono survey. (Figures from Ref. (Heitmann et al. (2006))). The right panel: the same light curves after one-parameter correction. (Figures from Ref. (Kim et al. (2004))) . . . 64
4.2 Left panel: Hubble diagram for the 307 SNeIa of the Union compilation. (The figures from Ref. (Kowalski et al. (2008))). The top panel: the red line corresponds to the ΛCDM universe ($\Omega_{\rm m} = 0.28$, $\Omega_\Lambda = 0.72$); the green line corresponds to the open universe ($\Omega_{\rm m} = 0.28$, $\Omega_\Lambda = 0$) and the blue line corresponds to the Einstein-de Sitter universe ($\Omega_{\rm m} = 1$, $\Omega_\Lambda = 0$). The bottom panel: the residuals of the distance modulus from the best fitting cosmology for the ΛCDM model. Right panel: Hubble diagram for the Union2.1 compilation. The best fit cosmology for the ΛCDM model is represented as a black solid line. (The figure from Ref. (Suzuki et al. (2012))) . . . 66
4.3 Left panel: the Planck spectrum of the CMBR, which is obtained by the experiments: FIRAS, DMR, UBC, LBL-Italy, Princeton, Cyanogen. (Figure from Ref. (Smoot & Scott (1997))) Right panel: the temperature fluctuations of the CMBR relative to the average temperature based on the results of the Planck 2013. (Figure from Ref. (Ade et al. (2014*b*))) The dipole anisotropy, which related with the motion of the solar system relative to the rest frame of the CMBR and the non-Planckian emission from the Galactic disk are subtracted. The amplitude of the temperature fluctuations relative to the background temperature is $\Delta T/T_0 \sim 10^{-5}$. . . . 69
4.4 The angular power spectrum of the CMBR temperature anisotropy obtained by the experiments: WMAP 5 year, Acbar, Boomerang, CBI. (Figure from Ref. (Nolta et al. (2009))) . . . 73
4.5 The influence of the cosmological parameters on the CMBR angular power spectrum. The values of the square root of the angular power spectrum, $\Delta_T = \sqrt{l(l+1)C_l/2\pi}T_0$, are plotted versus to the logarithmic scale of the angular momentum, l. (Figure from Ref. (Hu & Okamoto (2002))) . . . 74

4.6 Left panel: the predicted polarization spectra of the E-mode (red curve) and B-mode (blue curves) combined with the results of the experiments: WMAP, Planck and EPIC. (Figure from Ref. (Dodelson et al. (2009))) Right panel: the combination of the angular power spectrum of the temperature anisotropy and the signal of the E-mode polarization, according to the results of the experiments: BICEP, BOOMERANG, CBI, DASI and QUAD. (Figure from Ref. (Scott & Smoot (2010))) 78

4.7 The divergence E-mode and the curl B-mode of the polarized field. (Figure from Ref. (Dodelson et al. (2009))) 80

4.8 Baryon Acoustic Oscillations in the matter power spectrum discovered in: (a) 2dFGRS and SDSS main galaxies, (b) SDSS LRG sample, (c) both samples. Solid curves represent the best fit of the data. (Figure from Ref. (Percival et al. (2007))) 84

4.9 The large-scale redshift-space two-point correlation function, $\xi(s)$, of the SDSS sample. (Figure from Ref. (Eisenstein et al. (2005))) 85

6.1 The confidence contours at 68% and 95% as a result of the different measurements: SNIa (JLA) and SNIa (C11) compilations, the combination of the Planck temperature and WMAP polarization (Planck + WP) and the combination of the BAO scale. Left panel: for the $\Omega_{\rm m}$ and Ω_Λ cosmological parameters in the ΛCDM model. The black dashed line corresponds to a flat universe. Right panel: for the $\Omega_{\rm m}$ and w cosmological parameters in the flat $w - \Lambda CDM$ model. The black dashed line corresponds to the cosmological constant hypothesis. (Figure from Ref. (Betoule et al. (2014))) 100

6.2 The evolution of the radiation energy density, the matter energy density and the cosmological constant Λ. (Figure from Ref. (Samushia (2009))) 103

6.3 Left panel: the occupation of the thawing and the freezing scalar fields in the $w_\phi - dw_\phi/d\ln a$ phase space. (Figure from Ref. (Caldwell & Linder (2005))) Right panel: the regimes of the quick rolling down and the slow rolling down for the freezing scalar field, ϕ, to the minimum of its potential. 107

7.1 Left panel: dependence of the scalar field, $\phi(a)$, on the value of the parameter α. Right panel: dependence of the time derivative of the scalar field, $\dot{\phi}(a)$, on the value of the parameter α. 117

7.2 Left panel: dependence of the EoS parameter, $w(a)$, on the value of the parameter α. Right panel: dependence of the scale factor derivative of the EoS parameter, $w'(a)$, on the value of the parameter α. 118

7.3 Left panel: the EoS parameter, $w(a)$, for the different values of the parameter α along with the predictions computed from the CPL parametrization with the corresponding best fit values for w_0 and w_a. Right panel: the normalized Hubble expansion rate, $E(a)$, for the different values of the parameter α. . . 118

7.4 Left panel: the second derivative of the scale factor, $\ddot{a}$, for the different values of the parameter α. Right panel: the matter energy density parameter, $\Omega_{\rm m}(a)$, (dashed lines) and the scalar field density parameter, $\Omega_\phi(a)$, (solid lines) as functions of the scale factor for the different values of the parameter α. . . . 119

7.5 Left panel: the linear growth rate, $D(a)$, for the different values of the parameter α. Right panel: the growth rate, f(a), (solid lines) for the different values of the parameter α along with the predictions $\Omega_{\rm m}^\gamma$(a) (dashed lines), computed for the corresponding best fit values of the parameter γ. 120

7.6 Left panel: the growth rate, $f(a)$, for the different values of the parameter α (solid lines) along with the predictions $\Omega_{\rm m}^\gamma$ (dashed lines), computed for the corresponding best fit values of the γ parameter in the range of redshifts, $z \in (0; 10)$. Right panel: the $\gamma(a)$ function for the different values of the parameter α in the range of redshifts, $z \in (0; 10)$. 121

8.1 1σ and 2σ confidence level contours on the parameters $\Omega_{\rm m}$ and α in the ϕCDM model. This constraints are obtained from the growth rate data, Ref. (Gupta et al. (2012)). 124

8.2 1σ and 2σ confidence level contours on the parameters $\Omega_{\rm m}$ and α in the ϕCDM model. These constraints are obtained after adding BAO/CMBR measurements of the prior distances, Ref. (Giostri et al. (2012)). 127

9.1 The 2σ confidence level contour plots for various pairs of the free parameters (α, $\Omega_{\rm m0}$, h), for which the ϕCDM model with the Ratra-Peebles potential $V(\phi) = V_0 M_{\rm pl}^2 \phi^{-\alpha}$ is in the best fit with the ΛCDM model. 133

9.2 The 2σ confidence level contour plots for various pairs of the free parameters (V_0, $\Omega_{\rm m0}$, h, ϕ_0, $\dot{\phi}_0$), for which the ϕCDM model with the Zlatev-Wang-Steinhardt potential $V(\phi) = V_0(\exp(M_{\rm pl}/\phi) - 1)$ is in the best fit with the ΛCDM model. 134

9.3 The 2σ confidence level contour plots for various pairs of the free parameters (k, Ω_{m0}, h, V_0, ϕ_0, $\dot{\phi}_0$), for which the ϕCDM model with the phantom pseudo-Nambu-Goldstone boson potential $V(\phi) = V_0(1 - \cos(\phi/\kappa))$ is in the best fit with the ΛCDM model. 134
9.4 The comparison of the possible w_0 and w_a values for the quintessence dark energy potentials with the CPL-ΛCDM 3σ confidence level contours. 138
9.5 The comparison of the possible w_0 and w_a values for the phantom dark energy potentials with the CPL-ΛCDM 3σ confidence level contours. 139

10.1 The solutions of the mass equation, Eq. (10.32), for the different values of the α parameter. 146
10.2 The dependence of the energy density parameters for the photons, the matter and the neutrinos-dark energy fluid on redshift. The value of $z_\star$ denotes the epoch of the matter and dark energy equality. 147
10.3 The evolution of the neutrino masses, m_ν, for the value of the parameter $\alpha = 0.0001$. 151
10.4 Left panel: the evolution of the matter energy density parameter, Ω_{m}, and the neutrinos-dark energy density parameter, Ω_{couple}, for the value of the model parameter, $\alpha = 0.0001$. Right panel: the EoS parameter, $w_{\mathrm{couple}}(\mathrm{a})$, depending on the value of the scale factor for the value of the model parameter $\alpha = 0.0001$. 152

List of Tables

6.1 The list of the dark energy quintessence potentials. 105
6.2 The list of the dark energy phantom potentials. 109

8.1 Growth rate data, f_{obs}; redshift z; 1σ uncertainty of the growth rate data. . . 123

9.1 The list of the dark energy quintessence potentials and the free parameters. . 130
9.2 The list of the dark energy phantom potentials and the free parameters. . . . 131
9.3 The list of the dark energy quintessence potentials with the corresponding values of AIC, BIC and Bayes factor. 135
9.4 The list of the dark energy phantom potentials with the corresponding values of AIC, BIC and Bayes factor. 135

10.1 The value of the scale factor at the critical point, a_{cr}, the value of the sum of neutrino masses at the critical point, $m_\nu(a_{\mathrm{cr}})$, the value of the sum of neutrino masses today, $m_\nu(a_0)$, depending on the value of the model parameter α. . . 150

Contents

Abstract ii

Acknowledgments vi

Dedication vi

List Of Figures vii

List Of Tables xiii

Notations 1

1 Introduction 7

2 Cosmology as a Science 13

2.1 Expansion of the Universe . . . 15

2.2 Hubble's Law . . . 17

2.3 Short Review of the General Theory of Relativity . . . 19

2.3.1 Spacetime Metric for Curvilinear Coordinates . . . 19

2.3.2 Transformation of Curvilinear Coordinates . . . 20

2.3.3 Covariant Derivatives . . . 23

2.4 Riemann-Christoffel Tensor, Ricci Tensor, Einstein Tensor. Ricci Scalar. . . 24

2.4.1 Energy-Momentum Tensor . . . 26

2.4.2 Matter in the Universe . . . 29

2.4.3 Einstein's Field Equations . . . 32

2.5 Spatial Metrics . . . 34

2.5.1 Flat Euclidean Space . . . 34

2.5.2 Minkowski Spacetime . . . 36

2.5.3 Geodesic Equation . . . 39

2.5.4 Isotropic Four-Dimensional Spacetime Metric . . . 40
2.5.5 Friedmann's Equations . . . 43
2.5.6 Acceleration Parameter . . . 47

3 Distance in Cosmology **49**
3.1 Concept of Distance in Cosmology . . . 49
3.2 Trigonometric Parallax . . . 50
3.3 Cosmological Redshift . . . 51
3.4 Comoving Distance . . . 55
3.5 Physical Distance . . . 56
3.6 Interval of the Cosmological Time Between Two Events . . . 57
3.7 Luminosity Distance . . . 58
3.8 Angular Diameter Distance . . . 61

4 Observational Probes **63**
4.1 Type Ia Supernovae . . . 63
4.2 Cosmic Microwave Background Radiation . . . 67
4.2.1 Description of the CMBR . . . 67
4.2.2 CMBR Angular Power Spectrum of the Temperature Anisotropy . . . 69
4.2.3 CMBR Primary Temperature Anisotropy . . . 72
4.2.4 Basic Mechanisms Causing the CMBR Primary Anisotropy . . . 73
4.2.5 Secondary Anisotropy of the CMBR . . . 76
4.2.6 Polarization of the CMBR . . . 78
4.3 Barion Acoustic Oscillations . . . 82
4.4 Statistics of the Large-Scale Structure of the Universe . . . 85
4.4.1 Influence of the Gravitational Instability on the Formation of Large-Scale Structures in the Universe. . . . 86
4.4.2 Linear Perturbation Theory . . . 87
4.4.3 Linder γ-parametrization . . . 89

5 Elements of the Statistical Analysis **90**
5.1 Gaussian Probability Distribution . . . 90
5.1.1 Definition of Gaussian Probability Distribution . . . 90
5.1.2 Function χ^2 and the Likelihood Function . . . 90
5.1.3 Fisher Formalism . . . 92

5.1.4 Best Fit Model Parameters 93
5.2 Elements of the Theory of Monte Carlo Markov Chains 94
5.2.1 Definition of the Markov Chains. Transition Probabilities 94
5.2.2 Monte Carlo Method 95

6 Dark Energy **98**
6.1 Cosmological Constant Λ 98
6.2 Cosmological ΛCDM Model 100
6.2.1 Shortcomings of the ΛCDM Model 102
6.3 Scalar Field Models 103
6.3.1 Quintessence Scalar Field 105
6.3.2 Phantom Scalar Field 108
6.4 Coupled Models of Matter and Dark Energy 109
6.4.1 Coupling First Type 110
6.4.2 Coupling Second Type 111
6.5 Chevallier-Polarsky-Linder Parametrization 112

7 Dynamics and Growth Rate in the Ratra-Peebles ϕCDM Model **113**
7.1 Basic Equations 113
7.1.1 Calculation of the Model Parameter κ and the Initial Conditions . . . 115
7.1.2 Initial Conditions 116
7.2 Dynamics and Energy in the Ratra-Peebles ϕCDM Model 117
7.3 Structure Growth in the Ratra-Peebles ϕCDM Model 119
7.4 Growth Index in the Ratra-Peebles ϕCDM Model 120
7.5 Conclusion 122

8 Constraints on the Model Parameters in the Ratra-Peebles Model **123**
8.1 Constraints on the Model Parameters in the Ratra-Peebles Model from the Growth Rate Data 123
8.2 Constraints on the Model Parameters in the Ratra-Peebles Model from the BAO Data 125
8.3 Conclusion 127

9 Constraints on the Models Parameters in the Quintessence and Phantom ϕCDM Models **128**

9.1 Definition of the Model Parameters and the Initial Conditions 128
9.2 MCMC Analysis for Study of the Dark Energy Models 131
9.3 Bayesian Statistics 132
9.4 ϕCDM Models in the CPL Phase Space 136
9.5 Conclusion 137

10 Mass Varying Neutrino Model 140

10.1 Interaction of the Scalar Field and Dirac Field 141
10.2 Saddle Point Approximation 142
10.2.1 Fermionic Potential 144
10.2.2 Fermionic Energy Density 145
10.3 Mass Equation 145
10.4 Energy Balance in the Universe to the Critical Point 146
10.5 Joint Solution of the First Friedmann's and the Scalar Field Equations . . . 148
10.5.1 Relativistic Neutrino Before the Critical Point 148
10.5.2 Neutrino Masses Evolution after the Critical Point 149
10.5.3 Results 150
10.6 Conclusion 151

11 Conclusion 153

12 Future Projects 156

Notations

Natural Units	
Name	Value
Energy	1 GeV $= 1.6 \cdot 10^{-3}$ erg
Mass	1 GeV $= 1.8 \cdot 10^{-24}$ g
Temperature	1 GeV $= 1.16 \cdot 10^{13}$ K
Length	1 GeV$^{-1} = 2 \cdot 10^{-14}$ cm
Time	1 GeV$^{-1} = 6.6 \cdot 10^{-25}$ c
Particle number density	1 GeV$^3 = 1.3 \cdot 10^{41}$ cm^{-3}
Energy density	1 GeV$^4 = 2.1 \cdot 10^{38}$ erg cm^{-3}
Mass density	1 GeV$^4 = 2.3 \cdot 10^{17}$ erg cm^{-3}

Parameters			
Name	Notation	Units	
		SGC	Natural
Astronomocal unit	AU	$1.4960 \cdot 10^{13}$ cm	$7.5812 \cdot 10^{26}$ GeV^{-1}
Critical density	ρ_{crit}	$1.8791h^2 \cdot 10^{-29}$ g cm^{-3}	$8.0992h^2 \cdot 10^{-47}$ GeV^4
Hubble constant	H_0	$3.241h \cdot 10^{-18}$ sec^{-1}	$2.1332h \cdot 10^{-42}$ GeV
Megaparsec	Mpc	$3.0856 \cdot 10^{24}$ cm	$1.5637 \cdot 10^{38}$ GeV^{-1}
Newton's constant	G	$6.672 \cdot 10^{-8}$ cm^3 g^{-1} sec^{-2}	$6.707 \cdot 10^{-39}$ GeV^{-2}
Planck mass	M_{pl}	$2.1768 \cdot 10^{-5}$ g	$1.2211 \cdot 10^{19}$ GeV
Parsec	pc	$3.0856 \cdot 10^{18}$ cm	$1.5637 \cdot 10^{32}$ GeV^{-1}
Solar mass	$M_{\odot}$	$1.989 \cdot 10^{33}$ g	$1.116 \cdot 10^{57}$ GeV
Speed of light	c	$2.9979 \cdot 10^{10}$ cm sec^{-1}	1

Variables	
Symbol	Meaning
a	Scale factor
$a_{l,m}$	Multipole coefficients of the decomposition in the spherical harmonics
$c_{\rm s}$	Sound speed
ds^2	Metric
d_A	Angular diameter distance
d_L	Luminosity distance
e	Expectation
$f(x)$	Density distribution
$f(a)$	Growth rate function
g	Yukawa coupling constant
$\Omega_{\rm m}(a)$	Fractional matter density
h	Normalised Hubble parameter
$\hbar$	Reduced Planck constant
k	Conformal momentum
$k_{\rm phys}$	Physical momentum
l	Multiple moment
p	Pressure of the perfect fluid
p_ϕ	Scalar field pressure
p_{ij}	Transition probabilities
$\tilde{p}$	Parallax
q	Acceleration parameter of the universe
q_0	Acceleration parameter of the universe at the present epoch
r	Physical distance
$r_{\rm s}$	Comoving size of the sound horizon
m	Apparent magnitude
$m_{\rm ch}$	Chandrasekhar's mass
m_ν	Neutrino mass
$n_F(x)$	Fermi distribution
$r_\oplus$	Radius of the Earth's orbit
t	Physical time
v	Radial velocity
$v_{\rm f}$	Three dimensional velocity of the perfect fluid
w	Equation of state parameter
w_0	Current equation of state parameter
w_a	Value of the scale factor derivative of equation of state parameter at $a = 1/2$
$w_{\rm vac}$	Equation of state parameter for vacuum
w_Λ	Equation of state parameter for cosmological constant
w_ϕ	Scalar field equation of state parameter
z	Redshift
$z_{\rm dec}$	Redshift at photon decoupling epoch
$z_{\rm rec}$	Redshift at recombination epoch
C^{-1}	Covariance matrix
D	Linear growth factor
D_V	Distance scale
$\hat{D}$	Dirac operator

Variables	
Symbol	Meaning
E	Energy
$E(a)$	Normalized Hubble parameter
$\mathcal{E}$	Integral of the Bayes' evidence
F	Flux
G	Newton constant
H	Hubble parameter
H_B	Bosonic Hamiltonian
H_D	Dirac Hamiltonian
K	Curvature parameter
L	Luminosity
$\mathcal{L}$	Likelihood function
$\mathcal{L}^{\mathrm{f}}$	Likelihood function for the growth rate data
$\mathcal{L}^{\mathrm{bao}}$	Likelihood function for the BAO data
$\mathcal{L}_\phi$	Scalar field lagrangian density
M	Absolute magnitude
M_ϕ	Scalar particles mass scale
P_1	Transition matrix
P_l	Legendre's polynomials
$P(k)$	Power spectrum
R	Ricci scalar
$\mathbf{R}$	Radius
S_{M}	Matter action
S	Action
T_0	The average current CMBR temperature
$V(\phi)$	Scalar field potential
V_0	The parameter of the ϕCDM scalar field model
$\mathcal{Z}_{\mathrm{D}}$	Grassmann functional integral
Y_{lm}	Spherical harmonics
α	The parameter of the scalar field ϕCDM Ratra-Peebles model
δ	Matter density fluctuations
γ	Linder γ-parametrization
$\gamma(a)$	Effective growth index
$\delta\rho_{\mathrm{b}}$	Baryon density fluctuations
δ^μ_ν	Kronecker delta function
$\delta T_{\mathrm{dipol}}$	Dipole temperature anisotropy
η	Conformal time
λ	Wavelenght
μ	Distance modulus
ξ	Space curvature function
ρ_{b}	Energy density of the baryons
ρ_{b0}	Energy density of the baryons at present epoch
ρ_{m}	Energy density of the matter fluid
ρ_{ph}	Energy density of the photons
ρ_ϕ	Scalar field energy density
ρ_{r}	Energy density of the relativistic fluid
ρ_{s}	Fermionic energy density

Variables	
Symbol	Meaning
$\rho_{\rm K}$	Energy density of the curvature
ρ_{Λ}	Vacuum energy density
$\rho_{\rm m0}$	Energy density of the matter fluid at present epoch
$\rho_{\rm r0}$	Energy density of the relativistic fluid at present
$\rho_{\rm K0}$	Energy density of the curvature at present
σ	Standard deviation
σ_8	rms linear fluctuation in the mass density distribution on scales $8h^{-1}$ Mpc
σ^2	Variance
$\Delta\rho$	Matter density fluctuation
ϕ	Scalar field
χ^2	χ^2 function
ω_0	Frequency of the plane monochromatic wave
$\Gamma^{\lambda}_{\mu\nu}$	Christoffel symbols
Λ	Cosmological constant
$\Omega_{\rm m}$	Density parameter for matter
$\Omega_{\rm m0}$	Density parameter for matter at present
$\Omega_{\rm r}$	Density parameter for radiation
$\Omega_{\rm r0}$	Density parameter for radiation at present
$\Omega_{\rm K}$	Density parameter for curvature
$\Omega_{\rm K0}$	Density parameter for curvature at present
Ω_{Λ}	Density parameter for vacuum
Ω_{ϕ}	Density parameter for scalar field

Special Designations	
Designation	Meaning
$(+,-,-,-)$	Spacetime signature
Conventions for indices:	
$*$ $(\alpha,\beta,\gamma,\mu,\nu)$ run from 0 to 3	Greek letters
$*$ (i,j,k,l,m,n) run from 1 to 3	Roman letters
$(t,x,y,z)\equiv(x^0,x^1,x^2,x^3)=x^\mu$	Four dimensional coordinates
$(x,y,z)\equiv(x^1,x^2,x^3,)=x^i$	Three dimensional Cartesian coordinates
(r,φ)	Polar coordinates
(r,φ,z)	Cylindrical coordinates
(r,θ,φ)	Spherical coordinates
$(\varrho,\varsigma,\varphi)$	Pseudo spherical coordinates
Vectors:	
A_i	Covariant vector
A^i	Contravariant vector
Tensors:	
A_{ij}	Second rank covariant tensor
A^{ij}	Second rank contravariant tensor
A^i_j	Second rank mixed tensor
$g_{\mu\nu}$	Spacetime metric tensor
u_μ	Four dimensional velocity
$G_{\mu\nu}$	Einstein tensor
R_{ik}	Ricci tensor
R_{iklm}	Riemann tensor
$T_{\mu\nu}$	Stress-energy tensor

Abbreviations	
Symbol	Full Form
AIC	Akaike information criterion
BIC	Bayesian information criterion
BAO	Baryon Acoustic Oscillations
CDM	Cold Dark Matter
CMBR	Cosmic Microwave Background Radiation
DESI	Dark Energy Spectroscopic Instrument
ISW	Integrated-Sachs-Wolfe
CPL	Chevallier-Polarsky-Linder
EoS	Equation of State
GTR	General Theory of Relativity
FRII	Fanaroff-Riley Type II
FLRW	Friedmann-Lemaître-Robertson-Walker
MCMC	Markov Chain Monte Carlo
SDSS	Sloan Digital Sky Survey
SZ	Sunyaev-Zel'dovich
SNeIa	Supernovae Ia
WMAP	Wilkinson Microwave Anisotropy Probe
WFIRST	Wide-Field Infrared Survey Telescope
Λ**CDM**	Lambda Cold Dark Matter
ϕ**CDM**	Phi Cold Dark Matter
2dFGRS	2dF Galaxy Redshift Survey
MaVaN	Mass Varying Neutrino
VAMPs	Varying Mass Particles

Chapter 1

Introduction

In 1998, the accelerated expansion of our universe was discovered on the basis of the measurements of the Supernovae type Ia magnitudes, Refs. (Riess et al. (1998), Perlmutter et al. (1999), Riess et al. (2007)). In 2011, Saul Perlmutter, Brian Schmidt and Adam Riess were awarded the Nobel Prize in Physics for this discovery. The accelerated expansion of the universe is confirmed by the other cosmological observations, in particular: by the measurements of the temperature anisotropy and the polarization in the cosmic microwave background radiation, Refs. (Hinshaw et al. (2009), Nolta et al. (2009), Komatsu et al. (2011), Ade et al. (2014*c*), Ade et al. (2016)); by the studies of the large-scale structure of the universe, Refs. (2dFGRS (2002), Eisenstein et al. (2005), Percival et al. (2007), SDSS (2017)).

There are numerous models explaining the current accelerated expansion of the universe, Refs. (Frieman et al. (2008), Caldwell & Kamionkowski (2009), Yoo & Watanabe (2012)). The most popular model suggests that a significant part of the universe is in the form of *dark energy* or *dark fluid*, for a review Refs. (Peebles & Ratra (2003), Copeland et al. (2006*a*), Tsujikawa (2010), Tsujikawa (2011)). The unusual property of dark energy is that it exerts a negative pressure on space, *i.e.*, dark energy has the property of "antigravity". For the time being, the nature and the origin of dark energy is one of the most important and still unresolved issues of modern cosmology.

The simplest description of dark energy is the concept of the vacuum energy or the cosmological constant Λ, first introduced by Albert Einstein, Refs. (Einstein (1915*a*), Einstein (1915*b*)). The cosmological model based on such a description of dark energy is called the Lambda Cold Dark Matter (ΛCDM) model, which has been the *standard* model of the universe since 2003, Refs. (Zeldovich (1968), Blumenthal et al. (1984)); the monographs:

Refs. (Peebles (1994), Dodelson (2003), Weinberg (2008)); for the reviews: Refs. (Carroll et al. (1992), Carroll (2001), Peebles & Ratra (2003), Copeland et al. (2006*b*), Martin (2012), Padilla (2015)). This model is based on the General Theory of Relativity (GTR), which was developed by Albert Einstein in order to describe the gravity in the universe on the cosmological length scales.

In addition, there is still an unresolved problem of *dark matter* in the universe, which, in particular, manifests itself in the anomalously high velocity of rotation of the outer regions of the galaxies, Ref. (Rubin et al. (1980)). The dark matter particles do not interact with the electromagnetic radiation and weakly gravitationally interact with the ordinary baryonic matter.

Based on GTR, about 95% of the energy in the universe is in the "dark" form, *i.e.*, in the form of dark energy and dark matter. Recent observations of the Planck space telescope show that the universe consists of $4,8\%$ of ordinary matter, 26% of dark matter and $69,2\%$ of dark energy, Ref. (Ade et al. (2016)).

The ΛCDM model is a *concordance* model of the universe, since this model is in a good agreement with the currently available cosmological observations. However, the ΛCDM model still has unsolved problems: the *cosmological constant problem* or, in other words, the *fine turning problem* and the *coincidence problem*, Refs. (Weinberg (1989), Weinberg (2000), Padmanabhan (2003), Padilla (2015)). The cosmological constant problem is that the observed value of the cosmological constant is 120 values less than its theoretically predicted value, Ref. (Weinberg (2000)). The coincidence problem is that, based on the precise cosmological observations, the density of dark energy is comparable to the energy of dark matter at the present epoch: $\rho_{\rm DM}/\rho_{\rm DE} \simeq 1/3$, $\rho_{\rm DE}$ and $\rho_{\rm DM}$ are the dark energy density and the dark matter energy density, respectively. This fact is a mystery, because according to the standard ΛCDM model, the energy of the cosmological constant does not depend on time, $\rho_{\rm DE} = \rho_\Lambda$=const, while the energy of dark matter varies over time as $\rho_{\rm DM} \sim a^{-3}(t)$, see Fig. (6.2). Therefore, the ratio of these quantities should be time-dependent: $\rho_{\rm DM}/\rho_{\rm DE} \propto 1/a^3(t)$, $a(t)$ and t are the scale factor and physical time, respectively.

In order to solve the problems of the ΛCDM model, many alternative models have been elaborated. These models are divided into two types: the models based on the gravity of the GTR and the models with the different gravity from the GTR on the cosmological scales in the universe (*i.e.*, on the scales comparable to the current size of the universe). The first type of the models includes the dynamical scalar fields models of dark energy: the quintessence models, Refs. (Ratra & Peebles (1988*b*), Ratra & Peebles (1988*a*), Wetterich

(1988a)), the k-essence models, Refs. (Armendariz-Picon et al. (1999), Armendariz-Picon et al. (2000), Armendariz-Picon et al. (2001)), the phantom scalar field models, (Caldwell (2002)); the coupled dark energy and matter models, Refs. (Amendola (2000), Zimdahl & Pavon (2001)), in particular, the mass varying neutrino model, Refs. (Farrar & Peebles (2004), Fardon et al. (2004)); the unified model of dark energy and matter, the so-called Chaplygin gas model, Refs. (Kamenshchik et al. (2001), Bento et al. (2002)) and the k-essence model, as an unified model of dark energy and matter, Ref. (Scherrer (2004)); the heterogeneous model of Lemaître-Tolman-Bondi, Refs. (Lemaitre (1933), Tolman (1934), Bondi (1947), Tomita (2001)), and etc. The second type of the models are: the models with Lagrangian densities that are more complex functions of spacetime curvature, the so-called f(R) models, Refs. (Capozziello et al. (2003), Carroll et al. (2004), Mukhanov (2005), Nojiri & Odintsov (2006)); the warped brane world scenarios, the so-called the model of Dvali-Gabadadze-Poratti, Refs. (Dvali et al. (2001)), Gabadadze (2007)); the massive gravity models, Refs. (Fierz & Pauli (1939), de Rham & Gabadadze (2010), de Rham et al. (2011), Hassan & Rosen (2012)); quantum gravity and string-motivated modifications of gravity, Refs. (Polchinski (2007a), Polchinski (2007b), Mercuri (2009)); the Galilean gravity models, Ref. (Nicolis et al. (2009)); the scalar-tensor gravity models, Refs. (Brans & Dicke (1961), Moffat (2006), Mishra & Singh (2013)); degravitation and cascading gravity, Refs. (Arkani-Hamed et al. (1998), Khoury & Wyman (2009), Dvali et al. (2003), de Rham et al. (2008), Nojiri & Odintsov (2003)), the models with large extra spatial dimensions, Refs. (Shifman (2010)) and etc.

The main alternative to the ΛCDM model is the dynamical dark energy scalar field ϕCDM models, Refs. (Ratra & Peebles (1988a), Ratra & Peebles (1988b), Wetterich (1988a), Brax & Martin (2002), Linder (2008), Cai et al. (2010), Bahamonde et al. (2017), Ryan et al. (2019)). The scalar field models avoid the cosmological constant problem of the ΛCDM model. In the scalar field models, the equation of state (EoS) parameter, w, depends on time: $w \equiv p_{\rm DE}/\rho_{\rm DE}$, $p_{\rm DE}$ - a dark energy pressure, whereas in the ΛCDM model the EoS parameter is a constant, $w = -1$. Depending on the value of the EoS parameter, the ϕCDM scalar field models are divided into: the quintessence models, with $-1 < w < -1/3$, Refs. (Peebles & Ratra (2003), Caldwell & Linder (2005), Schimd et al. (2007)), and the phantom models, with $w < -1$, Refs. (Caldwell (2002), Elizalde et al. (2004), Scherrer & Sen (2008a), Dutta & Scherrer (2009), Frampton et al. (2012), Frampton et al. (2011), Ludwick (2017)). The quintessence models are divided into two classes: the tracker (freezing) models, in which the scalar field evolves more slowly than the Hubble expansion rate, and the thawing models, in which the scalar field evolves faster than the Hubble expansion rate, Refs. (Steinhardt et al. (1999), Caldwell & Linder (2005), Dutta & Scherrer (2009), Chiba et al. (2013), Lima et al. (2015)).

In the quintessence tracker models, the energy density of the scalar field first tracks the radiation energy density and then the matter energy density, while it remains a subdominant, Ref. (Zlatev et al. (1999)). Only recently the scalar field becomes dominant and begins to behave as a component with the negative pressure, which leads to the accelerated expansion of the universe, Refs. (Schimd et al. (2007), Linder (2015), Bag et al. (2017)). For the certain shape of the potential, the quintessence tracker models have an attractor solution that is insensitive to the initial conditions, Ref. (Zlatev et al. (1999)). The simplest example of the tracker scalar field models with an attractor solution is the scalar field model with the inverse-power-law Ratra-Peebles potential. This model was for the first time proposed by Bharat Ratra and Jim Peebles in 1988, Refs. (Ratra & Peebles (1988a), Ratra & Peebles (1988b)).

The study of the quintessence ϕCDM scalar field model with the Ratra-Peebles potential is one of the main objectives of this thesis. In particular, we investigated the dynamics of the scalar field with this potential, the influence of the scalar field with the Ratra-Peebles potential on the dynamics of the universe and its energy components. We also studied the influence of the dark energy scalar field Ratra-Peebles model on the large-scale structure evolution of the universe.

The interest to the dark energy phantom models among the cosmologists has increased recently, due to the fact that some modern observations are consistent with these models, Refs. (Hinshaw et al. (2013), Ade et al. (2016)). The dark energy phantom models have a negative non-canonical kinetic component in the action, as a result of which the energy density in these models increases over time, Refs. (Caldwell (2002), Scherrer & Sen (2008b), Scherrer & Sen (2008a), Ludwick (2017)). During the accelerated expansion of the universe, driven by the phantom scalar field, the rip can occur between all gravitationally bound structures (from the disruption of superclusters and clusters of galaxies to the disruption of atomic nuclei), Refs. (Caldwell et al. (2003), Nojiri et al. (2005), Frampton et al. (2011), Frampton et al. (2012)). To study the history of the universe expansion, the large-scale structure of the universe, the nature of dark energy and dark matter, the Wide-Field Infrared Telescope (WFIRST), the Dark Energy Spectroscopic Instrument (DESI) and the Euclidean Space Telescope (Euclid) will be launched in the next decade, Refs. (Amendola et al. (2013), Levi et al. (2013), Font-Ribera et al. (2014), Spergel et al. (2015), Aghamousa et al. (2016)).

After completing these missions, very precise measurements of the expansion rate of the universe, the angular diameter distances and the growth rate of the matter density fluctuations in the universe will be performed to redshifts $z \sim 2$. These precise measurements can constrain the numerous dark energy models and some of them can be discarded. We studied 10 quintessence and 7 phantom ϕCDM scalar field models, which were first presented in the papers: Refs. (Frieman et al. (1995), Ferreira & Joyce (1998), Zlatev et al. (1999), Brax & Martin (1999), Sahni & Wang (2000), Barreiro et al. (2000), Albrecht & Skordis (2000), Urena-Lopez & Matos (2000), Caldwell & Linder (2005), Scherrer & Sen (2008a), Dutta & Scherrer (2009), Rakhi & Indulekha (2009), Chang & Scherrer (2016), Bag et al. (2017)). We proposed a phenomenological method for studying the potentials in these models. As a result, for each potential the following ranges were found: the model parameters, the EoS parameters, the initial conditions for differential equations describing the dynamics of the universe. We also investigated how the various scalar field models can be approximated by the Chevallier-Polarsky-Linder (CPL) parametrization. We determined the location of each model in the phase space of the CPL parameters. One of the objectives of this study is to answer the question: "Is it possible to distinguish these models from the standard ΛCDM model at the present epoch using the predicted data from the future DESI observations?" For this purpose the expansion rate, the angular diameter distance and the measurements of the matter density fluctuations growth rate were calculated both for each ϕCDM model under investigation and the ΛCDM model. We also applied the comparison criteria in the Bayesian statistics, such as Bayes coefficients, as well as Akaike and Bayesian information criteria.

The coupled models of matter and dark energy were developed to resolve the problems in the standard ΛCDM model, Refs. (Amendola (2000), Zimdahl & Pavon (2001)). In the Mass Varying Neutrino model, the interaction of the bosonic scalar field with the fermionic field (massless neutrino) is considered. As a consequence of this interaction, the neutrino acquires a mass that varies over time, Ref. (Fardon et al. (2004)). In the Mass Varying Neutrino model, we investigated the interaction of the fermionic field and the bosonic scalar field with the Ratra-Peebles potential. The equations describing the dynamics of the universe are obtained: before the moment of neutrinos interaction with the scalar field (before a critical point) and after the critical point to the present epoch. We calculated the value of the scale factor and the value of the sum of neutrino masses at the critical point, as well as the value of the sum of neutrino masses at the present epoch depending on the value of the model parameter α of the Ratra-Peebles potential.

This thesis is organized as follows: the theoretical foundations of cosmology are discussed in Chapter II; the various types of distances used in cosmology are described in Chapter III; the different cosmological observations are presented in Chapter IV; Chapter V is devoted to the basics of the statistical analysis; the various dark energy models are considered in Chapter VI; the investigations of the Ratra-Peebles ϕCDM scalar field model are described in Chapter VII; the observational constraints on the model parameters in the Ratra-Peebles ϕCDM model are considered in Chapter VIII; the observational constraints in the flat quintessence and in the phantom scalar field ϕCDM models are discussed in Chapter IX; the Mass Varying Neutrino model is described in Chapter X; the conclusion is contained in Chapter XI; a plan for the future research is presented in Chapter XII.

In this thesis, we used the natural system of units: $c = \hbar = k_B = 1$.

Chapter 2

Cosmology as a Science

Since ancient times, people have always been interested in the structure of the world in which they live. Staring into the night sky, they asked themselves the questions: "How did the universe originate and how is it arranged? Will the universe exist forever, and if not, how will it cease its existence? Is the universe finite and what is its size or is it infinite?" Namely, the curiosity of people to learn more about the universe caused the emergence and development of the science *cosmology*.

Cosmology studies the universe as a whole (as a single system), explores its origin, evolution, dynamics, structure and ultimate fate. The peculiarity of this science is that the object of research is exclusive and, apparently, exists in a single instance. The study of the universe also presents a considerable difficulty, since it is very difficult for the researcher to draw the objective conclusions about the universe (about the system) part of which he is. While the empirical foundation of cosmology is an extragalactic astronomy, the theoretical foundation is the basic physical theories, such as the general theory of relativity, field theory, etc.

Cosmology is based on the results of a study of the most common properties such as the homogeneity, the isotropy[1] and the expansion of the part of the universe that is available for the astronomical observations. Due to the fact that the speed of light has a finite value, we can observe only a certain part of the expanding universe, whose radius is approximately 14.25 Gpc. On the cosmological length scale, the average value of which is more than 100 Mpc, the large-scale structures such as galaxies, clusters and super clusters are not observable in the universe. The principle of relativity or the so-called *Copernicus's principle*

[1] The concept of the homogeneity implies that the universe looks the same at every point in space; the concept of the isotropy means that the universe looks the same in all directions. The fulfillment of the isotropy condition does not automatically follow from the fulfillment of the homogeneity condition and vice versa. The homogeneity condition follows only from the requirement that the isotropy condition is satisfied with respect to each point in space.

is applicable on these length scales. According to this principle, the privileged points do not exist in the universe, and the human beings are not privileged observers in it. Thus, our universe can be considered as *isotropic* and *homogeneous* on the cosmological length scales.

The spatial distribution of the nearby galaxies according to the Two-degree-Field (2dF) Galaxy Redshift Survey is presented in Fig. (2.1). Our Milky Way galaxy is located at the center. With an increase of the distance (or redshift respectively) from our galaxy, the distribution structure of the galaxies becomes less clear. At the large distances (or large redshifts respectively), the galaxies are randomly arranged, *i.e.*, the isotropic and uniform distribution of the galaxies is observed on these length scales. Based on the theoretical

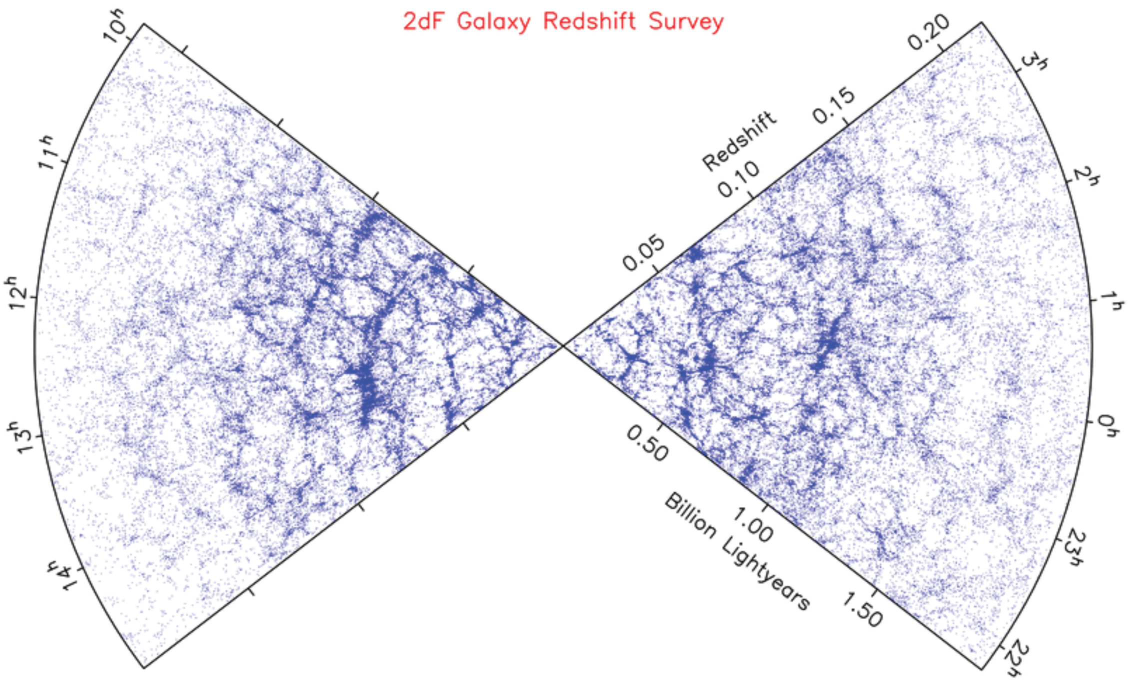

Figure 2.1: The spatial distribution of the galaxies in the Two-degree-Field (2dF) Galaxy Redshift Survey. The escape velocities (redshifts) are plotted in the radial direction, the polar angle is a right ascension. This distribution is obtained for 200 000 galaxies using 350 000 spectra. (Figure from Ref. (Colless et al. (2003)))

and experimental results, Vesto Slipher, George Lemaitre, and Edwin Hubble discovered that the universe is expanding, and this expansion is an essential feature of our universe. According to the model of the hot universe, that is the most common in modern cosmology, the universe began its evolution or, in other words, expansion about 13.7 billion years ago as a result of the Big Bang. At early stages of the universe development the matter and the radiation had a very high temperature and density. The expansion of the universe led to its gradual cooling, the formation of the atoms, and, an consequence, stars, protogalaxies, galaxies, clusters of galaxies, superclusters and other cosmic bodies that exist today.

2.1 Expansion of the Universe

In 1917, while the American astronomer Vesto Slipher was studying the spectra of the galaxies, he discovered a shift in the spectral lines of these galaxies to the red end of the spectrum[2]. Based on these data, Vesto Slipher concluded that the galaxies are moving away from us.

In 1929, the American scientist Edwin Hubble discovered that the radial velocities of the galaxies, v, measured by the Doppler shift of the spectral lines, proportionally increase with the physical distances to them, $d = |\vec{d}|$, Ref. (Hubble (1929)). Hubble identified a linear relationship between the radial velocities and the physical distances[3] between the galaxies, $v \propto d$, called the Hubble's law.

The mathematical form of this law is:

$$\vec{v} = H_0 \vec{d}, \tag{2.1}$$

where H_0 is a coefficient of the proportionality, called the Hubble constant[4]. The values of the radial velocities as a function of the physical distances, d, are shown in the Hubble diagram, see Fig. (2.2). In this figure, the points are approximated by a straight line, whose slope is determined by the value of the Hubble constant, H_0. The linear increase in the value of the radial velocities of the galaxies with an increase in the value of the physical distances to them can be interpreted as the moving away of the galaxies from each other as a result of the expansion of the universe. With such an interpretation, the radial velocities are the recessional velocities of the galaxies from each other (the explanation of this logical conclusion is given below). The expansion of the universe, called the Hubble expansion, is one of the main features of our universe.

Let's introduce the following terminology[5]:

[2] Redshift occurs due to the Doppler effect. This effect is associated with a change in the frequency and, accordingly, in the wavelength of the radiation, perceived by the observer, due to the motion of the source of radiation. When the source of radiation moves away from the observer, the wavelength increases. Conversely, when the source of radiation moves towards the observer, the wavelength decreases.

[3] The definition of the notion of the physical distance is given below.

[4] The coefficient of the proportionality in the Hubble's law, H_0, is a constant at the present epoch. In the general case, this coefficient is a function depending on time (a more detailed description of this function is presented below).

[5] The detailed information about the different types of the distances, used in cosmology, is contained in Chapter III.

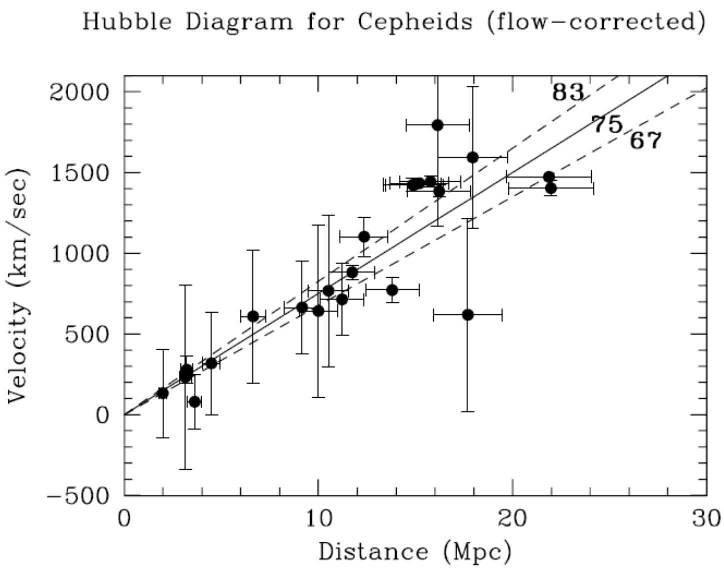

Figure 2.2: The Hubble diagram, which is based on the observations of the remote Cepheids from Hubble Space Telescope. The solid line corresponds to the Hubble's law with $H_0 = 75$ km c^{-1} Mpc^{-1}. (Figure from Ref. (Freedman et al. (2001)))

Proper (physical) distance

The physical distance, $\vec{d}(t)$, is a real, measured distance between two objects in space, where t is cosmological or physical time.

Comoving Distance

Let's consider a radially expanding or contracting homogeneous sphere[6]. We choose a moment of time, $t = t_0$, which corresponds to the present moment of time, and we introduce a reference frame, $\vec{x}$, with the origin that coincides with the center of this sphere. As a result of the expansion or contraction of the sphere, at the present moment of time, t_0, a particle will be in the position, $\vec{d}(t_0)$. At the arbitrary moment of time, t, the particle will be in the position, $\vec{d}(t)$. Due to the fact that the expansion or contraction is radial, the direction, $\vec{d}(t)$, will remain the constant.

Since $\vec{d}(t_0) = \vec{x}$, this means that:

$$\vec{d}(t) = a(t)\vec{x}, \tag{2.2}$$

where a function $a(t)$ is called a scale factor. This function depends only on time. The scale factor describes the change in the spatial separation between the objects over time and

[6]The expansion or contraction of a homogeneous sphere can serve as a model of an expanding (or contracting) universe.

characterizes the expansion or the contraction of the universe. At the present moment of time, the value of the scale factor is usually represented in the normalized form. In this thesis, we chose the normalization in which the value of the scale factor is equal to unity, $a(t_0) \equiv a_0 = 1$.

The observers who move in accordance with the equation, Eq. (2.2), are referred to the comoving observers, where $\vec{x}$ are the comoving coordinates that form the comoving reference frame.

In the expanding or contracting universe, the physical distance between two comoving objects increases or decreases over time, while the comoving distance between objects does not change over time.

Conformal Time

Conformal (comoving) time is time elapsed since the Big Bang in accordance with the clock of the comoving observer. The differential of physical time, t, and the differential of conformal time, η, are interrelated as follows:

$$dt = a(t)d\eta. \tag{2.3}$$

The value of conformal time, η, can be obtained from Eq. (2.3):

$$\eta = \int_0^t \frac{dt'}{a(t')}. \tag{2.4}$$

Eq. (2.4) can be rewritten as:

$$\eta = \int_0^a \frac{1}{a'H(a')}\frac{da'}{a'}. \tag{2.5}$$

2.2 Hubble's Law

The velocity of the comoving observer can be found as a time derivative from the comoving distance:

$$\vec{v}(d,t) = \frac{d}{dt}\vec{d}(t) = \frac{da}{dt}\vec{x} \equiv \frac{\dot{a}}{a}\vec{d}(t) \equiv H\vec{d}(t), \tag{2.6}$$

where the function H is called the *Hubble parameter* or the *expansion rate of the universe*[7]:

$$H = \frac{\dot{a}}{a}. \tag{2.7}$$

[7]Georges Lemaître, based on the results of Vesto Slipher's research, suggested that the universe is expanding and first introduced the concept of the expansion rate of the universe, H. The results of his theoretical studies were presented in the paper, Ref. (Lemaître (1927)). This paper was published in 1927, two years before the Edwin Hubble's publication.

The Hubble's law can be written in the general form for an arbitrary moment of time. Consider the relative velocity of two comoving objects located in the positions, $\vec{d}$ and $\vec{d}+d\vec{d}$, respectively:

$$d\vec{v}(t) = \vec{v}(\vec{d} + d\vec{d}(t)) - \vec{v}(\vec{d}, t) = H d\vec{d}(t). \tag{2.8}$$

Consequently, the relative velocity is proportional to the spatial separation of the comoving objects. The coefficient of proportionality, H, does not depend on the position of the observers but depends only on time.

The Hubble parameter for the present moment of time, $t = t_0$, is called the Hubble constant, $H(t_0) \equiv H_0$. The Hubble constant is usually represented in the parametrized form, $H_0 = 100h$ km $^{-1}$ Mpc^{-1}, where h is a dimensionless parameter.

At the present time, the universe is expanding with an acceleration, and the gravitationally uncoupled astronomical objects are moving away from each other, therefore, $\dot{a}(t_0) > 0$, *i.e.*, the scale factor is an increasing time-dependent function.

The value of the Hubble constant, H_0, is very important in cosmology, as it determines the age and the expansion rate of the universe at the present epoch. The Hubble constant is determined by the so-called Hubble distance or by the radius of the Hubble sphere, $r_{\rm HS}$. The radius of the Hubble sphere is the distance to the objects moving away from the observer at the speed of light. This radius determines the boundary between the objects that move slower and faster than the motion of the objects at the speed of light relative to the observer at the present time. In the general case, the radius of the Hubble sphere, $r_{\rm HS}$, is calculated as[8], $r_{\rm HS}(t) = c/H$. Consequently, at the present time, the radius of the Hubble sphere is defined as: $r_{\rm HS}(t_0) = c/H_0$ and its value is 4.1 Gpc.

According to the Hubble's law, Eq. (2.8), there are no privileged points in the homogeneous and isotropic universe, and the expansion will be the same at any point in space, see Fig. (2.3). This assumption is consistent with the Copernican's principle. Therefore, being a generalized characteristic of the universe, the value of the Hubble constant, H_0, is the same for all the galaxies and does not depend on the direction to the galaxy in the sky or the distance to it.

We find the time derivative of the physical distance to a galaxy, $\vec{d}$, represented in Eq. (2.2):

$$\dot{\vec{d}}(t) = \frac{\dot{a}}{a}\vec{d}(t) + \vec{u_p}(\vec{x}, t), \tag{2.9}$$

here $\vec{u_p}(\vec{x}, t)$ is a peculiar velocity, determining the random motions of the galaxy in space.

[8]Here the speed of light, c, reintroduced for clarity.

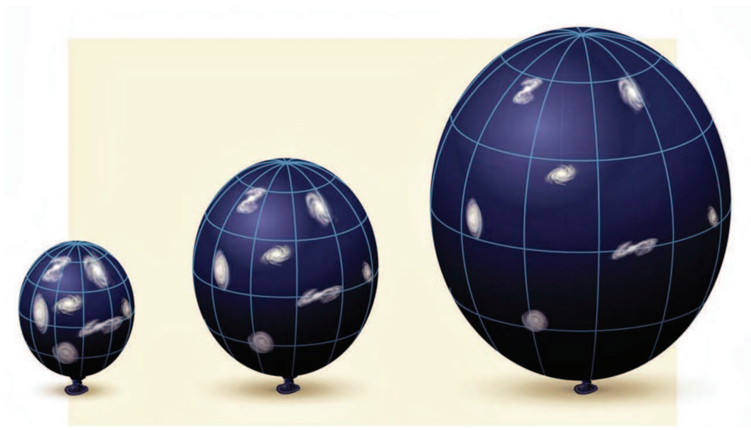

Figure 2.3: Hubble expansion. (Figure from https://www.nature.com)

The peculiar velocity characterizes the deviation of the motion of the nearby galaxy from the homogeneous Hubble expansion. On the length scales that are smaller than the cosmological scales, the value of the peculiar velocity, $\vec{u_p}(\vec{x},t)$ in Eq. (2.9), exceeds the value of the galaxy velocity under the influence of the Hubble expansion, $\vec{v} = \dfrac{\dot{a}}{a}\vec{d}$. On these length scales, the motion of the galaxies are determined to a greater extent by their random motion than by the influence of the Hubble expansion, therefore, this definition is not exact on these length scales. On the other hand, the motion of the distant galaxies is completely determined by the Hubble expansion on the cosmological scales, since the peculiar velocities of the galaxies are negligible in the comparison with the Hubble expansion rate. The motion of the astronomical objects, solely due to this expansion, is called the motion in accordance with the *Hubble flow*.

The discoveries of Vesto Slipher, George Lemaître, and Edwin Hubble are the foundation on which modern physical cosmology is built. These discoveries are marked by the beginning of the transition of cosmology from the descriptive philosophical science to the exact science, in which each proposed theory is verified by the results of the observational experiments.

2.3 Short Review of the General Theory of Relativity

2.3.1 Spacetime Metric for Curvilinear Coordinates

The GTR is the theoretical basis of modern cosmology, Refs. (Einstein (1915*a*), Einstein (1915*b*); the monographs: Refs. (Landau & Lifshitz (1971), Weinberg (1972), Misner et al. (1973), Carroll (2004)). In GTR, spacetime with the four-dimensional curvilinear coordinates is considered as, $x^\mu = (x^0, x^1, x^2, x^3)$. The spatial part of spacetime is denoted as, x^1, x^2, x^3, while the temporary part as, $x^0 = t$. The distance between two nearby points with the coordinates, x^μ and $x^\mu + dx^\mu$, is given by a linear element, whose square in the curvilinear coordinates is a quadratic form of the differentials, dx^μ, or by a metric:

$$ds^2 \equiv g_{\mu\nu} dx^\mu dx^\nu, \tag{2.10}$$

where $g_{\mu\nu}$ is a covariant spacetime metric tensor, which is a function of the coordinates. The value of the metric is an invariant during the transition from one reference frame to another. The covariant metric tensor, $g_{\mu\nu}$, is symmetrical in the indexes μ and ν, $g_{\mu\nu} = g_{\nu\mu}$. The covariant metric tensor is inverse to the contravariant metric tensor, $g^{\mu\nu}$:

$$g_{m\mu} g^{\mu\nu} = \delta^\nu_m, \tag{2.11}$$

where δ^ν_m is a Kronecker delta function.

Kronecker Delta Function

The Kronecker delta function is a single four-dimensional tensor, which is defined as:

$$\delta^\nu_m x^m = x^\nu. \tag{2.12}$$

In the matrix form this expression can be represented as:

$$\delta^\nu_m = \begin{cases} 1, & m = l \\ 0, & m \neq 1 \end{cases} \tag{2.13}$$

A trace[9] of the Kronecker delta function is equal to $\sum_i \delta^i_i = 4$. The Kronecker delta function has the following property: the components of this function are the same in any reference frame.

2.3.2 Transformation of Curvilinear Coordinates

Consider the scalar, vector and tensor transformation from one curvilinear reference frame, x^0, x^1, x^2, x^3, to another, $x^{'0}, x^{'1}, x^{'2}, x^{'3}$.

[9]A trace (or Spur-Germ.) of the matrix is a sum of the elements on the main diagonal. If b_{ij} are the elements of the matrix B, then the trace of this matrix will be defined as, $\mathrm{tr}(B) = \sum_i b_{ii}$.

Scalar (Zero Rank Tensor)

A scalar is a value that in any reference frame is completely determined by a single number (or a function). The value of the scalar does not change during the transition from one reference frame to another. If φ is a scalar value in one reference frame, x^0, x^1, x^2, x^3, and φ' is a scalar value in another reference frame, x'^0, x'^1, x'^2, x'^3, then:

$$\varphi'(x'^0, x'^1, x'^2, x'^3) = \varphi(x^0, x^1, x^2, x^3). \tag{2.14}$$

Usually a scalar has one component. Examples of the scalars: pressure, density, temperature, volume, length, area, etc.

Vector (First Rank Tensor)

A four-dimensional vector is defined in the four-dimensional curvilinear reference frame by four numbers in the case of a contravariant vector as: $A^i = A^0, A^1, A^2, A^3$; in the case of a covariant vector as: $A_i = A_0, A_1, A_2, A_3$.

For example, during a Lorentz transformation from a four-dimensional reference frame to another, the contravariant components of the four-dimensional vectors, A^i, are converted as follows[10]:

$$A^0 = \frac{A'^0 + (V/c)A'^1}{\sqrt{1 - V^2/c^2}}, \quad A^1 = \frac{A'^1 + (V/c)A'^0}{\sqrt{1 - V^2/c^2}}, \quad A^2 = A'^2, \quad A^3 = A'^{3'}, \tag{2.15}$$

where V is a speed of motion of one inertial reference frame relative to another.

The covariant vector, A_i, is the covector of the contravariant vector, A^i. The elements of the covariant vector, A_i, and the contravariant vector, A^i, are interrelated as follows:

$$A_0 = A^0, \quad A_1 = -A^1, \quad A_2 = -A^2, \quad A_3 = -A^3. \tag{2.16}$$

The components of the four-dimensional vector can be written as:

$$A^i = (A^0, \vec{A}), \quad A_i = (A^0, -\vec{A}), \tag{2.17}$$

where A^0 is a temporal coordinate which is a scalar; $\vec{A}$ is a three-dimensional vector, which

[10] Here the speed of light, c, reintroduced for clarity.

contains the spatial coordinates. The square of the four-dimensional vector is defined as[11]:

$$\sum_{i=0}^{3} = A^i A_i = A^0 A_0 + A^1 A_1 + A^2 A_2 + A^3 A_3. \tag{2.18}$$

The connection between the covariant vector and the contravariant one is carried out through the metric tensor, $g_{\mu\nu}$, which is used to increase or decrease the indices of both the vectors and the tensors[12]:

$$g^{ik} A_k = A^i, \quad g_{ik} A^k = A_i. \tag{2.19}$$

In general, in the curvilinear coordinates, a contravariant four-dimensional vector, A^i, and a covariant one, A_i, are transformed as follows:

$$A^i = \frac{\partial x^i}{\partial x'^k} A'^k, \qquad A_i = \frac{\partial x'^k}{\partial x^i} A'_k. \tag{2.20}$$

Tensors (Second and Higher Rank Tensors)

A four-dimensional second-rank tensor is called a set of the $4^2 = 16$ components of this tensor. In the transition from one reference frame to another, these components are transformed as a product of the components of two four-dimensional vectors. Similarly, one can define the four-dimensional tensors of the third rank (with $4^3 = 64$ components) and the tensors of the higher N-th rank, constituting 4^N components.

The components of the four-dimensional tensor can be represented as: contravariant, A^{ik}, covariant, A_{ik}, and mixed, A^i_k.

A contravariant second-rank tensor, A^{ik}, is formed as a result of the product of two four-dimensional contravariant vectors, $A^i = \frac{\partial x^i}{\partial x'^l} A'^l$, and, $A^k = \frac{\partial x^k}{\partial x'^m} A'^m$. In the transition from one reference frame to another, the components of the second-rank contravariant tensor are transformed as:

$$A^{ik} = A^i \cdot A^k = \frac{\partial x^i}{\partial x'^l} \frac{\partial x^k}{\partial x'^m} A'^{lm}. \tag{2.21}$$

A covariant second-rank tensor, A_{ik}, is formed as a result of the product of two four-dimensional covariant vectors, $A_i = \frac{\partial x'^l}{\partial x^i} A'_l$, and, $A_k = \frac{\partial x'^m}{\partial x^k} A'_m$. In the transition from one reference frame to another, the components of the second-rank covariant tensor are

[11] In the tensor analysis, the Einstein rule is applied, according to which: the repeating indices twice in the expression (one of them is at the top and the other is at the bottom) means summation, and the sign of the sum is omitted.

[12] In the particular case, considering the Minkowski space, a Kronecker symbol, δ^ν_m, is used for raising or lowering the indices.

transformed as:

$$A_{ik} = A_i \cdot A_k = \frac{\partial x'^l}{\partial x^i}\frac{\partial x'^m}{\partial x^k}A'_{lm}. \tag{2.22}$$

A mixed second-rank tensor, A^i_k, is formed as a result of the product of the four-dimensional contravariant vector, $A^i = \dfrac{\partial x^i}{\partial x'^l}A'^l$, and the four-dimensional covariant vector, $A_k = \dfrac{\partial x'^m}{\partial x^k}A'_m$. In the transition from one reference frame to another, the components of the second-rank mixed tensor are transformed as[13]:

$$A^i_k = A^i \cdot A_k = \frac{\partial x^i}{\partial x'^l}\frac{\partial x'^m}{\partial x^k}A'^l_m. \tag{2.23}$$

The four-dimensional tensors (contravariant, covariant, mixed) of the N-th rank are transformed as a result of the product of N four-dimensional (contravariant, covariant, mixed) vectors, respectively. In the transition from one reference frame to another, the components of the tensors (contravariant, covariant, mixed) of N-th rank are transformed, respectively, as:

$$A^{\beta_1...\beta_N} = \frac{\partial x^{\beta_1}}{\partial x'^{\gamma_1}}...\frac{\partial x^{\beta_N}}{\partial x'^{\gamma_N}}A'^{\gamma_1...\gamma_N}, \tag{2.24}$$

$$A_{\beta_1...\beta_N} = \frac{\partial x'^{\gamma_1}}{\partial x^{\beta_1}}...\frac{\partial x'^{\gamma_N}}{\partial x'^{\beta_N}}A_{'\gamma_1...'\gamma_N}, \tag{2.25}$$

$$A^{\beta_1...\beta_l}_{\beta_{l+1}...\beta_N} = \frac{\partial x^{\beta_1}}{\partial x'^{\gamma_1}}...\frac{\partial x^{\beta_l}}{\partial x'^{\gamma_l}}\frac{\partial x'^{\gamma_{l+1}}}{\partial x^{\beta_{l+1}}}...\frac{\partial x'^{\gamma_N}}{\partial x'^{\beta_N}}A'^{\gamma_1...'\gamma_l}_{'\gamma_{l+1}...'\gamma_N}. \tag{2.26}$$

Tensors Operations

- Addition: $A^{\alpha\beta}_{\gamma\delta} + B^{\alpha\beta}_{\gamma\delta} = C^{\alpha\beta}_{\gamma\delta}$
- Subtraction: $A^{\alpha\beta}_{\gamma\delta} - B^{\alpha\beta}_{\gamma\delta} = F^{\alpha\beta}_{\gamma\delta}$
- Product: $A^{\alpha\beta}_{\gamma\delta}B^{\eta\nu}_{\gamma\delta} = C^{\alpha\beta\eta\nu}_{\gamma\delta\gamma\delta}$
- Contraction of the tensors as a result of summing over the identical indices: $B^{\lambda\chi}_{\chi\xi} = H^{\lambda}_{\xi}$
- Inner product: $F^{\alpha\beta}_{\phi\sigma}K^{\sigma\psi}_{\gamma\omega} = M^{\alpha\beta\sigma\psi}_{\phi\sigma\gamma\omega} = N^{\alpha\beta\psi}_{\phi\gamma\omega}$

2.3.3 Covariant Derivatives

Consider a vector, A_i, in the curvilinear coordinates. The differential, dA_i, of this vector is not a vector and the derivative, $\partial A_i/\partial x^k$, is not a tensor too. This is due to the fact that the differential, dA_i, is the difference of the vectors located at the different points of curved

[13] Here and above the following notations are used: $A'^{lm} = A'^l A'^m$, $A'_{lm} = A'_l A'_m$, $A'^l_m = A'^l A'_m$.

space. The vectors in curved space at the different points are transformed according to the different laws, so a special type of the derivatives is used for the curvilinear coordinates - the covariant or contravariant derivatives.

The covariant derivatives for the contravariant and covariant vectors are defined as:

$$A^i_{;j} = \frac{\partial A^i}{\partial x^j} + \Gamma^i_{kj} A^k, \qquad A_{i;j} = \frac{\partial A_i}{\partial x^j} - \Gamma^k_{ij} A_k, \tag{2.27}$$

where the functions, $\Gamma^\lambda_{\mu\nu}$, are called the Christoffel symbols or the affine connection. They are expressed in the terms of the derivatives of the metric tensor as follows:

$$\Gamma^\lambda_{\mu\nu} = \frac{1}{2} g^{\lambda\kappa} \left(\frac{\partial g_{\kappa\mu}}{\partial x^\nu} + \frac{\partial g_{\kappa\nu}}{\partial x^\mu} - \frac{\partial g_{\mu\nu}}{\partial x^\kappa} \right). \tag{2.28}$$

The covariant derivatives for the second-rank tensors: contravariant, A^{ik}, covariant, A_{ik}, and mixed type, A^i_k, are defined as:

$$A^{ik}_{;j} = \frac{\partial A^{ik}}{\partial x^j} + \Gamma^i_{mj} A^{mk} + \Gamma^k_{mj} A^{im}, \tag{2.29}$$

$$A_{ik;j} = \frac{\partial A_{ik}}{\partial x^j} - \Gamma^m_{ij} A_{km} - \Gamma^m_{kj} A_{im}, \tag{2.30}$$

$$A^i_{k;j} = \frac{\partial A^i_k}{\partial x^j} - \Gamma^m_{kj} A^i_m + \Gamma^i_{mj} A^m_k. \tag{2.31}$$

The contravariant derivatives can be formed from the covariant ones by the raising the index, which means the differentiation. This can be done using a contravariant metric tensor:

$$A_i^{;k} = g^{kj} A_{i;j}, \qquad A^{i;k} = g^{kj} A^i_{;j}. \tag{2.32}$$

2.4 Riemann-Christoffel Tensor, Ricci Tensor, Einstein Tensor. Ricci Scalar.

Riemann-Christoffel Tensor

The combination of the Christoffel symbols and their derivatives form the curvature tensor, or the so-called fourth-rank Riemann-Christoffel tensor, R^i_{klm}:

$$R^i_{klm} = \frac{\partial \Gamma^i_{km}}{\partial x^l} - \frac{\partial \Gamma^i_{kl}}{\partial x^m} + \Gamma^i_{nl} \Gamma^n_{km} - \Gamma^i_{nm} \Gamma^n_{kl}. \tag{2.33}$$

The Riemann-Christoffel tensor has the following properties:

- Cyclicality: $R^i_{klm} + R^i_{mkl} + R^i_{lmk} = 0$
- Antisymmetry of l and m indices: $R^i_{klm} = -R^i_{kml}$
- Symmetry: $R_{iklm} = R_{lmik}$
- Asymmetry: $R_{iklm} = -R_{kilm} = -R_{ikml}$
- First Bianchi identity: $R_{iklm} + R_{imkl} + R_{ilmk} = 0$
- Second Bianchi identity: $R^n_{ikl;m} + R^n_{imk;l} + R_{ilm;k} = 0$

The equality or non-equality to zero of the curvature Riemann – Christoffel tensor, R^i_{klm}, is a criterion for determining, whether four-dimensional spacetime is flat or curved. At the same time, the direct theorem is true: four-dimensional spacetime will be flat (curved) if the curvature tensor is zero (non-zero) and the inverse theorem is also true: if the curvature tensor is zero (non-zero), then four-dimensional spacetime will be flat (curved).

Ricci Tensor

The second-rank Ricci tensor, R_{ik}, is obtained by the contraction of the Riemann-Christoffel tensor:

$$R_{ik} = g^{lm} R_{limk} = R^l_{ilk}. \tag{2.34}$$

The Ricci tensor is defined as:

$$R_{ik} = \frac{\partial \Gamma^l_{ik}}{\partial x^l} - \frac{\partial \Gamma^l_{il}}{\partial x^k} + \Gamma^l_{ik}\Gamma^m_{lm} - \Gamma^m_{il}\Gamma^l_{km}. \tag{2.35}$$

The symmetry of the Ricci tensor is obvious from Eq. (2.35): $R_{ik} = R_{ki}$.

Ricci Scalar

Contracting the Ricci tensor, R_{ik}, we get a scalar value, R, which is called a Ricci scalar or the scalar curvature:

$$R = g^{ik} R_{ik} = g^{il} g^{km} R_{iklm}. \tag{2.36}$$

The Ricci scalar is a trace of the Ricci tensor, R_{ik}: $R = \sum_i R_{ii}$.

In the GTR, the action for the gravitational field, S_G, is expressed through the integral over the four-dimensional volume, $d\Omega$, from the scalar curvature density, $R\sqrt{-g}$, as follows:

$$S_G = 8\pi G \int_M R\sqrt{-g} d\Omega, \tag{2.37}$$

where g is a determinant, which composed from the matrix elements of the metric tensor, $g_{\mu\nu}$.

Einstein Tensor

The combination of the Ricci tensor, $R_{\mu\nu}$, the Ricci scalar, R, and the metric tensor, $g_{\mu\nu}$, defines the Einstein tensor:

$$G_{\mu\nu} = R_{\mu\nu} - \frac{1}{2} g_{\mu\nu} R. \tag{2.38}$$

The Einstein tensor, $G_{\mu\nu}$, is a second-rank tensor in N-dimensional spacetime. The Einstein tensor contains $N(N+1)/2$ independent components. This tensor can be constructed only from the quadratic (in the first derivatives from the metric) or the linear (in the second derivative from the metric) terms.

The Einstein tensor is symmetric due to the symmetry of the Ricci tensor, $R_{\mu\nu}$, and the metric tensor, $g_{\mu\nu}$, that form it:

$$G_{\mu\nu} = G_{\nu\mu}. \tag{2.39}$$

The Einstein tensor is an invariant under the covariant differentiation, *i.e.*, the covariant divergence of the Einstein tensor identically equals to zero:

$$G_{\mu\nu;\lambda} = 0. \tag{2.40}$$

2.4.1 Energy-Momentum Tensor

In the GTR, the notion of an energy-momentum tensor or a stress-energy tensor, $T_{\mu\nu}$, includes all the possible forms of matter and energy[14], that can distort spacetime. The energy-momentum tensor characterizes everything that can be contained in a specific region of spacetime: the energy fluid and the momentum fluid, the energy density and the momentum density, as well as energy and mass. The energy-momentum tensor is defined as the flux of a four-dimensional momentum, which passes through a three-dimensional surface of the constant coordinates.

The energy-momentum tensor, $T_{\mu\nu}$, is a second-rank tensor. Its properties are identical to the properties of the Einstein tensor, $G_{\nu\mu}$, such as, the symmetry of the energy-momentum tensor:

$$T_{\mu\nu} = T_{\nu\mu}, \tag{2.41}$$

[14] In accordance with the principle of the equivalence of mass and energy in the GTR.

and the equality to zero of the covariant divergence of the energy-momentum tensor or the fulfillment of the conservation law for the energy-momentum tensor:

$$T_{\mu\nu;\nu} = 0. \tag{2.42}$$

In the limiting case of the Minkowski metric (that is described below in Eq. (2.71)), the covariant derivative is transformed into the ordinary derivative:

$$\frac{T_{\mu\nu}}{\partial x^{\nu}} = 0. \tag{2.43}$$

In the presence of the gravitational field, the conservation law takes the form:

$$T_{\mu\nu;\nu} = \frac{\partial T_{\mu\nu}}{\partial x^{\nu}} + \Gamma^{k}_{\mu\nu} T_{k\nu} + \Gamma^{k}_{k\nu} T_{\mu\nu} = 0. \tag{2.44}$$

Consider the different forms of the energy-momentum tensor, $T_{\mu\nu}$, for the following cases: perfect fluid, vacuum and dust.

Perfect Fluid

The perfect fluid is isotropic with respect to the reference frame in which it is at rest. The perfect fluid can be completely characterized by its energy density, ρ, and the isotropic pressure, p, that are connected by the equation of state (EoS), $p = f(\rho)$. This fluid has no viscosity or heat conduction. In cosmology, the perfect fluid model is used to describe the early universe at the radiation dominated epoch.

For any reference frame the energy-momentum, tensor for the perfect fluid has the form:

$$T_{\mu\nu} = (\rho + p) u_{\mu} u_{\nu} - p g_{\mu\nu}, \tag{2.45}$$

here u_{μ} is a four-dimensional velocity.

The four-dimensional velocity is determined as:

$$u_{\mu} \equiv \frac{dx_{\mu}}{ds}. \tag{2.46}$$

The four-dimensional velocity is normalized as, $u^{\mu} u_{\mu} \equiv 1$.[15] Hence, for the observer in the comoving reference frame, relative to which the perfect fluid is at the rest, the four-

[15] In the geometric representation, u_{μ} is an unit four-dimensional vector, that is a tangent to the world line of the particle.

dimensional velocity, u_μ, has the form, $\vec{u} = (1, 0, 0, 0)$.

In the comoving reference frame, the energy-momentum tensor for the perfect fluid can be written as:

$$T_{\mu\nu} = \begin{pmatrix} \rho & 0 & 0 & 0 \\ 0 & p & 0 & 0 \\ 0 & 0 & p & 0 \\ 0 & 0 & 0 & p \end{pmatrix}. \tag{2.47}$$

From the energy-momentum conservation equation, Eq. (2.42), the continuity equation follows:

$$\frac{\partial \rho}{\partial t} + \nabla(\rho \vec{v}_{\mathrm{f}}) = 0, \tag{2.48}$$

where $\vec{v}_{\mathrm{f}}$ is the three-dimension velocity of the fluid.

This equation describes the behavior of the perfect fluid and expresses the fact of the matter conservation. Indeed, the converging velocity field leads to an increase of the density. Conversely, the diverging velocity field leads to the decrease of the density.

Vacuum

There are no fields, energy, matter in a certain region of spacetime in this case. The components of the energy-momentum tensor, $T_{\mu\nu}$, for this region are equal to zero:

$$T_{\mu\nu} = 0. \tag{2.49}$$

Dust

In cosmology, the matter in the universe is approximated by a dust fluid model or a dust matter model[16], consisting of the identical, electrically neutral, non-interacting massive particles. These particles move with the identical velocities, which are much smaller than the speed of light, $u \ll c$. The dust fluid is characterized by the zero pressure, the rest density, ρ, and the four-dimensional velocity, $u(\vec{r}, t)$[17].

In this case, the energy-momentum tensor for any reference frame is defined as:

$$T_{\mu\nu} = \rho u_\mu u_\nu. \tag{2.50}$$

[16]The validity of this approximation is related to the fact that in the astrophysical and cosmological gravitational issues, matter undergoes very high stresses, so it becomes the fluid.

[17]The real universe contains the multicomponent flows of the dust matter.

In the comoving reference frame, the energy-momentum tensor for the dust fluid takes the form:

$$T_{\mu\nu} = \begin{pmatrix} \rho & 0 & 0 & 0 \\ 0 & 0 & 0 & 0 \\ 0 & 0 & 0 & 0 \\ 0 & 0 & 0 & 0 \end{pmatrix}. \tag{2.51}$$

In the limiting case of the low velocity and zero pressure, a perfect fluid model is reduced to a dust fluid model. The dust fluid model is used for description of the universe at the matter dominated epoch.

2.4.2 Matter in the Universe

The nonrelativistic particles consisting of the baryons, the massive neutrinos and dark matter form matter in the universe. A general property of these particles is that they can accumulate under the action of the gravitational forces.

The observable universe contains 26% of dark matter; 4.8% of the ordinary baryonic matter; 0.1% of neutrino, according to Planck 2015 data, Ref. (Ade et al. (2016)).

The number density of these particles, $n(t)$, and the energy density of the matter, $\rho(t)$, change over time in the same way as[18]: $\rho(t) \sim n(t) \propto a^{-3}(\mathrm{t})$.

Baryonic Matter

The baryonic matter consists of the baryons. According to the Standard Model of particle physics, the baryons belong to the family of the hadrons. The baryons are formed from the odd number of the quarks. At the same time, the baryons are the fermions, due to the fact that they have a half-integer spin. The lightest baryons are the nucleons: protons and neutrons. The protons consist of one down (or d) quark and two up (or u) quarks, $p = uud$, and the neutrons consist of one u quark and two d quarks, $n = ddu$, Ref. (Okun (1988)).

The baryons are the components of the atomic nuclei of the ordinary matter, they constitute most of the visible matter in the universe and can also form the invisible baryonic dark matter. The energy density of the baryons at the present epoch is $\rho_{\mathrm{b}0} \approx 2.4 \cdot 10^{-7}$ GeV/cm^3. At the late stage of the evolution of the universe, which is characterized by the average temperature $\langle T \rangle \leq 100$ KeV, the ratio of the number density of the baryons to the number density of the photons remains constant, $\eta_{\mathrm{b}} \equiv n_{\mathrm{b}}/n_{\gamma} \approx 6.1 \cdot 10^{-10}$, Ref. (Rubakov (2014)).

[18] This result is valid only for cold dark matter.

Massive Neutrino

The neutrinos belong to the leptons family. The neutrinos, being leptons, can participate only in the weak gravitational interactions. The leptons are the fermions, their spin is 1/2. The leptons have no structure, so they are really the elementary particles. Being the neutral elementary particles, the neutrinos have three flavors: the electron neutrinos, ν_e, the muon neutrinos, ν_μ, and the tau neutrinos, ν_τ. If the neutrinos are the Dirac fermions, then there will be the anti-neutrinos, respectively: $\tilde{\nu}_e, \tilde{\nu}_\mu, \tilde{\nu}_\tau$. If the neutrinos are the Majorana fermions, then they will not have their antiparticle and, like the photons, they will be the really neutral particles.

The present number density for each type of the neutrinos is $n_{\nu_\alpha 0} = 110$ cm^{-3}, where $n_{\nu_\alpha} = \nu_e, \nu_\mu, \nu_\tau$. The energy density for all the types of neutrinos is $\rho_{\nu,\text{total}} \sim 6{\cdot}10^{-7}$ GeV/cm^3. The total mass of all the types of neutrinos is $\sum m_{\nu,\text{total}} < 0.23$ eV, Ref. (Ade et al. (2016)).

Dark Matter

Presumably, dark matter consists of the stable massive particles, the nature of which is not known yet. The dark matter particles do not interact with the observed electromagnetic radiation and weakly gravitationally interact with the ordinary baryonic matter.

Dark matter is located in the galaxies, as well as in the clusters of galaxies. The term "dark matter" was first introduced by Fritz Zwicky in 1933. He measured the radial velocity for eight galaxies in the constellation Coma, $v(R)$, which depends on the distance from the center of the galaxy, R. Zwicky concluded that for maintaining the stability of the galaxy, its total mass must be ten times more than the mass of the stars included in it.

Vera Rubin and Kent Ford were the first who presented the accurate calculations indicating the dark matter existence in the galaxies, Ref. (Rubin et al. (1980)). They found that in the spiral galaxies most of the stars, that are not too close to the center of the galaxies, move in the orbits with the same radial velocity, $v(R)$ =const, see Fig. (2.4) (left panel). For the regions, which contain the visible matter (considering only the visible matter), $v(R) \propto \sqrt{R}$, see Fig. (2.4) (left panel). For the large distances from the center of the galaxies, *i.e.*, for the peripheral regions of the galaxies, $v(R) \propto 1/\sqrt{R}$, see Fig. (2.4) (left panel). This discrepancy in the radial velocities of the stars can be explained by assuming that the visible matter of the galaxies is immersed in a much larger cloud — in the galactic halo. The galactic halo contains the significant mass of the invisible matter, the particles of which do not interact with the photons.

In the early stages of the evolution of the universe, the dark matter particles were in the thermodynamic equilibrium with the particles of the primordial plasma. During the universe expansion, at a certain moment of time, the temperature of the primordial plasma decreased so much that the interaction of the dark matter particles with the baryonic matter ceased, and the dark matter particles decoupled from the primordial plasma, see Fig. (2.4) (right panel).

Depending on the temperature at which this decoupling occurred (or depending on the mass of the dark matter particles at that moment), dark matter is subdivided on *Cold Dark Matter* (CDM), *Warm Dark Matter* (WDM) and *Hot Dark Matter* (HDM).

CDM consists of the heavy particles with the mass, $m_{\mathrm{CDM}} \geq 100$ KeV. The candidates for CDM are the slowly moving hypothetical particles, the so-called *weakly interacting massive particles* (WIMPs). The particles that form WDM have the mass, $m_{\mathrm{WDM}} \approx 3 - 30$ KeV. At the time of going out of the equilibrium with the primordial plasma, these particles were relativistic. During the decoupling of the HDM particles from the primordial plasma, their energy far exceeded their mass, *i.e.*, these particles were ultrarelativistic. Consequently, HDM may consist of the light particles such as the neutrinos.

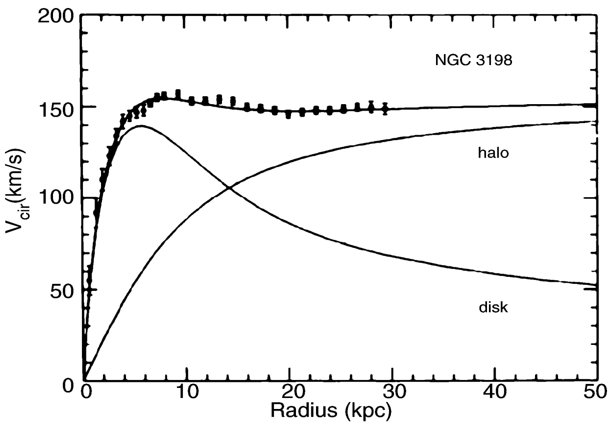

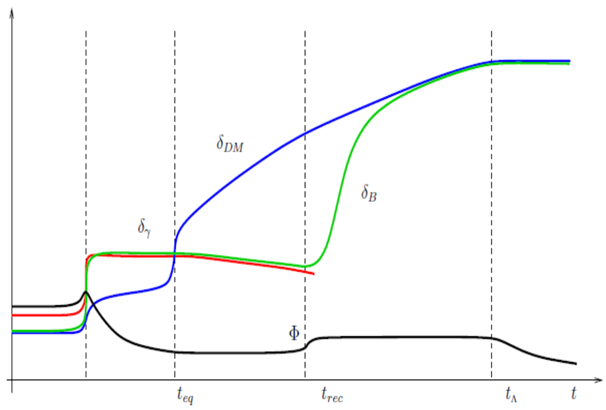

Figure 2.4: Left panel: the flat curve of the spiral galaxy NGC 3198 rotation (upper curve), which is a combination of the visible matter rotation (curve "disk") and dark matter (curve "halo"). (Figure from Ref. (Begeman et al. (1991))) Right panel: the evolution of the Newton's potential, Φ, and the relative density contrast for: dark matter, δ_{DM}, the baryons, δ_{B}, and the photons, δ_γ. t_{eq} is the transition from the radiation domination epoch to the matter domination epoch; t_{rec} is the beginning of the recombination epoch; t_Λ is the transition from the decelerated to accelerated expansion of the universe. (Figure from Ref. (Rubakov (2014)))

Dark matter plays a very important role in the large-scale structures formation of the universe. The formation of the galaxies happened in the regions with over density of dark matter. The decoupling of the dark matter particles from the primordial plasma occurred much earlier than the decoupling of the baryons. As a consequence of this, the growth of the dark matter density fluctuations happened much earlier than the growth of the baryonic matter density fluctuations, see Fig. (2.4) (right panel). The baryons fell into a potential well formed by dark matter, consequently, after recombination, the dark matter density fluctuations and the baryons density fluctuations developed together, inseparable from each other, see Fig. (2.4) (right panel).

There are numerous possible candidates for the role of dark matter. Dark matter can have of the baryonic or non-baryonic origin. Baryonic dark matter, the so-called *Massive Compact Halo Objects* (MACHOs), have low luminosity. Baryonic dark matter can be the brown dwarfs, the dark galactic halos, the massive planets, the compact objects at the final stages of the evolution: the neutron stars, the white and black dwarfs, the black holes. Non-barionic dark matter can be light or heavy neutrinos, axions, the supersymmetric particles. In addition, dark matter can be the primordial black holes and the topological defects of spacetime.

2.4.3 Einstein's Field Equations

The basic equations of the GTR are the gravitation field equations, which are called the *Einstein's field equations*:

$$G_{\mu\nu} \equiv R_{\mu\nu} - \frac{1}{2} g_{\mu\nu} R = 8\pi G T_{\mu\nu}. \tag{2.52}$$

The Einstein's field equations connect the metric of curved spacetime, $g_{\mu\nu}$, the Ricci curvature tensor, $R_{\mu\nu}$, the Ricci scalar, R, with the properties of the matter that fills this space, which is characterized by an energy-momentum tensor, $T_{\mu\nu}$. These equations establish the interrelation between the curvature (geometry) of spacetime (left side of the equation) and matter, as well as its motion (right side of the equation). Thus, the Einstein's field equations describe how the curvature of spacetime affects matter in the universe, and vice versa, how matter in the universe affects the curvature (geometry) of spacetime.

The gravitational field equations are the nonlinear second-order partial differential equations. This nonlinearity is associated with the effect of the gravity on itself, since the gravitational field carries the energy and the momentum. Due to the fact that the Einstein's field equations are nonlinear, the superposition principle is not valid for the gravitational fields. Linearization of the Einstein's field equations is possible in the case of the consideration of the gravitational waves with low amplitude or for the weak gravitational fields (for example, for the gravitational fields in the Newtonian limit). For such fields the deviations of the metric components of the equation from their values for flat spacetime are insignificant and, accordingly, the spacetime curvature generated by them is also small. In this case, the superposition principle of the fields can be applied.

In the case of the weak gravitational fields created by a nonrelativistic moving substance, the zero component of the Einstein tensor, G_{00}, is defined as:

$$G_{00} \approx \nabla^2 g_{00}, \tag{2.53}$$

for the Newtonian limit, the Einstein's field equations take the form:

$$G_{00} = -8\pi G T_{00}. \tag{2.54}$$

We obtain an alternative form of the Einstein's field equations, Eq. (2.52), contracting both sides by the contravariant metric tensor, $g^{\mu\nu}$:

$$R = -8\pi G T. \tag{2.55}$$

Substituting Eq. (2.52) into Eq. (2.55), we get another form of the Einstein's field equations:

$$R_{\mu\nu} = 8\pi G(T_{\mu\nu} - \frac{1}{2} g_{\mu\nu} T). \tag{2.56}$$

The value of the energy-momentum tensor is equal to zero for vacuum, Eq. (2.49). From Eq. (2.56) it follows that the following equation is fulfilled for vacuum:

$$R_{\mu\nu} = 0. \tag{2.57}$$

The result obtained in Eq. (2.57) does not mean that empty space is flat, and there are no gravitational fields in it. This statement requires the additional condition: the Riemann-Christoffel tensor must be equal to zero, $R^i_{klm} = 0$. In spacetime with two or three dimensions, the condition $R_{\mu\nu} = 0$ means that the Riemann-Christoffel tensor is zero and, accordingly, it means the absence of the gravitational fields there.

The full Riemann-Christoffel tensor can be non-zero under the fulfillment of the condition, $R_{\mu\nu} = 0$, in vacuum spacetime with four and higher dimensions. Therefore, in this case, the gravitational fields can exist.

2.5 Spatial Metrics

2.5.1 Flat Euclidean Space

The Euclidean geometry is based on five axioms:

1. Axiom of belonging
2. Axiom of order
3. Axiom of equality of segments and angles
4. Axiom of the parallel lines
5. Axiom of the continuity (Archimedes' axiom)

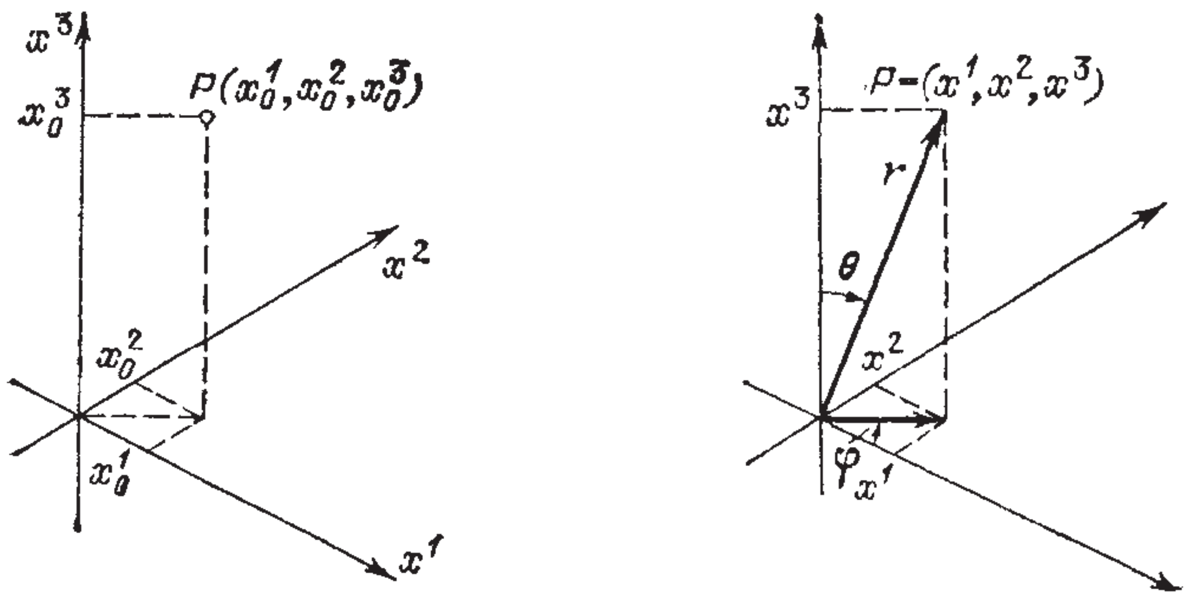

Figure 2.5: Left panel: the three-dimensional Cartesian coordinates. Right panel: the spherical coordinates. (Figure from Ref. (Dubrovin et al. (1979)))

From the "Axiom of the parallel lines" it follows the statement "The sum of the interior angles of the triangle is equal to 180°", which is very important feature of Euclidean space. Euclidian space is three-dimensional flat space. Each point in this space is defined by the orthogonal Cartesian coordinates, $(x^1, x^2, x^3 = x, y, z)$, see Fig. (2.5) (left panel).

The invariant metric in the Cartesian coordinates is defined as:

$$ds^2 = \sum_{i=1}^{3} dx^i = (x^1)^2 + (x^2)^2 + (x^3)^2. \tag{2.58}$$

The compact form of this metric is:

$$ds^2 = g_{\mu\nu} dx^\mu dx^\nu, \tag{2.59}$$

where $g_{\mu\nu} = \delta_{\mu\nu}$.

The metric tensor for Euclidean space in the Cartesian coordinates has the form[19]:

$$g_{\mu\nu} = \delta_{\mu\nu} = \begin{pmatrix} 1 & 0 & 0 \\ 0 & 1 & 0 \\ 0 & 0 & 1 \end{pmatrix}. \tag{2.60}$$

The invariant metric in the Cartesian coordinates, (dx^μ, dx^ν), can be expressed in the arbitrary coordinates, $(dx^{m'}, dx^{n'})$, as:

$$ds^2 = \delta_{\mu\nu} dx^\mu dx^\nu = \delta_{\mu\nu} \Big(\frac{\partial x^i}{\partial x^{m'}} dx^{m'}\Big)\Big(\frac{\partial x^j}{\partial x^{k'}} dx^{k'}\Big) = g_{m'k'} dx^{m'} dx^{k'}, \tag{2.61}$$

here $g_{m'k'}$ is the spatial metric tensor in an arbitrary reference frame.

Consider the Euclidean metric in the polar, cylindrical and spherical coordinates:

The polar coordinates

The Cartesian coordinates, (x^1, x^2), on the plane are expressed through the polar coordinates, $(y^1 = r,\ y^2 = \varphi)$, as:

$$x^1 = r\cos\varphi, \quad x^2 = r\sin\varphi \tag{2.62}$$

and

$$g_{m'k'} = \delta_{\mu\nu} = \begin{pmatrix} 1 & 0 \\ 0 & r^2 \end{pmatrix}. \tag{2.63}$$

The metric in the polar coordinates is given by:

$$ds^2 = (dr)^2 + r^2(d\varphi)^2. \tag{2.64}$$

The cylindrical coordinates

[19] The isotropy and the homogeneity of space is expressed in the diagonal form of the metric tensor and vice versa, the metric tensor for isotropic and homogeneous space must be diagonal.

The Cartesian coordinates, (x^1, x^2, x^3), are expressed through the cylindrical coordinates, $(y^1 = r,\ y^2 = \varphi,\ y^3 = z)$, as:

$$x^1 = r\cos\varphi, \quad x^2 = r\sin\varphi, \quad x^3 = z \tag{2.65}$$

and

$$g_{m'k'} = \begin{pmatrix} 1 & 0 & 0 \\ 0 & r^2 & 0 \\ 0 & 0 & 1 \end{pmatrix}. \tag{2.66}$$

The metric in the cylindrical coordinates is given by:

$$ds^2 = (dr)^2 + r^2(d\varphi)^2 + \sin^2(d\varphi)^2. \tag{2.67}$$

The spherical coordinates

The Cartesian coordinates, (x^1, x^2, x^3), are expressed through the spherical coordinates, $(y^1 = r, y^2 = \theta, y^3 = \varphi)$, see Fig. (2.5) (right panel) as:

$$x^1 = r\cos\varphi\sin\theta, \quad x^2 = r\sin\varphi\sin\theta, \quad x^3 = r\cos\theta \tag{2.68}$$

and

$$g_{m'k'} = \begin{pmatrix} 1 & 0 & 0 \\ 0 & r^2 & 0 \\ 0 & 0 & r^2\sin^2\varphi \end{pmatrix}. \tag{2.69}$$

The metric in the spherical coordinates is given by:

$$ds^2 = dr^2 + r^2[(d\theta)^2 + r^2\sin^2\theta(d\varphi)^2]. \tag{2.70}$$

2.5.2 Minkowski Spacetime

In 1908, Hermann Minkovski first introduced four coordinates for description of four-dimensional vector space or the spacetime continuum. The points of this spacetime are called the events or the *world points*. Each event corresponds to a set of four numbers (x^0, x^1, x^2, x^3), where $x^0 = t$ is a moment of time when the event occurred and (x^1, x^2, x^3) is the location of the event. In four-dimensional space, the process of life for each object is identified by the line $x^i(t)$ $(i = 1, 2, 3)$, which is called the *world line*. The values of (t, x^1, x^2, x^3) can be regarded

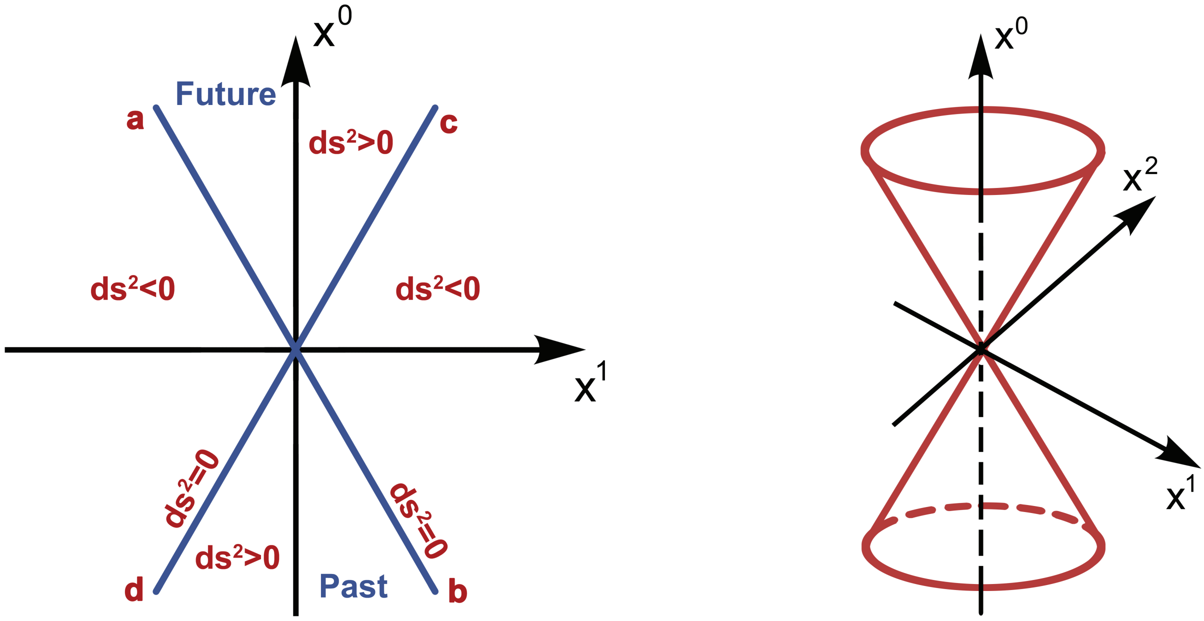

Figure 2.6: Left panel: two-dimensional Minkovski diagram. Right panel: three-dimensional light cone.

as the Cartesian coordinates in the spacetime continuum. Thereby, the spacetime continuum can be considered as four-dimensional Cartesian space. On the contrary, three-dimensional space, in which the classical geometry unfolds, will be a surface of the constant level (where t=const).

The metric tensor of Minkowski spacetime is defined as[20]:

$$\eta_{\mu\nu} = \delta_{\mu\nu} = \begin{pmatrix} 1 & 0 & 0 & 0 \\ 0 & -1 & 0 & 0 \\ 0 & 0 & -1 & 0 \\ 0 & 0 & 0 & -1 \end{pmatrix}. \tag{2.71}$$

This metric tensor describes flat four-dimensional isotropic and homogeneous spacetime. The metric for the Minkovski metric tensor is represented as:

$$ds^2 = \eta_{\mu\nu} dx^\mu dx^\nu. \tag{2.72}$$

The metric, ds^2, can take the following values in four-dimensional spacetime: to be equal to zero, to be positive or negative. The metric, $ds^2 = 0$, corresponds to the propagation of a signal with the speed of light or a motion of the massless particles in four-dimensional

[20]Hereinafter, the metric signature is used, $(1, -1, -1, -1)$.

spacetime. The zero metric, $ds^2 = 0$, describes the lightlike events. The positive metric, $ds^2 > 0$, describes the timelike events. For the timelike events, there is a frame of reference in which these events can occur in the same place. In this case, the linear interval between two events, ds, is a real number. A negative metric, $ds^2 < 0$, describes the spacelike events. There is a frame of reference for the spacelike events, in which these events can occur simultaneously. In this case, the linear interval between two events, ds, is an imaginary number.

The above-mentioned types of the events are presented on the two-dimensional, (x^0, x^1), Minkovski diagram, see Fig. (2.6) (left panel). The origin of the coordinate, O, corresponds to the present point in time. The lines ab and cd are consistent with two different signals, which propagate at the speed of light, so $ds^2 = 0$ for them. The spacelike events are contained in the dOa and cOb regions with $ds^2 < 0$, while the regions aOc and dOb correspond to the timelike events with $ds^2 > 0$.

Since the time from the aOc region has a positive value, $t > 0$, the events from this region will happen in the future with respect to the present moment of time, O. The time from the dOb region has a negative value, $t < 0$, consequently, the events from this region happened in the past with respect to the present point in time, O. In other words, the events from the aOc region can be called the "absolutely future", consequently, the events from the dOb region can be called the "absolutely past" with respect to the present point in time, O. Since it can be unambiguously determined which of the events with a timelike interval occurred earlier and which later, these events can be causally-related to each other.

The metric for the Minkowski spacetime, Eq. (2.72), is timelike, so it can be located in the aOc and dOb regions on the Minkowski diagram. This metric can be written in the extended form:

$$ds^2 = (x^0)^2 - (x^1)^2 - (x^2)^2 - (x^3)^2. \tag{2.73}$$

Eq. (2.73) describes a so-called light cone or, in other words, a cone of the causal events. The three-dimensional Minkowski coordinates, (x^0, x^1, x^2), can be expressed in the terms of the pseudospherical coordinates, $(\varrho, \varsigma, \varphi)$:

$$\chi(r) = \begin{cases} x^0 = \varrho \cosh \varsigma \\ x^1 = \varrho \sinh \varsigma \\ x^2 = \varrho \sinh \varsigma \sin \varphi \end{cases} \tag{2.74}$$

From Eq. (2.74) it follows:

$$(x^0)^2 - (x^1)^2 - (x^2)^2 = \varrho^2 > 0. \tag{2.75}$$

Therefore, the coordinates, $(\varrho, \varsigma, \varphi)$, are defined only in the region, $(x^0)^2 - (x^1)^2 - (x^2)^2 > 0$. This region is located inside of the light cone in three-dimensional spacetime, $(x^0)^2 = (x^1)^2 + (x^2)^2$, see Fig. (2.6) (right panel). The metric for this region has the form:

$$ds^2 = d\varrho^2 - \varrho^2[(d\chi)^2 + \sinh^2\chi(d\varphi)^2]. \tag{2.76}$$

2.5.3 Geodesic Equation

Suppose that a point with the coordinates x^i moves along a certain trajectory with the four-dimensional velocity, $u^i = x^i/ds$. According to the GTR, a free material point moves in the gravitational field in four-dimensional spacetime, so its world line is extremal. This extremal world line is called the *geodesic* line between two given world points.

The motion of the particle in the gravitational field is determined by the **principle of least action**, according to which the action functional takes the minimum value:

$$\delta S = \delta \int ds = 0, \tag{2.77}$$

where $ds^2 = g_{ik}dx^i dx^k$ is a metric in four-dimensional curved spacetime.

Applying the principle of least action, we obtain the equation of motion of the particle in the gravitational field.

Due to the fact that:

$$\delta ds^2 = 2ds\delta ds = \delta(g_{ik}dx^i dx^k) = dx^i dx^k \frac{\partial g_{ik}}{dx^l}\delta x^l + 2g_{ik}dx^i d\delta x^k. \tag{2.78}$$

Substituting this result into Eq. (2.77), we get:

$$S = \int \Big(\frac{dx^i}{ds}\frac{dx^k}{ds}\frac{dg_{ik}}{dx^l}\delta x^l + g_{ik}\frac{dx^i}{ds}\frac{d\delta x^k}{ds}\Big)ds = 0. \tag{2.79}$$

While we integrate Eq. (2.79) by parts and take into account that in the second term at the boundaries of integration $\delta x^k = 0$, we obtain:

$$S = \int \Big(\frac{1}{2}\frac{dx^i}{ds}\frac{dx^k}{ds}\frac{dg_{ik}}{dx^l}\delta x^l - \frac{d}{ds}\Big(g_{ik}\frac{dx^i}{ds}\Big)\delta x^k\Big)ds = 0. \tag{2.80}$$

Replacing the index k with the index l, in the second term of Eq. (2.80):

$$\frac{1}{2}u^i u^k \frac{dg_{ik}}{dx^l} - \frac{d}{ds}(dg_{il}u^i) = \frac{1}{2}u^i u^k \frac{dg_{ik}}{dx^l} - g_{il}\frac{du^i}{ds} - u^i u^k \frac{dg_{il}}{dx^k} = 0. \tag{2.81}$$

We represent the third term in Eq. (2.81) as:

$$u^i u^k \frac{dg_{il}}{dx^k} = \frac{1}{2}u^i u^k \Big(\frac{dg_{il}}{dx^k} + \frac{dg_{kl}}{dx^i}\Big). \tag{2.82}$$

Multiplying the left and right sides of Eq. (2.81) by g^{im}:

$$g^{im}g_{il}\frac{du^i}{ds} + \frac{1}{2}g^{im}u^i u^k \Big(\frac{dg_{il}}{dx^k} + \frac{dg_{kl}}{dx^i} - \frac{dg_{ik}}{dx^l}\Big) = 0. \tag{2.83}$$

Considering that $g^{im}g_{il} = \delta_l^m$, we replace the index l with the index m in the expression located in the parentheses, Eq. (2.83):

$$\frac{du^i}{ds} + \frac{1}{2}g^{im}u^i u^k \Big(\frac{dg_{il}}{dx^k} + \frac{dg_{km}}{dx^i} - \frac{dg_{ik}}{dx^m}\Big) = 0. \tag{2.84}$$

As a result of replacing the index i to the index l in the expression located in the parentheses, Eq. (2.84), and introducing the Christoffel symbols, $\Gamma^i_{kl} = \frac{1}{2}g^{im}\left(\frac{\partial g_{mk}}{\partial x^l} + \frac{\partial g_{ml}}{\partial x^k} - \frac{\partial g_{kl}}{\partial x^m}\right)$, we obtain the equation of motion of a material point in the gravitational field along the geodesic line:

$$\frac{d^2x^i}{ds^2} + \Gamma^i_{kl}\frac{dx^k}{ds}\frac{dx^l}{ds} = 0. \tag{2.85}$$

The geodesic line has a curved shape in four-dimensional spacetime, (x^0, x^1, x^2, x^3), and the motion of the particle is not uniform and rectilinear.

2.5.4 Isotropic Four-Dimensional Spacetime Metric

The metric tensor for four-dimensional homogeneous and isotropic spacetime, which is spatially expanding or contracting with dependence on the scale factor, $a(t)$[21], is defined as follows:

$$g_{\mu\nu} = \begin{pmatrix} 1 & 0 & 0 & 0 \\ 0 & -a^2(t) & 0 & 0 \\ 0 & 0 & -a^2(t) & 0 \\ 0 & 0 & 0 & -a^2(t) \end{pmatrix}. \tag{2.86}$$

[21] This metric tensor describes the expanding spacetime, since a scale factor is the time-dependent increasing function, $\dot{a}(t) > 0$.

The metric for this spacetime is:

$$ds^2 \equiv g_{\mu\nu}dx^\mu dx^\nu = dt^2 - a^2(t)\gamma_{ij}dx^i dx^j, \tag{2.87}$$

where γ_{ij} is a metric of three-dimensional space.

The function γ_{ij} in the spherical coordinates, (r, θ, φ), Eq. (2.87), is represented as:

$$\gamma_{ij} = dr^2 + \chi(r)^2(d\theta^2 + \sin^2\theta d\varphi^2), \tag{2.88}$$

here $\chi(r)$ is a space curvature function, which is defined as:

$$\chi(r) = \begin{cases} \frac{1}{\sqrt{\mathrm{K}}}\sin\left(\sqrt{\mathrm{K}}\ r\right) & \text{for K} > 0 \\ r & \text{for K} = 0 \\ \frac{1}{\sqrt{-\mathrm{K}}}\sinh\left(\sqrt{-\mathrm{K}}\ r\right) & \text{for K} < 0 \end{cases}, \tag{2.89}$$

here K is a curvature parameter.

Replacing the variable $x = \xi$ in Eq. (2.89) and expressing the variable r through x, we find the square of the differential dr^2:

$$dr^2 = \begin{cases} \frac{1}{1-\mathrm{K}x^2}dx^2 & \text{for K} > 0 \\ dx^2 & \text{for K} = 0 \\ \frac{1}{1-\mathrm{K}x^2}dx^2 & \text{for K} < 0 \end{cases}. \tag{2.90}$$

Substituting Eq. (2.89) and Eq. (2.90) into Eq. (2.87), we get the expression for the Friedmann-Lemaître-Robertson-Walker (FLRW) spacetime metric:

$$ds^2 = dt^2 - a^2(t)\left[\frac{dr^2}{1-\mathrm{K}r^2} + r^2(d\theta^2 + \sin^2\theta d\varphi^2)\right]. \tag{2.91}$$

This metric describes the homogeneous and isotropic expanding space. The coordinates, $(r,\ \theta,\ \varphi)$, are the comoving coordinates, *i.e.*, the moving object is at rest relative to these coordinates.

The FLRW metric in the Cartesian coordinates can be written as:

$$ds^2 = dt^2 - a^2(t)\frac{1}{(1+\frac{\mathrm{K}}{4}r^2)^2}\delta_{ij}dx^i dx^j. \tag{2.92}$$

Depending on the sign of the curvature parameter, K, Eq. (2.91) describes the geometrically

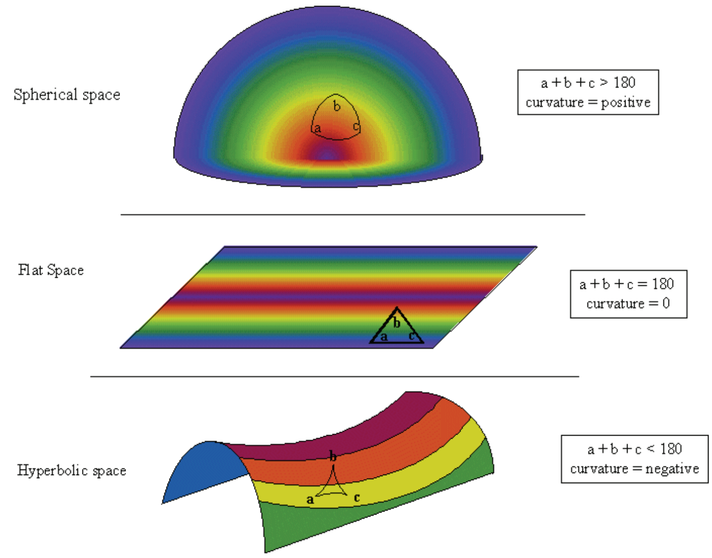

Figure 2.7: The examples of closed, flat and open two-dimensional spaces. (Figure from http://www.astro.cornell.edu/academics/courses/astro201/)

different types of the universe. The case $\mathrm{K} > 0$ corresponds to the so-called *closed universe* (to spherical three-dimensional space). The two-dimensional analogue of this universe is the surface of a sphere, see Fig. (2.7), and the function, $1/\sqrt{\mathrm{K}}$, can be interpreted as its curvature radius. The case $\mathrm{K} = 0$ corresponds to the so-called *flat universe* (to Euclidean three-dimensional space), see Fig. (2.7). The case $\mathrm{K} < 0$ corresponds to the so-called *open universe* (to three-dimensional hyperbolic space). The two-dimensional analogue of this universe is the surface of a saddle, see Fig. (2.7).

The curvature of the universe can be neglected in the study of the certain processes. For example, when a photon moves freely in the homogeneous and isotropic universe, the wavelength of the photon will be much smaller than the radius of the spatial curvature of the universe (in the case of an open or closed universe). In this case, the universe can be considered as spatially flat and the metric presented in Eq. (2.87) can be used.

In the terms of conformal time, which is defined in Eq. (2.4), the Eq. (2.87) takes the form:

$$ds^2 = a^2(\eta)d\eta^2 - a^2(\eta)\gamma_{ij}dx^i dx^j = a^2(\eta)[\eta^2 - \gamma_{ij}dx^i dx^j]. \tag{2.93}$$

From Eq. (2.93), it follows the relation between the Minkowski metric tensor $\eta_{\mu\nu}$ and the metric tensor $g_{\mu\nu}$:

$$g_{\mu\nu} = a^2(\eta)\eta_{\mu\nu}. \tag{2.94}$$

Hence, the metric tensor, $g_{\mu\nu}$, has a conformally flat form in the coordinates, (η, x^μ).

For the different types of the curvature, Eq. (2.93) has the form:

$$ds^2 = a^2(\eta)(d\eta^2 - d\xi^2 - \varpi^2(d\theta^2 + \sin^2\theta d\varphi^2)), \tag{2.95}$$

where the variable ϖ is defined as:

$$\varpi = \begin{cases} \sin\xi & \text{for} \quad \mathrm{K} > 0,\ r = a(\eta)\sin\xi,\ \xi \in [0, \pi] \\ \xi & \text{for} \quad \mathrm{K} = 0,\ r = a(\eta)\xi,\ \xi \in [0, \infty] \\ \sinh\xi & \text{for} \quad \mathrm{K} < 0,\ r = a(\eta)\sinh\xi,\ \xi \in [0, \infty] \end{cases} \tag{2.96}$$

2.5.5 Friedmann's Equations

Substituting the FLRW metric, Eq. (2.91), and the energy-momentum tensor, Eq. (2.45), into the Einstein's equations, Eq. (2.52), the first and the second Friedmann's equations can be derived:

$$\frac{\dot{a}^2}{a^2} = \frac{8\pi G}{3}\rho - \frac{\mathrm{K}}{a^2} \tag{2.97}$$

and

$$\frac{\ddot{a}}{a} = -\frac{4\pi G}{3}(\rho + 3p). \tag{2.98}$$

If we know the evolution of the scale factor, $a(t)$, which characterizes the expansion history of the universe, we will be able to determine the value of the curvature parameter and the mass-energy composition of the universe using the Friedmann's equations. Conversely, if we know the value of the curvature parameter and the matter-energy content of the universe, we will be able to calculate the evolution of the scale factor, $a(t)$. For example: the expansion history of the universe depends on the value of the curvature parameter, K: for $\mathrm{K} < 0$ (the open universe), the universe will expand forever, see Fig. (2.8); for $\mathrm{K} = 0$ (the flat universe), the universe will expand forever either, but for $t \to \infty$, the expansion will occur with the constant velocity, *i.e.*, $\dot{a} \to 0$, see Fig. (2.8); for $\mathrm{K} > 0$ (the close universe), the universe will expand till certain moment, after that the expansion will turn into a contraction and the universe will re-collapse, see Fig. (2.8).

As mentioned previously, all the matter-energy components of the universe on the cosmological scales can be modeled as the perfect fluid. The relation between the energy density and the pressure for the perfect fluid is defined by the EoS:

$$p = w\rho, \tag{2.99}$$

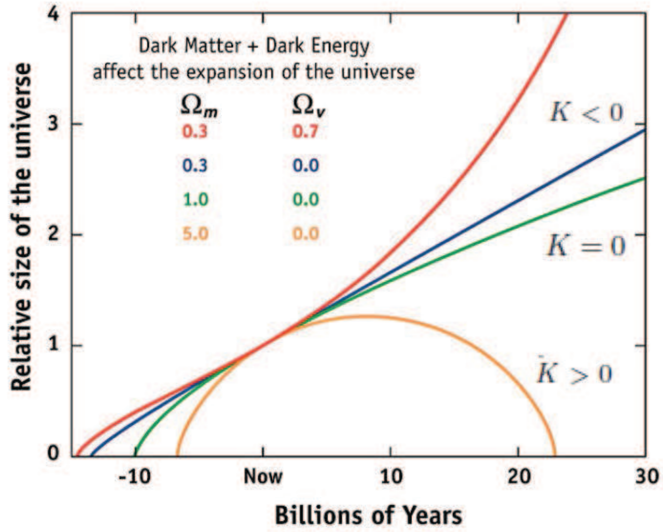

Figure 2.8: The evolution of the scale factor, $a(t)$, for the different signs of the curvature parameter, K. (Figure from https://wmap.gsfc.nasa.gov/universe/)

where w is an EoS parameter, the value of which is different for each matter-energy component in the universe.

If we solve the continuity equation, Eq. (2.48), and the Friedmann's equation, Eq. (2.97), for a flat universe, $\mathrm{K}=0$, we will get the following equations:

$$\rho \propto a^{-3(1+w)}, \quad a(t) \propto t^{\frac{2}{3(1+w)}} \quad \Rightarrow \quad H = \frac{2}{3(1+w)t}, \tag{2.100}$$

where the value of the EoS parameter, w, is time-independent and $w \neq 1$.

The equations, which are determined in Eq. (2.100), describe the evolution of the energy density, ρ, the scale factor, a, and the Hubble parameter, H, in dependence on the value of the EoS parameter, w, and the physical time, t. Let's analyze Eq. (2.100) for the different values of the EoS parameter, w. We suppose that only one matter-energy component is contained in the universe, which is described by the given EoS parameter.

The EoS parameter, $w=1/3$, corresponds to the perfect fluid of the relativistic particles (the photons and the neutrinos), which is called the radiation. For this case Eq. (2.100) takes the form:

$$\rho_{\mathrm{r}} \propto a^{-4}, \quad a(t) \propto t^{\frac{1}{2}} \quad \Rightarrow \quad H = \frac{1}{2t}. \tag{2.101}$$

The EoS parameter, $w=0$, corresponds to the perfect fluid of the non-relativistic particles or the dust (matter), which consists of CDM and the baryons. Accordingly, in this case, Eq. (2.100) takes the form:

$$\rho_{\rm m} \propto a^{-3}, \quad a(t) \propto t^{\frac{2}{3}} \quad \Rightarrow \quad H = \frac{2}{3t}. \tag{2.102}$$

The EoS parameter, $w = -1/3$, corresponds to the universe with the nonzero spatial curvature, *i.e.*, for the close or open universe. In this case, Eq. (2.100) takes the form:

$$\rho_{\rm K} \propto a^{-2}, \quad a(t) \propto t \quad \Rightarrow \quad H = \frac{1}{t}. \tag{2.103}$$

If we substitute the EoS, which is defined in Eq. (2.99), in the second Friedmann's equation, Eq. (2.98), we will get:

$$\frac{\ddot{a}}{a} = -\frac{4\pi G\rho}{3}(1+3w). \tag{2.104}$$

If the value of the EoS parameter, w, satisfies the condition, $-1 \leq w < -\frac{1}{3}$, then $\ddot{a} \leq -1$, *i.e.*, the universe will expand with an acceleration. The accelerated expansion of the universe is explained by the presence of dark energy in it. The case $w = -1$ corresponds to the simplest model of dark energy, the so-called vacuum energy or the cosmological constant Λ. In this case, the universe is accelerating with a constant energy density, ρ_Λ, and with a constant Hubble parameter, whereas the scale factor changes exponentially over time:

$$\rho_\Lambda = \text{const}, \quad a(t) \propto e^{Ht} \quad \Rightarrow \quad H = \text{const}. \tag{2.105}$$

The total energy density of the universe includes the following components: the radiation, the matter, the curvature and dark energy:

$$\rho = \rho_{\rm r} + \rho_{\rm m} + \rho_{\rm K} + \rho_\Lambda. \tag{2.106}$$

If we consider the dependence of the energy density components on the scale factor, which is presented in the equations, Eq. (2.101)- Eq. (2.105), we will get:

$$\rho = \rho_{\rm r0}a^{-4} + \rho_{\rm m0}a^{-3} + \rho_{\rm K0}a^{-2} + \rho_\Lambda, \tag{2.107}$$

where $\rho_{\rm r0}$, $\rho_{\rm m0}$, $\rho_{\rm K0} = -{\rm K}/H_0^2$, and ρ_Λ are the values for the energy densities at the present epoch: for the radiation, the matter, the curvature and dark energy, respectively.

The equation for the total energy density, ρ_0, at the present epoch, $a = a_0 = 1$:

$$\rho_0 = \rho_{\rm r0} + \rho_{\rm m0} + \rho_{\rm K0} + \rho_\Lambda. \tag{2.108}$$

Eq. (2.107) can be represented in more convenient form through the dimensionless density parameters. The dimensionless density parameters are usually applied for the description of the matter-energy content in the universe:

$$\Omega = \rho/\rho_{\rm cr} = \Omega_{\rm r0}a^{-4} + \Omega_{\rm m0}a^{-3} + \Omega_{\rm K0}a^{-2} + \Omega_\Lambda, \tag{2.109}$$

where Ω is a total energy density parameter, which is defined for an arbitrary moment of time; Ω_{i0} is an energy density parameter for the 'i' component at the present epoch, which is characterized by the corresponding energy density, ρ_{i0}; $\rho_{\rm cr}$ is a critical density in the universe at the present epoch[22]. The value of the critical energy today is equal to $\rho_{\rm cr} = 3H_0^2/8\pi G = 1.8791h^2 \cdot 10^{-29}$ g cm^{-3}

At the present epoch, Eq. (2.109) has the form:

$$\Omega_0 = \rho_{i0}/\rho_{\rm cr} = \sum_i \Omega_{i0} = \sum_i \Omega_{i0} = \Omega_{\rm r0} + \Omega_{\rm m0} + \Omega_{\rm K0} + \Omega_\Lambda, \tag{2.110}$$

where Ω_0 is a total energy density parameter at the present epoch. This parameter is one of the most important cosmological parameters.

The first Friedmann's equation, which is defined in Eq. (2.97), can be expressed in the terms of the current energy density parameters, Ω_{i0}, as:

$$H(a) = H_0(\Omega_{\rm r0}a^{-4} + \Omega_{\rm m0}a^{-3} + \Omega_{\rm K0}a^{-2} + \Omega_\Lambda)^{1/2}. \tag{2.111}$$

Eq. (2.111) can be represented as:

$$E(a) = (\Omega_{\rm r0}a^{-4} + \Omega_{\rm m0}a^{-3} + \Omega_{\rm K0}a^{-2} + \Omega_\Lambda)^{1/2}, \tag{2.112}$$

where $E(a) = H(a)/H_0$ is a dimensionless Hubble parameter.

If we rewrite Eq. (2.111) at the present epoch, we will get:

$$\Omega_0 - 1 = \frac{\rm K}{H_0^2}. \tag{2.113}$$

[22] The critical density is a total energy density in the universe which is necessary for the universe to be spatially flat.

From Eq. (2.113) it follows that the value of the total density parameter, $\Omega_0 > 1$, corresponds to the closed universe with the positive curvature parameter, $\mathrm{K} > 0$, see Fig. (2.8). The value of the total density parameter, $\Omega_0 < 1$, corresponds to the open universe, where the curvature parameter is negative, $\mathrm{K} < 0$, see Fig. (2.8). The value of the total density parameter, $\Omega_0 = 1$, corresponds to the flat universe with the zero curvature parameter, $\mathrm{K} = 0$, see Fig. (2.8). According to Planck 2015, Ref. (Ade et al. (2016)), the current curvature density parameter is $\Omega_{\mathrm{K}0} = 0.006$ (at the 68% confidence level). Thus, the critical density in the universe corresponds to the average energy density in the universe, $\langle\rho\rangle$, *i.e.*, $\rho_{\mathrm{cr}} = \langle\rho\rangle$, with an accuracy of the order of 1%.

2.5.6 Acceleration Parameter

Take a time derivative from the Hubble parameter which is defined in Eq. (2.7):

$$\dot{H} = \frac{a\ddot{a} - \dot{a}^2}{a^2} = -H^2 + \frac{\ddot{a}}{a} = -H^2\Big(1 - \frac{\ddot{a}}{H^2 a}\Big) = -H^2(1-q), \tag{2.114}$$

and

$$q \equiv \frac{\ddot{a}}{aH^2}, \tag{2.115}$$

where a dimensionless parameter, q, is called an *acceleration parameter*[23]. The current value of the acceleration parameter, q_0, is defined as:

$$q_0 \equiv \frac{1}{H_0^2}\Big(\frac{\ddot{a}}{a}\Big)_0. \tag{2.116}$$

The acceleration parameter characterizes the state of the acceleration or deceleration of the universe. A positive value of this parameter, $q > 0$, corresponds to the acceleration expansion of the universe, for which $\ddot{a} > 0$, and a negative value, $q < 0$, corresponds to the deceleration expansion of the universe, for which $\ddot{a} < 0$.

The acceleration parameter can be expressed in terms of the values of the EoS parameter, w_i, and the energy density parameter, Ω_i:

$$q(t) = -\frac{1}{2}\sum_i (1 + 3w_i)\Omega_i(t), \tag{2.117}$$

here, the index "i" indicates a certain component of the energy density in the universe and

[23] In the literature, the so-called deceleration parameter is the most commonly mentioned, which is defined as, $q \equiv -\ddot{a}/aH^2$. Here we use the designation "acceleration parameter" because this designation better describes the current state of the universe.

the corresponding EoS parameter. If we use the values of the EoS parameter for the matter, the radiation and vacuum, respectively: $w_{\mathrm{m}} = 0, w_{\mathrm{r}} = 1/3, w_{\Lambda} = -1$, we will get:

$$q(t) = -(\Omega_{\mathrm{m}}/2 + \Omega_{\mathrm{r}} - \Omega_{\Lambda}). \tag{2.118}$$

By applying the data from Planck 2015, Ref. (Ade et al. (2016)), we can calculate the value of the current acceleration parameter of the universe:

$$[q_0]_{\mathrm{Planck}} \approx 0.54. \tag{2.119}$$

A positive sign of the current acceleration parameter, q_0, indicates that our universe is in the accelerated state nowadays. This state began at the value of the scale factor, $a \approx 0.60$, or at redshift, $z \approx 0.65$, according to Planck 2015 data, Ref. (Ade et al. (2016)).

Chapter 3

Distance in Cosmology

3.1 Concept of Distance in Cosmology

The definition of the distances between the astronomical objects in the expanding universe is one of the main and most difficult problems in cosmology.

There is no concept of a single distance in cosmology. The different types of the cosmological distances are used, such as: the physical distance, the comoving distance[1], the luminosity distance, the angular diameter distance, etc. These distances differ from each other in the methods of their determination and measurement.

In cosmology, the concept of the "exact distance" to a remote object is vague. The values of the cosmological distances depend on the chosen cosmological model and, therefore, they are the functions of the model parameters. Thus, the accuracy in the determining the distances depends on the correctness of the considering cosmological model and on the accuracy of determining the model parameters[2].

The above-mentioned cosmological distances are united by the fact that these distances are a measure of the separation of two objects located on a radial trajectory from each other.

A vivid example of the importance of the exact cosmological distances definition is the evidence of the existence of dark energy in the universe. This definition is largely based on the measured luminosity distances to the type Ia supernovae. The position of an object on a sphere gives us the two-dimensional picture. To obtain the three-dimensional information, very precise distance measurements are required. In addition, the knowledge of the distances

[1] The definition of the physical distance and the comoving distance (length scales) was given in Chapter II.

[2] In cosmology, all the values obtained from the observations (the distances, the model parameters, etc.) are found using the statistical methods or the probability theory (for more information, see Chapter V). Therefore, when a calculated value is mentioned, it is always necessary to indicate the accuracy with which it was obtained. Usually the confidence level are indicated, 1σ, 2σ, 3σ, or the corresponding accuracy levels, 68.27%, 95.45%, 99.73%, where σ is a standard deviation in the Gaussian distribution.

to the remote astronomical objects is necessary to determine the physical parameters of the universe.

3.2 Trigonometric Parallax

The trigonometric parallax is one of the most important distance measurement methods used in astronomy. This method is based on a geometrical effect. Due to the rotation of the Earth around the Sun, for an observer located on the surface of the Earth, the positions of the nearby stars change against the background of the distant objects, see Fig. (3.1). During the year, the visible position of the nearby star follows an ellipse on the sphere, see

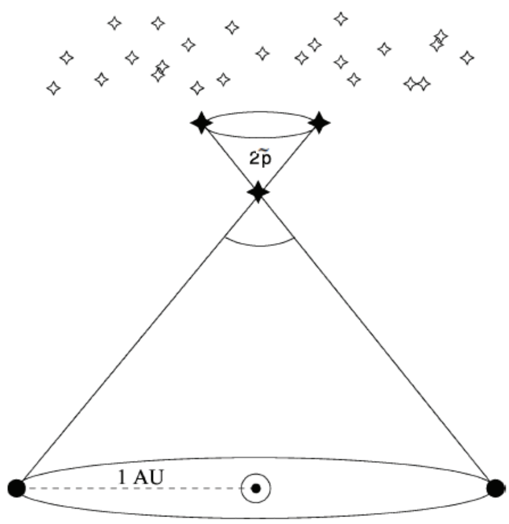

Figure 3.1: Illustration of the parallax effect. (Figure from Ref. (Schneider (2006)))

Fig. (3.1). The semimajor axis of this ellipse is called a *parallax*, $\tilde{p}$. The value of the parallax, $\tilde{p}$, depends on the physical distance to the star, d, and the radius of the Earth's orbit, $r_{\oplus}$, which is equal to one astronomical unit (AU)[3], see Fig. (3.1). The value of the parallax is defined as:

$$\frac{r_{\oplus}}{d} = \tan \tilde{p} \approx \tilde{p}, \tag{3.1}$$

where $\tilde{p} \ll 1$ and $\tilde{p}$ are measured in the radians.

[3]More precisely, $1\mathrm{AU} = 1.496 \cdot 10^{13}$ cm is a semimajor axis of the Earth's ellipsoidal orbit.

The physical distance to the object corresponding to the measured parallax, $\tilde{p}$, can be found as:

$$d = \left(\frac{\tilde{p}}{1''}\right)^{-1} \text{ pc}. \tag{3.2}$$

The trigonometric parallax is also applied to determine one of the basic units of the distance in astronomy, the *parsec*. The parsec (pc)[4] is the distance to the object for which the parallax is one second, $\tilde{p} = 1''$, where $1'' \approx 4.8484 \cdot 10^{-6}$ radian and $\tilde{p}/1'' = 206265$ pc, so:

$$1 \text{ pc} = 206265 \text{ AU} = 3.086 \cdot 10^{18} \text{ cm}. \tag{3.3}$$

The trigonometric parallax is a very accurate method for determining distances, but it can be used only for the nearby stars. Using this method, the distances to the stars can be defined only within a distance ~ 5 Kpc, Refs. (Gaia (2013), Brown et al. (2018)).

3.3 Cosmological Redshift

Relativistic Doppler Shift[5]

Consider a distant source of light that emits the consequent light signals at the time moments, $t_{\rm em}$ and $t_{\rm em} + \Delta t_{\rm em}$, respectively. The measurements were carried out according to the clock, which was at rest relative to the source. This source of light moves relative to the observer with the velocity, $\vec{u}$, see Fig. (2.8). The time interval between two consequent light signals, which were emitted by the source, $\Delta t_{\rm obs}$, will be affected: by the relativistic effect of time dilation associated with the motion of the source, $\Delta t_{\rm em}/\sqrt{1-u^2/c^2}$, and by the effect associated with the difference of the distances traveled by two signals from the moving source of light to the observer, $\Delta d = u \cos\theta \Delta t_{\rm em}/\sqrt{1-u^2/c^2}$, see Fig. (3.2).

Thus, the time interval between two signals registered by the observer is:

$$\Delta t_{\rm obs} = \frac{\Delta t_{\rm em}}{\sqrt{1-u^2/c^2}} + \frac{u/c \Delta t_{\rm em} \cos\theta}{\sqrt{1-u^2/c^2}} = \frac{\Delta t_{\rm em}}{\sqrt{1-u^2/c^2}}(1 + u/c\cos\theta). \tag{3.4}$$

Suppose that a photon with the wavelength, $\lambda_{\rm em}$, (or the frequency, $\nu_{\rm em}$)[6], was emitted at the moment of time, $t_{\rm em}$. This photon is observed at the moment of time, $t_{\rm obs}$, with the wavelength, $\lambda_{\rm obs}$, (or with the frequency, $\nu_{\rm obs}$). The time interval between two consequent

[4] The scales of the greater length are considered in cosmology, so 1 Mpc $= 10^6$ pc is used as an unit of the measurement.

[5] In this section, the speed of light, c, is reintroduced for clarity.

[6] The wavelength and the frequency of the electromagnetic radiation are interconnected as, $\lambda\nu = c$

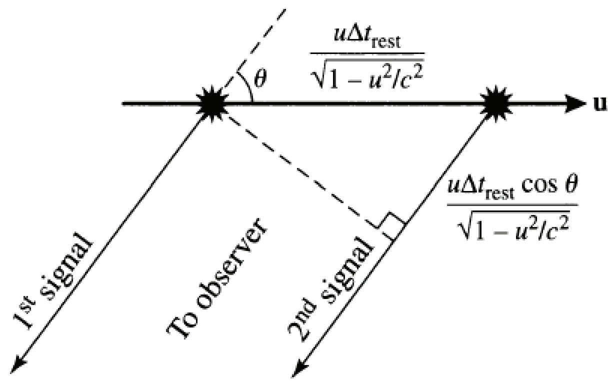

Figure 3.2: Illustration of the relativistic Doppler shift. (Figure from Ref. (Carroll & Ostlie (2007)))

light signals emitted by the source, Δt_{em}, and registered by the observer, Δt_{obs}, is related to the frequency of the emitted photons, Δt_{obs}, and the frequency of the registered photons, ν_{em}, like $\nu_{\text{em}} = c/\Delta t_{\text{em}}$ and $\nu_{\text{obs}} = c/\Delta t_{\text{obs}}$. Using these relationships, Eq. (3.4) can be rewritten as:

$$\nu_{\text{obs}} = \frac{\nu_{\text{em}}}{\sqrt{1-u^2/c^2}}(1 + u/c\cos\theta), \tag{3.5}$$

this equation describes the **relativistic Doppler shift**.

Consider the velocity projection of the object in two perpendicular directions: transverse and radial (longitudinal) to the line of sight. In Eq. (3.5), setting $\theta = 90°$, we get the equation for the **transverse relativistic Doppler shift**:

$$\nu_{\text{obs}} = \nu_{\text{em}}\sqrt{1-u^2/c^2}. \tag{3.6}$$

The transverse relativistic Doppler shift occurs due to the effect of time dilation associated with the motion of the source of light relative to an observer.

In Eq. (3.5), if the source moves away from the observer, we will assume, $\theta = 0°$, and if the source moves toward the observer, we will assume, $\theta = 180°$. As a result, we obtain the equation of the **radial relativistic Doppler shift**, in which $v = u\cos\theta$ is the radial velocity of the source relative to the observer:

$$\nu_{\text{obs}} = \nu_{\text{em}} \frac{\sqrt{1 - u^2/c^2}}{1 + u/c \cos\theta} = \nu_{\text{em}} \frac{\sqrt{1 - u^2/c^2}}{1 + v/c}. \tag{3.7}$$

Accordingly, Eq. (3.7), for the wavelengths λ_{obs} and λ_{em}, has the form:

$$\lambda_{\text{obs}} = \lambda_{\text{em}} \sqrt{\frac{1 + v/c}{1 - v/c}}. \tag{3.8}$$

Determination of Redshift

Redshift (or blueshift), z, is defined by the relative difference between the observed and emitted wavelengths (or the frequency):

$$z = \frac{\lambda_{\text{obs}} - \lambda_{\text{em}}}{\lambda_{\text{em}}} = \frac{\nu_{\text{em}} - \nu_{\text{obs}}}{\nu_{\text{obs}}}. \tag{3.9}$$

For the redshift, with $z > 0$, the source of light moves away from the observer, and the emitted energy of light, registered by the observer, shifts to the lower values. For the blueshift, with $z < 0$, the source of light moves to the observer, and the emitted energy of light, which is registered by the observer, shifts to the higher values.

From Eq. (3.9) we get:

$$1 + z = \frac{\lambda_{\text{obs}}}{\lambda_{\text{em}}} = \frac{\nu_{\text{em}}}{\nu_{\text{obs}}}. \tag{3.10}$$

Relativistic Redshift

Substituting the obtained results from Eq. (3.7) or from Eq. (3.8) into Eq. (3.9), we get the **relativistic redshift** equation:

$$z = \sqrt{\frac{1 + v/c}{1 - v/c}} - 1, \tag{3.11}$$

Redshift at Low Velocities of the Source of Light

Consider the limiting case of a small radial velocity of the source, $v \ll c$, in Eq. (3.11):

$$\begin{aligned} z &= \lim_{v/c\to 0}\Big(\sqrt{\frac{1+v/c}{1-v/c}}-1\Big) \\ &= \lim_{v/c\to 0}\Big(\sqrt{1+\frac{2v/c}{1-v/c}}-1\Big) \approx \frac{v/c}{1-v/c} \approx v/c. \end{aligned} \tag{3.12}$$

Relation of Cosmological Redshift with Scale Factor

Consider a reference frame described by the FLRW metric. An observer is at the center of this reference frame. The light ray moves towards the observer in the radial direction along the zero geodesic line, which is described by the metric, $ds^2 = 0$, for $d\theta = d\phi = 0$.
From Eq. (2.91) we get:

$$dt = \pm a(t)\frac{dr}{\sqrt{1-\mathrm{K}r^2}}. \tag{3.13}$$

We choose a negative sign in Eq. (3.13) due to the fact that a ray of light comes from a source of light located at the distance, $r = r_{\mathrm{em}}$. This ray of light moves in the direction of the center of the reference frame, $r = r_{\mathrm{obs}} = 0$, therefore, $dr < 0$ and $dt > 0$:

$$\int_{t_{\mathrm{em}}}^{t_{\mathrm{obs}}}\frac{dt}{a(t)} = \int_0^{r_{\mathrm{em}}}\frac{dr}{\sqrt{1-\mathrm{K}r^2}}. \tag{3.14}$$

Differentiating Eq. (3.14) and considering that a radial coordinate, r_{em}, of the comoving sources does not depend on time:

$$\frac{\Delta t_{\mathrm{em}}}{a(t_{\mathrm{em}})} = \frac{\Delta t_{\mathrm{obs}}}{a(t_{\mathrm{obs}})}. \tag{3.15}$$

Assuming that the light signals are the successive wave crests, the emitted frequency and the observed frequency are defined as $\nu_{\mathrm{em}} = 1/\Delta t_{\mathrm{em}}$ and $\nu_{\mathrm{obs}} = 1/\Delta t_{\mathrm{obs}}$, respectively.

Rewritting Eq. (3.15), as:

$$\nu_{\mathrm{obs}}/\nu_{\mathrm{em}} = a(t_{\mathrm{em}})/a(t_{\mathrm{obs}}). \tag{3.16}$$

A scale factor, $a(t)$, is an increasing time-dependent function, while the frequency, $\nu(t)$, is a decreasing function by the factor $(1+z)$ according to Eq. (3.10). By combining the equations, Eq. (3.10) and Eq. (3.16), we get:

$$1 + z = a(t_{\rm obs})/a(t_{\rm em}) = a_0/a(t_{\rm em}). \tag{3.17}$$

The relation between the redshift and the scale factor, which is specified in Eq. (3.17), is very important in cosmology. The redshift can be measured and it is sometimes the only information about the distances of the most distant objects.

3.4 Comoving Distance

The comoving distance is a distance between two astronomical objects, measured along the geodesic line (along the radial direction) at the present epoch of the cosmological time. The comoving distances and the conformal time form the *comoving reference frame*. The comoving distance between two objects in the comoving reference frame remains constant provided that these objects move only with the Hubble flow[7].

Based on the symmetry of the issue, we use the four-dimensional Minkowski metric, presented in the spherical coordinates:

$$ds^2 = g_{\mu\nu} dx^\mu dx^\nu = dt^2 - a^2(t)[dr^2 + r^2(d\theta)^2 + r^2 \sin^2\theta (d\varphi)^2]. \tag{3.18}$$

In Eq. (3.18) we assume $ds^2 = 0$ and $d\theta = d\phi = 0$. The comoving distance from the distant object to the observer is determined as:

$$r = \int_{t_{\rm em}}^{t_0} \frac{dt'}{a(t')} = \int_{a_{\rm em}}^{a_0} \frac{da}{a\dot{a}} = \frac{1}{a_0 H_0} \int_0^z \frac{dz'}{E(z')}, \tag{3.19}$$

where $t_{\rm em}$, $a_{\rm em}$ and $z_{\rm em}$ are the cosmological time, the scale factor and redshift of the source of light registered by the observer at the moment of time, t_0, respectively; a_0 is the scale factor at the time of observation, t_0.

Consider the dependence of the comoving distance on the different values of the curvature parameter, K, for the FLRW metric, Eq. (2.91). Assuming $ds^2 = 0$ and $d\theta = d\phi = 0$ in

[7] The solar system moves with a peculiar velocity of 370.6 ± 0.4 km c^{-1} relative to the Hubble flow in the direction of the Leo constellation, which is determined by the equatorial coordinates, $(\alpha, \delta) = (11.2^h, -7^\circ)$.

Eq. (2.91):

$$r = \begin{cases} \frac{1}{\sqrt{\mathrm{K}}}\sin\left(\frac{\sqrt{\mathrm{K}}}{a_0 H_0}\int_0^z \frac{dz'}{E(z')}\right) & \text{for K} > 0 \\ \frac{1}{a_0 H_0}\int_0^z \frac{dz'}{E(z')} & \text{for K} = 0 \\ \frac{1}{\sqrt{-\mathrm{K}}}\sinh\left(\frac{\sqrt{-\mathrm{K}}}{a_0 H_0}\int_0^z \frac{dz'}{E(z')}\right) & \text{for K} < 0 \end{cases} . \tag{3.20}$$

In Eq. (3.20) we express the curvature parameter, K, through the curvature density parameter, $\Omega_{\mathrm{K}0}$:

$$r(z) = \begin{cases} \frac{1}{H_0\sqrt{\Omega_{\mathrm{K}0}}}\sin\left(\frac{\sqrt{\Omega_{\mathrm{K}0}}}{H_0}\int_0^z \frac{dz'}{E(z')}\right) & \text{for } \Omega_{\mathrm{K}0} > 0 \\ \frac{1}{a_0 H_0}\int_0^z \frac{dz'}{E(z')} & \text{for } \Omega_{\mathrm{K}0} = 0 \\ \frac{1}{H_0\sqrt{-\Omega_{\mathrm{K}0}}}\sinh\left(\frac{\sqrt{-\Omega_{\mathrm{K}0}}}{H_0}\int_0^z \frac{dz'}{E(z')}\right) & \text{for } \Omega_{\mathrm{K}0} < 0 \end{cases} . \tag{3.21}$$

3.5 Physical Distance

A physical distance is a distance to the distant object, which can be measured at some moment of the cosmological time, t, with a physical ruler. The value of the physical distance varies due to the universe expansion.

To determine the distances to the astronomical objects with a small redshift value, $z \ll 1$, the following method can be applied. For small redshifts, the relation between the radial velocity and redshift of the object is[8], $v \approx z$, Eq. (3.12). In this case, the Hubble' law, described in Eq. (2.1), is transformed into the *local Hubble's law*:

$$z \approx H_0 d \quad \Rightarrow \quad d \approx \frac{z}{H_0} \quad \text{for } z \ll 1. \tag{3.22}$$

The physical distance obtained by this method is called the distance determined from redshift.

The following expression establishes the relationship between the physical distance, $d(t)$, and the comoving distance, r:

$$d(t) = a(t)r. \tag{3.23}$$

According to the expression, Eq. (3.23), the values of the physical and comoving distances are equal to each other only at the present epoch:

$$d(t_0) = a(t_0)r \quad \Rightarrow \quad d(t_0) = r = \frac{1}{H_0}\int_0^z \frac{dz'}{E(z')}. \tag{3.24}$$

[8]For small redshifts, $v \approx cz$, but in our convention $c = 1$.

Let's decompose the integral in Eq. (3.19) into a Taylor series near $z = 0$. We also apply the relation, $\dot{H}_0 = -H_0^2(1 - q_0)$, from Eq. (2.114), where q_0 is an acceleration parameter defined in Eq. (2.116):

$$d(t_0) = \frac{z}{H_0}\int_0^z \left[1 - (1 - q_0)z' + \left(\frac{1}{2} + 2q_0 - \frac{3}{2}q_0^2 + \frac{1}{2}\Omega_{K0}\right)z'^2\right]dz' + ... \tag{3.25}$$

As a result of the integrating in Eq. (3.25), we get:

$$d(t_0) = \frac{1}{H_0}\left[z - (1 - q_0)z^2 + \left(\frac{1}{6} - \frac{2}{3}q_0 - \frac{1}{2}q_0^2 + \frac{1}{6}\Omega_{K0}\right)z^3\right] + ... \tag{3.26}$$

Restricting Eq. (3.26) by the first two terms of the Taylor expansion:

$$d(t_0) \simeq \frac{z}{H_0}\Big[1 - (1 - q_0)z\Big] \text{ for } z \ll 1. \tag{3.27}$$

Eq. (3.27) is an approximate expression for determining the physical distance to an object taking into account the acceleration of the universe. The second term in this equation is a deviation from a classical definition of the physical distance using the Hubble's law, Eq. (3.22). With an increase in the value of the mass energy density parameter, $\Omega_{\rm m0}$, the value of the acceleration parameter, $q_0 = -(\Omega_{\rm m0}/2 + \Omega_{\rm r0} - \Omega_\Lambda)$, decreases, *i.e.*, an increase in the value of the mass in the universe leads to a slower accelerated expansion of the universe. In turn, it leads to decrease in the value of the physical distance to an object, Eq. (3.27).

3.6 Interval of the Cosmological Time Between Two Events

A photon with a redshift, z, was emitted by the source of light and then registered by the observer at $z = 0$. A photon traveled for the time, $\Delta t = d/c$, where d is the physical distance.

Consider the FLRW reference frame and the observer is at its center. Light propagates along the zero geodesic line, which is described by the zero lightlike metric, $ds^2 = 0$, see Fig. (2.5) (left panel). In Eq. (2.91) we set $ds^2 = 0$ and $d\theta = d\phi = 0$. From Eq. (2.91), we find the time, which is elapsed between two moments of the cosmological time, $t(z)$ and $t(0)$, respectively:

$$\Delta t = t(z) - t(0) = \int_{t(0)}^{t(z)} dt = \int_{a_0}^{a(z)} d(d(t)) = \int_{a_0}^{a(z)} adr. \tag{3.28}$$

In the equations, Eq. (2.111) and Eq. (3.19), we go over to the differential, $da = -dza_0/(1+z)^2$, for $a = a_0/(1 + z)$.

Suchwise, Eq. (3.28) can be rewritten as:

$$\begin{aligned}\Delta t &= \frac{1}{a_0 H_0}\int_0^z \frac{dz'}{(1+z)E(z')},\\ &= \frac{1}{a_0 H_0}\int_0^z \frac{dz'}{(1+z)\sqrt{\Omega_{\rm r0}(1+z')^4+\Omega_{\rm m0}(1+z')^3+\Omega_{\rm K0}(1+z')^2+\Omega_\Lambda}}.\end{aligned} \tag{3.29}$$

From Eq. (3.29) it follows that the interval of the cosmological time between two events is uniquely related to the value of redshift. The value of the interval of the cosmological time depends on the chosen cosmological model and on its model parameters.

The age of the universe can be determined from Eq. (3.29), provided that the upper boundary of the integration tends to infinity, $z \to \infty$:

$$\Delta t = \frac{1}{a_0 H_0}\int_0^\infty \frac{dz'}{(1+z)\sqrt{\Omega_{\rm r0}(1+z')^4+\Omega_{\rm m0}(1+z')^3+\Omega_{\rm K0}(1+z')^2+\Omega_\Lambda}}. \tag{3.30}$$

According to Planck 2015 under the assumption that the model with the cosmological constant Λ is correct, the age of our universe is $t_0 = 13.799 \pm 0.038$ billion years, at the confidence level at 68%, Ref. (Ade et al. (2016)).

3.7 Luminosity Distance

A luminosity distance, d_L, is a distance from which an astronomical object at redshift, z, and with a bolometric luminosity[9], L, creates a bolometric (*i.e.*, it is integrated over all the frequencies) flux, F, under the assumption that the following relation between the luminosity and the flux is fulfilled:

$$F = \frac{L}{4\pi d_L^2}. \tag{3.31}$$

Thereby, the luminosity distance to an object is defined as:

$$d_L = \sqrt{\frac{L}{4\pi F}}. \tag{3.32}$$

The luminance distance, d_L, is a measure of the value of the energy flux, F, created by an object with a known luminosity, L.

Due to the universe expansion, the absolute bolometric luminosity, L, which is created by the source of light at redshift, z, differs from the luminosity, $L_{\rm obs}$, which is registered by

[9] A bolometric luminosity is the total radiation power measured in Watts.

the receiver of light at redshift, $z = 0$. The absolute bolometric luminosity, L, is defined as an energy, $E_{\rm em}$, which is emitted by a source of light at redshift, z, for the time interval, $\Delta t_{\rm em}$:

$$L = \frac{E_{\rm em}}{\Delta t_{\rm em}}. \tag{3.33}$$

Respectively, the observed bolometric luminosity, $L_{\rm obs}$, is determined as an energy registered by the receiver of light, $E_{\rm obs}$, for the time interval, $\Delta t_{\rm obs}$:

$$L_{\rm obs} = \frac{E_{\rm obs}}{\Delta t_{\rm obs}}. \tag{3.34}$$

Consider the ratio of the absolute bolometric luminosity, L, to the observed bolometric luminosity, $L_{\rm obs}$:

$$\frac{L}{L_{\rm obs}} = \frac{E_{\rm em}}{\Delta t_{\rm em}} \cdot \frac{\Delta t_{\rm obs}}{E_{\rm obs}} = \frac{E_{\rm em}}{E_{\rm obs}} \cdot \frac{\Delta t_{\rm obs}}{\Delta t_{\rm em}}. \tag{3.35}$$

Owing to the fact that the energy of the photon is proportional to its frequency, and taking into account the results obtained in Eq. (3.16) and Eq. (3.17):

$$\frac{E_{\rm em}}{E_{\rm obs}} = \frac{\nu_{\rm em}}{\nu_{\rm obs}} = 1 + z. \tag{3.36}$$

The obtained result reflects the fact of the decrease in the photon energy by virtue of redshift as a consequence of the universe expansion.

On the contrary, considering the relations obtained in Eq. (3.15) and Eq. (3.17), we get:

$$\frac{\Delta t_{\rm obs}}{\Delta t_{\rm em}} = 1 + z. \tag{3.37}$$

This result illustrates the fact, that due to the universe expansion, there is an increase of the propagation time of the photons, which leads to the decrease in the intensity of the photons, registered by the receiver of light.

Thereby, based on the results obtained in Eq. (3.36) and Eq. (3.37), we can rewrite Eq. (3.35) as:

$$\frac{L}{L_{\rm obs}} = (1 + z)^2. \tag{3.38}$$

The energy flux is defined as an energy, $E_{\rm em}$, transferred per unit of time and per unit of the area of a certain surface, S. According to this definition, we can write $F = L_{\rm obs}/S$. The energy, $E_{\rm em}$, emitted by the source of light, was distributed over a spherical surface of a radius, $R = a_0 r$, at time of registration by the receiver of light at $z = 0$. Thus, the energy flux received from the source of light is defined as:

$$F = \frac{L}{4\pi d_L^2} = \frac{L_{\rm obs}}{4\pi(a_0 r)^2}. \tag{3.39}$$

From this equation it follows:

$$d_L^2 = (a_0 r)^2 \frac{L}{L_{\rm obs}}. \tag{3.40}$$

If we substitute Eq. (3.38) in Eq. (3.40), we will get:

$$\begin{aligned} d_L^2 &= (a_0 r)^2 (1+z)^2, \\ \Rightarrow \quad d_L &= a_0 r (1+z). \end{aligned} \tag{3.41}$$

Let's substitute the expressions, Eq. (3.21), for the comoving distance, r, in Eq. (3.41). As a result, the expression for the luminosity distance, which is represented in terms of the cosmological parameters[10], can be obtained:

$$d_L(z) = \begin{cases} \frac{(1+z)}{H_0\sqrt{\Omega_{\rm K0}}} \sin\left(\frac{\sqrt{\Omega_{\rm K0}}}{H_0}\int_0^z \frac{dz'}{E(z')}\right) & \text{for } \Omega_{\rm K0} > 0 \\ \frac{(1+z)}{a_0 H_0}\int_0^z \frac{dz'}{E(z')} & \text{for } \Omega_{\rm K0} = 0 \\ \frac{(1+z)}{H_0\sqrt{-\Omega_{\rm K0}}} \sinh\left(\frac{\sqrt{-\Omega_{\rm K0}}}{H_0}\int_0^z \frac{dz'}{E(z')}\right) & \text{for } \Omega_{\rm K0} < 0 \end{cases}. \tag{3.42}$$

The coefficient $(1+z)$ characterizes the loss of the energy flux because of the effects, associated with the universe expansion: i) decrease of the intensity of the photons due to the extension of the propagation time of the photons; ii) decrease of the energy of the photons due to redshift. Therefore, an object with the luminosity, $L_{\rm obs}$, seems more distant than it really is.

For the small values of redshift, z, the luminosity distance can be defined as:

$$d_L \simeq \frac{z}{H_0}\left[1 + \frac{1}{2}(1+q_0)z\right] \quad \text{for } z \ll 1. \tag{3.43}$$

By comparing Eq. (3.26) and Eq. (3.43), we can conclude, that the physical distance to an object at present time and the luminosity distance to this object are equal only for very small redshifts. This occurs with the domination of the first term in these equations. For larger redshifts, the luminosity distance is greater than the physical distance, $d_L > d(t_0)$.

The values of the luminosity of the type Ia supernovae have the small dispersions. In cosmology, these objects are the *standard candles* for determining the distances to the distant

[10] Assuming that dark energy is represented by the cosmological constant, Λ.

objects. By measuring the energy flux, which is obtained from the type Ia supernovae for different redshifts, z, it is possible to determine the luminosity distances to these objects by the different way and to refine the values of the model parameters for considered cosmological model from Eq. (3.42).

3.8 Angular Diameter Distance

Consider an astronomical object at redshift, z, with a linear transverse diameter, $\mathbf{R}$, and with an apparent angular diameter, θ, measured in radians. The angular diameter distance to this object, denoted as, d_A, is defined as the ratio of its linear transverse diameter, $\mathbf{R}$, to the apparent angular diameter, θ:

$$d_A = \frac{\mathbf{R}}{\theta}. \tag{3.44}$$

We introduce the FLRW reference frame with the observer at the center. In the FLRW reference frame an astronomical object at redshift, z, has a comoving coordinate, r. The linear transverse diameter of this object is the physical distance between two events at the same redshift, z, and separated in space by a small angle, $d\theta$. Assuming $dt = dr = d\phi = 0$ in the FLRW metric, Eq. (2.91). As a result, we get:

$$\begin{aligned} ds^2 &= a(t)^2 r(t)^2 d\theta^2, \\ \Rightarrow \quad ds &= d\mathbf{R} = a(t) r(t) d\theta. \end{aligned} \tag{3.45}$$

Integrating the FLRW metric in the transverse direction to the line of sight direction in Eq. (3.45):

$$\mathbf{R} = a(t) r(t) \theta. \tag{3.46}$$

Substituting the result obtained in Eq. (3.46) into Eq. (3.44):

$$d_A(z) = \frac{a r(z) \theta}{\theta} = \frac{r(z)}{(1+z)}. \tag{3.47}$$

Plugging the values of the comoving distance, r, from Eq. (3.21) into Eq. (3.47), we obtain the values of the angular diameter distance depending on the model parameters:

$$d_A(z) = \begin{cases} \frac{1}{(1+z)H_0\sqrt{\Omega_{\mathrm{K0}}}} \sin\left(\frac{\sqrt{\Omega_{\mathrm{K0}}}}{H_0} \int_0^z \frac{dz'}{E(z')}\right) & \text{for } \Omega_{\mathrm{K0}} > 0 \\ \frac{1}{(1+z)H_0} \int_0^z \frac{dz'}{E(z')} & \text{for } \Omega_{\mathrm{K0}} = 0 \\ \frac{1}{(1+z)H_0\sqrt{-\Omega_{\mathrm{K0}}}} \sinh\left(\frac{\sqrt{-\Omega_{\mathrm{K0}}}}{H_0} \int_0^z \frac{dz'}{E(z')}\right) & \text{for } \Omega_{\mathrm{K0}} < 0 \end{cases} . \tag{3.48}$$

The relationship between the luminosity distance and the angular diameter distance is expressed through the equation:

$$d_L(z) = (1+z)^2 d_A(z). \tag{3.49}$$

The luminosity distance and the angular diameter distance defined in Eq. (3.42) and Eq. (3.48) depend on the chosen cosmological model. These distances coincide at small redshifts, $z \ll 1$, at which the spacetime curvature can be neglected. At large redshifts (respectively, at large distances), the specific cosmological effects, such as the nonstationarity and the spacetime curvature, already appear. Therefore, the concept of an unambiguous distance to an object becomes inapplicable.

The radio galaxies Fanaroff-Riley Type II (FRII) have the small dispersions in their linear transverse diameters, so these objects can serve as the *standard ruler* for determining the distances to the distant objects in cosmology, Ref. (Buchalter et al. (1998)). Knowing the angular size, θ, and redshift of these objects, z, it is possible to determine the angular diameter distance to these objects in the different way and, using Eq. (3.48), to refine the values of the model parameters in the given cosmological model.

Chapter 4

Observational Probes

4.1 Type Ia Supernovae

A supernova explosion is observed as a sudden increase in the brightness of the star by about 10 orders of the magnitude. As a result of this explosion, the supernova shines at the maximum of the light curve like all the stars of a galaxy.

The supernovae are recorded from the distant galaxies up to redshift, $z \approx 1.7$. Depending on the spectral properties, the supernovae are divided into two main types: I - there are no hydrogen lines in the spectra and II - there are hydrogen lines in the spectra. Type I supernovae (SNeIa) are in turn subdivided into: Ia - light curves have an universal form, Ib - light curves are similar to the light curves of the supernovae type II and Ic - there are no helium lines in the spectra and their light curves are similar to the light curves of the supernovae type II.

The most plausible model of SNeIa is considered to be a model of a white dwarf thermonuclear explosion with the radius of $\mathbf{R} \sim 10^3$ km, whose mass reached Chandrasekhar's mass, $m_{\rm ch} \approx 1.44\ M_\odot$, as a result of the mass accretion from a satellite-star with the energy release, $E \approx 2 \cdot 10^{52}$ erg. This explosion is caused by the thermonuclear carbon fusion and the radioactive decay of nickel, ^{56}Ni (^{56}Ni $\to$ ^{56}Co $\to$ ^{56}Fe). The radioactive decay of ^{56}Ni is the main source of the observed light curves of SNeIa and determines the shape of these light curves. The luminosity in the maximum of the light curves depends only on the mass of the ejected nickel, ^{56}Ni, ($L_{\rm max} \approx 1.4 \cdot 10^{43}$ erg/sec, for nickel mass $m_{\rm Ni} = 0.5\ M_\odot$). This luminosity corresponds to the absolute magnitude, $M_{\rm max} = -19^m.2$[1]. It can be expected that all the SNeIa emit the same amount of light, assuming that the white dwarf is com-

[1] The definition of the absolute magnitude is given below.

pletely burned out. Since the explosion mechanism is universal, all the SNeIa located at the same distance from us should have approximately the same luminosity at the maximum, so these objects are used as the *standard candles* for determining the distances to the distant galaxies. The furthest galaxy, in which the Type Ia supernova (1997ff) was registered, has redshift $z = 1.7$.

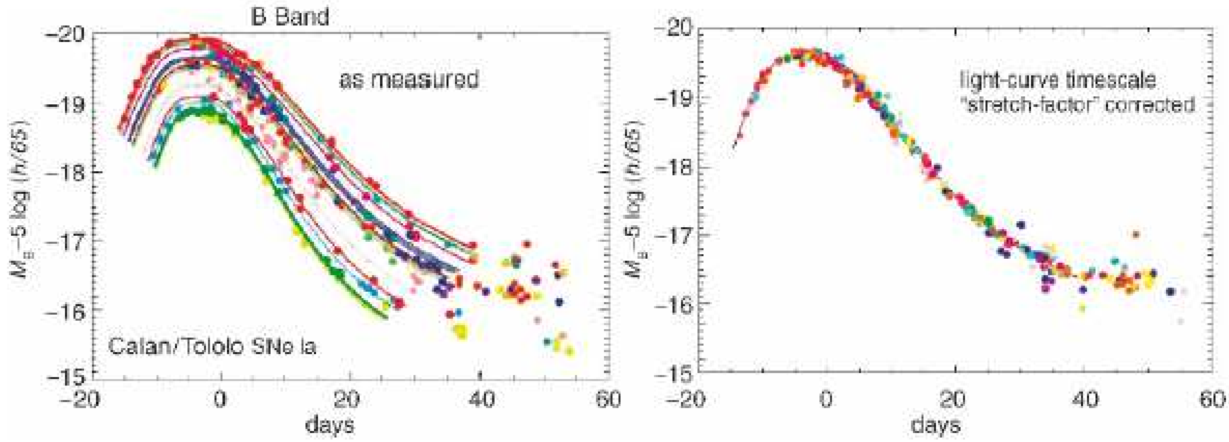

Figure 4.1: Left panel: B-band light curves for the different SNeIa from the Calan-Tolono survey. (Figures from Ref. (Heitmann et al. (2006))). The right panel: the same light curves after one-parameter correction. (Figures from Ref. (Kim et al. (2004)))

Among the various samples of the SNeIa light curves, there is a dispersion in the shapes of the curves, as well as in the maximum luminosity values (the dispersion reaches of 0.4 magnitudes in the blue light range), see Fig. (4.1) (left panel). This effect is caused by the effect of the redshift on the observed spectra of the objects in the expanding universe, since these observations were made in the specific wavelength range. These curves can be normalized by applying an empirically found correlation, the so-called K-correction, between the maximum luminosity and the width of the light curve, see Fig. (4.1) (right panel). After carrying out this correction, the SNeIa light curves can be used as the standard candles.

Distance Modulus

A distance modulus is a method for determining the distances to the distant objects based on the logarithmic scale of the magnitudes comparison.

The distance modulus, μ, is defined as a difference between the apparent magnitude, m, and the absolute magnitude, M, of a distant object with the corresponding bolometric energy fluxes, F_m and F_M. The apparent magnitude, m, is the magnitude of an object located at the luminosity distance, d_L, and the absolute magnitude, M, is defined as the apparent magnitude that the object would have if it were located at a distance, $d_L = 10$ pc. From the

Pogson's law, Ref. (Pogson (1857)), connecting the apparent magnitude of an astronomical object and the bolometric energy flux recorded from it, $10^m \propto F^{-2.5}$, we get:

$$\mu = m - M = -2.5 \log_{10}\left(\frac{F_m}{F_M}\right) = 5 \log_{10}\left(\frac{d_L}{10 \text{ pc}}\right),$$
$$= 5 \log_{10}(H_0 d_L) - 5 \log_{10} H_0 + 25. \quad (4.1)$$

From Eq. (4.1), it follows that the distance modulus, μ, is determined by the luminosity distance, d_L, of the object. In this equation, the Hubble constant, H_0, is considered as a nuisance parameter, and it is the reason for the uncertainty in the determination of the absolute magnitude of the SNeIa.

The value of the speed of light, $c = 3 \cdot 10^5$ km c^{-1}, should be taken into account to determine the actual distance modulus. Suchwise, to calculate the luminosity distance, the expression $c \cdot d_L$ is assumed, where d_L is obtained from Eq. (3.42). In this case, applying Eq. (4.1), we get an expression for the distance modulus, μ, depending on redshift and the model parameters:

$$\mu = 42.3856 - 5\log_{10}(h) + 5\log_{10}(1+z) + 5\log_{10} \begin{cases} \frac{1}{\sqrt{\Omega_{K0}}} \sin\left(\frac{\sqrt{\Omega_{K0}}}{H_0} \int_0^z \frac{dz'}{E(z')}\right) & \text{for } \Omega_{K0} > 0 \\ \int_0^z \frac{dz'}{E(z')} & \text{for } \Omega_{K0} = 0 \\ \frac{1}{\sqrt{-\Omega_{K0}}} \sinh\left(\frac{\sqrt{-\Omega_{K0}}}{H_0} \int_0^z \frac{dz'}{E(z')}\right) & \text{for } \Omega_{K0} < 0 \end{cases} . \quad (4.2)$$

Distance modulus is a function of the cosmological parameters, Eq. (4.2), therefore, the value of the distance modulus is very sensitive to the changes in the values of the cosmological parameters, see Fig. (4.2) (left panel). The SNeIa data correspond to the values of the distance modulus for the ΛCDM model by the best way, as shown in Fig. (4.2) (right panel).

In the mid-1990's, two independent astronomical groups: the Supernova Cosmology Project (SCP), led by Saul Perlmutter, Refs. (Riess et al. (1998), Perlmutter et al. (1999)) and the High-Z Supernova Cosmology Team (HZSNS Team), headed by Brian Schmidt, Ref. (Schmidt et al. (1998)), observed the SNeIa to determine the distances to these distant objects. Starting processing the gathered information, the scientists hoped to get the confirmation of the slowing expansion of the universe. Both groups of researchers independently discovered that SNeIa at redshift, $z = 0.5$, were dimmer by 0.25 of the magnitude compared to the magnitude predicted by the open model with the cosmological parameters: $\Omega_{m0} = 0.3$

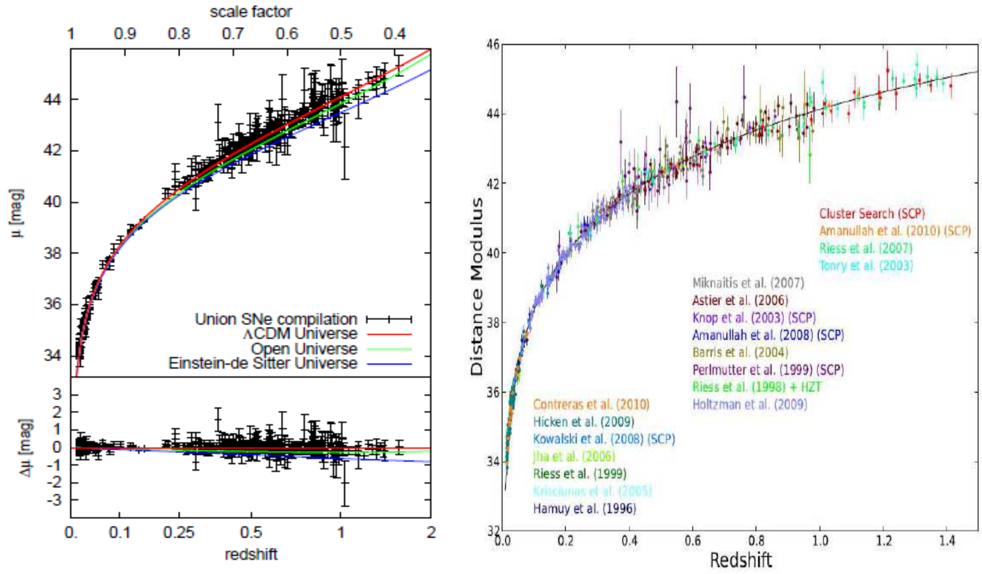

Figure 4.2: Left panel: Hubble diagram for the 307 SNeIa of the Union compilation. (The figures from Ref. (Kowalski et al. (2008))). The top panel: the red line corresponds to the ΛCDM universe ($\Omega_{\rm m} = 0.28$, $\Omega_\Lambda = 0.72$); the green line corresponds to the open universe ($\Omega_{\rm m} = 0.28$, $\Omega_\Lambda = 0$) and the blue line corresponds to the Einstein-de Sitter universe ($\Omega_{\rm m} = 1$, $\Omega_\Lambda = 0$). The bottom panel: the residuals of the distance modulus from the best fitting cosmology for the ΛCDM model. Right panel: Hubble diagram for the Union2.1 compilation. The best fit cosmology for the ΛCDM model is represented as a black solid line. (The figure from Ref. (Suzuki et al. (2012)))

and $\Omega_\Lambda = 0$, which describes the slowing down universe. The so-called Einstein-de Sitter model with the cosmological parameters: $\Omega_{\rm m0} = 1$ and $\Omega_\Lambda = 0$, which describes a flat slowing down universe, also failed to correctly approximate the obtained results. Thus, the SNeIa were at a greater distance than it was predicted by the cosmological models, which describe the open and flat slowing down universe.

The cosmological model of a flat accelerating universe with the cosmological parameters, $\Omega_{\rm m0} = 0.3$ and $\Omega_\Lambda = 0.7$, predicts well the results obtained by these observers. Thereby, the discovery of the accelerated expansion of our universe according to the SNeIa data was made by these two groups of researchers. In 2011, Saul Perlmutter, Brian Schmidt and Adam Riess were awarded the Nobel Prize in Physics for this discovery.

4.2 Cosmic Microwave Background Radiation

4.2.1 Description of the CMBR

Origination of the CMBR

In the universe, the *recombination* epoch began approximately $t_{\text{rec}} = 350000$ years after the Big Bang[2] at redshift $z_{\text{rec}} \approx 1400$, at the average temperature in the universe, $\langle T \rangle_{\text{rec}} \approx 3800\,\text{K}$, Ref. (Rubakov & Gorbunov (2017)). Due to the expansion and, therefore, the cooling of the universe, at the recombination epoch the charged electrons and protons become bound, forming the electrically neutral hydrogen atoms[3], Ref. (Peebles (1968)). At the same time, the matter from the plasma state, which is opaque for the most part of the electromagnetic radiation, passes into a gaseous and an electrically neutral state.

The CMBR appeared at the end of the recombination epoch, in the period of the last scattering of the photons on the electrons, in the so-called period of the *photon decoupling* from the hydrogen atoms. The last photon scattering occurred $t_{\text{dec}} \approx 379000$ years after the Big Bang at redshift $z_{\text{dec}} \approx 1100$, at an average temperature in the universe, $\langle T \rangle_{\text{dec}} \approx 3100\,\text{K}$. As a consequence of the decoupling of the radiation and the matter, the relic photons no longer interacted with the neutral hydrogen atoms. The free path of the relic photons becomes larger than the size of the Hubble horizon, and these photons begin to spread freely in the universe. Thus, at the present epoch, an observer registers the relic photons that last interacted with the matter at redshift z_{dec}.

According to the Big Bang model, the CMBR photons began its propagation in the

[2]In 1946, George Gamow developed the "hot universe" theory, also known as the Big Bang theory, Ref. (Gamov (1946)). Based on this theory, George Gamow, Ralph Alfer and Robert Herman predicted the existence of the microwave background radiation (CMBR), Refs. (Alpher & Herman (1948*a*), Alpher & Herman (1948*b*)). In 1965, the American radio astronomers Arno Penzias and Robert Wilson absolutely accidentally recorded this isotropic radiation, Ref. (Penzias & Wilson (1965)). Detection of CMBR, which was originated at the epoch of the primordial recombination of hydrogen, is one of the main evidence of the correctness of the Big Bang theory. In 1978, Arno Penzias and Robert Wilson were awarded the Nobel Prize in Physics for the discovery of the CMBR.

[3]Before recombination, the baryonic matter consisted of 75% of the protons and 25% of the α-particles or, in other words, the helium nuclei, ^{4}He. The ionization energy of the helium is greater than the ionization energy of the hydrogen; therefore, the helium recombination occurred much earlier, Ref. (Peebles (1966)). The first helium recombination, $\text{He}^{++} + e^- \to \text{He}^+ + \gamma$, happened at redshift, $z \approx 6000$. The second helium recombination, $\text{He}^+ + e^- \to \text{He} + \gamma$, occurred at redshift, $z \approx 2500$, Ref. (Hu (1995)). Despite the fact that after the recombination of the helium the universe is still optically opaque, the recombination of the helium affects the temperature power spectrum of the CMBR, which increases in the height of the 2nd, 3rd and 4th peaks by 0.2%, 0.4% and 1%, respectively, Refs. (Hu et al. (1995), Hu (1995)).

universe from the surface of a sphere called the *surface of last scattering*, whose radius is[4]:

$$r_{\rm dec} = \frac{1}{a_0 H_0}\int_0^{z_{\rm dec}} \frac{dz'}{E(z')}. \tag{4.3}$$

CMBR Properties

In 1989, the Cosmic Background Explorer (COBE) satellite was launched to study the CMBR. The results of the measurements obtained from this satellite are: the discovery of the CMBR Planck spectrum (the project Differential Microwave Radiometer (DMR)), Refs. (Mather et al. (1994), Mather et al. (1999)) and the discovery of the CMBR temperature anisotropy[5] (the project Far-InfraRed Absolute Spectrophotometer (FIRAS)), Ref. (Bennett et al. (1996)). In 2006, the leaders of these projects, George Smoot (the DMR project) and John Mather (the FIRAS project) received the Nobel Prize in Physics.

The CMBR is a thermal radiation, its spectrum corresponds to the spectrum of the absolutely black body with a temperature at the present epoch $T_0 \simeq 2,72548 \pm 0,00057$ K, see Fig. (4.2) (left panel). This temperature accords to the average temperature of the CMBR at the present epoch, $\langle T_\gamma \rangle = T_0$. The maximum of the Planck's spectrum accords to the frequency 160,4 GHz, which corresponds to a wavelength 1,9 mm, see Fig. (4.2) (left panel). The energy density of the CMBR is approximately equal to $\rho_\gamma = (\pi^2/15)T_0^4 \simeq 4.64 \cdot 10^{-34}$ g cm$^{-3} \simeq 0.26$ eV cm^{-3}. The mass density of the CMBR is $n_\gamma = (2\zeta(3)/\pi^2)T_0^3 \simeq 411$ cm^{-3}, where the ζ is a Riemann function, $\zeta(3) = 1.202$, Ref. (Scott & Smoot (2010)).

CMBR Temperature Anisotropy

The temperature of the CMBR, which was registered in the direction in the sky, (θ, φ), as $T(\theta, \varphi)$ is the main measurement in the investigation of the CMBR. The value of θ determines the polar angle on the sphere and the value of φ is the azimuth angle. The dimensionless value of the CMBR temperature anisotropy is defined as:

$$\frac{\delta T(\theta,\varphi)}{T_0} = \frac{T(\theta,\varphi) - T_0}{T_0}. \tag{4.4}$$

[4]By virtue of the fact that the recombination is not an instantaneous process and takes place over a finite range of redshifts, the CMBR photons are scattered for the last time inside the surface of the finite thickness. The thickness of this surface during the recombination is approximately equal to the *photons diffusion length*, therefore, this effect is significant on the same length scales as the Silk damping (the Silk damping effect is described below), Ref. (Schneider (2006)).

[5]In 1983, the RELICT-1 experiment was carried out from the spacecraft PROGNOZ-9 in the USSR. The purpose of this experiment was to study the CMBR temperature anisotropy. The Soviet scientists failed to register the temperature anisotropy of the CMBR.

The CMBR is isotropic and uniform at the level of the temperature fluctuation, $\delta T(\theta,\varphi)/T_0 \simeq 10^{-4}$, see Fig. (4.3) (right panel).

The map of the temperature anisotropies of the CMBR is presented in Fig. (4.3) (right panel). This map is obtained by the project Planck 2013, Ref. (Ade et al. (2014*b*)). At the present epoch, the temperature anisotropy of the CMBR is $\delta T(\theta,\varphi)/T_0 \simeq 10^{-5}$.

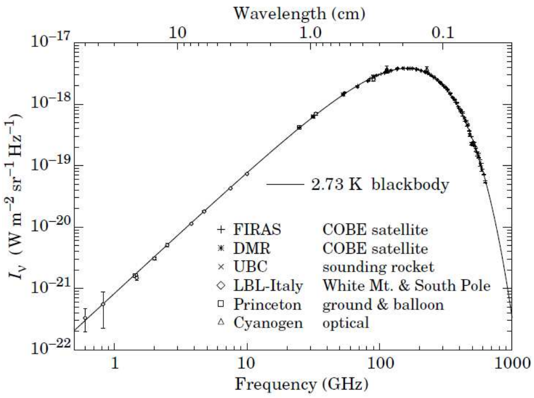

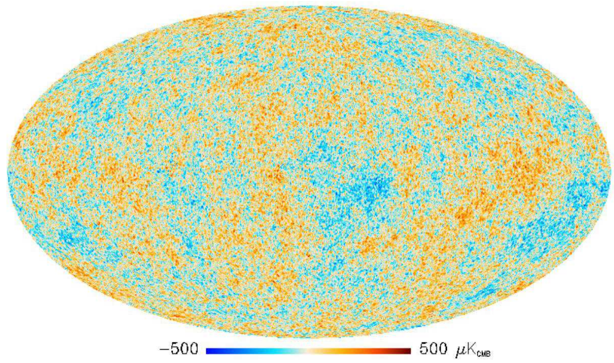

Figure 4.3: Left panel: the Planck spectrum of the CMBR, which is obtained by the experiments: FIRAS, DMR, UBC, LBL-Italy, Princeton, Cyanogen. (Figure from Ref. (Smoot & Scott (1997))) Right panel: the temperature fluctuations of the CMBR relative to the average temperature based on the results of the Planck 2013. (Figure from Ref. (Ade et al. (2014*b*))) The dipole anisotropy, which related with the motion of the solar system relative to the rest frame of the CMBR and the non-Planckian emission from the Galactic disk are subtracted. The amplitude of the temperature fluctuations relative to the background temperature is $\Delta T/T_0 \sim 10^{-5}$.

4.2.2 CMBR Angular Power Spectrum of the Temperature Anisotropy

Since the temperature anisotropy of the CMBR depends on the direction of the observation, the value of the temperature anisotropy can be represented as the decomposition in the spherical orthonormal harmonics, $Y_l^m(\theta,\varphi)$. This decomposition is the analogous to the Fourier decomposition on a spherical surface:

$$\frac{\delta T(\theta,\varphi)}{T_0} = \sum_{l=1}^{\infty}\sum_{m=-l}^{l} a_{l,m} Y_l^m(\theta,\varphi), \tag{4.5}$$

where $a_{l,m}$ are the multipole coefficients of the decomposition in the spherical harmonics, $Y_l^m(\theta,\varphi)$. The coefficients $a_{l,m}$ characterize the amplitude of the temperature fluctuations at the different angular scales and have the following property, $a^*_{l,m} = (-1)^m a_{l,-m}$.

The study of the statistical properties of the coefficients $a_{l,m}$ are very important for the analysis of the distribution of the CMBR temperature anisotropy. The coefficients $a_{l,m}$

can have both positive and negative values. The value $|a_{l,m}|^2$ determines the deviation of the coefficient $a_{l,m}$ from zero and, accordingly, determines the amplitude of the temperature anisotropy. According to the observations, the distribution of the CMBR temperature fluctuations forms a random Gaussian field.

Assuming an isotropic and homogeneous universe, the coefficients $a_{l,m}$ for the different values of the indices l and m are statistically independent of each other, Ref. (Mukhanov (2005)):

$$\langle a_{l,m} a^*_{l',m'} \rangle = C_{lm} \delta_{ll'} \delta_{mm'}. \tag{4.6}$$

The value of the coefficients C_{lm} determines the **temperature angular power spectrum anisotropy** of the CMBR.

The requirement of the independence of the statistical properties of the coefficients $a_{l,m}$ on the choice of the origin for any direction of the observation or the so-called requirement of the rotational invariance leads to the fact that the value of the angular power spectrum $C_{l,m}$ does not depend on the value of the index m but depends only on the index l, *i.e.*, $C_{l,m} = C_l$, Ref. (Durrer et al. (1998)). Therefore, Eq. (4.6) with the coincidence of the indices, $l = l'$, can be rewritten as, Ref. (Mukhanov (2005)):

$$\langle |a_{l,m}|^2 \rangle = C_l. \tag{4.7}$$

The angle brackets, $\langle\rangle$, in Eq. (4.6) and in Eq. (4.7), denote the averaging over a hypothetical ensemble of the universes like our. Assuming that our universe is an ergodic dynamic system[6], these angle brackets can be interpreted as averaging over all the possible observers in our universe. The fact is that each observer in the universe can observe only one realization of all the possible observable universes. For example, the observers from the Earth can study the CMBR, which is visible only from the Earth. In the universe, each observer registers the photons of the CMBR with their own distribution of the temperature fluctuations, which differs from each other. The difference between our region of the observable universe in comparison with the averaged region of the observable universe is called the *cosmic variance*. The value of the cosmic variance for each measurement, C_l, is defined as, Ref. (Scott & Smoot (2010)):

$$(\Delta C_l)^2 = \frac{2}{2l+1} C_l^2. \tag{4.8}$$

The value of the cosmic variance is negligible on the small angular scales, it becomes sig-

[6]The ergodic systems are characterized by the coincidence of the expectation of the time series with the expectation of the spatial series.

nificant for the angular scales $\vartheta \geq 10°$. The value of the angular power spectrum, C_l, characterizes the size of temperature fluctuations on the angular scale $\vartheta = 180°/l$. The index l determines the value of the angular scale. A small value of the index l corresponds to a large angular scale and vice versa, a large value of l corresponds to a small angular scale. With an increase in the value of the index l, the spherical harmonics have the variations on the smaller angular scales. The values of the index l in the range from one to several thousand are applied in the current observations.

The value of the index $l = 1$ determines the properties of the CMBR, called the **dipole**. In 1969, the dipole component was detected in the CMBR. It manifests itself in the fact that in the direction of the constellation Leo the temperature of this radiation is 0.1 K, above the average temperature of the CMBR, respectively, in the opposite direction the temperature of this radiation is on the same value below. This temperature anisotropy is explained by the Doppler effect due to the motion of the solar system relative to the CMBR in the direction of the constellation Leo with the velocity 370.6 ± 0.4 km c^{-1}. The velocity of this motion determines the value of the dipole component of the temperature anisotropy, $\delta T_{\rm dipol} = 3.355 \pm 0.008$ mK, Ref. (Hinshaw et al. (2009)). The maximum value of the temperature fluctuations for the dipole component, which is averaged over a year, is $\delta T/T_0 \simeq 1.23 \cdot 10^{-3}$. The observations of the dipole component do not contain the information about the intrinsic properties of the CMBR. In this regard, the dipole is considered separately, and the study of the CMBR begins with the minimum value of the index $l = 2$, with the so-called quadrupole anisotropy.

Consider the analysis of the temperature anisotropy of the CMBR without taking into account the dipole:

$$\frac{\delta T(\theta,\varphi)}{T_0} \equiv \frac{T(\theta,\varphi) - T_0 - \delta T_{\rm dipol}}{T_0} = \sum_{l=2}^{\infty} \sum_{m=-l}^{l} a_{l,m} Y_l^m(\theta,\varphi). \tag{4.9}$$

The spherical harmonics, $Y_l^m(\theta,\varphi)$, are expressed in terms of the Legendre functions, $P_l^m(\cos\vartheta)$, as, Ref. (Arfken (1985)):

$$Y_l^m(\theta,\varphi) = (-1)^m \sqrt{\frac{2l+1}{2} \frac{(l-m)!}{(l+m)!}} P_l^m(\cos\vartheta) e^{im\varphi}. \tag{4.10}$$

The requirement for fulfillment of the rotational invariance or the fulfillment of the conditions of the isotropy relative to the value of the azimuth angle, φ, is equivalent the equality to zero the value of m, $m = 0$. In this case, Eq. (4.10) takes the form:

$$Y_l(\theta, \varphi) = \sqrt{\frac{2l+1}{2}} P_l(\cos\vartheta). \tag{4.11}$$

Thus, in Eq. (4.11), the spherical harmonics are reduced to the ordinary Legendre's polynomials, $P_l(\cos\vartheta)$.

In this case, the temperature correlation function between two directions is:

$$\left\langle \frac{\delta T(\theta_1, \varphi_1)}{T_0} \cdot \frac{\delta T(\theta_2, \varphi_2)}{T_0} \right\rangle = \sum_l \frac{2l+1}{4\pi} C_l P_l(\cos\vartheta), \tag{4.12}$$

where ϑ is the value of the polar angle between the directions (θ_1, φ_1) and (θ_2, φ_2). The coefficients C_l set the correlation between the temperature fluctuations in the different directions.

The expression for the square of the value of the temperature fluctuations is a particular case of Eq. (4.12):

$$\left\langle \frac{\delta T(\theta_1, \varphi_1)}{T_0} \cdot \frac{\delta T(\theta_2, \varphi_2)}{T_0} \right\rangle = \sum_l \frac{2l+1}{4\pi} C_l \approx \int \frac{l(l+1)}{2\pi} C_l d\ln l. \tag{4.13}$$

Under the derivation of this formula, it was taken into account that the polar angle between two collinear co-directional vectors is zero, $\vartheta = 0$, and $P_l(\cos 0) = 1$. The value of $\frac{l(l+1)C_l}{2\pi}$ determines the total contribution of the angular moments of the same order.

The dependence of the angular power spectrum of the CMBR temperature anisotropy, $\frac{l(l+1)C_l}{2\pi} T_0^2$, on the angular momentum, l, is shown in Fig. (4.4).

4.2.3 CMBR Primary Temperature Anisotropy

The temperature fluctuations that occur during the decoupling period in the recombination epoch are called the *primary anisotropy*.

Consider the angular power spectrum of the CMBR temperature anisotropy, which is presented in Fig. (4.5). The angular power spectrum of the CMBR temperature anisotropy is mainly characterized by three regions of the angular momentum values, l: $l \leq 100$, $l \geq 100$ and $l \geq 1000$, see Fig. (4.5), Refs. (Hu & Okamoto (2002), Scott & Smoot (2010)).

For the first region with $l \leq 100$, the function $(2l + 1)/4\pi$ will be almost flat, if the Harrison-Zeldovich power spectrum is considered in the calculations.[7]. The second region

[7]The power spectrum $P(k) = k^{n_s}$ with $n_s = 1$ is called the Harrison-Zeldovich spectrum, where k is a

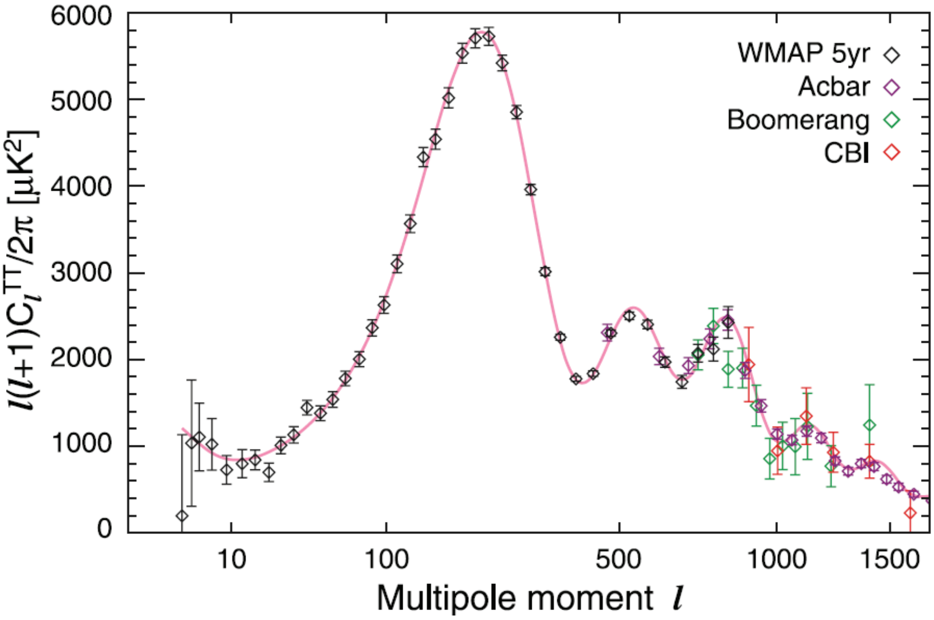

Figure 4.4: The angular power spectrum of the CMBR temperature anisotropy obtained by the experiments: WMAP 5 year, Acbar, Boomerang, CBI. (Figure from Ref. (Nolta et al. (2009)))

with $l \geq 100$ contains the peaks with the different amplitudes. These peaks are caused by the acoustic oscillations that arose in the baryon-photon plasma before decoupling of the photons from the baryons during the recombination epoch. After the termination of the recombination, their positions were shifted as a result of the expansion of the universe. Therefore, the positions and the amplitudes of the acoustic peaks contain the important information about the evolution of the universe. The first acoustic peak defines the sound horizon of the baryons, the value of which serves as the *standard ruler* for determining the distances in cosmology. On the other hand, the size of the sound horizon can be determined by measuring the angular scale of the first sound peak. In the third region with $l \geq 2000$, the amplitude of the power anisotropy spectrum decreases sharply due to the Silk damping (a description of this effect is given below).

4.2.4 Basic Mechanisms Causing the CMBR Primary Anisotropy

- Matter density fluctuations in the primordial plasma, Refs. (Hu & Okamoto (2002), Kosowsky (2001))

conformal momentum.

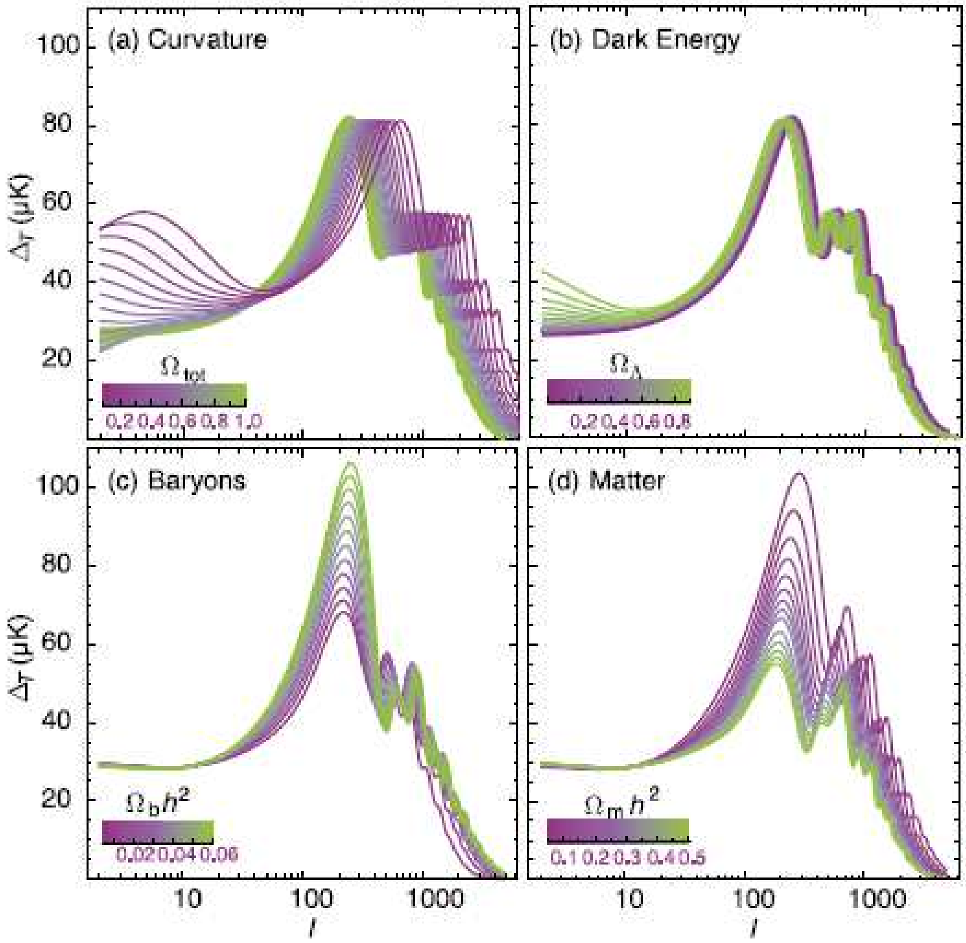

Figure 4.5: The influence of the cosmological parameters on the CMBR angular power spectrum. The values of the square root of the angular power spectrum, $\Delta_T = \sqrt{l(l+1)C_l/2\pi}T_0$, are plotted versus to the logarithmic scale of the angular momentum, l. (Figure from Ref. (Hu & Okamoto (2002)))

The density of the baryons is directly related to the energy density of dark matter. On the scales larger than the event horizon during the recombination, the distribution of the baryons follows the distribution of dark matter. On the smaller scale, the pressure of the baryon-photon plasma is effective, since before the recombination these components were closely related to the Thompson scattering. In the regions with the increased dark matter density, the density of the baryons is also increased. In such regions, the temperature of the baryons increases due to their adiabatic compression, which leads to an increase in the value of the temperature of the photons.

- Doppler effect, Ref. (Schneider (2006))

  The electrons, which scatter the CMBR photons for the last time during the recombination, have the additional peculiar velocities relative to the Hubble flow. These velocities are associated with the fluctuations in the matter density and, accordingly, with the temperature fluctuations. As a consequence of the Doppler effect, the CMBR photons, which move away from us at the velocities greater than the Hubble expansion, experience the additional redshift. This leads to the decrease in the value of the temperature measured in this direction.

- Silk damping, Refs. (Hu & Okamoto (2002), Kosowsky (2001), Scott & Smoot (2010))

  The Silk damping or, in other words, the photon diffusion damping is a physical process that reduces the energy density anisotropy, Ref. (Silk (1968)). Since the mean free path of the photons is finite, the baryons and the photons become separated from each other on the small spatial scales. This means that on the small length scales (for $l \geq 1000$), the temperature fluctuations can be smeared out by the diffusion of the photons, see Fig. (4.5) (d).

- Integrated Sachs-Wolfe effect, Refs. (Sachs & Wolfe (1967), White & Hu (1997), Hu & Okamoto (2002), Scott & Smoot (2010))

  The spatial distribution of the potential in the universe changes at the radiation dominated epoch or at the dark energy dominated epoch. When the CMBR photons pass through this evolving potential, the energy of these photons changes, *i.e.*, the differential gravitational redshift of the photons occurs. This is the so-called *Integrated Sachs-Wolfe effect* (ISW), Ref. (Sachs & Wolfe (1967)). The ISW effect mainly affects the low values of the CMBR multipoles, see Fig. (4.5) (a). On the large scales, the CMBR temperature anisotropy is associated with the density fluctuations owing to the ISW effect, Ref. (White & Hu (1997)).

- Primary metric tensor perturbations, Refs. (Hu & White (1997), Scott & Smoot (2010))

  The cause of the CMBR primary temperature anisotropy is the metric perturbations. These perturbations can generate the scalar, vector and tensor modes. The tensor modes (the transverse metric perturbations with zero trace) or, the so-called gravitational waves generate the primary temperature anisotropies of the CMBR due to the total effect of the anisotropic expansion of space, Ref. (Scott & Smoot (2010)). The contribution of the tensor modes to the angular power spectrum of the CMBR temperature anisotropy can occur at $\vartheta > 1$, respectively, at $l > 180$. The tensor mode can be distinguished from the angular power spectrum of the CMBR temperature anisotropy using the polarization data of the CMBR (information about this is presented below).

4.2.5 Secondary Anisotropy of the CMBR

Propagating through the universe, the CMBR photons can experience a number of the distortions, which can change the temperature distribution of the CMBR photons on the sky. In the angular power spectrum of the CMBR temperature anisotropy, these effects are considered as the *secondary anisotropies*. Consider the effects that cause the secondary anisotropes:

- Thomson scattering of the CMBR photons, Refs. (Hu & Dodelson (2002),Schneider (2006))

  The Thomson scattering of the CMBR photons on the free electrons occurred in the redshift range, $z \in (6; 20)$. These free electrons appeared as a result of the reionization of the neutral hydrogen atoms in the universe by the dwarf galaxies, and/or by the very first generation of the stars (by the Population III stars), and/or by the first quasars. The Thomson scattering is isotropic, so the direction of the photons after scattering becomes almost independent of their original directions of the motion. The scattered CMBR photons form the isotropic component of the radiation with the CMBR temperature. As a result of this effect, the primary temperature anisotropy is suppressed, *i.e.*, the measured CMBR temperature fluctuations will decrease due to the fraction of the photons that experienced the Thompson scattering. In addition to suppressing of the primary temperature anisotropy, the re-scattering of the CMBR photons causes the generation of the additional polarization at the large angles and the Doppler effect at the large angles, Ref. (Hu & Dodelson (2002)).

- Gravitational lensing of the CMBR photons, Refs. (Hu & Dodelson (2002), Schneider (2006))

  The gravitational field of the matter density fluctuations in the universe causes the gravitational lensing (the gravitational deviation) of the CMBR photons, which leads to the change of the initial direction of the motion of the photons. This means that while at the present epoch we observe two photons separated by an angle, θ, the physical separation between them during the decoupling epoch differed from the value $d_A(z_{\rm dec})\theta$ due to the gravitational deviation of the photons. As a result of this effect, the correlation function of the temperature fluctuations becomes slightly blurred. The influence of this effect is significant at the small angular scales.

- Sunyaev-Zeldovich effect, Refs. (Scott & Smoot (2010), Yoo & Watanabe (2012))

The galactic clusters left an imprint on the CMBR photons, by the so-called *Sunyaev-Zeldovich* (SZ) effect[8], Ref. (Sunyaev & Zeldovich (1970)). If the CMBR photons move through a cluster of the galaxy, then they will experience the inverse Compton scattering on the high-energy electrons in this cluster. As a result of this scattering, the energy and the temperature of the CMBR photons increase. Thus, the spectrum of the CMBR becomes distorted.

Influence of the Cosmological Parameters on the CMBR Angular Power Spectrum

The influence of the cosmological parameters on the angular power spectrum of the CMBR is shown in Fig. (4.5). The dependence of the CMBR angular power spectrum on the space curvature of the universe is shown in Fig (4.5) (a). There are two effects associated with the influence of the space curvature on the CMBR angular power spectrum: the shift of the minima and maxima of the Doppler peaks and the strong dependence of the angular power spectrum in the region with $l \leq 100$ on the total energy density parameter, $\Omega_{\rm tot}$, Refs. (Hu & Dodelson (2002), Schneider (2006)). The latter effect is a consequence of the ISW effect, since an increase in the values of the space curvature leads to a greater time variation of the gravitational potential. The shift of the acoustic peak is due to the fact that the value of the angular diameter distance, $d_A(z_{\rm rec})$, is sensitive to the space curvature variation, therefore, the angular diameter distance scale, which corresponds to the sound horizon, also changes.

The influence of dark energy (the cosmological constant Λ) on the CMBR angular power spectrum in the case of a flat universe is shown in Fig. (4.5) (b). The location of the acoustic peaks is almost independent of the value of the dark energy density parameter, Ω_Λ.

The dependence of the CMBR angular power spectrum on the baryons energy density is shown in Fig. (4.5) (c). An increase in the value of the energy density parameter, $\Omega_{\rm b}h^2$, leads to an increase in the amplitude of the first acoustic peak and a decrease in the amplitude of the second acoustic peak.

The influence of the value of the matter energy density parameter, $\Omega_{\rm m}h^2$, on the CMBR angular power spectrum is presented in Fig. (4.5) (d). Changing in the value of this parameter causes a change in the acoustic peaks amplitudes and the acoustic peaks locations, Refs. (Hu

[8] The SZ effect is scattering and its value does not depend on redshift, so the clusters of the galaxies can be found at any distances. The measurements of the SZ effect are used to search for the clusters of the galaxies in order to estimate their masses, as well as to clarify the value of the Hubble constant, H_0, Ref. (Scott & Smoot (2010)). In addition, in combination with the accurate values of redshift and masses for the clusters of the galaxies (for example, with the X-ray observations), the SZ effect can be applied as the *standard ruler* in cosmology, Ref. (Cooray et al. (2001)).

& Dodelson (2002), Schneider (2006)).

4.2.6 Polarization of the CMBR

The CMBR is polarized at the level of several mkK, Ref. (Hu & White (1997)). The cause of both the temperature anisotropy and its polarization are the scalar and tensor gravitational perturbations of the metric[9]. Since the sources of the CMBR temperature anisotropy and the polarization are the same, their power spectra should be correlated, Refs. (Kosowsky (2001), Scott & Smoot (2010)). The combination of the angular power spectrum of the CMBR temperature anisotropy and the signal of the CMBR E-mode polarization according to the results of the experiments: BICEP, BOOMERANG, CBI, DASI and QUAD, are shown in Fig. (4.6) (right panel).

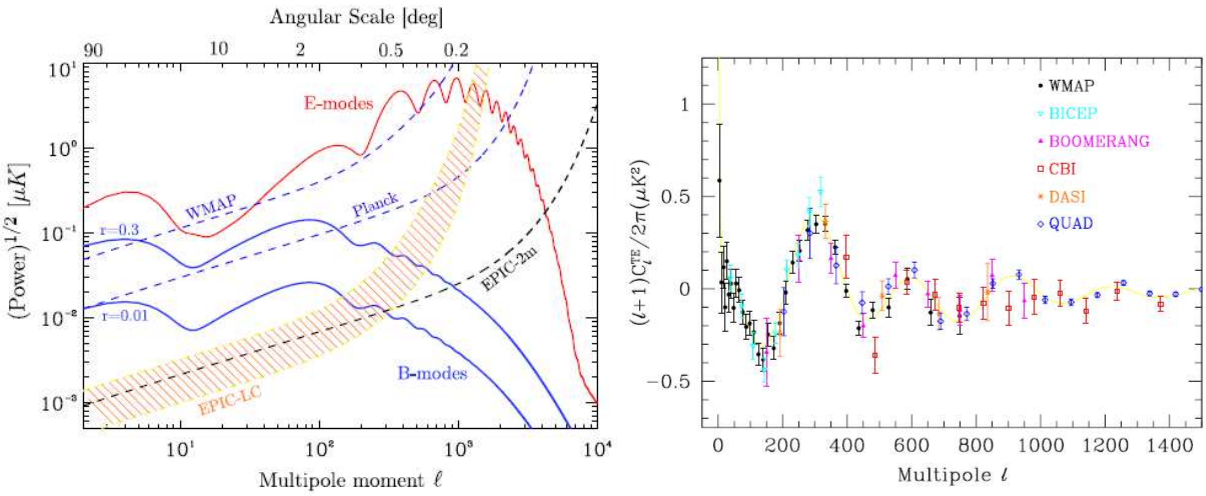

Figure 4.6: Left panel: the predicted polarization spectra of the E-mode (red curve) and B-mode (blue curves) combined with the results of the experiments: WMAP, Planck and EPIC. (Figure from Ref. (Dodelson et al. (2009))) Right panel: the combination of the angular power spectrum of the temperature anisotropy and the signal of the E-mode polarization, according to the results of the experiments: BICEP, BOOMERANG, CBI, DASI and QUAD. (Figure from Ref. (Scott & Smoot (2010)))

Stokes Parameters

Mathematically, the polarization vector of the electromagnetic waves is described by the *Stokes parameters*, Ref. (Kosowsky (1996)).

Suppose a plane monochromatic wave, which is characterized by a frequency of ω_0, propagates along the direction of z. The projections of the electric field vector, $\vec{E}$, on the x and

[9] The vector perturbations are not usually taken into account due to their absence in the standard cosmological scenario.

y axes have the form, respectively, Refs. (Kosowsky (1996), Kosowsky (2001)):

$$E_x = a_x(t)\cos(\omega_0 t - \beta_x(t)), \qquad E_y = a_y(t)\cos(\omega_0 t - \beta_y(t)), \tag{4.14}$$

where the amplitudes of the projections of the electric field vector a_x and a_y, as well as the phase angles β_x and β_y, are the slowly varying functions of time relative to inverse frequency of the electromagnetic wave.

The Stokes parameters are determined by the time-averaged values of the amplitudes projections and the phases of the electric field vector:

$$I \equiv \langle a_x^2\rangle + \langle a_y^2\rangle, \tag{4.15}$$

$$Q \equiv \langle a_x^2\rangle - \langle a_y^2\rangle, \tag{4.16}$$

$$U \equiv \langle 2a_x a_y \cos(a_x - a_y)\rangle, \tag{4.17}$$

$$V \equiv \langle 2a_x a_y \sin(a_x - a_y)\rangle. \tag{4.18}$$

The parameter I is the intensity of the electromagnetic radiation, therefore, this parameter has a positive value. The sign and the values of the parameters Q, U and V characterize the polarization state of the electromagnetic wave. For the natural unpolarized light, these parameters are equal to zero, $Q = U = V = 0$. The value of the parameter V determines the difference between the intensities of the right and left-side circular (rotor) polarizations. The parameter V depends on the rotation of the axes of the coordinate system, while the parameters Q and U are invariant with respect to the rotation of the axes of the coordinate system.

The linear polarization of the electromagnetic wave is determined by the parameters Q and U. The linear polarization matrix is formed from these parameters as:

$$A = \begin{pmatrix} Q & U \\ U & -Q \end{pmatrix}. \tag{4.19}$$

The determinant of this matrix is defined as:

$$\det(A) = -(Q^2 + U^2). \tag{4.20}$$

The linear polarization will be absent if the determinant of the matrix A is equal to zero. Suppose that the electromagnetic radiation is linearly polarized, *i.e.*, $Q^2 + U^2 \neq 0$. Then it is possible to determine the degree of the linear polarization, p, and the value of the angle, ψ, with respect to the axis, x, as:

$$p = \frac{\sqrt{Q^2 + U^2}}{I}, \qquad \psi = \frac{1}{2} \arctan \frac{U}{Q}, \tag{4.21}$$

the value of the parameter, I, determines the intensity of the electromagnetic radiation, Ref. (Kosowsky (1996)).

Divergence and Curl Components of the CMBR Polarization

The CMBR polarization can be decomposed into the divergence part (called "E-mode") and the curl part (called "B-mode"), Ref. (Kosowsky (1996)). The direction of the polarization of the B-mode is rotated by 45° relative to the direction of the polarization of the E-mode, see Fig. (4.7). The E-mode of the CMBR polarization has parity $(-1)^l$, similar to the spherical

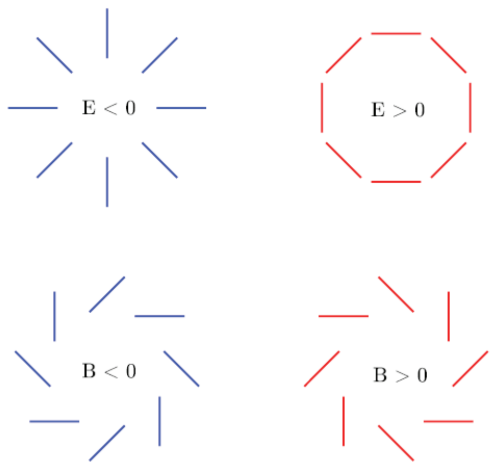

Figure 4.7: The divergence E-mode and the curl B-mode of the polarized field. (Figure from Ref. (Dodelson et al. (2009)))

harmonics, see Fig. (4.7), while the B-mode has parity $(-1)^{l+1}$. The scalar perturbations cannot generate the B-mode of the polarization. The contribution of the vector perturbations to the B-mode formation is a factor of 6 larger than to the E-mode formation, while the contribution of the tensor perturbations to the B-mode formation is a factor of 8/13 smaller than to the E-mode formation, Ref. (Hu & White (1997)). The appearance of the E-mode is due to the Thomson scattering on the electrons from the CMBR photons propagating in an inhomogeneous plasma, Refs. (Kosowsky (1999), Kosowsky (2001)). In 2002, the E-mode was registered by the Degree Angular Scale Interferometer (DASI) experiment, Ref. (Leitch et al. (2002)), see Fig. (4.6) (right panel).

The maximum amplitude of the CMBR polarization is of the order of 0.1 mkK, Ref. (Hu & White (1997)). The cosmologists predict the existence of two types of the B-mode of the CMBR polarization. The emergence of the first type of the B-mode is associated with the interaction of the CMBR with the primordial gravitational waves (tensor mode), *i.e.*, with the rotational, vorticity perturbations (vector mode[10]) arising during inflation. The relic gravitational waves are generated by the tensor perturbations of the metric.

The second type of the B-mode is associated with the gravitational lensing of the E-mode or, in other words, with the cosmological birefringence effect, based on the interaction of the electromagnetic field with the scalar field, Refs. (Lepora (1998), Galaverni et al. (2015)). The second type of the B-mode appeared at a later time than the first type of the B-mode. In addition, the B-mode of polarization can also cause the interaction of the CMBR photons with the particles of the background galactic dust. The second type of the B-mode was discovered in 2013 by the South Pole Telescope and the Herschel Space Observatory, Ref. (Hanson et al. (2013)).

The discovery and the study of the first type of the B-mode is of the great interest for cosmologists. The amplitude of the first type of B-mode corresponds to the amplitude of the primordial gravitational waves and, accordingly, determines the energy scale of inflation, Ref. (Gawiser & Silk (2000)). Therefore, the registration of this type of the B-mode, *i.e.*, the registration of the primordial gravitational waves would be a direct evidence of the correctness of the theory of inflation. In March 2014, the registration of the first type of the B-mode was announced by the BICEP2 experiment, Ref. (Ade et al. (2014*a*)). However, a later analysis, published in September 2014 and provided by another group of researchers, which used data from the Planck Observatory, showed that the result obtained in the BICEP2 experiment was caused by the CMBR photons scattering on the particles of the galactic dust, Ref. (Adam et al. (2016)). Unfortunately, so far the first type of the B-mode is not detected.

The difficulty in detecting of the first type of B-mode is due to the small value of the B-

[10]In the standard cosmology, the vector mode already decays at the inflation stage. The presence of the neutrinos, Ref. (Lewis (2004)), or/and the primordial magnetic fields, Ref. (Kahniashvili & Ratra (2005)), can counteract to the vector mode decay. Taking into account these effects, the contribution of the vector mode must be considered.

mode amplitude of the CMBR polarization, as well as the influence of the birefringence effect on the B-mode, Ref. (Zhao & Li (2014)) and with the impact of the intergalactic medium (in particular, with the influence of the galactic dust). The birefringence effect influences the vector and tensor fluctuations. As a result of this effect, the B-mode is transformed into the E-mode and the tensor perturbations, which generate the B-mode and the E-mode, also occur, Ref. (Lepora (1998)).

In this thesis, we obtained the constraints on the model parameters α and $\Omega_{\rm m}$ in the ϕCDM Ratra-Peebles scalar field model using the BAO/CMBR analysis. In the BAO/CMBR analysis, we compared the observational and theoretical values of the ratio of the comoving angular diameter distance to the distance scale at the decoupling epoch. A more detailed description of the BAO/CMBR analysis and its results is presented in Chapter VIII.

4.3 Barion Acoustic Oscillations

Before the recombination epoch, the photons, the baryons and the electrons were closely interrelated. In the primary plasma, the regions of the over matter density, which consist of dark matter and the baryons, can be randomly formed. Such the regions attract another matter to themselves and, on the other hand, as a result of the baryons and the photons interaction, a strong radiation pressure is created. Oppositely directed the gravitational and radiation pressures induce the joint oscillations of the baryons and the photons. These oscillations are called the *Baryon Acoustic Oscillations* (BAO), which are the sound waves, and they are characterized by the fluctuations, $\delta_{\rm b}$, in the baryon-photon medium.

The radial pressure leads to the emergence of the spherical sound wave of both the baryons and the photons moving outward from the region with the over matter density. The baryon-photon medium before recombination is almost relativistic, *i.e.*, the photons energy density, ρ_γ, is greater than the baryons energy density, $\rho_{\rm b}$: $\rho_{\rm b} < \rho_\gamma$. The photons pressure, P_γ, is related to the photons energy density, ρ_γ, as $P_\gamma = 1/3\rho_\gamma$. The value of the sound speed in the primordial plasma is defined as, Ref. (Rubakov (2014)):

$$v_s = \sqrt{\partial P_\gamma / \partial \rho_\gamma} = \sqrt{1/3} \approx 0.58. \tag{4.22}$$

Thus, the value of the sound speed (the speed of the sound wave) is no much more than half the speed of light[11]. Dark matter interacts only gravitationally and, therefore, it remains at

[11] Taking into account the value of the speed of light, this formula has the form, $v_{\rm s} \approx 0.58c$.

the center of the sound wave being the primary cause of the emergence of the regions with the over matter density.

At the end of the recombination epoch, the decoupling of the photons and the baryons occurs at redshift $z_{\rm dec} \approx 1100$. If before decoupling the baryons and the photons move from the center of the over matter density region together, then after decoupling the photons will cease to interact with the baryons and dissipate. As a result, the radiation pressure in the over matter density region decreases and, eventually, the over As a result, the radiation pressure in the over matter density region decreases and, eventually, the over density region with a fixed radius is formed density region with a fixed radius is formed, which is called the *sound horizon*, $r_{\rm s}$. The comoving size of the sound horizon at the photons decoupling is determined by the equation[12]:

$$r_{\rm s} = \int_0^{t_{\rm dec}} v_{\rm s} \frac{dt'}{a(t')}. \tag{4.23}$$

The energy distribution of BAO within the sound horizon is defined as, Ref. (Rubakov (2014)):

$$\delta_{\rm b} \sim \cos\left(k r_{\rm s}\right) = \cos\left(\int_0^{t_{\rm dec}} v_s \frac{k}{a(t')} dt'\right), \tag{4.24}$$

here k is the conformal momentum[13].

The energy distribution of BAO outside of the sound horizon, $\delta_{\rm b}$=const, *i.e.*, the baryon fluctuations are frozen. According to Eq. (4.24), before recombination, the baryon-photon fluctuations are the oscillating function of the conformal momentum, k. The baryon density fluctuations, $\delta\rho_{\rm b}$, oscillate as:

$$\delta\rho_{\rm b}(k) \approx \rho_{\rm b}\delta\rho_{\gamma}(k) \sim \rho_{\rm b}\cos(k r_{\rm s}). \tag{4.25}$$

The baryon density oscillations, $\delta\rho_{\rm b}$, are preserved to the present epoch. The baryon density oscillations in the matter power spectrum, $P(k)$, as the tiny fluctuations are represented in Fig. (4.8).

After recombination, the baryons remain at the distance of the sound horizon from each other, $r_{\rm s}$, and dark matter is located at the center of the over density region. Dark matter and the baryonic matter attract each other[14], which ultimately leads to the formation of the galaxies in the universe. Thus, the galaxies are separated from each other by the sound

[12] The physical size of the sound horizon at the photons decoupling is equal to $a(t_{\rm dec}) r_{\rm s}$.

[13] The physical momentum is described by the equation, $k_{\rm phys} = k/a(t)$.

[14] Due to the dominance of dark matter, the gravitational potential, which is formed by dark matter, is also dominant. The baryonic matter follows this potential, rolling down into its potential well.

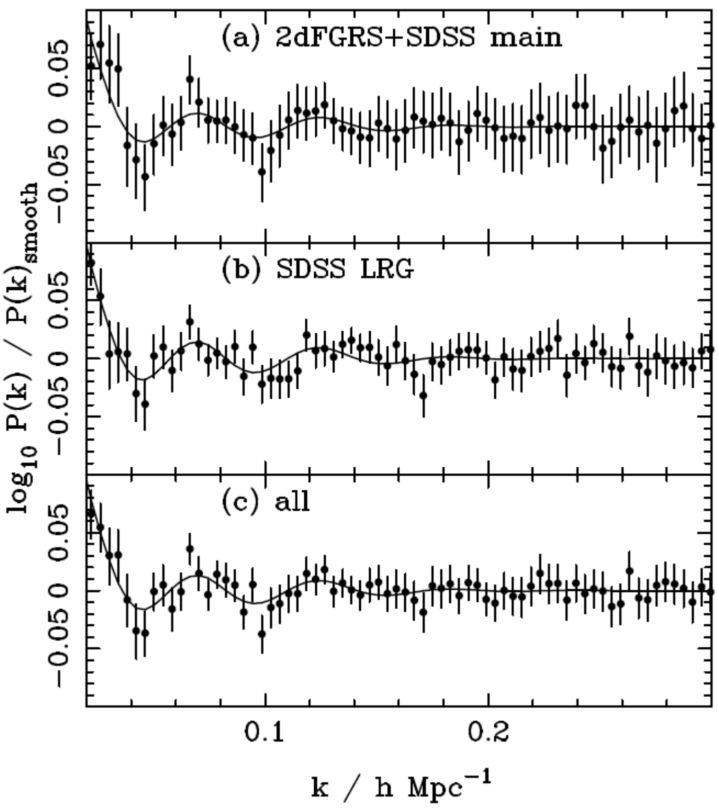

Figure 4.8: Baryon Acoustic Oscillations in the matter power spectrum discovered in: (a) 2dFGRS and SDSS main galaxies, (b) SDSS LRG sample, (c) both samples. Solid curves represent the best fit of the data. (Figure from Ref. (Percival et al. (2007)))

horizon or the BAO signal, the size of which increases over time due to the Hubble expansion, Ref. (Rubakov (2014)). The theoretical predictions of the current comoving size of the BAO sound horizon give the following results, Ref. (Yoo & Watanabe (2012)):

$$r_{\rm s} = \int_{t_{\rm dec}}^{\infty} \frac{c_{\rm s} dt}{a} = \int_{t_{\rm dec}}^{\infty} \frac{c_{\rm s}}{H(z)} dz \sim 150 \text{ Mpc} \sim 100 h^{-1} \text{ Mpc}, \tag{4.26}$$

where $h = 0.678$, according to Plank 2015, Ref. (Ade et al. (2016)).

Using the observational data on the large-scale structure of the galaxies, one can measure the sound horizon scale and compare the result obtained with the theoretical predicted value of this scale. The two-point correlation function, $\xi(s)$, depends on the comoving distance, s, of the galaxy. This function describes the probability that one galaxy will be found at a given distance from another, Ref. (Rubakov (2014)). The Sloan Digital Sky Survey (SDSS) provides the redshift distribution of the galaxies in the range up to the value $z = 0.47$, Ref. (Eisenstein et al. (2005)). This information can be used to estimate the size of the BAO signal. The two-point correlation function fixes the BAO signal at the distance, $100h^{-1}$ Mpc,

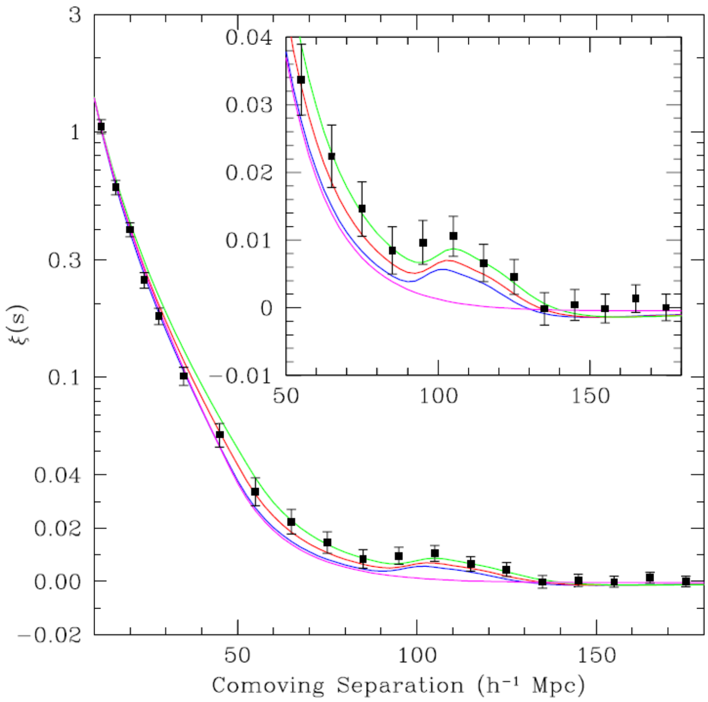

Figure 4.9: The large-scale redshift-space two-point correlation function, $\xi(s)$, of the SDSS sample. (Figure from Ref. (Eisenstein et al. (2005)))

in the redshift range, $z \in (0.16; 0.47)$, see Fig. (4.9). The size of the BAO signal is used as the *standard ruler* to determine the distance scale in cosmology, Ref. (Yoo & Watanabe (2012)).

Comparing Fig. (4.4) and Fig. (4.9), we can conclude that the measurements of the CMBR angular power spectrum of the temperature anisotropy and the measurements of the BAO signal indicate that the current radius of the sound horizon is approximately 150 Mpc. This result coincides with the theoretically calculated value of the BAO signal in Eq. (4.26).

4.4 Statistics of the Large-Scale Structure of the Universe

The large-scale structures, which are observed at the present epoch in the universe, such as galaxies, clusters of galaxies and superclusters, were formed as a result of the evolution of the small initial matter density fluctuations in the expanding universe, Ref. (Lifshitz (1946)).

4.4.1 Influence of the Gravitational Instability on the Formation of Large-Scale Structures in the Universe.

The temperature fluctuations of the CMBR, which is detected by the COBE satellite, are caused by the inhomogeneities in the matter density that originated in the early universe, Ref. (Kosowsky (2001)). The cause of the matter density fluctuations could be the quantum fluctuations of the scalar field or the topological defects resulting from the phase transitions during inflation, Ref. (Kamionkowski & Kosowsky (1998)). The theory that describes the formation and the growth of these inhomogeneities is based on the Jeans instability or, in other words, on the gravitational instability of the matter density fluctuations, Ref. (Jeans (1902)). The matter density fluctuations, being a source of the additional gravitational field, attract the surrounding matter to themselves. As a result of this process, an increase in the size of these fluctuations occurs, since the force of the radiation pressure prevails over the force of gravity, which leads to the spread of the matter density fluctuations in the medium. The growth of the matter density fluctuations continues until the equilibrium is reached between the force of gravity and the force of the radiation pressure. This equilibrium occurs at a critical size of the matter density fluctuations, at the so-called *Jeans wavelength*, λ_J. The value of the Jeans wavelength is determined by the speed of the sound wave, v_{s}, and the average density of the medium, $\langle\rho\rangle$, in which the matter density fluctuations develop, Ref. (Gorbunov & Rubakov (2011)):

$$\lambda_J = v_{\mathrm{s}}\sqrt{\frac{\pi}{G\langle\rho\rangle}}. \tag{4.27}$$

After reaching the Jeans wavelength, the force of gravity prevails over the force of the radiation pressure. At the same time, the process of an increase in the size of the matter density fluctuations is replaced by the process of the adiabatic compression. As a result, the relaxation (the collapse) of the matter density fluctuations occurs. The particles tend to a common gravitational center, in the end, most particles concentrate at the center, and a new object, the protogalaxy, is formed. The emergence of the protogalaxies in the universe occurs at redshift $z \sim 10$. The subsequent evolution of the protogalaxies led to the formation of the large-scale structures in the universe.

4.4.2 Linear Perturbation Theory

Relative Density Contrast

The value of the matter density fluctuations is determined by the relative contrast of the matter density:

$$\delta\rho(\vec{r},t) = \frac{\delta\rho(\vec{r},t)}{\langle\rho\rangle} = \frac{\rho(\vec{r},t) - \langle\rho\rangle}{\langle\rho\rangle}, \tag{4.28}$$

here $\rho(\vec{r},t)$ is the value of the density in the universe in the direction, $\vec{r}$, and at the moment of time, t.

From Eq. (4.28), it follows that $\delta \geq -1$ because $\rho > 0$. The small value of the temperature anisotropy of the CMBR, $\delta T/T_0 = 1/3\delta\rho/\langle\rho\rangle \sim 10^{-5}$ assumes that $|\delta| \ll 1$ at redshift $z_{\rm dec}$. The protogalaxies that arose in the universe are characterized by a large density contrast, $\delta\rho/\langle\rho\rangle > 1$.

The gravitational field formed by the average matter density, $\langle\rho\rangle$, determines the dynamics of the Hubble expansion of the universe. The fluctuations of the matter density from the average value, $\delta\rho(\vec{r},t) = \rho(\vec{r},t) - \langle\rho\rangle$, generate the additional gravitational field.

Linear Perturbation Equation

Consider the growth of the matter density fluctuations on the length scale, which is significantly smaller than the Hubble radius[15]. Suppose that the matter in the universe is approximated by the dust fluid. The dust fluid is characterized by: the energy density, $\rho(\vec{r},t)$; the three-dimensional velocity, $v(\vec{r},t)$, and the zero pressure, p.
The behavior of the dust fluid is described by the following equations:

1. **The continuity equation**, presented earlier, Eq. (2.42).

2. **The Euler's equation**[16]:

$$\frac{\partial\vec{v}}{\partial t} + (\vec{v}\cdot\nabla)\vec{v} + \nabla\Phi + \frac{\nabla p}{\rho} = 0, \tag{4.29}$$

where Φ is the Newton's gravitational potential corresponding to the Poisson's equation.

[15] On these length scales, the growth of the structures in the universe is described by the Newton's theory of gravity. Considering the growth of the matter density fluctuations on the length scales comparable or more than the Hubble radius, it is necessary to take into account the influence of the spacetime curvature and, therefore, it is necessary to apply the GTR.

[16] The Euler's equation expresses the conservation law of the momentum. This equation also describes the matter behavior under the action of forces on it, which are represented through the pressure gradient, ∇p, and the gradient of the Newton's gravitational potential, $\nabla\Phi$.

3. **The Poisson's equation**[17]:

$$\nabla^2\Phi = 4\pi G\left(\rho + 3p\right). \tag{4.30}$$

As a result of solving the system of the aforementioned equations: the continuity equation, Eq. (2.42), the Euler's equation, Eq. (4.29), and the Poisson's equation, Eq. (4.30), and then linearizing this solution with $|\delta| \ll 1$, we can obtain a linear equation for the matter density fluctuations, the so-called *linear perturbation equation*, Ref. (Pace et al. (2010)):

$$\delta'' + \left(\frac{3}{a} + \frac{E'}{E}\right)\delta' - \frac{3\Omega_{\mathrm{m0}}}{2a^5E^2}\delta = 0, \tag{4.31}$$

here the prime means the derivative with respect to the scale factor, $' = d/da$.

The linear perturbation equation, Eq. (4.31), completely describes the evolution of the matter density fluctuations in the universe.

Growth Rate Function of the Matter Density Fluctuations

The evolution of the fluctuations is expressed in terms of the linear growth factor, $D(a)$, which is usually normalized arbitrarily. We chose the normalization in which the value of the linear growth factor is equal to unity at the present epoch, $D(a_0 = 1) = 1$. Thereby, the linear growth factor is defined as:

$$D(a) = \delta(a)/\delta(a_0), \tag{4.32}$$

where $\delta(a_0)$ is a value of the matter density contrast today. The relation $D(a) = a$ for $a \ll 1$ is fulfilled for the matter dominated epoch.

The fractional matter density is given as:

$$\Omega_{\mathrm{m}}(a) = \Omega_{\mathrm{m0}}a^{-3}/E^2(a). \tag{4.33}$$

The growth rate of the matter density fluctuations is described by the logarithmic derivative of the linear growth rate, or, in other words, by the the growth rate function, Ref. (Wang & Steinhardt (1998)):

$$f(a) = d\ln D(a)/d\ln a. \tag{4.34}$$

[17]The Poisson's equation is given as the 0-0 component of the Einstein's equation, Eq. (2.52). Since only the matter is considered to study the growth of the matter density fluctuations, in Eq. (4.30) the pressure is equal to zero, $p = 0$.

The growth rate function, $f(a)$, is highly dependent on the fractional matter density, $\Omega_{\rm m}(a)$, and its dependence can be parametrized by the power law, Ref. (Wang & Steinhardt (1998)):

$$f(a) \approx (\Omega_{\rm m}(a))^{\gamma(a)}, \tag{4.35}$$

here $\gamma(a)$ is the *effective growth index*, which is a time-dependent function. The value of the effective growth index depends on both the dark energy model and the theory of gravity. The dependence of the effective growth index, $\gamma(a)$, on the scale factor can be determined by the expression presented in Eq. (4.35), Ref. (Wu et al. (2009)):

$$\gamma(a) = \frac{\ln f(a)}{\ln(\Omega_{\rm m}(a))}. \tag{4.36}$$

4.4.3 Linder γ-parametrization

Assuming that the GTR is a correct theory of gravity, the effective growth index, $\gamma(a)$, can be parametrized by the independent way, by the Linder γ-parametrization, Ref. (Linder & Cahn (2007)):

$$\gamma = \begin{cases} 0.55 + 0.05(1 + w_0 + 0.5w_a), & \text{if } w_0 \geq -1; \\ 0.55 + 0.02(1 + w_0 + 0.5w_a), & \text{if } w_0 < -1, \end{cases} \tag{4.37}$$

where $w_0 = w(z = 0)$ and $w_a = (dw/dz)|_{z=1}$. We determined that this parametrization is precise up to redshift, $z = 5$ ($a = 0.2$), see Fig. (7.6) (right panel). The value of γ depends on the characteristics of the dark energy model, for example, on the EoS parameter, w.

In the ΛCDM model based on the GTR, the value of the Linder γ-parametrization, γ, is equal to 0.55, Ref. (Linder & Cahn (2007)). In the models based on a theory of gravity different from GTR, the value of the Linder γ-parametrization, γ, differs from the value of the γ in the models based on GTR gravity. For example, in the Dvali-Gabadadze-Poratti model, $\gamma \approx 0.68$, Refs. (Dvali et al. (2000), Linder (2005), Linder & Cahn (2007)). The value of the Linder γ-parametrization, γ, which is obtained from the observations in the combination with the constraints on other cosmological parameters, can be used to verify the accuracy of GTR on the cosmological length scales, Refs. (Pouri et al. (2014), Taddei & Amendola (2015)).

Chapter 5

Elements of the Statistical Analysis

5.1 Gaussian Probability Distribution

5.1.1 Definition of Gaussian Probability Distribution

The Gaussian or, in other words, the normal distribution of a random variable x is described by the probability density:

$$f(x) = \frac{1}{\sigma\sqrt{2\pi}} e^{-(x-e)/2\sigma^2}. \tag{5.1}$$

The Gaussian distribution is determined by the parameters e and σ. The parameter e is the mathematical expectation and the parameter σ is the standard deviation of the random variable x. The value of σ^2 is the variance of the random variable x. The values 1σ, 2σ and 3σ determine the probability of the event realization or the confidence levels, respectively, at 68.27%, 95.45%, 99.73%.

5.1.2 Function χ^2 and the Likelihood Function

Function χ^2 and the Likelihood Function for Independent Measurements

Suppose that the model parameters, $\mathbf{p}$, are distributed according to the Gaussian distribution, Eq. (5.1). N independent measurements, $X^{\rm obs}(z_i)$, were carried out to determine the values of these model parameters. The standard deviation for each measurement, σ_i, is known. These measurements are obtained at redshifts z_i. The theoretical model predicts the corresponding values, $X^{\rm th}(\mathbf{p}, z_i)$.

The function $\chi^2(\mathbf{p})$ is a function of the model parameters, $\mathbf{p}$, is given as:

$$\chi^2(\mathbf{p}) = \sum_{i=1}^{N} \frac{[\mathbf{X}^{\mathbf{obs}}(z_i) - \mathbf{X}^{\mathbf{th}}(\mathbf{p}, z_i)]^2}{\sigma_i^2}. \tag{5.2}$$

The function $\chi^2(\mathbf{p})$ determines the deviation of the theoretical predictions from the observations at the particular values of the parameters, $\mathbf{p}$. A small value of $\chi^2(\mathbf{p})$ means a good approximation by the chosen theory of the observations and, accordingly, a large value of $\chi^2(\mathbf{p})$ means a poor approximation by the theory of the observations.

The likelihood function, $\mathcal{L}(\mathbf{p})$, for the independent variables is defined as:

$$\mathcal{L}(\mathbf{p}) = \exp\Big\{-\frac{1}{2}\chi^2(\mathbf{p})\Big\}. \tag{5.3}$$

The likelihood function, $\mathcal{L}(\mathbf{p})$, determines the probability that the theoretical predictions of the parameters values, $\mathbf{p}$, coincide with the observations. The large value of the likelihood function, $\mathcal{L}(\mathbf{p})$, means a good approximation of the observations by this theory and the parameter values, $\mathbf{p}$, are the best fit values[1]. Conversely, the small value of the likelihood function, $\mathcal{L}(\mathbf{p})$, means a poor approximation of the observations by this theory.

In the case of the combining of M types of the independent variables, $p_1, p_2, ..., p_{\mathrm{M}}$, the resulting value of the function $\chi^2(\mathbf{p})$ is calculated as a sum of the functions $\chi^2(p_1), ..., \chi^2(p_{\mathrm{M}})$, each of which characterizes a specific type of the independent variables:

$$\chi^2(\mathbf{p}) = \chi^2(p_1) + ... + \chi^2(p_{\mathrm{M}-1}) + \chi^2(p_{\mathrm{M}}). \tag{5.4}$$

In this case, the resulting probability function is calculated as the product of the likelihood functions, $\mathcal{L}(p_1), \mathcal{L}(p_2), ..., \mathcal{L}(p_{\mathrm{M}})$, each of which defines a specific type of the independent variables:

$$\mathcal{L}(\mathbf{p}) = \mathcal{L}(p_1) \cdot \mathcal{L}(p_2) ... \mathcal{L}(p_{M-1}) \cdot \mathcal{L}(p_{\mathrm{M}}). \tag{5.5}$$

Function χ^2 and the Likelihood Function for the Dependent Measurements

For the dependent measurements, function $\chi^2(\mathbf{p})$ is defined as:

$$\chi^2(\mathbf{p}) = [\mathbf{X}^{\mathbf{obs}}(z_i) - \mathbf{X}^{\mathbf{th}}(\mathbf{p}, z_i)]^T C^{-1} [\mathbf{X}^{\mathbf{obs}}(z_i) - \mathbf{X}^{\mathbf{th}}(\mathbf{p}, z_i)], \tag{5.6}$$

[1]It is necessary to distinguish between the notions the **best fit values** of the parameters, $\mathbf{p}$, and the **true values** of the parameters, $\mathbf{p}$. The likelihood function, $\mathcal{L}(\mathbf{p})$, determines the probability with which the values of the arbitrary parameters, $\mathbf{p}$, will be the true values (which are unknown to us). The best fit values are the values of the parameters, $\mathbf{p}$, which are likely to be the true values.

where C =cov$[X_i, X_j]$ is a covariance matrix of the dependent measurements; $\mathbf{X^{obs}}(z_i)$ is a vector of the values of the dependent measurements; $\mathbf{X^{th}}(\mathbf{p}, z_i)$ is a vector of the theoretically predicted values; the superscript T denotes a vector transposition.

The likelihood function for the dependent measurements is:

$$\mathcal{L}(\mathbf{p}) = \exp\Big\{-\frac{1}{2}\Big[\mathbf{X^{obs}}(z_i) - \mathbf{X^{th}}(\mathbf{p}, z_i)\Big]^T C^{-1}\Big[\mathbf{X^{obs}}(z_i) - \mathbf{X^{th}}(\mathbf{p}, z_i)\Big]\Big\}. \tag{5.7}$$

5.1.3 Fisher Formalism

The **inverse Fisher matrix**, $[F^{-1}]$, is a matrix that is inverse to the covariance matrix, $[C]$:

$$[F]^{-1} = [C] = \begin{bmatrix} \sigma_{p_1}^2 & \sigma_{p_1p_2} \\ \sigma_{p_1p_2} & \sigma_{p_2}^2 \end{bmatrix}, \tag{5.8}$$

where the standard deviations $\sigma_{p_1}^2$ and $\sigma_{p_2}^2$ are the 1σ uncertainties of the parameters, p_1 and p_2, respectively; $\sigma_{p_1p_2} = \varrho\sigma_{p_1}\sigma_{p_2}$; ϱ is a correlation coefficient. The absolute value of the correlation coefficient ϱ does not exceed unity, $\mid \varrho \mid \leq 1$. If $\varrho = 0$, then the parameters, p_1 and p_2, are independent of each other, *i.e.*, they are mutually uncorrelated. If $\mid \varrho \mid = 1$, then the parameters will be completely correlated with each other. If $\mid \varrho \mid < 1$, then the parameters will be partially correlated with each other.

Consider the function $\chi^2(p_1, p_2)$, which depends on two parameters, p_1 and p_2. The elements of the Fisher matrix are the second-order expansion coefficients in the Taylor series of the function $\chi^2(p_1, p_2)$ near the minimum of this function.

The two-dimensional Fisher matrix, $[F]$, is calculated as:

$$[F] = \frac{1}{2}\begin{bmatrix} \frac{\partial^2}{\partial p_1^2} & \frac{\partial^2}{\partial p_1 \partial p_2} \\ \frac{\partial^2}{\partial p_1 \partial p_2} & \frac{\partial^2}{\partial p_2^2} \end{bmatrix}\chi^2. \tag{5.9}$$

In other words, the elements of the Fisher matrix, $[F]$, are calculated as the second derivatives of the function χ^2 with respect to the parameters, p_1 and p_2:

$$F_{p_1p_2} = \frac{1}{2}\frac{\partial\chi^2}{\partial p_1 \partial p_2}. \tag{5.10}$$

The covariance matrix, $[C]$, is defined through the Fisher matrix as: $[C] = [F]^{-1}$.

Transformation of the Variables

Formulation of the problem: the Fisher matrix, $[F]$, is defined via the variables[2], $\mathbf{p} = p_1, p_2, p_3$. In turn, these variables depend on the other variables, $\mathbf{p'} = p'_1, p'_2, p'_3$. It is necessary to calculate the Fisher matrix, $[F']$, with respect to the variables, $\mathbf{p'} = p'_1, p'_2, p'_3$, based on the information about the original Fisher matrix, $[F]$.

The elements of the Fisher matrix, $[F'_{\text{mn}}]$, are calculated according to the derivative of the composition of two functions:

$$F'_{mn} = \sum_{ij} \frac{\partial p_i}{\partial p'_m} \frac{\partial p_j}{\partial p'_n} F_{ij}. \tag{5.11}$$

The Fisher matrix, $[F']$, can be obtained as, Ref. (Coe (2009)):

$$[F'] = [M]^T [F][M]. \tag{5.12}$$

The matrix, $[M]$, is defined as:

$$[M] = \begin{bmatrix} \frac{\partial p_1}{\partial p'_1} & \frac{\partial p_1}{\partial p'_2} & \frac{\partial p_1}{\partial p'_3} \\ \frac{\partial p_2}{\partial p'_1} & \frac{\partial p_2}{\partial p'_2} & \frac{\partial p_2}{\partial p'_3} \\ \frac{\partial p_3}{\partial p'_1} & \frac{\partial p_3}{\partial p'_2} & \frac{\partial p_3}{\partial p'_3} \end{bmatrix}. \tag{5.13}$$

Thereby, the elements of the matrix, $[M]$, are calculated as: $M_{ij} = \partial p_i / \partial p'_j$.

5.1.4 Best Fit Model Parameters

Regardless of the type of the observations, the model parameters, $\mathbf{p_0}$, for which the function $\chi^2(\mathbf{p})$ takes the minimum value, are called the best fit model parameters for this theory. In this case, the minimum value of the function $\chi^2(\mathbf{p_0})$ determines the smallest value of the variance, σ^2, for this theory. For the model with two parameters, the boundaries of the confidence intervals at 1σ, 2σ and 3σ are defined, respectively, as: $\chi^2(\mathbf{p}) = \chi^2(\mathbf{p_0}) + 2.3$, $\chi^2(\mathbf{p}) = \chi^2(\mathbf{p_0}) + 6.17$ and $\chi^2(\mathbf{p}) = \chi^2(\mathbf{p_0}) + 11.8$.

The likelihood function, $\mathcal{L}(\mathbf{p})$, has a maximum value with the best fit of the model parameters, $\mathbf{p_0}$. The values of the model parameters, $\mathbf{p_0}$, for which the likelihood function is maximal, have the maximum probability of being the true parameters.

[2]The number of the variables can be arbitrarily large, $\mathbf{p} = p_1, p_2 ... p_{\text{N}}$. In this case, we limited ourselves to the number of the variables $N = 3$.

5.2 Elements of the Theory of Monte Carlo Markov Chains

The Monte Carlo Markov Chain (MCMC) method is used in constructing the vectors for the multidimensional distribution functions. In the statistics, this method is applied to study the posterior distributions of the model parameters.

5.2.1 Definition of the Markov Chains. Transition Probabilities

In 1907, A. A. Markov developed a new type of the random processes. In this process, the result of the experiment affects the result of the subsequent experiment. This type of process is called a Markov chain.

The Markov chain can be described as follows. Consider a set of the states, $S = s_1, s_2, ..., s_r$. The process begins in one of these states and sequentially moves from one state to another. Each movement is called a step. If the chain is currently in the s_i state, then it will go to the s_j state in the next step with the probability, denoted as p_{ij}, and this probability does not depend on the states in which the chain was located before the current state. The probabilities, p_{ij}, are called the **transition probabilities**. The initial probability distribution, S, determines the initial state[3].

Transition Matrix. Homogeneous Markov Chain.

In the notation, p_{ij}, the first index indicates the number of the previous state i, and the second index indicates the number of the next state j. The process can remain in the state in which it is located, and this happens with the probability, p_{ii}.

Suppose that the number of the states is finite and equals k. The **transition matrix** of the system is a matrix, which contains all the transition probabilities of this system, Ref. (Gmurman (2003)):

$$P_1 = \begin{pmatrix} p_{11} & p_{12} & \cdots & p_{1k} \\ p_{21} & p_{22} & \cdots & p_{2k} \\ \cdots & \cdots & \cdots & \cdots \\ p_{k1} & p_{k2} & \cdots & p_{kk} \end{pmatrix}. \tag{5.14}$$

Since the transition probabilities of the events from the state i to the state j placed in each row of the matrix form a complete group, the sum of the probabilities of these events is

[3]Often the Markov chains are compared to a frog jumping on a set of lily pads. The frog starts on one of the lily pads and then jumps from a lily pad to a lily pad with the corresponding transition probabilities, p_{ij}, Ref. (Howard (1971)).

equal to unity. In other words, the sum of the transition probabilities for each row in the transition matrix is equal to unity:

$$\sum_{j=1}^{k} p_{ij} = 1, \ (i = 1, 2..., k). \tag{5.15}$$

The Markov chain is called the **homogeneous** chain, when the conditional probability, p_{ij}, does not depend on the number of the test.

Markov Equality

Let's denote by $P_{ij}(n)$ the probability that the system S will transit from the state i to the state j as a result of n steps (tests). For example, $P_{25}(10)$ is the transition probability from the second to the fifth state as a result of 10 steps. We emphasize that for $n = 1$ we get the transition probability:

$$P_{ij}(1) = p_{ij}. \tag{5.16}$$

Markov problem: knowing the transition probabilities, p_{ij}, find the probabilities, P_{ij}, of the transition of the system from the state i to the state j in n steps.

Let's introduce the intermediate state r between the states i and j. In other words, we assume that the system will move from the initial state i to the intermediate state r with the probability, $P_{ir}(m)$, in m steps. After that, the system moves from the intermediate state r to the final state j with the probability, $P_{rj}(n - m)$, in $(n - m)$ steps.

The transition probability, P_{ij}, of the system from the state i to the state j in n steps can be found using the Markov equality:

$$P_{ij}(n) = \sum_{r=1}^{k} P_{ir}(m) P_{rj}(n - m). \tag{5.17}$$

In our calculations, we apply the normal distribution of the random variable x, which is described by Eq. (5.1).

5.2.2 Monte Carlo Method

In 1949, N. Metropolis and S. Ulam published the paper entitled "Monte Carlo Method" in which this method was presented. The Monte Carlo method is a statistical method for studying the problems based on using of the random numbers, similar to the numbers generated in gambling. Applying the Monte Carlo method, it is required to find a set of the random numbers, which corresponds to a certain probability distribution.

Essence of the Monte Carlo Method

It is required to find the expectation value e of some random variable. For this purpose a random variable is chosen X whose expectation is equal to e:

$$M(X) = e. \tag{5.18}$$

In reality, n tests are performed, as a result of n possible values X are obtained, after which their arithmetic average is calculated:

$$\bar{x} = \left(\sum x_i\right)/n. \tag{5.19}$$

The value of $\bar{x}$ is considered as an approximate value of e^* of the number e:

$$e \simeq e^* = \bar{x}. \tag{5.20}$$

Since the Monte Carlo method requires a large number of the tests, it is often called the **method of the statistical tests**. To use the Monte Carlo method, a reliable set of the random numbers is needed. Such numbers are hard to get, so the pseudo-random numbers are usually used. These numbers must be uncorrelated and evenly distributed over a prior range of the numbers.

Transformation Method

The transformation method is used to search for the pseudo-random numbers from the known probability distributions. It is required to reproduce a continuous random variables X, *i.e.*, to obtain a sequence of its possible values, $X = x_1, x_2, ..., x_k$, which is characterized by the distribution function $F(x)$.

Theorem: consider a possible random value x_i with the distribution function $F(x)$. The value of a random number r_i will correspond to the value of x_i, if it is the solution of the following equation:

$$F(x_i) = r_i. \tag{5.21}$$

In other words, in order to find a possible value of x_i a continuous random variable X, determined by the density distribution $f(x)$, we must choose a random number r_i and solve one of the equations with respect to x_i:

$$\int_{-\infty}^{x_i} f(x)dx = r_i \quad or \quad \int_{b}^{x_i} f(x)dx = r_i, \tag{5.22}$$

where b is a finite, smallest value of a random variable X.

Chapter 6

Dark Energy

As it was described in Chapter I, our universe is in the state of the accelerated expansion. One possible explanation of this phenomenon is the existence of so-called *dark energy*. Dark energy is characterized by the value of the EoS parameter, w, which is defined as a ratio between the pressure, $p_{\rm DE}$, and the energy density, $\rho_{\rm DE}$, $w \equiv p_{\rm DE}/\rho_{\rm DE}$. The accelerated expansion requires that $w < -1/3$. Dark energy is approximately 69% of the total energy density in the universe, its distribution is highly spatially uniform and isotropic, Ref. (Ade et al. (2016)). The negative effective pressure of dark energy causes an accelerated expansion of the universe. The nature of dark energy still remains an unresolved mystery for cosmologists.

6.1 Cosmological Constant Λ

The simplest model of dark energy is a concept of vacuum energy or, in other words, a time-independent cosmological constant denoted as Λ, which was first proposed by Albert Einstein, Ref. (Einstein (1917)), for the review: Refs. (Carroll (2001), Peebles & Ratra (2003), Martin (2012)). In 1917, in order to obtain a static solution, $\dot{a} = 0$, Albert Einstein introduced a new term, $\Lambda g_{\mu\nu}$, into the Einstein tensor, Eq. (2.38), Ref. (Einstein (1917)). As a result, the Einstein's equation, Eq. (2.52), took the form:

$$R_{\mu\nu} - \frac{1}{2} g_{\mu\nu} R - \Lambda g_{\mu\nu} = 8\pi G T_{\mu\nu}, \tag{6.1}$$

where Λ is called the cosmological constant. The addition of this term violates the condition for the transition of the strong gravitational fields to the weak gravitational fields (the transition to the Newtonian limit), imposed on the Einstein tensor in the equations Eq. (2.53) and

Eq. (2.54). In order to fulfill the conditions of this transition, the value of the cosmological constant must be negligible.

Einstein did not have a real physical interpretation of the cosmological constant Λ. After the discovery of the expansion of the universe by Edwin Hubble in 1929, Ref. (Hubble (1929)), Einstein removed the cosmological constant from his equations in 1931. He called the introduction of Λ into these equations his "biggest blunder", Ref. (Gamov (1956)). From the 1930s to the end of the 1990s, the cosmologists were not taken the cosmological constant into account, assuming its value to be zero. After the discovery of the accelerated expansion of the universe in 1998, Refs. (Riess et al. (1998), Perlmutter et al. (1999), Schmidt et al. (1998)), the cosmologists began to use the cosmological constant with a positive nonzero value to explain this phenomenon. Taking into account the cosmological constant Λ in the Friedmann's equations, Eq. (2.97) and Eq. (2.98), a non-static solution can be found. This solution describes an expanding universe.

It is now accepted that the cosmological constant is equivalent to a final energy density of the vacuum, Ref. (Zeldovich (1968)). Suchwise, if the cosmological constant is determined by the vacuum energy density, ρ_{vac}, then the energy density of the cosmological constant, ρ_Λ, will not depend on time:

$$\rho_\Lambda = \rho_{\text{vac}} = \text{const.} \tag{6.2}$$

The energy density of the cosmological constant is defined as:

$$\rho_\Lambda = \frac{\Lambda}{8\pi G}, \tag{6.3}$$

where $\Lambda = 4.33 \cdot 10^{-66}$ eV^2.

The EoS for the cosmological constant:

$$p_\Lambda = -\rho_\Lambda = \text{const.} \tag{6.4}$$

Therefore, the EoS parameter for the cosmological constant is defined as:

$$w_\Lambda = -1. \tag{6.5}$$

The action for the cosmological constant:

$$S = -\frac{1}{16\pi G}\int d^4x\sqrt{-g}(R + 2\Lambda) + S_{\text{M}}, \tag{6.6}$$

where S_{M} is an action for matter.

The Friedmann's equations with the cosmological constant have the form:

$$\frac{\dot{a}^2}{a^2} = \frac{8\pi G}{3}\rho - \frac{K}{a^2} + \frac{\Lambda}{3} \tag{6.7}$$

and

$$\frac{\ddot{a}}{a} = -\frac{4\pi G}{3}(\rho + 3p) + \frac{\Lambda}{3}. \tag{6.8}$$

6.2 Cosmological ΛCDM Model

The Lambda Cold Dark Matter (ΛCDM) model is the *standard* model of the universe. This model describes a spatially flat universe and it is the simplest parametrization of the cosmological Big Bang model. In the ΛCDM model, dark energy is represented by the cosmological constant Λ, which is assumed to be associated with the vacuum energy density. Dark matter is the *cold dark matter* in the ΛCDM model. The ΛCDM model is based on the GTR in order to describe the gravity in the universe at the cosmological scales.

The ΛCDM model is a *concordance* model of the universe, since this model is in a good agreement with the currently available cosmological observations, see Fig. (6.1). In addition,

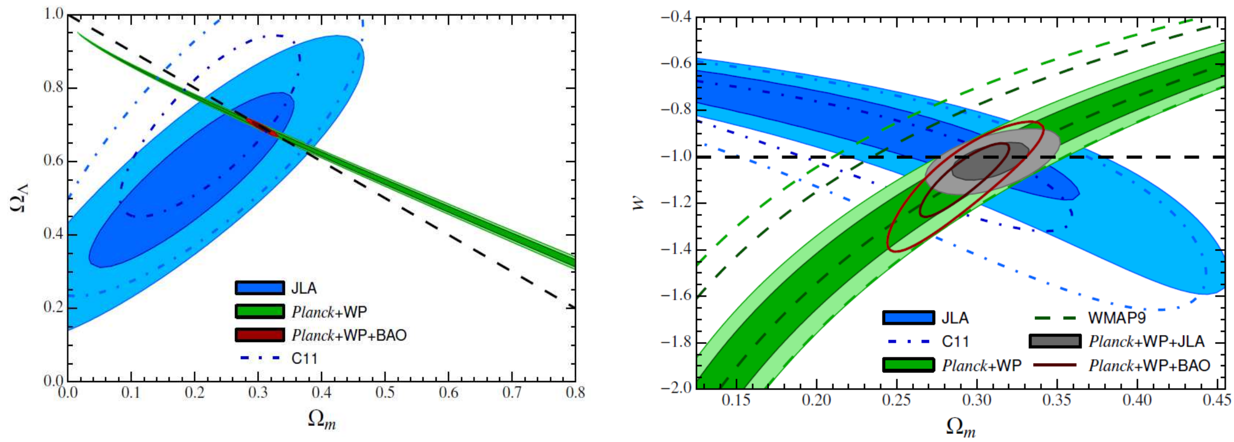

Figure 6.1: The confidence contours at 68% and 95% as a result of the different measurements: SNIa (JLA) and SNIa (C11) compilations, the combination of the Planck temperature and WMAP polarization (Planck + WP) and the combination of the BAO scale. Left panel: for the Ω_{m} and Ω_Λ cosmological parameters in the ΛCDM model. The black dashed line corresponds to a flat universe. Right panel: for the Ω_{m} and w cosmological parameters in the flat $w - \Lambda CDM$ model. The black dashed line corresponds to the cosmological constant hypothesis. (Figure from Ref. (Betoule et al. (2014)))

the ΛCDM model explains: the accelerated expansion of the universe; the large-scale structure in the distribution of the galaxies; the CMBR temperature anisotropy; the chemical composition of the universe (the content of hydrogen, helium and lithium[1]), Ref. (Schneider (2006)).

The ΛCDM model is characterized by main six *independent parameters*: the physical baryon density parameter, $\Omega_{\mathrm{b}}h^2$; the dark matter physical density parameter, $\Omega_{\mathrm{c}}h^2$; the age of the universe, t_0; the scalar spectral index, n_{s}; the amplitude of the curvature fluctuations, Δ^2_{R}; the optical depth during the reionization period[2], τ. In addition to these parameters, the ΛCDM model is described by six extended *fixed parameters*: the total energy density parameter, Ω_{tot}; the EoS parameter, w; the total mass of three types of the neutrinos, $\sum m_\nu$; the effective number of the relativistic degrees of freedom, N_{eff}; the tensor/scalar ratio, r; the running scalar index, $dn_{\mathrm{s}}/d\ln k$.

According to the ΛCDM model, our universe consists of 69,2% of dark energy; 26% of dark matter; 4.8% of the ordinary baryonic matter; 0.1% of the neutrinos; 0.01% of the photons, Ref. (Ade et al. (2016)).

The first Friedmann's equation, which describes the universe expansion in the spatially flat ΛCDM model, is:

$$E(a) = (\Omega_{\mathrm{r0}}a^{-4} + \Omega_{\mathrm{m0}}a^{-3} + \Omega_\Lambda)^{1/2}, \tag{6.9}$$

where Ω_{r0}, Ω_{m0} and Ω_Λ are the energy density parameters for the radiation, the matter and vacuum, respectively, at the present epoch. Until the moment of the neutrinos non-relativization[3], the neutrinos are the relativistic particles, therefore, the neutrinos energy density parameter, Ω_ν, changes with the dependence on the scale factor as a^{-4}. Thus, before the moment of the neutrinos non-relativization, the total radiation energy density consists of the energy densities of the relativistic particles: the photons and the neutrinos. After the moment of the neutrinos non-relativization, the neutrinos become the non-relativistic particles and the energy density parameter of the neutrinos, Ω_ν, evolves as a^{-3}. Therefore, the total energy density parameter of the matter, Ω_{m}, contains all the non-relativistic components, including the non-relativistic neutrinos.

[1]The process of the formation of these chemical elements began during the *primordial nucleosynthesis* in the universe. This epoch began at the temperature of about 1 MeV when the age of the universe was approximately 1 sec. At this time, the following reactions are terminated: $e^- + p \leftrightarrow n + \nu_e$ and the "freezing" of neutrons occurs from these reactions. Approximately from 10 seconds to 20 minutes after the Big Bang, the thermonuclear reactions took place, forming more complex elements: $p + n \to {}^2H + \gamma$, ${}^2H + p \to {}^3He + \gamma$, ${}^3He + {}^2H \to {}^4He + p$, ..., up to ${}^7Li$, Ref. (Rubakov (2014)).

[2]The reionization is the process of the ionization of the neutral hydrogen atoms, which happened in the universe at the range of redshifts, $z \in (6; 20)$.

[3]The neutrino transition from the relativistic to the non-relativistic state occurs at the matter dominated epoch. The earlier this transition occurs, the greater value of the mass acquired by the neutrino. The results of this study are presented in Chapter X.

6.2.1 Shortcomings of the ΛCDM Model

If, indeed, the vacuum energy is the origin of the cosmological constant, then there is a problem with the energy scale of the cosmological constant. The theoretically predicted energy density of the cosmological constant, ρ_Λ, is defined as:

$$\rho_\Lambda \sim \hbar M_{\text{pl}}^4 \sim 10^{72}\ \text{Gev}^4 \sim 2 \cdot 10^{110}\ \text{erg/cm}^3, \tag{6.10}$$

where $M_{\text{pl}} \sim 10^{18}$ Gev is a Planck mass scale; $\hbar$ is a reduced Planck constant[4]. The result obtained in Eq. (6.10) is confirmed by the laboratorian measurements of the vacuum fluctuations by the Casimir effect, Ref. (Casimir (1948)). However, the cosmological observations of the cosmological constant, as dark energy, show a completely different result:

$$\rho_\Lambda^{\text{obs}} \sim 10^{-48}\ \text{Gev}^4 \sim 2 \cdot 10^{-10}\ \text{erg/cm}^3. \tag{6.11}$$

Thus, the observed value of the energy scale of the cosmological constant is by 120 magnitudes less than its value derived from the theoretical predictions. This discrepancy in 120 values of the energy scale is called the cosmological constant problem or the *fine turning* problem, Refs. (Carroll et al. (1992), Carroll (2001)).

The second problem of the cosmological constant is the so-called *coincidence* problem. The essence of this problem is that the energy density of dark energy is comparable with the energy density of dark matter at the present epoch. The radiation energy density, the matter energy density and dark energy depend on the scale factor by the different laws, which are described in Eq. (2.101), Eq. (2.102) and Eq. (2.105), respectively: for the radiation it is $\rho_{\text{r}} \sim a^{-4}$, for the baryons and cold dark matter it is $\rho_{\text{m}} \sim a^{-3}$ and for the cosmological constant it is ρ_Λ=const. The precise cosmological observations show that the ratio between the density of the matter and the density of dark energy today is of the order of unity, $\rho_{\text{m}}/\rho_\Lambda \simeq 1/3$. This fact is a mystery, since the standard ΛCDM model predicts that this ratio must be time-dependent, $\rho_{\text{m}}/\rho_\Lambda \propto a^{-3}$.

Since the vacuum energy does not change over time, it was insignificant during both at the radiation domination epoch and at the matter domination epoch. While the vacuum energy has become the dominant component only recently, at $a \approx 0.76$ (or $z \approx 0.31$), according to Planck 2015 data, Ref. (Ade et al. (2016)), and it will be the only component in the universe in the future, see Fig. (6.2). The energy density of the matter and the energy density of

[4]In accordance with our convention, $\hbar = 1$.

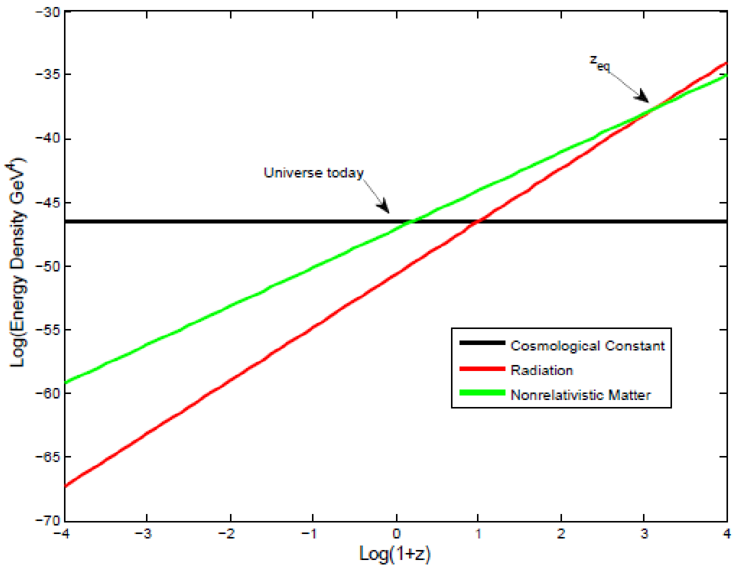

Figure 6.2: The evolution of the radiation energy density, the matter energy density and the cosmological constant Λ. (Figure from Ref. (Samushia (2009)))

the cosmological constant are comparable for a very short period of time, see Fig. (6.2), therefore, the following question arises: "Why did it happen that we live in this short (by the cosmological scale) period of time?" After all, this fact is in the contradiction with the Copernican's principle.

The so-called *anthropic* principle, proposed by Steven Weinberg in 1987, Ref. (Weinberg (1987)), can explain the cosmological constant problems and answer the questions: "Why is the energy density of the cosmological constant so small?" and "Why has the accelerated expansion of the universe started recently?" According to the anthropic principle, the energy density of the cosmological constant, observed today, ρ_Λ, must be suitable for the evolution of the intelligent beings in the universe, Ref. (Barrow & Tipler (1988)).

6.3 Scalar Field Models

There are the numerous alternative models for the ΛCDM model, Refs. (Copeland et al. (2006*b*), Yoo & Watanabe (2012)). Despite the diversity of these models, the ΛCDM model still remains the basic model, the model of the comparison with other dark energy models.

The main alternative to the ΛCDM model are the dynamical scalar field models[5] or, in other words, the so-called ϕCDM models, Refs. (Wetterich (1988*b*), Ratra & Peebles (1988*b*), Peebles & Ratra (2003)). In these models, dark energy is represented in the form of a slowly

[5] A scalar field is a field that is characterized by a scalar value, which is defined at any point in this field. This field is an invariant under the Lorentz transformations.

varying cosmological uniform scalar field, ϕ. The self-interacting spatially uniform scalar field is minimally related to the gravity on the cosmological scales. The ϕCDM models do not have the fine tuning problem of the ΛCDM model. These models have a more natural explanation for the observable low-energy scale of dark energy. If in the ΛCDM model the EoS parameter is constant, $w = -1$, then in the ϕCDM model the EoS parameter will be time-dependent. When the energy density of the scalar field begins to dominate over the energy density of both the radiation and the matter, the universe begins the stage of the accelerated expansion.

At the early epochs of the universe evolution (at large redshifts), the dynamical scalar field is different from the behavior of the ΛCDM model. At the later epoch of the universe evolution (at small redshifts), the dynamical scalar field is almost indistinguishable from the behavior of the cosmological constant Λ.

The ϕCDM models are divided into two classes: the *quintessence models*, Ref. (Zlatev et al. (1999)), and the *phantom models*, Refs. (Caldwell (2002), Caldwell et al. (2003)). These models differ from each other:

- *By the value of the EoS parameter*

  In the quintessence fields $-1/3 < w_\phi < -1$ and in the phantom fields $w_\phi < -1$.

- *In the sign of the kinetic component in Lagrangian*

  The positive sign for the quintessence fields and the negative sign for the phantom fields.

- *In the dynamics of the scalar fields*

  The quintessence field rolls down to the minimum of its potential, the phantom field rolls to the maximum of its potential.

- *In the dynamics of dark energy*

  In the quintessence fields, dark energy almost do not change over time and in the phantom fields it increase over time.

- *In the forecasting the future of the universe*

  In the quintessence models, either the eternal expansion of the universe, or a repeated collapse is predicted depending on the spatial curvature of the universe. In the phantom models, the destruction of any gravitationally-related structures in the universe is predicted. Depending on the asymptotic behavior of the Hubble parameter, $H(t)$, the future scenarios of the universe are divided into: a big rip, for which $H(t) \to \infty$ for finite time, $t = \text{const}$; a little rip for which $H(t) \to \infty$ for infinite time, $t \to \infty$ and a pseudo rip, for which $H(t) \to \text{const}$ for infinite time, $t \to \infty$.

The full action for the scalar field is defined as:

$$S = \int d^4x\sqrt{-g}\Big[-\frac{M_{\rm pl}^2}{16\pi}R + \mathcal{L}_\phi\Big] + S_{\rm M}, \tag{6.12}$$

where $\mathcal{L}_\phi$ is the Lagrangian density of the scalar field, the shape of which depends on the type of the chosen model.

6.3.1 Quintessence Scalar Field

The quintessence scalar field is described by the Lagrangian density:

$$\mathcal{L}_\phi = \frac{1}{2}g^{\mu\nu}\partial_\mu\phi\partial_\nu\phi - V(\phi). \tag{6.13}$$

There are many different quintessence potentials, but so far no preference has been given to any of them. The incomplete list of the quintessence potentials[6] are presented in Table[7] 6.1.

Name	Form	Reference
Ratra-Peebles	$V(\phi) = V_0 M_{\rm pl}^2 \phi^{-\alpha}$; $\alpha = \text{const} > 0$	Ref. Ratra & Peebles (1988*b*)
Ferreira-Joyce	$V(\phi) = V_0 \exp(-\lambda\phi/M_{\rm pl})$; $\lambda = \text{const} > 0$	Ref. Ferreira & Joyce (1998)
Zlatev-Wang-Steinhardt	$V(\phi) = V_0(\exp(M_{\rm pl}/\phi) - 1)$	Ref. Zlatev et al. (1999)
Sugra	$V(\phi) = V_0\phi^{-\chi}\exp(\gamma\phi^2/M_{\rm pl}^2)$; $\chi, \gamma = \text{const} > 0$	Brax & Martin (1999)
Sahni-Wang	$V(\phi) = V_0(\cosh(\varsigma\phi) - 1)^g$; $\varsigma = \text{const} > 0$, $g = \text{const} < 1/2$	Ref. Sahni & Wang (2000)
Barreiro-Copeland-Nunes	$V(\phi) = V_0(\exp(\nu\phi) + \exp(\upsilon\phi))$; ν, $\upsilon = \text{const} \geq 0$	Barreiro et al. (2000)
Albrecht-Skordis	$V(\phi) = V_0((\phi - B)^2 + A)\exp(-\mu\phi)$; A, $B = \text{const} \geq 0$, $\mu = \text{const} > 0$	Albrecht & Skordis (2000)
Urẽna-López-Matos	$V(\phi) = V_0 \sinh^m(\xi M_{\rm pl}\phi)$; $\xi = \text{const} > 0$, $m = \text{const} < 0$	Urena-Lopez & Matos (2000)
Inverse exponent potential	$V(\phi) = V_0 \exp(M_{\rm pl}/\phi)$	Caldwell & Linder (2005)
Chang-Scherrer	$V(\phi) = V_0(1 + \exp(-\tau\phi))$; $\tau = \text{const} > 0$	Chang & Scherrer (2016)

Table 6.1: The list of the dark energy quintessence potentials.

The energy-momentum tensor of the quintessence scalar field, $T_{\mu\nu}$, is defined as:

$$T_{\mu\nu} = 2\frac{\partial \mathcal{L}_\phi}{\partial g^{\mu\nu}} - g_{\mu\nu}\partial\mathcal{L}_\phi. \tag{6.14}$$

Substituting Eq. (6.13) into Eq. (6.14), we get:

$$T_{\mu\nu} = \partial_\mu\phi\partial_\nu\phi - g_{\mu\nu}\left[\frac{1}{2}g^{\alpha\beta}\partial_\alpha\phi\partial_\beta\phi - V(\phi)\right]. \tag{6.15}$$

The components of the quintessence scalar field energy-momentum tensor, $T_{\mu\nu}$, is defined as:

$$T_{00} \equiv \rho_\phi = \frac{1}{2}\dot{\phi}^2 + V(\phi), \tag{6.16}$$

$$T_{0i} = 0, \tag{6.17}$$

$$T_{ij} = 0\ (i \neq j), \tag{6.18}$$

$$T_{ii} \equiv p_\phi = \frac{1}{2}\dot{\phi}^2 - V(\phi), \tag{6.19}$$

where ρ_ϕ and p_ϕ are the energy density and the pressure of the scalar field under the assumption that this scalar field is described by the ideal barotropic fluid model[8].

The components of the scalar field energy-momentum tensor can be represented in the matrix form, as in Eq. (2.47). The EoS parameter for the quintessence scalar field is defined as:

$$w_\phi \equiv \frac{p_\phi}{\rho_\phi} = \frac{\dot{\phi}^2/2 - V(\phi)}{\dot{\phi}^2/2 + V(\phi)}. \tag{6.20}$$

The Klein-Gordon equation of motion for the quintessence scalar field can be obtained by varying the action in Eq. (6.12), where the Lagrangian density is defined by Eq. (6.13):

$$\ddot{\phi} + 3H\dot{\phi} + \frac{\partial V(\phi)}{\partial\phi} = 0, \tag{6.21}$$

here the overdots denote the derivatives with respect to physical time, t.

The influence of the scalar field, ϕ, on the dynamics of the universe is reflected in the

[6]The Ferreira-Joyce potential was investigated earlier by Lucchin and Matarrese, Ref. (Lucchin & Matarrese (1985)), as well as by Ratra and Peebles, Ref. (Ratra & Peebles (1988*a*)), although the complete detailed description of the model was given by Ferreira and Joyce, Ref. (Ferreira & Joyce (1998)).

[7]In Table 6.1 and in Table 6.2, the model parameter, V_0, has a dimension of GeV^4. This model parameter is related to the dark energy density parameter at the present epoch.

[8]The barotropic fluid is a fluid whose density depends only on the pressure.

first Friedmann's equation:

$$H = H_0(\Omega_{\mathrm{r}0}a^{-4} + \Omega_{\mathrm{m}0}a^{-3} + \Omega_\phi(a))^{1/2}, \tag{6.22}$$

where $\Omega_\phi(a)$ is an energy density parameter of the scalar field depending on time. In many ways, the evolution of the function $\Omega_\phi(a)$ is determined by the form of the scalar field potential, $V(\phi)$.

Depending on the shape of the potentials, the quintessence models are subdivided into the *thawing models* and the *freezing models*, Ref. (Caldwell & Linder (2005)). On the $w_\phi - dw_\phi/d\ln a$ phase space, the thawing and the freezing scalar models can be located at the strictly designated regions for each of them, see Fig. (6.3) (left panel). At the early stages of

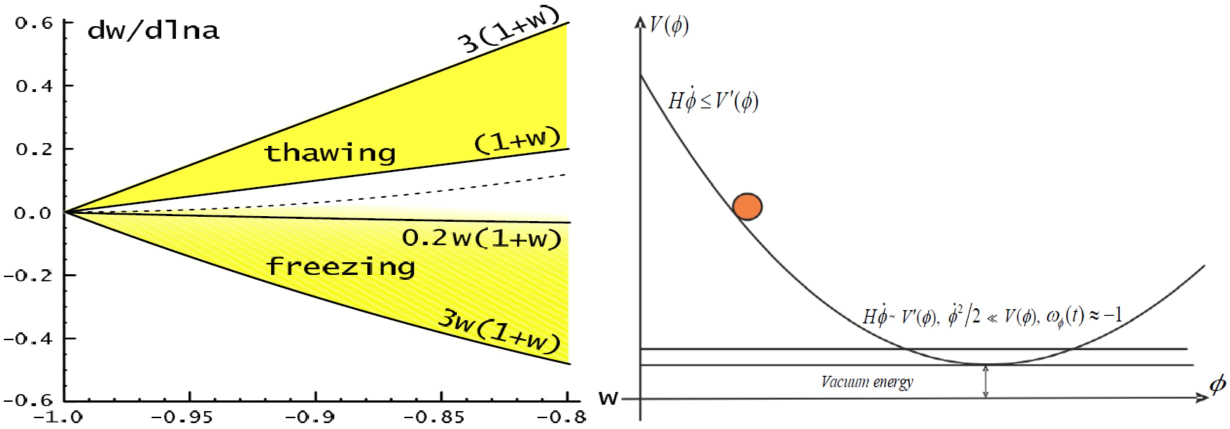

Figure 6.3: Left panel: the occupation of the thawing and the freezing scalar fields in the $w_\phi - dw_\phi/d\ln a$ phase space. (Figure from Ref. (Caldwell & Linder (2005))) Right panel: the regimes of the quick rolling down and the slow rolling down for the freezing scalar field, ϕ, to the minimum of its potential.

the evolution of the universe, the thawing scalar field was too suppressed by the retarding effect of the Hubble expansion, which represented by the term, $3H\dot\phi$, in Eq. (6.21)). Thereby, the scalar field evolution happened much slower compared to the Hubble expansion rate. The result of the overwhelming effect of the Hubble expansion on the thawing scalar field is the freezing of this scalar field.

This field manifests itself as the vacuum energy with the EoS parameter $w_\phi = -1$. The Hubble expansion rate, $H(a)$, is a decreasing function over time. After the Hubble expansion rate reaches the value of $H < \sqrt{\partial^2 V(\phi)/\partial t^2}$, the scalar field begins to roll to the minimum of its potential. This leads to the fact that the value of the EoS parameter for the scalar field, w_ϕ, increases over time and becomes $w_\phi > -1$.

The scalar field in the freezing models is always suppressed (it is damped), *i.e.*, $H > \sqrt{\partial^2 V(\phi)/\partial t^2}$. There are the fast and slow rolling regimes for the freezing models. The scalar field equation of motion, Eq. (6.21), describes: the fast rolling regime (with $3H\dot{\phi} < \partial V(\phi)/\partial t$), therefore, $\ddot{\phi} \gg V(\phi)$), or the slow rolling regime (for $3H\dot{\phi} < \partial V(\phi)/\partial t$) depending on the ratio of the term $3H\dot{\phi}$ and the term $\partial V(\phi)/\partial t$. In the slow-roll regime, the scalar field tends to minimize its potential and almost does not change over time, $\ddot{\phi} \ll V(\phi)$, therefore, from Eq. (6.20), it follows that $w_\phi \approx -1$, see Fig. (6.3) (right panel).

The freezing scalar field models have the so-called tracking solutions. Energy density for the freezing scalar field models is almost constant over time. The contribution of this energy density to the total energy density of the universe, both at the radiation domination epoch and at the matter domination epoch, is almost negligible. Therefore, the scalar field energy density remains subdominant at these epochs. It tracks first the radiation energy density and then the matter energy density. The radiation energy density and the matter energy density decrease over time due to the universe expansion. The scalar field energy density increases over time. Eventually, it becomes the dominant component and begins to behave as a component with the negative effective pressure. That is manifested in the accelerated expansion of the universe at the later stages of the universe evolution.

6.3.2 Phantom Scalar Field

The Lagrangian density for the phantom scalar fields is described by the equation:

$$\mathcal{L}_\phi = -\frac{1}{2} g^{\mu\nu} \partial_\mu \phi \partial_\nu \phi - V(\phi). \tag{6.23}$$

The incomplete list of the phantom potentials is given in Table 6.2.

The energy-momentum tensor for the phantom scalar field, $T_{\mu\nu}$, is defined as:

$$T_{\mu\nu} = -2\frac{\partial \mathcal{L}_\phi}{\partial g^{\mu\nu}} - g_{\mu\nu} \partial \mathcal{L}_\phi. \tag{6.24}$$

Substituting Eq. (6.23) into Eq. (6.24), we get:

$$T_{\mu\nu} = -\partial_\mu \phi \partial_\nu \phi - g_{\mu\nu} \left[\frac{1}{2} g^{\alpha\beta} \partial_\alpha \phi \partial_\beta \phi - V(\phi) \right]. \tag{6.25}$$

The components of the energy-momentum tensor for the phantom scalar field, $T_{\mu\nu}$, are

Name	Form	Reference
Fifth power	$V(\phi) = V_0\phi^5$	Scherrer & Sen (2008*a*)
Inverse square power	$V(\phi) = V_0\phi^{-2}$	Scherrer & Sen (2008*a*)
Exponent	$V(\phi) = V_0 \exp(\beta\phi)$, $\beta = \text{const} > 0$	Scherrer & Sen (2008*a*)
Quadratic	$V(\phi) = V_0\phi^2$	Dutta & Scherrer (2009)
Gaussian	$V(\phi) = V_0(1 - \exp(\phi^2/\sigma^2))$,$\sigma = \text{const}$	Dutta & Scherrer (2009)
pseudo-Nambu-Goldstone boson (pNGb)	$V(\phi) = V_0(1-\cos(\phi/\kappa))$, $\kappa = \text{const} > 0$	Frieman et al. (1995)
Inverse hyperbolic cosine	$V(\phi) = V_0(\cosh(\psi\phi))^{-1}$, $\psi = \text{const} > 0$	Dutta & Scherrer (2009)

Table 6.2: The list of the dark energy phantom potentials.

represented as:

$$T_{00} \equiv \rho_\phi = -\frac{1}{2}\dot{\phi}^2 + V(\phi), \tag{6.26}$$

$$T_{0i} = 0, \tag{6.27}$$

$$T_{ij} = 0 \ (i \neq j), \tag{6.28}$$

$$T_{ii} \equiv p_\phi = -\frac{1}{2}\dot{\phi}^2 - V(\phi). \tag{6.29}$$

The EoS parameter for the phantom scalar field is defined as:

$$w_\phi \equiv \frac{p_\phi}{\rho_\phi} = \frac{-\dot{\phi}^2/2 - V(\phi)}{-\dot{\phi}^2/2 + V(\phi)}. \tag{6.30}$$

The Klein-Gordon equation of motion for the phantom scalar field:

$$\ddot{\phi} + 3H\dot{\phi} - \frac{\partial V(\phi)}{\partial\phi} = 0. \tag{6.31}$$

6.4 Coupled Models of Matter and Dark Energy

As it was mentioned earlier, one of the unresolved problems of modern cosmology is the problem of coincidence in the standard ΛCDM model. Due to the fact that the dark energy density and the matter energy density in the modern universe have the same order, it can be assumed that the matter and dark energy somehow interact with each other.

In the coupled models between the matter and dark energy, the transformation of dark energy and the energy of the matter into each other is considered. The interaction between the matter and dark energy is described by the following modified continuity equations for the matter and dark energy, respectively, as:

$$\dot{\rho}_{\mathrm{m}} + 3H\rho_{\mathrm{m}} = \delta_{\mathrm{couple}}, \tag{6.32}$$

$$\dot{\rho}_{\phi} + 3H(\rho_{\phi} + p_{\phi}) = -\delta_{\mathrm{couple}}, \tag{6.33}$$

where ρ_{m} is the matter energy density; ρ_{ϕ} and p_{ϕ} are the energy density and the pressure of dark energy represented as the scalar field; δ_{couple} is the coupling coefficient between the matter and dark energy.

In the interaction models between the matter and dark energy, the following forms of the coupling coefficient, δ_{couple}, are used, Refs. (Amendola (2000), Zimdahl & Pavon (2001)):

$$\delta_{\mathrm{couple}} = nQ\rho_{\mathrm{m}}\dot{\phi}, \tag{6.34}$$

$$\delta_{\mathrm{couple}} = \alpha H(\rho_{\mathrm{m}} + \rho_{\phi}), \tag{6.35}$$

where $n = \sqrt{8\pi G}$; α and Q are the dimensionless constants. According to the Planck 2015 data, Ref. (Ade et al. (2016)), $Q < 0.1$.

The coupling models of the matter and dark energy are divided into two types.

6.4.1 Coupling First Type

The coupled models of the matter and dark energy of the first type are characterized by the exponential potential and the linear interaction determined by the interaction coefficient, which is presented in Eq. (6.34), Ref. (Amendola (2000)).

The coupled quintessence scalar field equation is:

$$\ddot{\phi} + 3H\dot{\phi} - \frac{\partial V(\phi)}{\partial \phi} = -nQ\rho_{\mathrm{m}}\dot{\phi}, \tag{6.36}$$

where $V(\phi) = V_0 e^{-n\lambda\phi}$ is a scalar field potential and λ is a model parameter.

The coupled continuity equation for dark energy:

$$\dot{\rho}_{\phi} + 3H(\rho_{\phi} + p_{\phi}) = -nQ\rho_{\mathrm{m}}\dot{\phi}. \tag{6.37}$$

The matter energy density evolves as:

$$\dot{\rho}_{\rm m} + 3H\rho_{\rm m} = nQ\rho_{\rm m} \quad \Rightarrow \quad \rho_{\rm m} = \rho_{\rm m0}a^{-3}e^{nQ\phi}. \tag{6.38}$$

6.4.2 Coupling Second Type

For the second type of the coupled models, the potential and the dynamics of the interaction between the matter and dark energy are constructed under the fulfillment of the requirement $\rho_{\rm m}/\rho_{\rm DE}$=const, Ref. (Zimdahl & Pavon (2001)).

The coupled equation, Eq. (6.33), is equivalent to:

$$\dot{\phi}\Big[\ddot{\phi} + 3H\dot{\phi} - \frac{\partial V(\phi)}{\partial\phi}\Big] = -\delta_{\rm couple}. \tag{6.39}$$

The coupling coefficient is defined as:

$$\delta_{\rm couple} = -3H\Pi_{\rm m} = 3H\Pi_{\phi}, \tag{6.40}$$

$$\Pi_{\rm m} = -\Pi_{\phi} = \frac{\rho_{\rm m}\rho_{\phi}}{\rho}(\gamma_{\phi} - 1), \tag{6.41}$$

where $\gamma_{\phi} = \frac{p_{\phi}+\rho_{\phi}}{\rho_{\phi}} = \frac{\dot{\phi}^2}{\rho_{\phi}}$ and $\rho = \rho_{\rm m} + \rho_{\phi}$.

The continuity equations for the matter and dark energy have the form:

$$\dot{\rho}_{\rm m} + 3H(\rho_{\rm m} + \Pi_{\rm m}) = 0, \tag{6.42}$$

$$\dot{\rho}_{\phi} + 3H(\rho_{\phi} + p_{\phi} + \Pi_{\phi}) = 0. \tag{6.43}$$

The form of the scalar field potential is constructed as follows:

$$V(\phi) = \frac{1}{6\pi G}\Big(1 - \frac{\gamma_{\phi}}{2}\Big)\frac{1+r}{(\gamma_{\phi}+r)^2}\frac{1}{t^2} \quad \Rightarrow \quad \frac{\partial V(\phi)}{\partial\phi} = -\lambda V(\phi), \tag{6.44}$$

where $r \equiv \dfrac{\rho_{\rm m}}{\rho_{\phi}}$ =const and $\lambda = \sqrt{\frac{24\pi G}{\gamma_{\phi}(1+r)}}$.

From Eq. (6.44) it follows that the potential has the exponential form:

$$V(\phi) = V_0 e^{-\lambda(\phi-\phi_0)}. \tag{6.45}$$

The significant drawback of this model is the absence of the convincing explanation for the onset of the interaction of dark energy and the matter at the transition epoch from the decelerated to accelerated expansion of the universe.

6.5 Chevallier-Polarsky-Linder Parametrization

The EoS parameters in the time-dependent models of dark energy are modeled as: $p = w(a)\rho$. This type of parametrization is called the wCDM parametrization[9]. This parametrization has no physical motivation. The application of the wCDM parametrization is typically used as an ansatz in data analysis for the quantifying of the time-dependent dark energy models. The parametrization of the EoS parameter, $w(a)$, is used to distinguish the different dark energy models. In particular, this approach can be used to distinguish the ΛCDM model from the other dark energy models at the present epoch.

The time-dependent EoS parameter in the dark energy models is often characterized by the Chevallier-Polarsky-Linder (CPL) $w_0 - w_a$ parametrization, Refs. (Chevallier & Polarski (2001), Linder (2003)):

$$w(a) = w_0 + w_a(1 - a), \tag{6.46}$$

here $w_0 = w(a = 1)$ and $w_a = (dw/dz)|_{z=1} = -a^{-2}(\mathrm{d}w/\mathrm{d}a)|_{a=1/2}$. Although this parametrization is very simple, it is flexible enough to accurately describe the EoS parameters in the most dark energy models. The CPL parametrization cannot describe the arbitrary dark energy models with good accuracy (up to the several percent) in a wide redshift range, Ref. (Linder (2003)).

The normalized Hubble parameter, expressed through the CPL parametrization of the EoS parameter, $w(a)$, can be written as:

$$E(a) = (\Omega_{\mathrm{r0}}a^{-4} + \Omega_{\mathrm{m0}}a^{-3} + \Omega_\Lambda a^{-3(1+w_0+w_a)}e^{-3w_a(1-a)})^{1/2}. \tag{6.47}$$

[9]Dark energy is sometimes characterized only by the EoS parameter and the corresponding cosmological models are called the wCDM models, Ref. (Barger et al. (2007)).

Chapter 7

Dynamics and Growth Rate in the Ratra-Peebles ϕCDM Model

This chapter is based on the results of the research presented in the papers, Ref. (Avsajanishvili et al. (2014)) and Ref. (Avsajanishvili et al. (2017)).

In this chapter, the Ratra-Peebles inverse-power-law potential, $V(\phi) \propto 1/\phi^{\alpha}$, is investigated in detail. This potential was first considered by Jim Peebles and Bharat Ratra in 1988, Refs. (Ratra & Peebles (1988*b*), Ratra & Peebles (1988*a*)). The scalar field model with the Ratra-Peebles potential is the simplest quintessence scalar field ϕCDM model of the freezing type. This model was proposed to solve the fine-tuning problem in the standard ΛCDM model.

7.1 Basic Equations

The Ratra-Peebles potential has the form:

$$V = \frac{\kappa}{2} M_{\rm pl}^2 \phi^{-\alpha}, \tag{7.1}$$

here α is a positive model parameter. The value of this parameter affects the steepness of the potential, thereby determining the shape of the potential. In our studies, we consider the values of the α parameter in the range of $0 < \alpha \leq 0.7$. This range corresponds to modern cosmological observations, Ref. (Samushia (2009)). For the value of the model parameter, α=0, the ϕCDM Ratre-Peebles model is reduced to the ΛCDM model. The positive κ parameter[1] is defined by the parameter α.

[1] The calculation of the κ parameter is presented below.

The parameter κ relates to the mass scale of the particles, M_ϕ, as:

$$M_\phi \sim \left(\frac{\kappa M_{\rm pl}^2}{2}\right)^{\frac{1}{\alpha+4}}. \tag{7.2}$$

We consider a flat and isotropic universe, which is described by the spacetime FLRW metric:

$$ds^2 = dt^2 - a(t)^2 d\mathbf{x}^2. \tag{7.3}$$

The Klein-Gordon equation of motion in the Ratra-Peebles model has the form:

$$\ddot{\phi} + 3H\dot{\phi} - \frac{1}{2}\kappa\alpha M_{\rm pl}^2 \phi^{-(\alpha+1)} = 0. \tag{7.4}$$

The energy density, the pressure and the EoS parameter in the Ratra-Peebles model are defined, respectively, as:

$$\rho_\phi = \frac{M_{\rm pl}^2}{32\pi}\left(\dot{\phi}^2 + \kappa M_{\rm pl}^2 \phi^{-\alpha}\right), \tag{7.5}$$

$$p_\phi = \frac{M_{\rm pl}^2}{32\pi}\left(\dot{\phi}^2 - \kappa M_{\rm pl}^2 \phi^{-\alpha}\right), \tag{7.6}$$

$$w_\phi = \frac{\dot{\phi}^2 - \kappa M_{\rm pl}^2 \phi^{-\alpha}}{\dot{\phi}^2 + \kappa M_{\rm pl}^2 \phi^{-\alpha}}. \tag{7.7}$$

From Eq. (7.7) it follows that the requirement for the fulfillment of the condition, $w_0 \simeq -1$, the following restriction imposes, $\dot{\phi}^2/2 \ll V(\phi)$. The Ratra-Peebles ϕCDM scalar field model has the tracker solutions. This means that the scalar field energy density, ρ_ϕ, at the early epochs of the universe evolution, first tracks the radiation energy density and then the matter energy density, while remaining a subdominant. Only in late times the energy density of the scalar field, ρ_ϕ, becomes dominant.

The value of the EoS parameter for the scalar field Ratra-Peebles model at the radiation domination epoch or at the matter domination epoch can be approximately defined as, Ref. (Zlatev et al. (1999)):

$$w_\phi \approx \frac{\frac{\alpha}{2} w_{\rm bac} - 1}{1 + \frac{\alpha}{2}}, \tag{7.8}$$

where $w_{\rm bac}$ is the background EoS parameter at the radiation domination epoch or at the matter domination epoch. For the radiation domination epoch $w_{\rm bac} = 1/3$ and for the matter domination epoch $w_{\rm bac} = 0$. The approximation, which is presented in Eq. (7.8), is true for $\rho_{\rm bac} \gg \rho_\phi$, where $\rho_{\rm bac}$ is a value of the background energy density.

The scalar field model with the Ratra-Peebles potential has both the tracker solutions and the attractor solutions[2]. This means that the evolution of the scalar field energy density, ρ_ϕ, in the Ratra-Peebles model is insensitive to the initial conditions, $(\phi_{\rm in}, \dot{\phi}_{\rm in})$, and the solutions for the wide range of the initial conditions converge into the same common solution at the present epoch.

The energy density parameter and the first Friedmann's equation for the Ratra-Peebles potential are defined, respectively, as:

$$\Omega_\phi(a) = \frac{1}{12H_0^2}\left(\dot{\phi}^2 + \kappa M_{\rm pl}^2\phi^{-\alpha}\right), \tag{7.9}$$

$$E(a) = \left(\Omega_{\rm r0}a^{-4} + \Omega_{\rm m0}a^{-3} + \frac{1}{12H_0^2}\left(\dot{\phi}^2 + \kappa M_{\rm pl}^2\phi^{-\alpha}\right)\right)^{1/2}. \tag{7.10}$$

7.1.1 Calculation of the Model Parameter κ and the Initial Conditions

The calculations of the κ parameter and the initial conditions are based on: Ref. (Farooq (2013), Sec. 3.6.3,) and Ref. (Avsajanishvili et al. (2014), Appendix A).

In the scalar field equation, Eq. (7.4), we represent the scale factor, $a(t)$, and the scalar field, $\phi(t)$, in the form of the power law:

$$a(t) = a_\star\left(\frac{t}{t_\star}\right)^n, \qquad \phi(t) = \phi_\star\left(\frac{t}{t_\star}\right)^p, \tag{7.11}$$

here $a_\star \equiv a(t_\star)$ and $\phi_\star \equiv \phi(t_\star)$ are the values of the scale factor and the scalar field at time, $t = t_\star$, respectively. A parameter, p, is associated with the parameter, α, by the following expression, $p = 2/(2+\alpha)$.

As a result:

$$\phi_\star^{\alpha+2} = \frac{(\alpha+2)^2}{4(6n+3n\alpha-\alpha)}\kappa\alpha M_{\rm pl}^2 t_\star^2. \tag{7.12}$$

Using the equations, Eq. (7.11), Eq. (7.12), Eq. (7.5) and Eq. (7.10), we find:

$$\rho = \frac{3n}{8\pi}\left(\frac{M_{\rm pl}}{t_\star}\right)^2\frac{\phi_\star^2}{\alpha(\alpha+2)}\left(\frac{t}{t_\star}\right)^{\frac{-2\alpha}{\alpha+2}}, \tag{7.13}$$

$$\left(\frac{n}{t}\right)^2 = \frac{8\pi}{3M_{\rm pl}^2}\rho, \tag{7.14}$$

where $\rho \equiv \rho_\phi$ is the dark energy density that dominates in the universe at the moments of

[2] An attractor is a set of the numerical values toward which a system tends to evolve for a wide variety of the starting conditions of this system.

time, $t < t_\star$. Assuming $\rho(t) = \rho_\star (t/t_\star)^\beta$, we get $\beta = -2\alpha/(\alpha+2)$. On the other hand, considering that the dominant dark energy component is represented as $\rho_\star$, at the moment of time $a = a_\star$:

$$\rho = \rho_\star \left(\frac{a_\star}{a}\right)^{\frac{2}{n}}, \tag{7.15}$$

where $n = 1/2$ and $n = 2/3$ are the values of the parameter n for the radiation domination epoch and the matter domination epoch, respectively.

In order to get an expression for, $\phi_\star^2$, we find $1/t^2$ from Eq. (7.14). Substituting Eq. (7.15) into Eq. (7.13), assuming $a = a_\star$ and $\rho = \rho_\star$. Comparing the obtained result with Eq. (7.12), we find:

$$\kappa = \frac{32\pi}{3nM_{\rm pl}^4}\left(\frac{6n+3n\alpha-\alpha}{\alpha+2}\right)[n\alpha(\alpha+2)]^{\frac{\alpha}{2}}\rho_\star. \tag{7.16}$$

Plugging Eq. (7.16) into Eq. (7.12) and using Eq. (7.14), we get:

$$\phi_\star = [n\alpha(\alpha+2)]^{\frac{1}{2}}, \tag{7.17}$$

$$\phi = [n\alpha(\alpha+2)]^{\frac{1}{2}}\left(\frac{a}{a_\star}\right)^{\frac{2}{n(\alpha+2)}}. \tag{7.18}$$

Substituting the value of $n = 1/2$ into Eq. (7.18) and assuming $a_\star = a_0$, we can obtain the equations for the initial conditions at the radiation domination epoch, Eq. (7.22) and Eq. (7.23).

Plugging Eq. (7.18) into Eq. (6.21):

$$\kappa = \frac{4n}{M_{\rm pl}^2 t_\star^2}\left(\frac{6n+3n\alpha-\alpha}{\alpha+2}\right)[n\alpha(\alpha+2)]^{\alpha/2}. \tag{7.19}$$

Since Eq. (7.16) must be true for an arbitrary moment of time, $t_\star$, we assume $t_\star = M_{\rm pl}^{-1}$.

As a result, for the values $n = 1/2$ and $n = 2/3$, we get:

$$\kappa(n=1/2) = \left(\frac{\alpha+6}{\alpha+2}\right)\left[\frac{1}{2}\alpha(\alpha+2)\right]^{\alpha/2}, \tag{7.20}$$

$$\kappa(n=2/3) = \frac{8}{3}\left(\frac{\alpha+4}{\alpha+2}\right)\left[\frac{2}{3}\alpha(\alpha+2)\right]^{\alpha/2}. \tag{7.21}$$

7.1.2 Initial Conditions

We numerically integrated the system of the equations, Eq. (7.4) and Eq. (7.10). The initial conditions were established at the radiation domination epoch, for the moment $a_{\rm in} = 5\cdot 10^{-5}$. The calculations were carried out to the present epoch, $a_0 = 1$. Despite the fact that the Ratra-Peebles potential has an attractor solution, for the best numerical convergence we chose a specific solution at the radiation dominated epoch with the following initial conditions:

$$\phi_{\rm in} \;=\; \left[\frac{1}{2}\alpha(\alpha+2)\right]^{1/2} t_{\rm in}^{\frac{4}{\alpha+2}}, \tag{7.22}$$

$$\dot{\phi}_{\rm in} \;=\; \left(\frac{8\alpha}{\alpha+2}\right)^{1/2} t_{\rm in}^{\frac{2-\alpha}{2+\alpha}}. \tag{7.23}$$

The value of the κ parameter was obtained from Eq. (7.20). In our calculations, we applied the current values of the matter energy density parameter and the dark energy density parameter, the reduced Hubble parameter, respectively: $\Omega_{\rm m0} = 0.315$, $\Omega_{\phi 0} = 0.685$, $h = 0.673$. These results were obtained by the Planck 2013 collaboration, Ref. (Ade et al. (2014c)).

7.2 Dynamics and Energy in the Ratra-Peebles ϕCDM Model

We analyzed the dependence of the scalar field, ϕ, and its time derivative, $\dot{\phi}$, depending on the model parameter α. The results of this analysis are presented in Fig. (7.1) and in Fig. (7.2). In the ϕCDM model, a larger value of the α parameter induces a stronger time

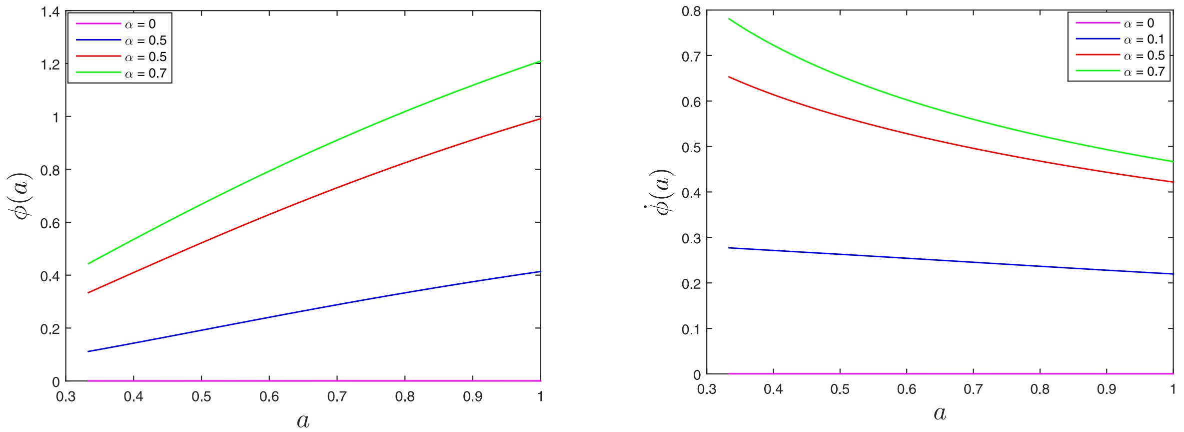

Figure 7.1: Left panel: dependence of the scalar field, $\phi(a)$, on the value of the parameter α. Right panel: dependence of the time derivative of the scalar field, $\dot{\phi}(a)$, on the value of the parameter α.

dependence of the EoS parameter w and its scale factor derivatives, dw/da. As expected, in the ΛCDM model the value of w is equal to minus one and the values of ϕ, $\dot{\phi}$ and dw/da are equal to zero.

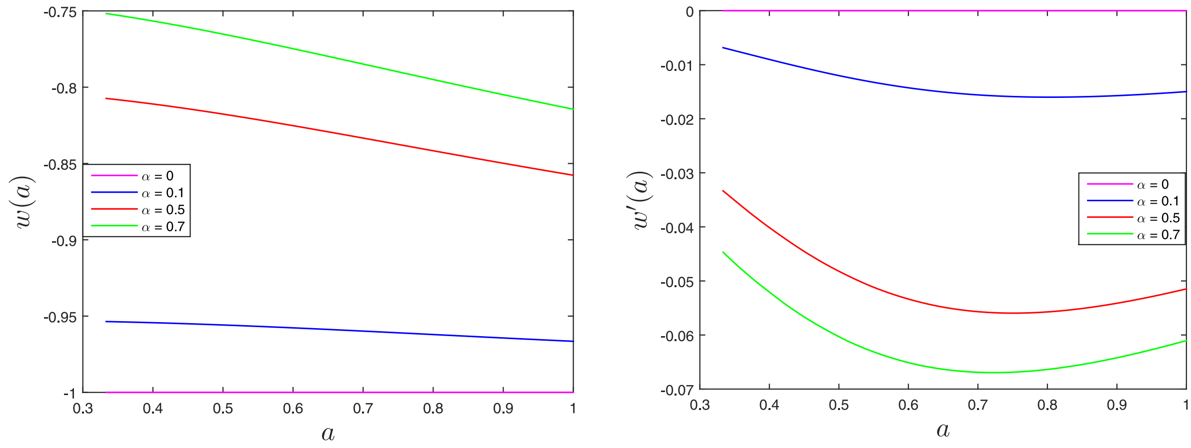

Figure 7.2: Left panel: dependence of the EoS parameter, $w(a)$, on the value of the parameter α. Right panel: dependence of the scale factor derivative of the EoS parameter, $w'(a)$, on the value of the parameter α.

We applied the CPL parametrization to the effective EoS parameter, $w(a)$, in the Ratra-Peebles ϕCDM model, Eq. (6.46). This parametrization provides a good approximation in the scale factor range, $a \in (0.98; 1)$, see Fig. (7.3) (left panel). We investigated the evolution

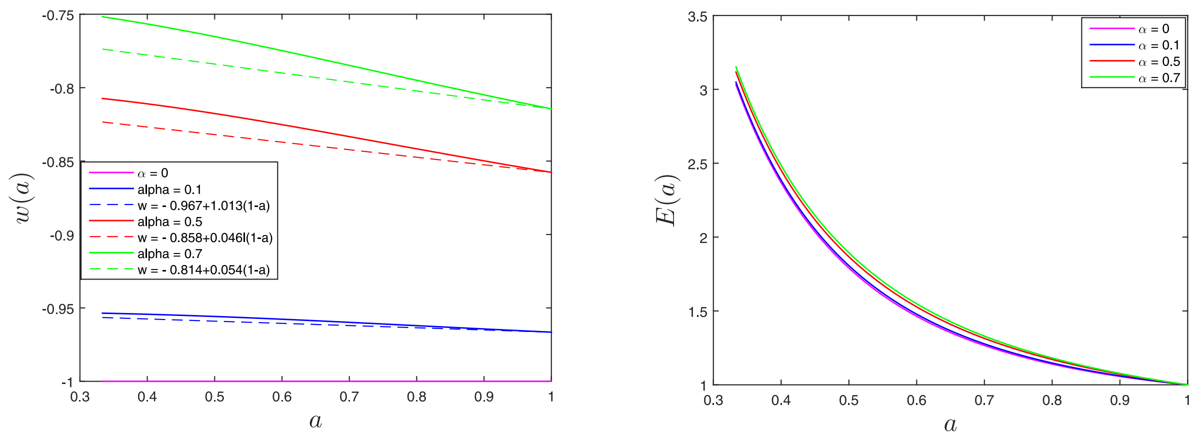

Figure 7.3: Left panel: the EoS parameter, $w(a)$, for the different values of the parameter α along with the predictions computed from the CPL parametrization with the corresponding best fit values for w_0 and w_a. Right panel: the normalized Hubble expansion rate, $E(a)$, for the different values of the parameter α.

of the normalized Hubble parameter, $E(a)$, which determines the expansion rate of the universe for the different values of the α parameter in the ϕCDM model. The results of this study are presented in Fig.(7.3) (right panel). With an increase in the value of the α parameter, the universe is expanding faster. The slowest expansion rate corresponds to the ΛCDM model.

The relationship between the dynamics and the energy components in the universe in

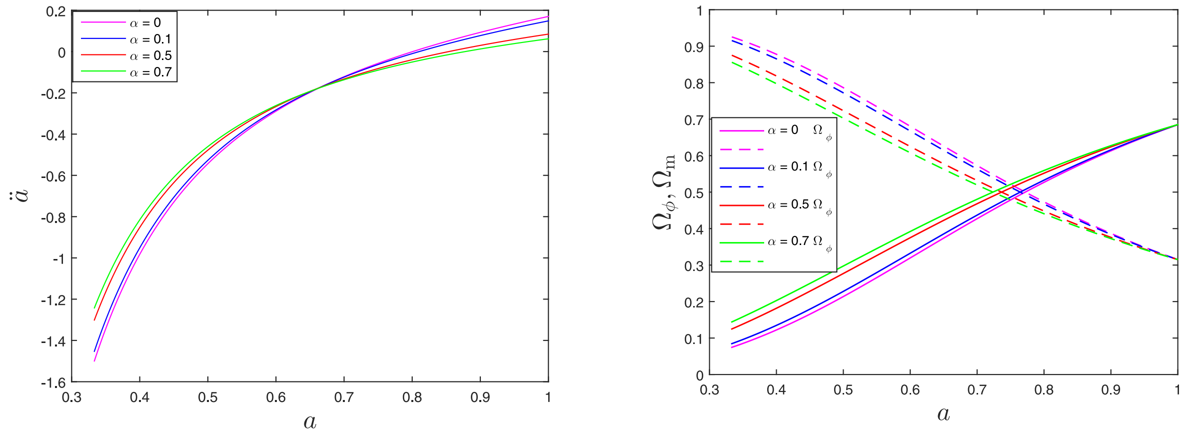

Figure 7.4: Left panel: the second derivative of the scale factor, $\ddot{a}$, for the different values of the parameter α. Right panel: the matter energy density parameter, $\Omega_{\mathrm{m}}(a)$, (dashed lines) and the scalar field density parameter, $\Omega_{\phi}(a)$, (solid lines) as functions of the scale factor for the different values of the parameter α.

the ϕCDM model is shown in Fig. (7.4). With the same value of the α parameter, the dynamic dominance of dark energy begins earlier, see Fig. (7.4) (left panel), than the energetic dominance, see Fig. (7.4) (right panel). With an increase in the value of the α parameter, the energetic dominance of dark energy begins earlier, see Fig. (7.4) (right panel).

7.3 Structure Growth in the Ratra-Peebles ϕCDM Model

The evolution of the matter density fluctuations depends on the given cosmological model of dark energy. The influence of dark energy on the large-scale structure evolution in the universe is due to its influence on the expansion rate of the universe, E(a). In turn, the expansion rate of the universe affects the growth of the matter density fluctuations. We investigated the evolution of a large-scale structure in the expanding universe in the Ratra-Peebles ϕCDM model. To calculate the growth of the matter density fluctuations, we used the linear perturbation equation, Eq. (4.31). The evolution of the linear growth rate function, $D(a) = \delta(a)/\delta(a_0)$, depending on the α parameter is shown in Fig. (7.5) (left panel). With an increase in the value of the α parameter the linear growth factor, D(a), becomes more dependent on time.

As it was discussed earlier, with an increase in the value of the α parameter, the Hubble expansion occurs faster, see Fig. (7.3) (right panel), while the domination of the scalar field energy begins earlier, see Fig. (7.4) (right panel). The growth of the matter density fluctuations occurs only during the matter dominated epoch, Ref. (Frieman et al. (2008)),

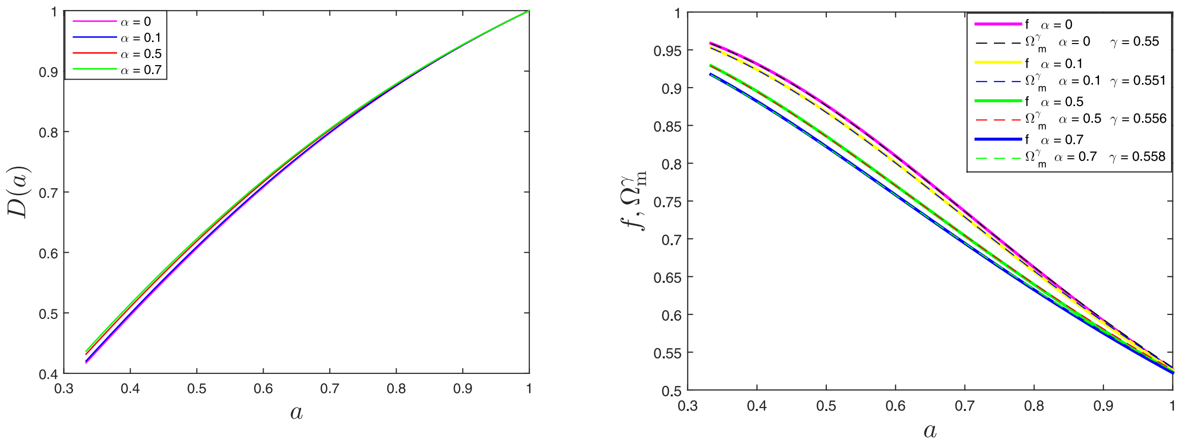

Figure 7.5: Left panel: the linear growth rate, $D(a)$, for the different values of the parameter α. Right panel: the growth rate, $f(\mathrm{a})$, (solid lines) for the different values of the parameter α along with the predictions $\Omega_{\mathrm{m}}^{\gamma}(\mathrm{a})$ (dashed lines), computed for the corresponding best fit values of the parameter γ.

therefore, with an increase in the value of the α parameter, less time remains for the growth of the matter density fluctuations. To achieve the same amplitude of the matter density fluctuations at present epoch, $\delta(a_0)$, in the scalar field Ratra-Peebles ϕCDM model with a larger value of the α parameter is required a larger initial amplitude for the matter density fluctuations. Thus, the scalar field with the larger value of the α parameter induces a larger amplitudes of the matter fluctuations at the beginning of their formation and at the all subsequent moments of their growth until the present epoch.

7.4 Growth Index in the Ratra-Peebles ϕCDM Model

We investigated how well the power-law parametrization of the growth rate of the matter density fluctuations, $f(a)$, and the fractional matter density parameter, $\Omega_{\mathrm{m}}(a)$, which is described in Eq. (4.35), can be applied in the Ratra-Peebles ϕCDM model. Provided that instead of the effective growth index, $\gamma(a)$, we applied the value of the Linder γ-parametrization, γ, which is defined in Eq. (4.37).

The results of these investigations are shown in Fig. (7.5) (right panel). The value of the Linder γ-parametrization, γ, in the ϕCDM model depends on the value of the α parameter, herewith the value of the Linder γ-parametrization, γ, increases with an increase in the value of the α parameter. The value of the Linder γ-parametrization, γ, is slightly higher in the ϕCDM model than the value of the Linder γ-parametrization, γ, in the ΛCDM model, for which $\gamma \approx 0.55$.

The growth rate of the matter density fluctuations occurs slower with an increase in the value of the parameter α, see Fig. (7.5) (right panel). This is a result of the fact that the Hubble expansion and the growth rate of the matter density fluctuations are interrelated and oppositely directed processes. The faster Hubble expansion, which corresponds to a larger value of the α parameter, see Fig. (7.3) (right panel), leads to a greater suppression of the growth rate of the matter density fluctuations.

We explored the applicability of the Linder γ-parametrization for large redshifts. We found, that this parametrization can be applied in the range of redshifts, $z \in (0; 5)$ and it is not applicable for the larger values of redshift, see Fig. (7.6) (left panel).

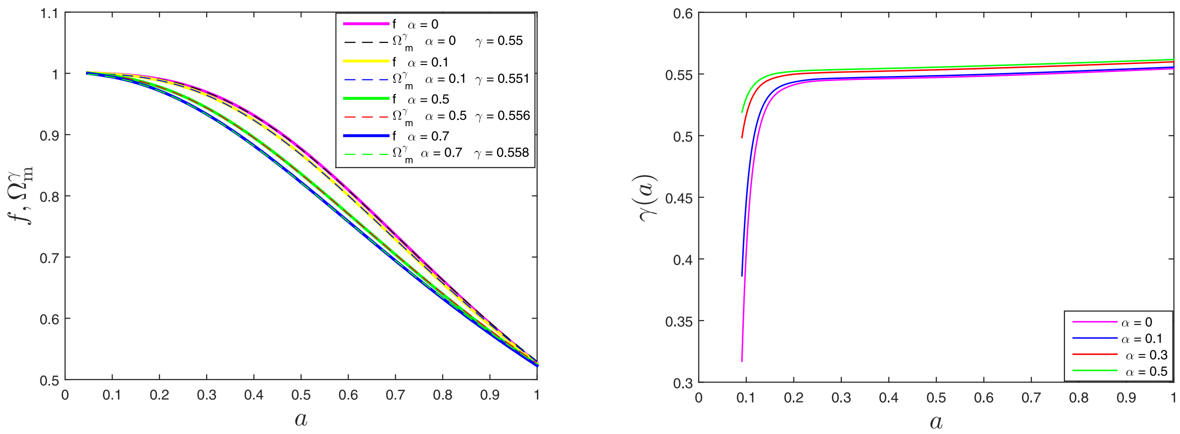

Figure 7.6: Left panel: the growth rate, $f(a)$, for the different values of the parameter α (solid lines) along with the predictions $\Omega_{\rm m}^{\gamma}$ (dashed lines), computed for the corresponding best fit values of the γ parameter in the range of redshifts, $z \in (0; 10)$. Right panel: the $\gamma(a)$ function for the different values of the parameter α in the range of redshifts, $z \in (0; 10)$.

We studied the behavior of the effective growth index function, $\gamma(a)$, was presented in Eq. (4.36), at large redshifts, see Fig. (7.6) (right panel). We found that in a certain range of scalar factor values, the function of the effective growth index, $\gamma(a)$, is almost independent of the value of the scalar factor. The weak dependence of the effective growth index function on the value of the scalar factor occurs in the range of the values of the scalar factor: in the ΛCDM model, $a \in (0.25; 1)$ (or $z \in (0; 3)$); in the Ratra-Peebles ϕCDM model, $a \in (0.18; 1)$ (or $z \in (0; 5)$). Suchwise, with an decrease in the value of the parameter α, the weak dependence of the effective growth index function ceases later in the ϕCDM model. Thus, in the ΛCDM model, the applicability of the Linder γ-parametrization is completed later than in the ϕCDM model. Comparing Fig. (7.6) (left panel) and Fig. (7.6) (right panel), we see that the cessation of the Linder γ-parametrization for the different values of the parameter α coincides with the termination of the weak dependence of the effective growth index function,

$\gamma(a)$, on the scalar factor. Thus, only in the range of the values of the scalar factor at which the effective growth index function almost does not depend on the value of the scalar factor, the Linder γ-parametrization can be applied.

7.5 Conclusion

We scrupulously investigated the various properties of the Ratra-Peebles ϕCDM model in comparison with the ΛCDM model. In particular, we studied the dynamics of the Ratra-Peebles ϕCDM model with dependence on the model parameter α. Since the larger value of the parameter α increases, the steepness of the potential and, thereby, it induces the stronger time dependence of the scalar field, ϕ, its time derivatives $\dot{\phi}$, as well as the EoS parameter, w, and its scale factor derivatives, dw/da.

We showed that the Ratra-Peebles ϕCDM model differs from ΛCDM model in number of characteristics. These characteristics are generic to a class of the freezing quintessence ϕCDM models, and these characteristics do not depend on the value of the model parameter α:

- *In the ϕCDM models, the expansion rate of the universe, $E(a)$, is always greater than the expansion rate of the universe in the ΛCDM model.*

- *The moment of dark energy domination in the ϕCDM models starts earlier than in the ΛCDM model (provided that other cosmological model parameters are fixed).*

- *The Ratra-Peebles ϕCDM model and the ΛCDM model differ in their predictions for the growth rate of the matter density fluctuations in the universe: the scalar field model predicts a slower growth rate of the matter density fluctuations than the ΛCDM model.*

- We studied the applicability of the Linder γ- parametrization in the Ratra-Peebles ϕCDM model. We found that this parametrization works well in this model. The value of the growth index in the Linder γ-parametrization in the Ratra-Peebles ϕCDM model increases with an increase in the value of the model parameter α. *The value of the growth index in the Linder γ-parametrization in the ϕCDM model is slightly larger than in the ΛCDM model.*

- We defined the boundaries of applicability in the Linder γ-parametrization in the Ratra-Peebles ϕCDM model, $z \in (0; 5)$. *The applicability of the Linder γ-parametrization ceases later in the ΛCDM model than in the ϕCDM model.*

Chapter 8

Constraints on the Model Parameters in the Ratra-Peebles Model

8.1 Constraints on the Model Parameters in the Ratra-Peebles Model from the Growth Rate Data

We carried out the constraints on the α and $\Omega_{\rm m}$ parameters in the Ratra-Peebles ϕCDM model using a compilation of the growth rate observations obtained from, Ref. (Gupta et al. (2012)). These data are presented in Table 8.1:

$f_{\rm obs}$	z	σ
0.51	0.15	0.11
0.60	0.22	0.10
0.654	0.32	0.18
0.700	0.35	0.18
0.700	0.41	0.07
0.75	0.55	0.18
0.730	0.60	0.07
0.910	0.77	0.36
0.700	0.78	0.08
0.90	1.40	0.24
1.460	3.00	0.29

Table 8.1: Growth rate data, $f_{\rm obs}$; redshift z; 1σ uncertainty of the growth rate data.

To get the theoretical values of the growth rate, $f_{\rm th}$, we numerically solved the linear perturbation equation, Eq. (4.31), for a series values of α and $\Omega_{\rm m}$ parameters. After that we calculated the function $\chi^2(\alpha, \Omega_{\rm obs})$ as:

$$\chi^2(\alpha, \Omega_{\rm obs}) = \frac{[f_{\rm obs} - f_{\rm th}(\alpha, \Omega_{\rm m})]^2}{\sigma^2}, \tag{8.1}$$

here σ is the standard deviation of the growth rate data. We calculated the likelihood function, $\mathcal{L}^{\rm f}(\alpha, \Omega_{\rm m})$, assuming that it obeys the Gaussian distribution:

$$\mathcal{L}^{\rm f}(\alpha, \Omega_{\rm m}) \propto \exp[-\chi^2(\alpha, \Omega_{\rm m})/2]. \tag{8.2}$$

The results of these calculations are presented in Fig. (8.1). The 1σ and 2σ confidence level

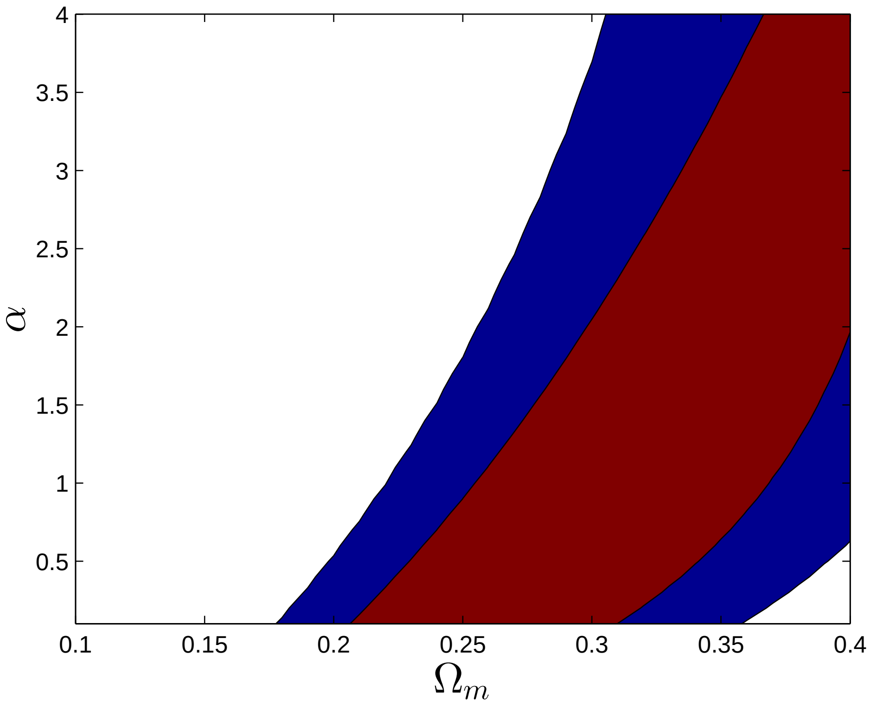

Figure 8.1: 1σ and 2σ confidence level contours on the parameters $\Omega_{\rm m}$ and α in the ϕCDM model. This constraints are obtained from the growth rate data, Ref. (Gupta et al. (2012)).

contours in the α - $\Omega_{\rm m}$ phase space are strongly degenerated with respect to the constraint on the α parameter. Thus, the observations on the growth rate alone cannot simultaneously restrict both parameters, α and $\Omega_{\rm m}$, in the Ratra-Peebles ϕCDM model. However, we found the constraint on the $\Omega_{\rm m}$ parameter in the ΛCDM model and in the Ratra-Peebles ϕCDM model, using only the growth rate observations. If we fix the ordinate with $\alpha = 0$, see Fig. (8.1), which corresponds to the spatial flat ΛCDM model, we will obtain the best fit value $\Omega_{\rm m} = 0.278 \pm 0.03$. This value is within of the 1σ confidence level of the Planck 2013 data, Ref. (Ade et al. (2014*c*)). In the ΛCDM model, the values of $0.18 \leq \Omega_{\rm m} \leq 0.36$ are contained at the 2σ confidence level, see Fig. (8.1). In the Ratra-Peebles ϕCDM model, the values of $\Omega_\mathrm{m} < 0.18$ are outside of the 2σ confidence level, but the values of $\Omega_\mathrm{m} \geq 0.36$ are still allowed for the large values of the model parameter α, see Fig. (8.1).

8.2 Constraints on the Model Parameters in the Ratra-Peebles Model from the BAO Data

To eliminate the degeneration between the model parameters α and Ω_m, which was obtained as a result of applying the constraints from the growth rate data, $f(a)$, we carried out the additional constraints using BAO data with small redshifts, which were taken from, Ref. (Giostri et al. (2012)). We also followed the approach used in the paper, Ref. (Giostri et al. (2012)).

We calculated the angular diameter distances:

$$d_\mathrm{A}(z, \alpha, \Omega_\mathrm{m}, H_0) = \int_0^z \frac{dz'}{H(z', \alpha, \Omega_\mathrm{m}, H_0)} \tag{8.3}$$

and the distance scale (dilaton scale):

$$D_\mathrm{V}(z, \alpha, \Omega_\mathrm{m}, H_0) = [d_\mathrm{A}^2(z, \alpha, \Omega_\mathrm{m}, H_0) z / H(z, \alpha, \Omega_\mathrm{m}, H_0)]^{1/3}. \tag{8.4}$$

We constructed a combination of the angular diameter distance, $d_\mathrm{A}(z_\mathrm{dec})$, and the distance scale, $D_\mathrm{V}(z_\mathrm{BAO})$, Ref. (Eisenstein et al. (2005)):

$$\eta(z) \equiv d_\mathrm{A}(z_\mathrm{rec}) / D_\mathrm{V}(z_\mathrm{BAO}). \tag{8.5}$$

The expression in Eq. (8.5) is the BAO/CMBR constraints.

The BAO and CMBR observations are dependent on each other. Assuming that these data obey the Gaussian distribution, we calculated the function χ_B^2 using the following covariant inverse matrix, $\boldsymbol{C}^{-1}$:

$$\chi_\mathrm{B}^2 = \boldsymbol{X}^\mathrm{T} \boldsymbol{C}^{-1} \boldsymbol{X}. \tag{8.6}$$

We also calculated the likelihood function by applying the results from Eq. (8.6):

$$\mathcal{L}^\mathrm{B}(\alpha, \Omega_\mathrm{m}, H_0) \propto \exp(-\chi_\mathrm{B}^2/2), \tag{8.7}$$

where $\boldsymbol{X} = \eta_{\rm th} - \eta_{\rm obs}$.

The value of a vector, $\boldsymbol{X}$, is calculated as:

$$\mathbf{X} = \begin{pmatrix} \dfrac{d_{\rm A}(z_{\rm rec})}{D_{\rm V}(0.106)} - 30.95 \\ \dfrac{d_{\rm A}(z_{\rm rec})}{D_{\rm V}(0.2)} - 17.55 \\ \dfrac{d_{\rm A}(z_{\rm rec})}{D_{\rm V}(0.35)} - 10.11 \\ \dfrac{d_{\rm A}(z_{\rm rec})}{D_{\rm V}(0.44)} - 8.44 \\ \dfrac{d_{\rm A}(z_{\rm rec})}{D_{\rm V}(0.6)} - 6.69 \\ \dfrac{d_{\rm A}(z_{\rm rec})}{D_{\rm V}(0.73)} - 5.45 \end{pmatrix}. \tag{8.8}$$

The inverse covariance matrix for the observations, $\mathbf{C^{-1}}$, is defined as:

$$\mathbf{C^{-1}} = \begin{pmatrix} 0.48435 & -0.101383 & -0.164945 & -0.0305703 & -0.097874 & -0.106738 \\ -0.101383 & 3.2882 & -2.45497 & -0.0787898 & -0.252254 & -0.2751 \\ -0.164945 & -2.45497 & 9.55916 & -0.128187 & -0.410404 & -0.447574 \\ -0.0305703 & -0.0787898 & -0.128187 & 2.78728 & -2.75632 & 1.16437 \\ -0.097874 & -0.252254 & -0.410404 & -2.75632 & 14.9245 & -7.32441 \\ -0.106738 & -0.2751 & -0.447574 & 1.16437 & -7.32441 & 14.5022 \end{pmatrix}. \tag{8.9}$$

In the Gaussian distribution, we used the prior value of the Hubble constant, $H_0 = 74.3 \pm 2.1$, to restrict the H_0 parameter in the likelihood function, $\mathcal{L}^{\rm B}$, Ref. (Freedman et al. (2012)). The likelihood function obtained for the growth rate function, $\mathcal{L}^{\rm f}$, and the likelihood function obtained for BAO/CMBR constraints, $\mathcal{L}^{\rm B}$, are independent of each other, therefore, the combined likelihood function, $\mathcal{L}$, is simply a multiplication of the given likelihood functions, according to the results from Eq. (5.4): $\mathcal{L} = \mathcal{L}^{\rm f} \cdot \mathcal{L}^{\rm B}$.

The results of our calculations are presented in Fig. (8.2). After conducting the BAO/CMBR analysis, we received the new constraints on the $\Omega_{\rm m}$ and α model parameters. The model parameter $\Omega_{\rm m}$ is restricted within $0.26 < \Omega_{\rm m} < 0.34$ at the 1σ confidence level. For the parameter α we got a range of the values, $0 \leq \alpha \leq 1.30$, at the 1σ confidence level, see Fig. (9.1).

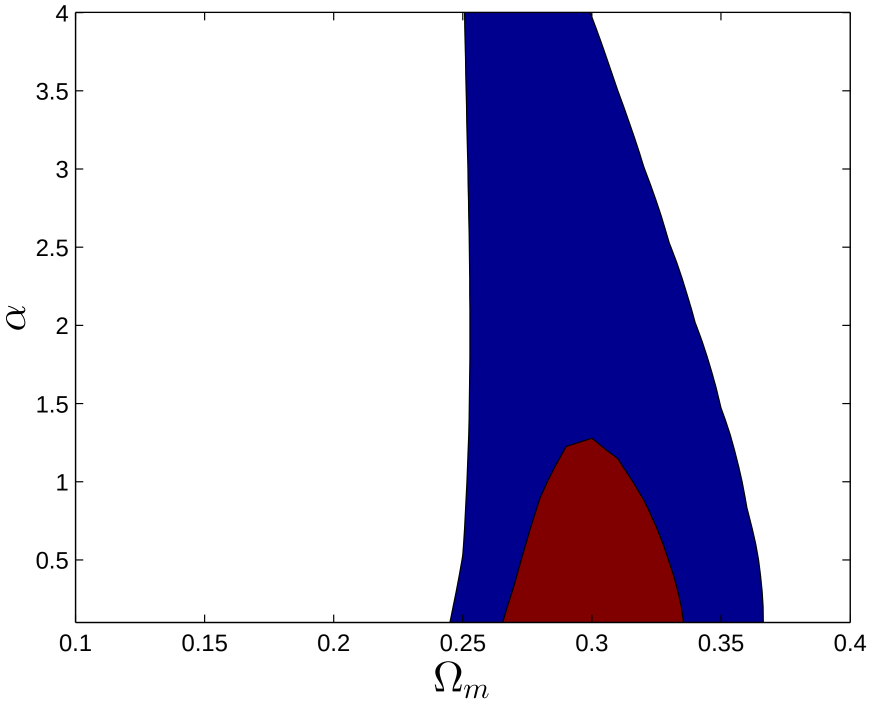

Figure 8.2: 1σ and 2σ confidence level contours on the parameters $\Omega_{\rm m}$ and α in the ϕCDM model. These constraints are obtained after adding BAO/CMBR measurements of the prior distances, Ref. (Giostri et al. (2012)).

8.3 Conclusion

To constrain the parameters in the Ratra-Peebles ϕCDM scalar field model, we used a compilation of the observations: the growth rate data and BAO data with the prior distances from the CMBR. Using only the growth rate data, there is a strong degeneracy between the values of the model parameters $\Omega_{\rm m}$ and α. It means that the larger values of the parameter α are allowed with an increase in the value of the parameter $\Omega_{\rm m}$. The degeneracy is eliminated after combining the constraints on the growth rate data with the constraints on the distance-redshift ratio of the BAO data and the prior distance from the CMBR.

As a result, we received the constraints on the model parameters in the Ratra-Peebles ϕCDM model: $\Omega_{\rm m} = 0.30 \pm 0.04$ and $0 \leq \alpha \leq 1.30$ at the 1σ confidence level. The best fit value for the parameter α is $\alpha = 0.00$.

Chapter 9

Constraints on the Models Parameters in the Quintessence and Phantom ϕCDM Models

This chapter is based on the research, which was carried out in the paper, Ref. (Avsajanishvili et al. (2018)).

We studied the quintessence (canonical scalar fields) and the phantom (non-canonical scalar fields) scalar field models in the case of flat spacetime. There is still no final decision, which of these models is preferable, Refs. (Suzuki et al. (2012), Novosyadlyj et al. (2013), Ade et al. (2014*c*), Betoule et al. (2014), Ade et al. (2016)). We applied the predicted data, calculated for the upcoming DESI experiment and studied the scalar fields models compared to the standard ΛCDM model. Our study is based on the comparison of data on the expansion rate of the universe, the growth rate of the matter density fluctuations and the measurements of the angular diameter distance, which will be obtained from the DESI experiment.

9.1 Definition of the Model Parameters and the Initial Conditions

We studied the scalar field models with 10 quintessential and 7 phantom potentials, a list of which is presented in Table 6.1 and in Table 6.2. All the scalar field models presented in these Tables have the same parameters Ω_{m0} and H_0. In addition to these parameters, each scalar field model has its own set of the extra model parameters that determine the shape and the strength of the potential, $V(\phi)$.

For each potential, we numerically solved the system of the differential equations: the Klein-Gordon equation of motion for the quintessence (the phantom) model, respectively Eq. (6.21) (Eq. (6.31)), the first Friedmann's equation, Eq. (6.22) and then the perturbation equation, Eq. (4.31), for a wide range of the free parameters and the initial conditions (ϕ_0, $\dot{\phi}_0$) for the matter dominated epoch. Due to the fact that for all the potentials the ranges of the initial conditions and the model parameters are unknown precisely, we developed a method for defining these ranges. For each potential, we found the plausible solutions, for which the following three criteria were simultaneously fulfilled:

1. The transition between the matter and dark energy equality ($\Omega_{\rm m} = \Omega_\phi$) happens relatively recently, $a \in (0.6; 0.8)$, see Fig. (7.4) (right panel).

2. The growth rate of the matter density fluctuations, $f(a)$, and the fractional matter density, $\Omega_{\rm m}(a)$, are parametrized by the Linder γ-parametrization, Eq. (4.37).

3. The EoS parameter predicted by the different dark energy models should be in the agreement with the expected current value of the EoS parameter (for the phantom models $w_0 < -1$; for the quintessence models $-1 < w_0 < -0.75$, for the freezing type $w_a < 0$ and for the thawing type $w_a > 0$).

Despite the fact that the Ratra-Peebles potential has an attractor solution, for the best numerical convergence we chose a specific solution at the matter dominated epoch with the following initial conditions, Refs. (Ratra & Peebles (1988*b*), Farooq (2013), Avsajanishvili et al. (2014)):

$$V_0 = \frac{8}{3}\left(\frac{\alpha+4}{\alpha+2}\right)\left[\frac{2}{3}\alpha(\alpha+2)\right]^{\alpha/2}, \tag{9.1}$$

$$\phi_{\rm in} = \left[\frac{2}{3}\alpha(\alpha+2)\right]^{1/2} t_{\rm in}^{\frac{3}{\alpha+2}}, \tag{9.2}$$

$$\dot{\phi}_{\rm in} = \left[\frac{6\alpha}{\alpha+2}\right]^{1/2} t_{\rm in}^{\frac{1-\alpha}{2+\alpha}}. \tag{9.3}$$

The initial value of the scale factor, $a_{\rm in} \propto t_{\rm in}^{2/3}$, was chosen at the matter domination epoch, Eq. (2.101). In our calculations, we used the values of the model parameter α in the range, $\alpha \leq 0.7$, Ref. (Samushia (2009)).

We applied the aforementioned phenomenological method and found the following ranges for each potential: the allowed initial conditions and the model parameters, which describe the form and the strength of the potential. These ranges, along with the general free model parameters $\Omega_{\rm m0}$ and H_0, are presented in Table 6.1 and Table 6.2. We used this data for each dark energy model as the initial conditions for the MCMC calculations.

Quintessence potentials	Free parameters	
$V(\phi) = V_0 M_{\rm pl}^2 \phi^{-\alpha}$	$H_0(50 \div 90)$ $\Omega_{\rm m0}(0.25 \div 0.32)$	$V_0(3 \div 5)$ $\alpha(10^{-6} \div 0.7)$
$V(\phi) = V_0 \exp(-\lambda\phi/M_{\rm pl})$	$H_0(50 \div 90)$ $\Omega_{\rm m0}(0.25 \div 0.32)$ $V_0(10 \div 10^3)$	$\lambda(10^{-7} \div 10^{-3})$ $\phi_0(0.2 \div 1.6)$ $\dot{\phi}_0(79.8 \div 338.9)$
$V(\phi) = V_0(\exp(M_{\rm pl}/\phi) - 1)$	$H_0(50 \div 90)$ $\Omega_{\rm m0}(0.25 \div 0.32)$ $V_0(10 \div 10^2)$	$\phi_0(1.5 \div 10)$ $\dot{\phi}_0(350 \div 850)$
$V(\phi) = V_0 \phi^{-\chi} \exp(\gamma\phi^2/M_{\rm pl}^2)$	$H_0(50 \div 90)$ $\Omega_{\rm m0}(0.25 \div 0.32)$ $V_0(10^{-2} \div 10^{-1})$ $\chi(4 \div 8)$	$\gamma(6.5 \div 7)$ $\phi_0(5.78 \div 10.55)$ $\dot{\phi}_0(680.6 \div 879)$
$V(\phi) = V_0(\cosh(\varsigma\phi) - 1)^g$	$H_0(50 \div 90)$ $\Omega_{\rm m0}(0.25 \div 0.32)$ $V_0(5 \div 8)$ $\varsigma(0.15 \div 1)$	$g(0.1 \div 0.49)$ $\phi_0(1.8 \div 5.8)$ $\dot{\phi}_0(360 \div 685)$
$V(\phi) = V_0(\exp(\nu\phi) + \exp(\upsilon\phi))$	$H_0(50 \div 90)$ $\Omega_{\rm m0}(0.25 \div 0.32)$ $V_0(1 \div 12)$	$\nu(6 \div 12)$ $\phi_0(0.014 \div 1.4)$ $\dot{\phi}_0(9.4 \div 311)$
$V(\phi) = V_0((\phi - B)^2 + A)\exp(-\mu\phi)$	$H_0(50 \div 90)$ $\Omega_{\rm m0}(0.25 \div 0.32)$ $V_0(40 \div 70)$ $A(1 \div 40)$	$B(1 \div 60)$ $\mu(0.2 \div 0.9)$ $\phi_0(5.8 \div 8.45)$ $\dot{\phi}_0(681 \div 804.5)$
$V(\phi) = V_0 \sinh^m(\xi M_{\rm pl}\phi)$	$H_0(50 \div 90)$ $\Omega_{\rm m0}(0.25 \div 0.32)$ $V_0(1 \div 10)$ $m(-0.1 \div -0.3)$	$\xi(10^{-2} \div 1)$ $\phi_0(0.5 \div 2.5)$ $\dot{\phi}_0(190 \div 367)$
$V(\phi) = V_0 \exp(M_{\rm pl}/\phi)$	$H_0(50 \div 90)$ $\Omega_{\rm m0}(0.25 \div 0.32)$ $V_0(10^2 \div 10^3)$	$\phi_0(5.78 \div 10.55)$ $\dot{\phi}_0(680.6 \div 879)$
$V(\phi) = V_0(1 + \exp(-\tau\phi))$	$H_0(50 \div 90)$ $\Omega_{\rm m0}(0.25 \div 0.32)$ $V_0(1 \div 10^2)$	$\tau(10 \div 10^2)$ $\phi_0(0.01 \div 0.075)$ $\dot{\phi}_0(9.4 \div 32)$

Table 9.1: The list of the dark energy quintessence potentials and the free parameters.

Phantom potentials	Free parameters	
$V(\phi) = V_0\phi^5$	$H_0(50 \div 90)$ $\Omega_{\rm m0}(0.25 \div 0.32)$ $V_0(10^{-3} \div 10^{-2})$	$\phi_0(3.37 \div 3.94)$ $\dot{\phi}_0(523 \div 563.6)$
$V(\phi) = V_0\phi^{-2}$	$H_0(50 \div 90)$ $\Omega_{\rm m0}(0.25 \div 0.32)$ $V_0(30 \div 50)$	$\phi_0(2.83 \div 5.15)$ $\dot{\phi}_0(471.4 \div 600)$
$V(\phi) = V_0\exp(\beta\phi)$	$H_0(50 \div 90)$ $\Omega_{\rm m0}(0.25 \div 0.32)$ $V_0(1 \div 20)$	$\beta(0.08 \div 0.3)$ $\phi_0(0.2 \div 9.14)$ $\dot{\phi}_0(79.8 \div 830.9)$
$V(\phi) = V_0\phi^2$	$H_0(50 \div 90)$ $\Omega_{\rm m0}(0.25 \div 0.32)$ $V_0(1 \div 20)$	$\phi_0(0.67 \div 2.8)$ $\dot{\phi}_0(191 \div 450)$
$V(\phi) = V_0(1-\exp(\phi^2/\sigma^2))$	$H_0(50 \div 90)$ $\Omega_{\rm m0}(0.25 \div 0.32)$ $V_0(5 \div 30)$	$\sigma(5 \div 30)$ $\phi_0(0.67 \div 2.8)$ $\dot{\phi}_0(191 \div 450)$
$V(\phi) = V_0(1-\cos(\phi/\kappa))$	$H_0(50 \div 90)$ $\Omega_{\rm m0}(0.25 \div 0.32)$ $V_0(1 \div 4)$	$\kappa(1.1 \div 2)$ $\phi_0(2.3 \div 3.37)$ $\dot{\phi}_0(420 \div 500)$
$V(\phi) = V_0(\cosh(\psi\phi))^{-1}$	$H_0(50 \div 90)$ $\Omega_{\rm m0}(0.25 \div 0.32)$ $V_0(10^{-3} \div 10^2)$	$\psi(10^{-3} \div 1)$ $\phi_0(1.4 \div 2.3)$ $\dot{\phi}_0(310 \div 420.7)$

Table 9.2: The list of the dark energy phantom potentials and the free parameters.

9.2 MCMC Analysis for Study of the Dark Energy Models

We calculated the values of the normalized Hubble parameter for all the dark energy models, the angular diameter distance and the growth rate in the redshift range, $z \in (0.15; 1.85)$.

- *The normalized Hubble parameter, $E(z)$*

  We calculated the values of the normalized Hubble parameter, $E(\mathrm{z})$, from Eq. (6.22).

- *The angular diameter distance, $d_A(z)$*

  We computed the angular diameter distances using the equation:

$$d_A(z) = \frac{1}{H_0(1+z)} \int_0^z \frac{dz'}{E(z')}. \tag{9.4}$$

  This equation is a special case for the flat universe, it was obtained from Eq. (3.48).

- *The combination of the growth rate of the matter density fluctuations and the matter power spectrum amplitude, $f(a)\sigma_8(a)$*

  The value of the growth rate of the matter density fluctuations was found from Eq. (4.34).

The matter power spectrum amplitude can be determined through the function $\sigma_8(a) \equiv D(a)\sigma_8$, where $\sigma_8 \equiv \sigma_8(a_0)$ is the rms linear fluctuation in the mass density distribution on the scale $8h^{-1}$ Mpc. We fixed the value of σ_8 to its current best fit ΛCDM value of $\sigma_8 = 0.815$ from the Plank 2015 data, Ref. (Ade et al. (2016)).

Since the observations for the expansion rate of the universe, $H(z)$, the growth rate of the matter density fluctuations, $f(a)\sigma_8(a)$, and the angular diameter distances, $D_A(z)$, are dependent on each other, we calculated the covariant matrices for these measurements. We followed the standard approach for calculating the Fisher matrices, proposed in Ref. (Font-Ribera et al. (2014)). We assumed 14000 sq. deg. of sky coverage and the wavenumbers up to $k_{\max} = 0.2$ Mpc/h. Our variances matched the numbers in Table V of Ref. (Font-Ribera et al. (2014)). We also accounted for the covariances between the measurements within the same redshift bin. The $D_A(z)$ and $H(z)$ measurements are negatively correlated by approximately 40%, while the correlations with $f(a)\sigma_8(a)$ are below 10% for all the redshift bins.

After conducting the MCMC analysis, we found that the values of the parameters corresponding to the maximum probability are within of the prior ranges of these parameters presented in Table 9.1 and Table 9.2. We found that there is no need to adjust the prior ranges of the model parameters. The examples of the MCMC constraints for the quintessence Ratra-Peebles, the Golden-Wang-Steinhardt and the phantom pseudo-Nambu-Goldstone boson potentials are shown in Figs. (9.1-9.3).

9.3 Bayesian Statistics

To assess the quality of the different models and to distinguish them from each other, we applied the Akaike information criterion (AIC), Ref. (Akaike (1974)) and the Bayesian (or Schwarz) information criterion (BIC), Ref. (Schwarz (1978)). The AIC and BIC information criteria are the functions of the number of estimated model parameters, N. The information, which is obtained by these criteria, complement each other.

The AIC and BIC are defined respectively as:

$$AIC = -2\ln \mathcal{L}_{\max} + 2k \tag{9.5}$$

and

$$BIC = -2\ln \mathcal{L}_{\max} + k\ln N, \tag{9.6}$$

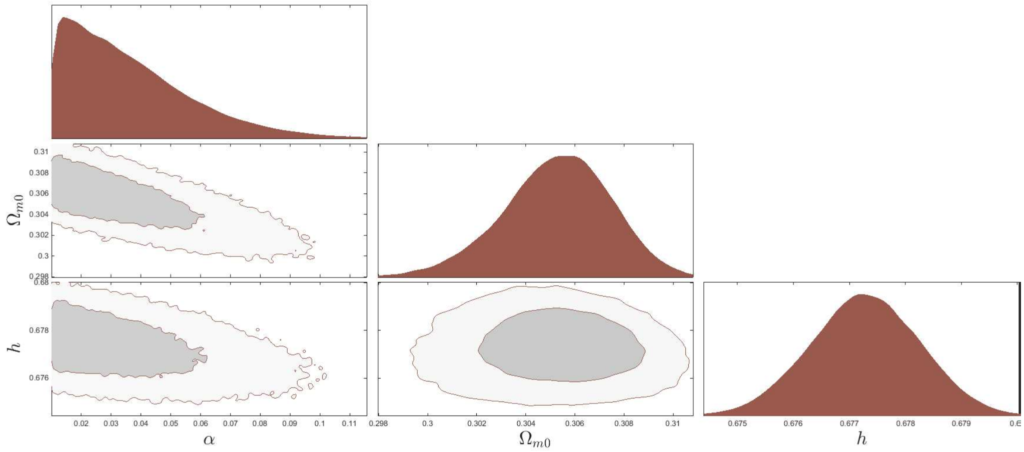

Figure 9.1: The 2σ confidence level contour plots for various pairs of the free parameters (α, $\Omega_{\rm m0}$, h), for which the ϕCDM model with the Ratra-Peebles potential $V(\phi) = V_0 M_{\rm pl}^2 \phi^{-\alpha}$ is in the best fit with the ΛCDM model.

where $\mathcal{L}_{\rm max} \propto \exp(-\chi^2_{\rm min}/2)$ is the maximum value of the probability function, k is the number of observations.

We also conducted the Bayes evidence analysis. The Bayes evidence for the model with a set of the parameters, $\boldsymbol{p}$, is determined by the integral:

$$\mathcal{E} = \int \mathrm{d}^3\boldsymbol{p}\mathcal{P}(\boldsymbol{p}), \tag{9.7}$$

where $\mathcal{P}$ is the posterior likelihood, which is proportional to the local density of the MCMC points. The boundaries of the integration are given by the prior on the extra parameters, *i.e.*, from the previously found ranges of the model parameters shown in Table 6.1 and Table 6.2.

The models with the higher values of the Bayes evidence are preferable to the models with the lower values of the Bayes evidence.

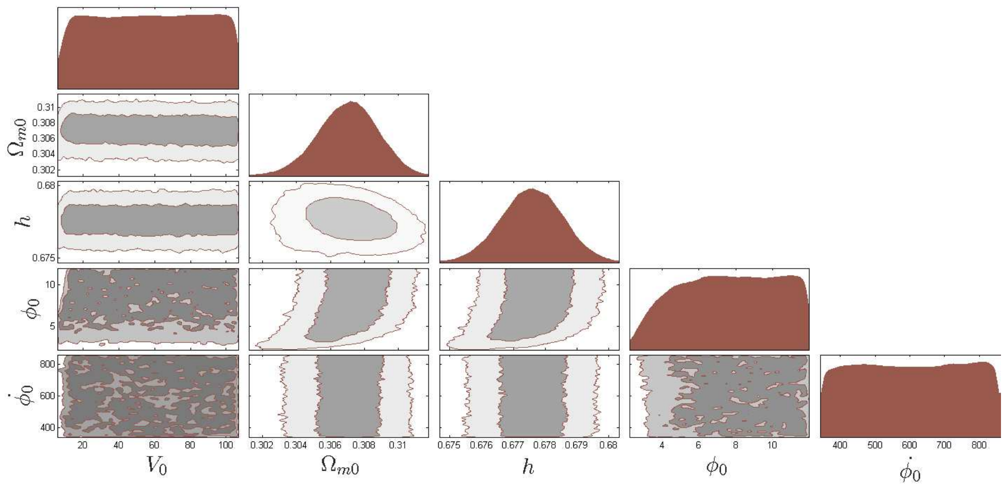

Figure 9.2: The 2σ confidence level contour plots for various pairs of the free parameters (V_0, $\Omega_{\mathrm{m}0}$, h, ϕ_0, $\dot{\phi}_0$), for which the ϕCDM model with the Zlatev-Wang-Steinhardt potential $V(\phi) = V_0(\exp(M_{\mathrm{pl}}/\phi) - 1)$ is in the best fit with the ΛCDM model.

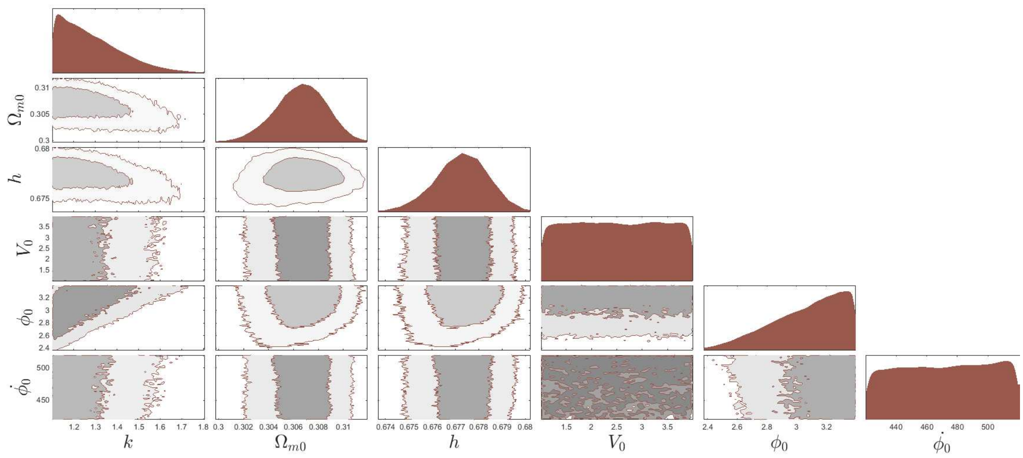

Figure 9.3: The 2σ confidence level contour plots for various pairs of the free parameters (k, $\Omega_{\mathrm{m}0}$, h, V_0, ϕ_0, $\dot{\phi}_0$), for which the ϕCDM model with the phantom pseudo-Nambu-Goldstone boson potential $V(\phi) = V_0(1 - \cos(\phi/\kappa))$ is in the best fit with the ΛCDM model.

Quintessence potentials	AIC	BIC	Bayes factor
$V(\phi) = V_0 M_{\rm pl}^2 \phi^{-\alpha}$	10	18.7	0.5293
$V(\phi) = V_0 \exp(-\lambda\phi/M_{\rm pl})$	12	22.4	0.0059
$V(\phi) = V_0(\exp(M_{\rm pl}/\phi) - 1)$	10	18.7	0.0067
$V(\phi) = V_0 \phi^{-\chi} \exp(\gamma\phi^2/M_{\rm pl}^2)$	14	26.2	0.0016
$V(\phi) = V_0(\cosh(\varsigma\phi) - 1)^g$	14	26.2	0.0012
$V(\phi) = V_0(\exp(\nu\phi) + \exp(\upsilon\phi))$	14	26.2	0.0053
$V(\phi) = V_0((\phi - B)^2 + A)\exp(-\mu\phi)$	16	29.9	0.0034
$V(\phi) = V_0 \sinh^m(\xi M_{\rm pl}\phi)$	14	26.2	0.0014
$V(\phi) = V_0 \exp(M_{\rm pl}/\phi)$	10	18.7	0.0077
$V(\phi) = V_0(1 + \exp(-\tau\phi))$	12	22.4	0.0024

Table 9.3: The list of the dark energy quintessence potentials with the corresponding values of AIC, BIC and Bayes factor.

Phantom potentials	AIC	BIC	Bayes factor
$V(\phi) = V_0\phi^5$	10.0	18.7	0.0921
$V(\phi) = V_0\phi^{-2}$	10.0	18.7	0.0142
$V(\phi) = V_0 \exp(\beta\phi)$	22.4	12.0	0.0024
$V(\phi) = V_0\phi^2$	10.0	18.7	0.0808
$V(\phi) = V_0(1 - \exp(\phi^2/\sigma^2))$	12.0	22.4	0.0113
$V(\phi) = V_0(1 - \cos(\phi/\kappa))$	12.0	22.4	0.0061
$V(\phi) = V_0(\cosh(\psi\phi))^{-1}$	12.0	22.4	0.0056

Table 9.4: The list of the dark energy phantom potentials with the corresponding values of AIC, BIC and Bayes factor.

We investigated how tight the prior on the extra model parameters should be for the competitiveness of the dark energy models (in the sense of the Bayes evidence) with the standard ΛCDM model. We checked that the priors ranges of the model parameters include the values of the model parameters from the posterior ranges.

We numerically integrated the posterior probability for all the models, the results of this integration are presented in Table 9.3 and Table 9.4. All these numbers are normalized relative to the fiducial ΛCDM model.

9.4 ϕCDM Models in the CPL Phase Space

To check how well the CPL parametrization approximates the dark energy models, how these models are consistent with the ΛCDM model and how they differ from each other, we presented a set of the possible values of the EoS parameters, w_0 and w_a, for each dark energy potential in the CPL - ΛCDM phase space.

The mapping of the dark energy models on the $w_0 - w_a$ plane is shown in Fig. (9.4) for the quintessence models and in Fig. (9.5) for the phantom models. In these figures, the curves represent the maximum ranges of the values of the EoS parameters, $w(a)$, for each dark energy model in the $w_0 - w_a$ plane. These CPL-ΛCDM contours at the 1σ, 2σ, and 3σ confidence levels were obtained by fitting the data $H(z)$, $d_A(z)$ and $f(a)\sigma_8(a)$ for each dark energy model under study and for the ΛCDM model of the CPL parametrization.

In order to check how well the CPL parametrization, Eq. (6.46), describes the dark energy models, we find the best fit effective values of $w_0 - w_a$ for a range of the free parameters for each model. For an easy visual representation of this information, we chose a parameter with respect to which the best fit w_0 and w_a values are the most sensitive and plotted these ranges within priors. These results are presented in Fig. (9.4) for the quintessence models and in Fig. (9.5) for the phantom models.

In Fig. (9.4) we show that some of the dark energy models are located very close to the ΛCDM model for a wide range values of the EoS parameter within our priors. The range of the values of the EoS parameters for the Ferreira-Joyce, the inverse exponent and the Sugra potentials is very small, it almost coincides with the value of the EoS parameter for the ΛCDM model, ($w_0 = -1, w_a = 0$), therefore, these models are absolutely impossible to distinguish from the ΛCDM model. The values of the EoS parameter for the Chang-Scherrer, the Urẽna-López-Matos, and the Barreiro-Copeland-Nunes potentials are inside of the 3σ confidence levels of the CPL - ΛCDM contours. Thus, these potentials cannot be distinguished from the standard ΛCDM model today. The values of the EoS parameter for the Ratra-Peebles, the Zlatev-Wang-Steinhardt, the Albrecht-Skordis, and the Sahni-Wang potentials are beyond of the 3σ confidence levels of the CPL - ΛCDM contours. This means that depending on the value of the EoS parameter at the present epoch, these models can either be distinguished or they cannot be distinguished from the ΛCDM model today.

The results obtained for the phantom potentials are presented in Fig. (9.5). Obviously, the values of the EoS parameter for the phantom quadratic potential are outside of the 3σ confidence levels of the CPL - ΛCDM contours, so this potential cannot imitate the

ΛCDM model today. The EoS parameter curves for the pseudo-Nambu-Goldstone boson, the inverse hyperbolic cosine, the exponent, the Gaussian, the inverse square power potentials are partially at the 3σ confidence levels of the CPL - ΛCDM contours and partly outside of these boundaries. Thus, these models either can mimic the ΛCDM model today or they can also manifest themselves as the dark energy models with a faster change of the EoS parameter over time than the EoS parameter in the ΛCDM model. The curve of the EoS parameter for the fifth power phantom potential is within the 3σ confidence levels of the CPL - ΛCDM contours, so this model cannot be distinguished from the ΛCDM model today.

For each potential we investigated whether a change in the value of one of the model parameters (provided that the values of the other model parameters and the values of the initial conditions are fixed) or a change in the values of the initial conditions (provided that the values of the model parameters are fixed) leads to the maximum range of the values of the EoS parameter. The result of this study is that we can divide all the considered potentials into two types: into the potentials whose evolution depends on the values of the initial conditions and into the potentials whose evolution doesn't depend on the values of the initial conditions, *i.e.*, such potentials have the attractor solutions. The first type includes the following quintessence potentials: the Zlatev-Wang-Steinhardt, the Sahni-Wang, as well as the following phantom potentials: the quadratic, the Gaussian, the fifth power, the inverse square power. The second type includes the following quintessence potentials[1]: the Sugra, the Urẽna-López-Matos, the Albrecht-Scordis, the Chang-Scherer, the Barreiro-Copeland-Nunes, as well as the following phantom potentials: the pseudo-Nambu-Goldstone boson, the inverse hyperbolic cosine, the exponent.

9.5 Conclusion

Applying the phenomenological method developed by us, we reconstructed the dark energy model of a scalar field, listed in Table 6.1 and in Table 6.2. Thus, we found the prior ranges for the initial conditions and the model parameters. The results are summarized in Table 9.1 and in Table 9.2.

The constraints on the dark energy models were obtained by comparing $H(z)$, $d_A(z)$, $f(a)\sigma_8(a)$ data with the corresponding data generated for the fiducial ΛCDM model. The examples of the constraints for the Ratra-Peebles, the Zlatev-Wang-Steinhardt quintessence

[1]The Ratra-Peebles potential is in the privileged position in comparison with the other potentials, since for this potential we considered a solution with the fixed initial conditions, Eq. (9.1). Thus, this potential was not considered in this study.

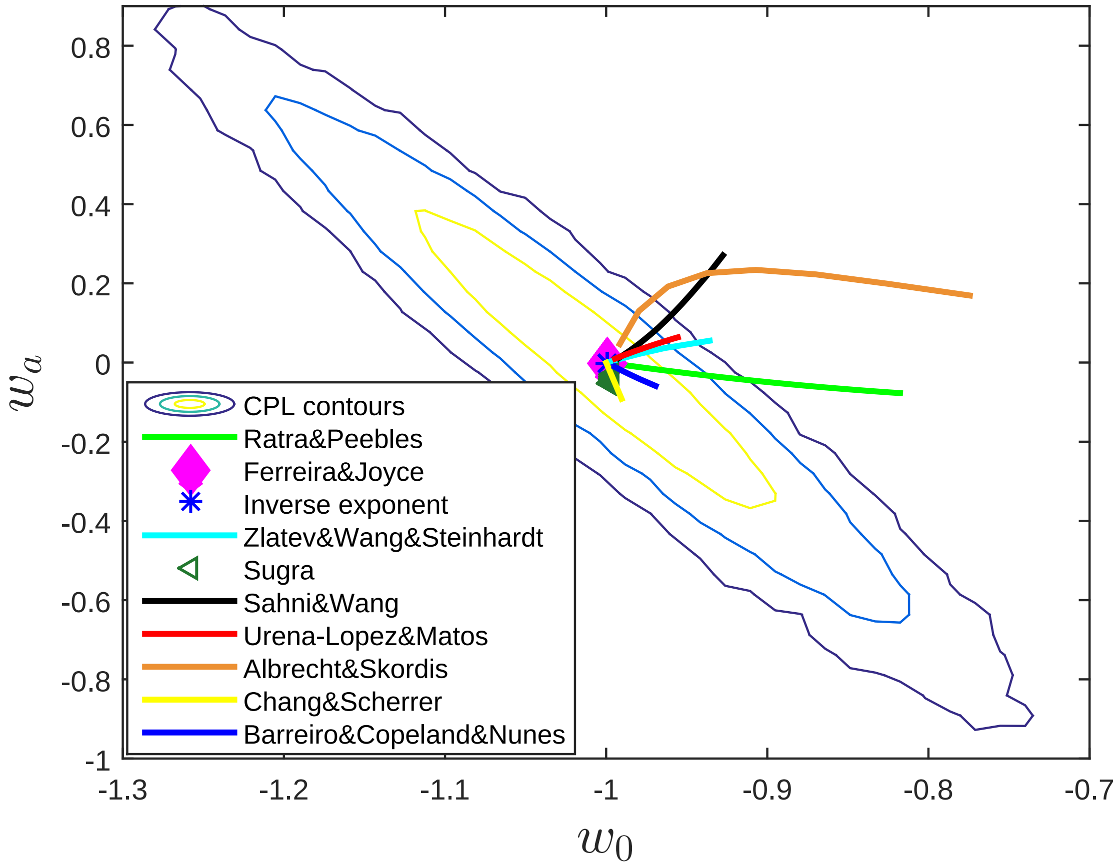

Figure 9.4: The comparison of the possible w_0 and w_a values for the quintessence dark energy potentials with the CPL-ΛCDM 3σ confidence level contours.

potentials and for the inverse hyperbolic cosine phantom potential are shown in Figs. (9.1-9.3).

We applied the Bayes statistical criteria to compare the models, such as the Bayes factor, as well as the AIC and BIC information criteria. To this end, we have integrated Eq. (9.7) within the boundaries corresponding to the previously found ranges of the model parameters given in Table 9.1 and in Table 9.2. The calculated values of AIC, BIC and Bayes factor for all the dark energy models are summarized in Table 9.3 and in Table 9.4. These numbers clearly demonstrated that if the ΛCDM model is the true description of dark energy, then the full DESI data will be able to strongly discriminate most of the scalar field dark energy models currently under consideration.

We investigated how the dark energy models are mapped on the $w_0 - w_a$ phase space of the CPL-ΛCDM contours, see Fig. (9.4) and Fig. (9.5).

We found that the Ferreira-Joyce, the inverse exponent, the Sugra, the Chang-Scherrer, the Urẽna-López-Matos, the Barreiro-Copeland-Nunes quintessence models and the fifth

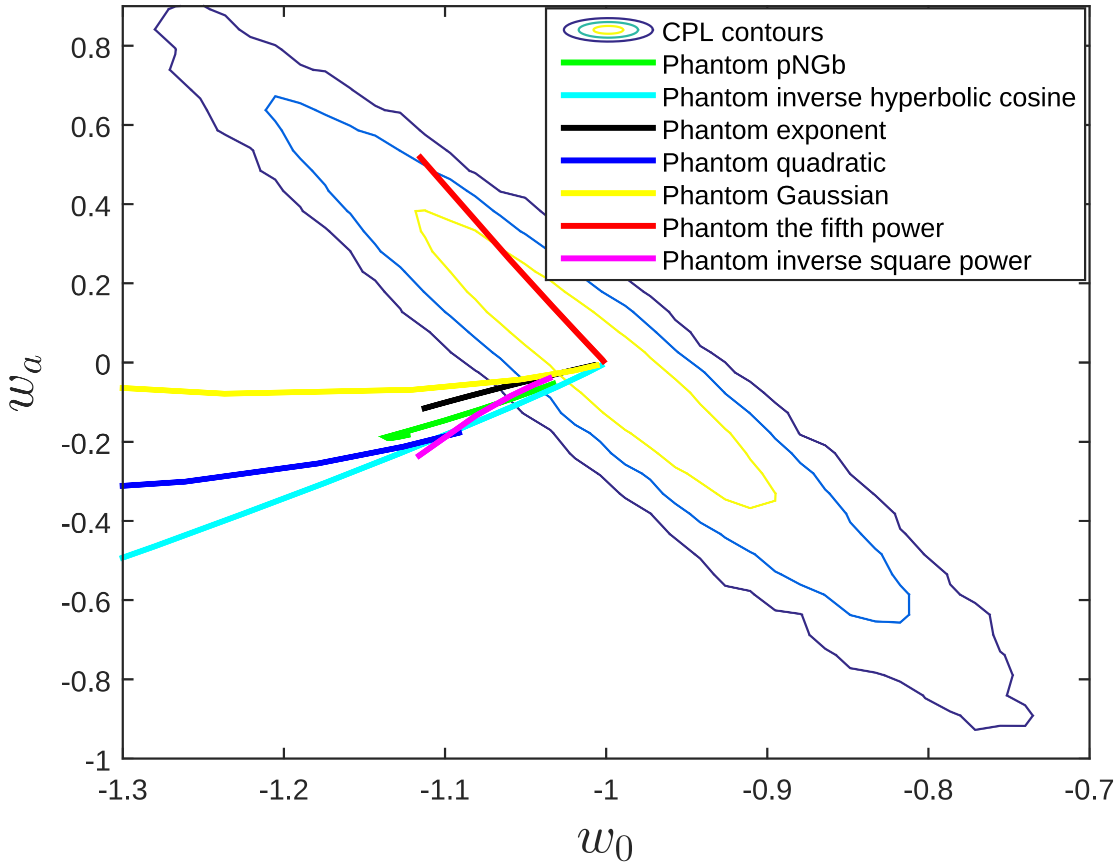

Figure 9.5: The comparison of the possible w_0 and w_a values for the phantom dark energy potentials with the CPL-ΛCDM 3σ confidence level contours.

power phantom model cannot be distinguished from the ΛCDM model for the present time. Whilst the Ratra-Peebles, the Zlatev-Wang-Steinhardt, the Albrecht-Skordis, the Sahni-Wang quintessence models and the pseudo-Nambu-Goldstone boson, the inverse hyperbolic cosine, the exponent, the Gaussian, the inverse square power phantom models can either be distinguished or cannot be distinguished from the ΛCDM model today. The quadratic phantom model can be absolutely distinguished from the ΛCDM model at the present epoch.

All the studied models can be divided into two types: on the models whose evolution depends on the values of the initial conditions and into the models whose evolution doesn't depend on the values of the initial conditions. The first type includes the following quintessence models: the Zlatev-Wang-Steinhardt, the Sahni-Wang and also the phantom models: the quadratic, the Gaussian, the fifth power, the inverse square power. The second type includes the following quintessence models: the Sugra, the Chang-Scherrer, the Albrecht-Skordis, the Urẽna-López-Matos, the Barreiro Copeland-Nunes, as well as the following phantom models: the pseudo-Nambu-Goldstone boson, the inverse hyperbolic cosine, the exponent.

Chapter 10

Mass Varying Neutrino Model

The coupled models of dark matter and dark energy were developed to resolve the coincidence problem in the standard ΛCDM model. Based on the essence of this problem, it follows that dark matter and dark energy interacted with each other during their evolution. At the same time, the assumed dark matter particles had the mass that varied over time.

One of the candidates for the role of dark matter can be considered the relic neutrinos. The neutrinos belong to the class of leptons and can participate only in the weak gravitational interactions. In addition, the neutrino has the mass. According to Planck 2015, the value of the sum of neutrino masses at the present epoch is $\sum m_\nu < 0.23$ eV under the assumption that the ΛCDM model is correct, Ref. (Ade et al. (2016)). Fardon, Nelson and Weiner elaborated the mechanism of the *Varying Mass Particles* (VAMPs). They applied the VAMPs mechanism to the neutrinos, as a result of which the model of *Mass Varying Neutrino* (MaVaN) was created, Ref. (Fardon et al. (2004)). In this model, the fermionic field interacts with the bosonic scalar field via the Yukawa coupling. If initially (before interaction) the relic neutrino is massless, then interacting with the scalar field the neutrino will acquire the mass, which subsequently varies over time.

The MaVaN model is quite compelling, since the cause of the neutrino mass emergence is explained in this model. In addition, the coincidence problem is resolved in this model, *i.e.*, the answer to the following question is given: "Why do the neutrinos (dark matter) and dark energy have the comparable energy scales at the present epoch?"

The disadvantage of the MaVaN model is the instability of a fluid, which consists of the neutrinos and dark energy. This instability is a consequence of the negative value of the square of the sound speed in this medium. A negative value of the square of the sound speed arises due to the exponential growth of the scalar fluctuations, which leads to the exponential clustering of the neutrinos, Refs. (Afshordi et al. (2005), Kaplinghat & Rajaraman (2007)). To get rid of this problem, the additional complications were introduced into the MaVaN model, for example, a multicomponent scalar field was considered, Ref. (Takahashi & Tanimoto (2007)). In the paper Ref. (Chitov et al. (2011)), the authors studied the stable, metastable and unstable phases of the MaVaN model and found a consistent solution for the equilibrium condition.

In this work, we consider the inverse-power Ratra-Peebles scalar field potential. This potential does not have a non-trivial minimum. The fermionic mass is generated due to the violation of the chiral symmetry in the Dirac sector of the Lagrangian. It is assumed that the fermionic mass is obtained from the minimizing the total thermodynamic potential. At the same time, the evolution of the mass is slow enough, so that the coupled system (fermions and dark energy) to be in the equilibrium at the temperature of $T(a)$.

10.1 Interaction of the Scalar Field and Dirac Field

The Hamiltonian of the bosonic scalar field for the FLRW metric and the Euclidean action of the bosonic scalar field are defined, respectively, as:

$$H_B = \int a^3 d^3x \left[\frac{1}{2}\dot{\phi}^2 + \frac{1}{2a^2}(\nabla\phi)^2 + V(\phi)\right] \tag{10.1}$$

and

$$S_B^E = \int_0^\beta d\tau \int a(t)^3 d^3x \left[\frac{1}{2}\Big(\frac{\partial\tau}{\partial\phi}\Big)^2 + \frac{1}{2a^2}(\nabla\phi)^2 + V(\phi)\right] , \tag{10.2}$$

where $\int d^3x = V$ is a comoving volume; $a^3 V = V_{\text{phys}}$ is a physical volume; $V(\phi)$ is a potential of the scalar field.

The Dirac Hamiltonian for the FLRW metric and the Euclidean action for the Dirac field are presented, respectively, as:

$$H_D = \int a^3 d^3x \; \bar{\psi}\big(- \frac{\imath}{a}\boldsymbol{\gamma}\cdot\boldsymbol{\nabla} + m_\nu\big)\psi \tag{10.3}$$

and

$$S_D^E = \int_0^\beta d\tau \int a(t)^3 d^3x \; \bar{\psi}(\mathbf{x},\tau)\Big(\gamma^o \frac{\partial}{\partial\tau} - \frac{\imath}{a}\boldsymbol{\gamma}\cdot\boldsymbol{\nabla} + m_\nu - \mu\gamma^o\Big)\psi(\mathbf{x},\tau), \tag{10.4}$$

where m_ν is the fermionic mass.

The grand partition function is defined by the Grassmann functional integral:

$$\mathcal{Z}_D \equiv \mathrm{Tr}\, \mathrm{e}^{-\beta(\hat{H}-\mu\hat{Q})} = \int \mathcal{D}\bar{\psi}\mathcal{D}\psi\, \mathrm{e}^{-S_D^E}. \tag{10.5}$$

Consider the interaction of the bosonic scalar field with the massless fermions via the Yukawa coupling:

$$\mathcal{S} = S_B^E + S_D^E\big|_{m_\nu=0} + g\int_0^\beta d\tau \int a^3 d^3x\ \phi\bar{\psi}\psi, \tag{10.6}$$

where g is the dimensionless Yukawa coupling constant, $g = 1$.

The Lagrangian for the Yukawa coupling is defined as:

$$\mathcal{L}_{\mathrm{Yuk}} = -g\bar{\psi}\phi\psi. \tag{10.7}$$

The path integral for the partition function in the interaction of the bosonic field with the fermionic field:

$$\mathcal{Z} = \int \mathcal{D}\phi\mathcal{D}\bar{\psi}\mathcal{D}\psi\, \mathrm{e}^{-\mathcal{S}}. \tag{10.8}$$

The Grassmann fields can be formally integrated, Ref. (Chitov et al. (2011)):

$$\mathcal{Z} = \int \mathcal{D}\phi\, \mathrm{e}^{-\mathcal{S}(\phi)} = \int \mathcal{D}\phi\, \exp\big[-S_B^E + \log \mathrm{Det}\hat{D}(\phi)\big]\ , \tag{10.9}$$

where the Dirac operator is defined as:

$$\hat{D}(\phi) = \gamma^o \frac{\partial}{\partial\tau} - \frac{\imath}{a}\boldsymbol{\gamma}\cdot\boldsymbol{\nabla} + g\phi(\mathbf{x},\tau) - \mu\gamma^o. \tag{10.10}$$

10.2 Saddle Point Approximation

The thermodynamic potential in the coupled model of the bosonic scalar field and the fermionic field, Eq. (10.6), can be found in the saddle point approximation, minimizing the path integral, Eq. (10.9). We take into account that the bosonic scalar field at the moment, $\phi = \phi_c$, minimizes the action, S. This is the so-called classical field value:

$$\phi_{\mathrm{cr}} = \langle\varphi\rangle. \tag{10.11}$$

In this case, we can precisely determine the value of $\log\det \hat{D}(\phi)$, where the fermions acquire the mass:

$$m_\nu = g\phi_{\rm cr}. \tag{10.12}$$

At the moment $\phi = \phi_{\rm cr}$ the partition function has the form:

$$\mathcal{Z}_{\phi\nu} = \mathcal{Z}_F \, e^{-\beta V V(\phi_{\rm cr})}. \tag{10.13}$$

In this case, the total thermodynamic potential, $V_{\phi\nu}(\phi_{\rm cr})$, is defined as:

$$V_{\phi\nu}(\phi_{\rm cr}) = V(\phi_{\rm cr}) + V_\nu(\phi_{\rm cr}), \tag{10.14}$$

where

$$V_{\phi\nu} = V_0 - \frac{1}{3\pi^2}\int_0^\infty \frac{dp\, p^4}{\epsilon(p)}\Big[n_F(\epsilon_+) + n_F(\epsilon_-)\Big], \tag{10.15}$$

here V_0 is a thermodynamic potential for vacuum[1]; $n_F(x)$ is a Fermi distribution function:

$$n_F(x) = \frac{1}{e^{\beta x}+1}. \tag{10.16}$$

Let's consider the approximation in the saddle point, $\phi = \phi_{\rm cr}$. This approximation will be a self-consistent if $\phi_{\rm cr}$ minimizes the free energy. The conditions for the minimum of the total thermodynamic potential, Eq. (10.14), at the saddle point (at fixed temperature and chemical potential):

$$\left.\frac{\partial V_{\phi\nu}(\phi)}{\partial\phi}\right|_{\mu,\beta;\phi=\phi_{\rm cr}} = 0, \qquad \left.\frac{\partial^2 V_{\phi\nu}(\phi)}{\partial\phi^2}\right|_{\mu,\beta;\phi=\phi_{\rm cr}} > 0. \tag{10.17}$$

Applying the first condition in Eq. (10.17) to the total thermodynamic potential, Eq. (10.14), we get:

$$V'(\phi_{\rm cr}) + g\rho_s = 0, \tag{10.18}$$

where ρ_s is a fermionic density.

$$\rho_s \equiv \frac{\langle \hat{N}\rangle}{V} = \frac{\partial V_\nu}{\partial m}, \tag{10.19}$$

here $\hat{N} = \int d^3\sqrt{-g}\,\mathbf{x}\bar{\psi}\psi$.

[1] Henceforth, the values of the potential, the pressure and the energy density will be redefined with respect to the corresponding vacuum values as: $V_{\phi\nu} \mapsto V_{\phi\nu} - F_0, P_\nu \mapsto P_\nu - P_0, \rho_s \mapsto \rho_s - \rho_0$.

The fermionic density is defined as:

$$\rho_s = \frac{m}{\pi^2} \int_0^\infty \frac{dp\, p^2}{\epsilon(p)} \Big[n_F(\epsilon_+) + n_F(\epsilon_-) - 1 \Big]. \tag{10.20}$$

10.2.1 Fermionic Potential

Consider the Dirac fermions, for which the number of the fermions and the antifermions is the same, *i.e.*, the chemical potential is zero, $\mu = 0$. The fermions with zero chemical potential are described by the Fermi distribution function, Eq. (10.16):

$$n_F(E) = \frac{1}{e^{\beta E} + 1}, \tag{10.21}$$

where E is a physical fermionic energy, which is defined as:

$$E(p) = \sqrt{m_\nu^2 + p^2}, \tag{10.22}$$

here p is a fermionic momentum.

The fermionic potential, V_ν, is completely determined by the fermionic pressure, p_ν:

$$\begin{aligned} V_\nu = -p_\nu = -\frac{N_F}{3\pi^2} \int_0^\infty \frac{p^4 dp}{E(p)} [n_F(E_-) + n_F(E_+)], \\ = -\frac{2N_F}{3\pi^2} \int_0^\infty \frac{p^4 dp}{E(p)(e^{\beta E} + 1)}, \ \mu = 0, \end{aligned} \tag{10.23}$$

where N_F is the number of the neutrinos species, $N_F = 3$; $\beta = 1/T$ and $T = T_{\nu 0}/a$, $T_{\nu 0} = 1.9454$ eV is a neutrinos temperature at the present epoch[2].

In Eq. (10.23), taking into account that $E_\pm = E(p) \pm \mu$, if $\mu = 0$, then $n_F(E_-) = n_F(E_+)$. Let's introduce the new variables to the integral, Eq. (10.23): $\overline{E} = \beta E$, $d\overline{E} = \beta dE$, where $\overline{E}^2 = \beta^2 m_\nu^2 + \beta^2 p^2$, Eq. (10.22); $pdp = \frac{E}{\beta} d\overline{E}$, $p^3 = \frac{(\overline{E}^2 - \beta^2 m_\nu^2)^{3/2}}{\beta^3} = \frac{(\overline{E}^2 - \overline{\varphi}^2)^{3/2}}{\beta^3}$. The new boundaries of the integration: for $p = 0$, $\overline{E} = \beta m_\nu = \overline{\phi}$ and for $p = \infty$, $\overline{E} = \infty$.
Eventually, Eq. (10.23) can be rewritten as:

$$V_\nu = -p_\nu = -\frac{2N_F}{3\pi^2} \int_{\overline{\varphi}}^\infty \frac{(\overline{E}^2 - \overline{\varphi}^2)^{3/2}}{\beta^3 E(e^{\overline{E}} + 1)} \frac{E}{\beta} d\overline{E} = -\frac{2N_F}{3\pi^2 \beta^4} \int_{\overline{\varphi}}^\infty \frac{(\overline{E}^2 - \overline{\varphi}^2)^{3/2}}{e^{\overline{E}} + 1} d\overline{E}. \tag{10.24}$$

[2]The neutrinos temperature at the present epoch can be obtained from the equation: $T_{\nu 0} = (4/11)^{1/3} T_{\gamma 0}$, where $T_{\gamma 0} = T_0$ is a photons temperature at the present epoch.

10.2.2 Fermionic Energy Density

The total thermodynamic potential, $V_{\phi\nu}$, is defined as:

$$V_{\phi\nu} = V(\phi) + V_\nu(\varphi) = V_\phi(\phi) - \frac{2N_F}{3\pi^2\beta^4}\int_{\overline{\varphi}}^{\infty} \frac{(\overline{E}^2 - \overline{\varphi}^2)^{3/2}}{e^{\overline{E}}+1} d\overline{E}. \tag{10.25}$$

We examine the Ratra-Peebles potential for the bosonic scalar field:

$$V(\phi) = \frac{M_\phi^{\alpha+4}}{\phi^\alpha}, \tag{10.26}$$

where M_ϕ is a mass scale for the Ratra-Peebles potential.

From the condition of the minimizing the total thermodynamic potential, Eq. (10.18), we have:

$$\rho_s = \frac{\partial V_\nu}{\partial m_\nu} = -\frac{1}{g}\frac{\partial V_\nu}{\partial \phi}. \tag{10.27}$$

Differentiating Eq. (10.24), we obtain the equation for the fermionic density:

$$\begin{aligned}\rho_s = -\frac{\partial V_\nu}{\partial \varphi} &= \frac{2N_F}{3\pi^2\beta^4}\int_{\beta m_\nu}^{\infty} \frac{3}{2}\frac{2\beta^2 m_\nu(\overline{E}^2 - (\beta m_\nu)^2)^{1/2}}{e^{\overline{E}}+1} d\overline{E},\\ &= \frac{2N_F m_\nu}{\pi^2\beta^2}\int_{\beta m_\nu}^{\infty} \frac{(\overline{E}^2 - (\beta m_\nu)^2)^{1/2}}{e^{\overline{E}}+1} d\overline{E}\ .\end{aligned} \tag{10.28}$$

Eq. (10.28) can be rewritten as:

$$\rho_s = \frac{2N_F}{3\pi^2\beta^4}\int_{\overline{\phi}}^{\infty} \frac{3}{2}\frac{2\phi\beta^2(\overline{E}^2 - \overline{\phi}^2)^{1/2}}{e^{\overline{E}}+1} d\overline{E} \ = \frac{2N_F\overline{\phi}}{\pi^2\beta^3}\int_{\overline{\phi}}^{\infty} \frac{(\overline{E}^2 - \overline{\phi}^2)^{1/2}}{e^{\overline{E}}+1} d\overline{E}\ . \tag{10.29}$$

10.3 Mass Equation

Plugging Eq. (10.26) into Eq. (10.18), we get:

$$\frac{\alpha M_\phi^{\alpha+4}}{\phi^{\alpha+1}} = g\rho_s \quad \Rightarrow \quad \alpha\overline{M_\phi}^{\alpha+4} g^\alpha = \beta^3\overline{\phi}^{\alpha+1}\rho_s, \tag{10.30}$$

here $\overline{\phi} = \beta m_\nu = \frac{g\phi}{T}$; $\overline{M_\phi} \equiv \frac{M_\phi}{T}$.

Substituting Eq. (10.29) into Eq. (10.30), we obtain the mass equation:

$$\alpha\overline{M_\phi}^{\alpha+4} g^\alpha = \beta^3\overline{\phi}^{(\alpha+1)}\frac{2N_F\overline{\phi}}{\pi^2\beta^3}\int_{\overline{\phi}}^{\infty} \frac{(\overline{E}^2 - \overline{\phi}^2)^{1/2}}{e^{\overline{E}}+1} d\overline{E}\ , \tag{10.31}$$

$$\frac{\alpha\pi^2 g^\alpha \overline{M_\phi}^{\alpha+4}}{2N_F} = I_\alpha(\overline{\phi}), \qquad I_\alpha(\overline{\phi}) = \overline{\phi}^{(\alpha+2)} \int_{\overline{\phi}}^{\infty} \frac{(\overline{E}^2 - \overline{\phi}^2)^{1/2}}{e^{\overline{E}}+1} d\overline{E}\ . \tag{10.32}$$

The numerical solutions of Eq. (10.32), which depend on the parameter α, are shown in Fig. (10.1).

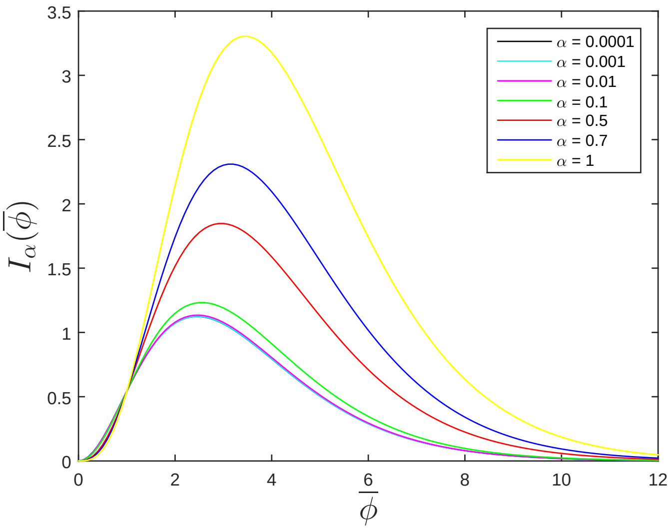

Figure 10.1: The solutions of the mass equation, Eq. (10.32), for the different values of the α parameter.

10.4 Energy Balance in the Universe to the Critical Point

We are considering a flat universe, which implies the equality of the total energy density and the critical density: $\rho_{\text{tot}} = \rho_{\text{cr}}$. Namely:

$$\rho_{\text{tot}} = \rho_{\gamma 0} a^{-4} + \rho_{\text{m}0} a^{-3} + \rho_{\text{couple}} = \frac{3H^2}{8\pi G}. \tag{10.33}$$

Equally, the total energy density can be represented as:

$$\rho_{\text{tot}} = \frac{7\pi^2 N_F}{60} T^4. \tag{10.34}$$

The energy density for the photons is defined as:

$$\rho_\gamma = \frac{\pi^2}{15} T^4 = \frac{\pi^2}{15} T_0^4 (1+z)^4. \tag{10.35}$$

From Eq. (10.35) and Eq. (10.34) we get[3]:

$$\rho_{\rm tot} \approx \rho_\gamma + \rho_{\rm couple} \approx \frac{\pi^2}{15}\left(1 + \frac{7N_F}{4}\right). \tag{10.36}$$

Hence, we have:

$$\Omega_{\rm couple} = \frac{7N_F}{4 + 7N_F} = 0.84, \qquad \Omega_\gamma = \frac{4}{4 + 7N_F} = 0.16. \tag{10.37}$$

The energy density parameters for the photons, the matter and the neutrinos-dark energy fluid depending on redshift are presented in Fig. (10.2). The evolution of the energy density

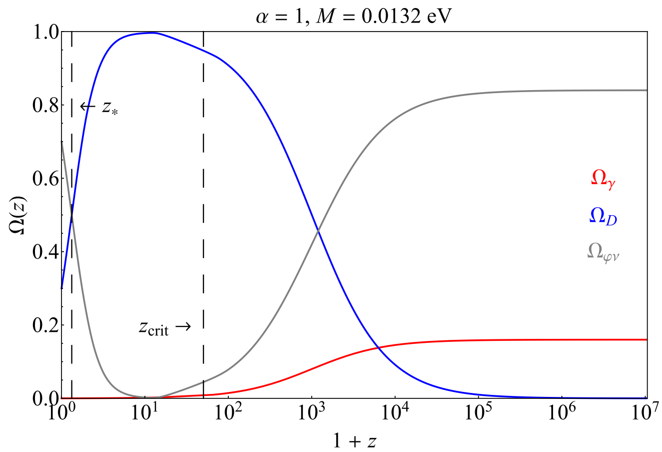

Figure 10.2: The dependence of the energy density parameters for the photons, the matter and the neutrinos-dark energy fluid on redshift. The value of $z_\star$ denotes the epoch of the matter and dark energy equality.

parameters was calculated from the moment $1+z = 10^7$, *i.e.*, starting with the temperature $T \sim 2.35$ KeV to the present epoch. Thus, the values of the temperature are lower than the value of the temperature at the epoch of the electron-positron pairs annihilation, the value of which is $T_{\rm e} = 0.5\,{\rm MeV}$, see Fig. (10.2).

[3] At the high temperatures, the value of which are in the range, $T_{\rm eq} \ll T < T_{\rm e}$, where $T_{\rm eq}$ is the temperature in the universe at the moment of the matter energy and dark energy equality; $T_{\rm e}$ is the temperature at the epoch of the electron-positron annihilation. We can ignore the contribution of the matter energy density to the total energy density, since the matter is a subdominant during this period of time.

10.5 Joint Solution of the First Friedmann's and the Scalar Field Equations

10.5.1 Relativistic Neutrino Before the Critical Point

At the values of the scale factor $a < a_{\rm cr}$, the fermionic and bosonic fields do not interact with each other, therefore, the neutrinos remain relativistic and, accordingly, the neutrinos have no mass, $\sum m_\nu = 0$.

For this period of time, the total potential, the energy density and the pressure for the scalar field and the relativistic neutrinos can be written, respectively, as:

$$V = V_\phi - \frac{2N_F}{3\pi^2\beta^4}\int_{\varphi\beta}^{\infty}\frac{(\overline{E}^2-\varphi^2\beta^2)^{3/2}}{e^{\overline{E}}+1}d\overline{E}, \tag{10.38}$$

$$\rho = \frac{\dot{\phi}^2}{2} + V_\phi + \frac{2N_F}{\pi^2\beta^4}\int_{\varphi\beta}^{\infty}\frac{\overline{E}^2(\overline{E}^2-\varphi^2\beta^2)^{1/2}}{e^{\overline{E}}+1}d\overline{E}, \tag{10.39}$$

$$p = \frac{\dot{\phi}^2}{2} - V_\phi + \frac{2N_F}{3\pi^2\beta^4}\int_{\varphi\beta}^{\infty}\frac{(\overline{E}^2-\varphi^2\beta^2)^{3/2}}{e^{\overline{E}}+1}d\overline{E}. \tag{10.40}$$

The first Friedmann's equation and the scalar field equation for the values of the scale factor $a < a_{\rm cr}$ are presented, respectively, as:

$$\left(\frac{\dot{a}}{a}\right)^2 = H_0^2\Big(\Omega_{r0}a^{-4} + \Omega_{\rm m0}a^{-3} + \frac{1}{\rho_{\rm cr}}\Big(V_\phi + \frac{\dot{\phi}^2}{2} + \frac{2N_F}{\pi^2\beta^4}\int_{\varphi\beta}^{\infty}\frac{\overline{E}^2(\overline{E}^2-\varphi^2\beta^2)^{1/2}}{e^{\overline{E}}+1}d\overline{E}\Big)\Big), \tag{10.41}$$

$$\ddot{\phi} + 3\frac{\dot{a}}{a}\dot{\phi} + \frac{\partial V_\phi}{\partial\phi} + \frac{2\varphi N_F}{\pi^2\beta^3}\int_{\varphi\beta}^{\infty}\frac{(\overline{E}^2-\varphi^2\beta^2)^{1/2}}{e^{\overline{E}}+1}d\overline{E} = 0. \tag{10.42}$$

Taking into account that $a < a_{\rm cr}$:

$$\varphi = m_\nu = 0 \quad\text{and}\quad \int_{\varphi}^{\infty}\frac{\overline{E}^2(\overline{E}^2-\varphi^2\beta^2)^{1/2}}{e^{\overline{E}}+1}d\overline{E} = \int_0^{\infty}\frac{\overline{E}^3}{e^{\overline{E}}+1}d\overline{E} = \frac{7\pi^4}{120}. \tag{10.43}$$

Therefore, the equations, Eq. (10.41) and Eq. (10.42), can be rewritten as:

$$\left(\frac{\dot{a}}{a}\right)^2 = H_0^2\Big(\Omega_{\rm r0}a^{-4} + \Omega_{\rm m0}a^{-3} + \frac{1}{\rho_{\rm cr}}\Big(V_\phi + \frac{\dot{\phi}^2}{2} + \frac{7\pi^2 N_F}{60\beta^4}\Big)\Big), \tag{10.44}$$

$$\ddot{\phi} + 3\frac{\dot{a}}{a}\dot{\phi} + \frac{\partial V_\phi}{\partial\phi} = 0. \tag{10.45}$$

10.5.2 Neutrino Masses Evolution after the Critical Point

At the critical point, the total thermodynamic potential reaches its equilibrium and, therefore, has a minimum value, as a result of which the neutrinos acquire the mass. After this point, the mass of the neutrinos varies over time. The behavior of the neutrinos obeys the law of change of the matter depending on the scale factor, *i.e.*, the neutrinos energy density varies as, $\rho_\nu \propto a^{-3}$ for $a \geq a_{\rm cr}$.

The total potential, the energy density and the pressure for the interaction of the neutrinos and the scalar field are presented, respectively, as:

$$V_{\rm couple} = V_\phi + \phi\rho_{\rm cr}\left(\frac{a_{\rm cr}}{a}\right)^3, \tag{10.46}$$

$$\rho_{\rm couple} = \frac{\dot{\phi}^2}{2} + V_\phi + \phi\rho_{\rm cr}\left(\frac{a_{\rm cr}}{a}\right)^3, \tag{10.47}$$

$$p_{\rm couple} = \frac{\dot{\phi}^2}{2} - V_\phi - \phi\rho_{\rm cr}\left(\frac{a_{\rm cr}}{a}\right)^3. \tag{10.48}$$

The EoS for interaction of the neutrinos and the scalar field:

$$w_{\rm couple} \equiv \frac{p_{\rm couple}}{\rho_{\rm couple}} = \frac{\frac{\dot{\phi}^2}{2} - V_\phi - \phi\rho_{\rm cr}\left(\frac{a_{\rm cr}}{a}\right)^3}{\frac{\dot{\phi}^2}{2} + V_\phi + \phi\rho_{\rm cr}\left(\frac{a_{\rm cr}}{a}\right)^3}. \tag{10.49}$$

The matter energy density parameter, $\Omega_{\rm m}$, and the dark energy density parameter, Ω_ϕ, are defined, respectively, as:

$$\Omega_{\rm m}(a) = \frac{\Omega_{\rm m0}a^{-3}}{E^2(a)}, \tag{10.50}$$

$$\Omega_\phi(a) = \frac{\frac{\dot{\phi}^2}{2} + \frac{M_\phi^{\alpha+4}}{\phi^\alpha} + \phi\rho_{\rm cr}\left(\frac{a_{\rm cr}}{a}\right)^3}{E^2(a)\rho_{\rm cr0}}. \tag{10.51}$$

The first Friedmann's equation and the scalar field equation are represented, respectively, as:

$$H = H_0\left(\Omega_{\rm m0}a^{-3} + \frac{1}{\rho_{\rm cr0}}\left(V_\phi + \frac{\dot{\phi}^2}{2} + \phi\rho_{\rm cr}\left(\frac{a_{\rm cr}}{a}\right)^3\right)\right)^{1/2}, \tag{10.52}$$

$$\ddot{\phi} + 3H\dot{\phi} + \frac{\partial V_\phi}{\partial\phi} + \rho_{\rm cr}\left(\frac{a_{\rm cr}}{a}\right)^3 = 0. \tag{10.53}$$

The mass scale, M_ϕ, is calculated as:

$$M_\phi = (\nu^\alpha \rho_{\phi\nu})^{\frac{\alpha+1}{\alpha+4}} \Delta_{\rm cr}^{-\alpha} T_0^{\frac{-3\alpha}{\alpha+4}}, \tag{10.54}$$

where $\rho_{\phi\nu}$ is the energy density for the matter and the neutrinos-dark energy fluid at the present epoch; $\nu \approx \overline{\phi}_{\rm cr} = \frac{m_\nu(a_{\rm cr})}{T_{\rm cr}}$, where $\nu = \alpha + 5/2$, $m_\nu(a_{\rm cr})$ is the value of the sum of neutrino masses at the critical point, $T_{\rm cr}$ is the value of the neutrinos temperature at the critical point.

The value of the neutrinos energy density at the critical point is defined as:

$$\rho_{\rm cr} = M_\phi^3 \alpha \left(\frac{\nu_{\rm cr}}{\nu}\right)^{\alpha+1}, \tag{10.55}$$

where

$$\nu_{\rm cr} = \left(\frac{\sqrt{2}}{\alpha\pi^{3/2}} \nu^\nu \exp^{-\nu}\right)^{\frac{1}{\alpha+4}} \tag{10.56}$$

and

$$\Delta_{\rm cr} = \left(\frac{\sqrt{2}\nu^\nu e^{-\nu}}{\alpha\pi^{3/2}}\right)^{\frac{1}{\alpha+4}}. \tag{10.57}$$

10.5.3 Results

We numerically integrated Eq. (10.52) and Eq. (10.53). The results of these calculations are presented in Table 10.1 and in Fig. (10.3).

α	$a_{\rm cr}$	$m_\nu(a_{\rm cr})$ eV	$m_\nu(a_0)$ eV
10^{-5}	0.00440	0.13366	0.13541
10^{-4}	0.00240	0.23779	0.23853
10^{-3}	0.00140	0.42491	0.42525
10^{-2}	0.00070	0.79610	0.79636
10^{-1}	0.00020	2.44842	2.44891
0.2	0.00010	5.32040	5.32085
0.3	0.00006	10.57513	10.57546
0.4	0.00003	20.02527	20.02550
0.5	0.00002	36.60875	36.60890

Table 10.1: The value of the scale factor at the critical point, $a_{\rm cr}$, the value of the sum of neutrino masses at the critical point, $m_\nu(a_{\rm cr})$, the value of the sum of neutrino masses today, $m_\nu(a_0)$, depending on the value of the model parameter α.

In Table 10.1 we present the values of the scale factor at the critical point, $a_{\rm cr}$, the

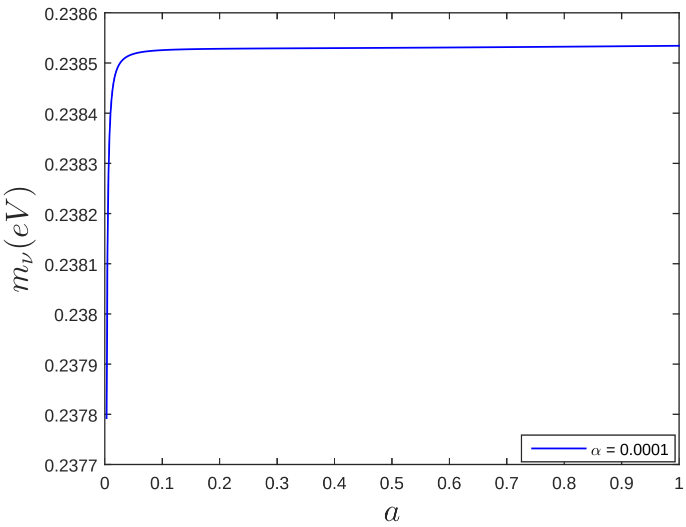

Figure 10.3: The evolution of the neutrino masses, m_ν, for the value of the parameter $\alpha = 0.0001$.

values of the sum of neutrino masses at the critical point, $m_\nu(a_{\rm cr})$, the values of the sum of neutrino masses today, $m_\nu(a_0)$, depending on the value of the model parameter, α. With an increase in the value of the model parameter, α, *i.e.*, with the strengthening of the scalar field potential: i) the value of the scale factor at the critical point, $a_{\rm cr}$, decreases, thus, the moment of the scalar and fermionic fields interaction occurs at the earlier time; ii) the value of the initial sum of neutrino masses and, accordingly, the final value of the sum of neutrino masses increases.

The evolution of the neutrino masses for the value of the model parameter $\alpha = 0.0001$ is shown in Fig. (10.3). The evolution of the matter energy density parameter, $\Omega_{\rm m}$, and the energy density parameter of the neutrinos-dark energy fluid, $\Omega_{\rm couple}$, for the value of the model parameter $\alpha = 0.0001$ is presented in Fig. (10.4) (left panel). The moment of the matter and dark energy equality occurs at the value of the scalar factor $a = 0.75$. The evolution of the EoS parameter in the interaction of the neutrinos and the scalar field for the value of the model parameter $\alpha = 0.0001$ is shown in Fig. (10.4) (right panel). With the given value of the model parameter α, the scalar field is very weak. Therefore, after reaching the critical point, the value of the EoS parameter tends to $w_{\rm couple} \approx -1$.

10.6 Conclusion

Studying the MaVaN model:

1. The analysis was carried out and the approximation was found for the possible values

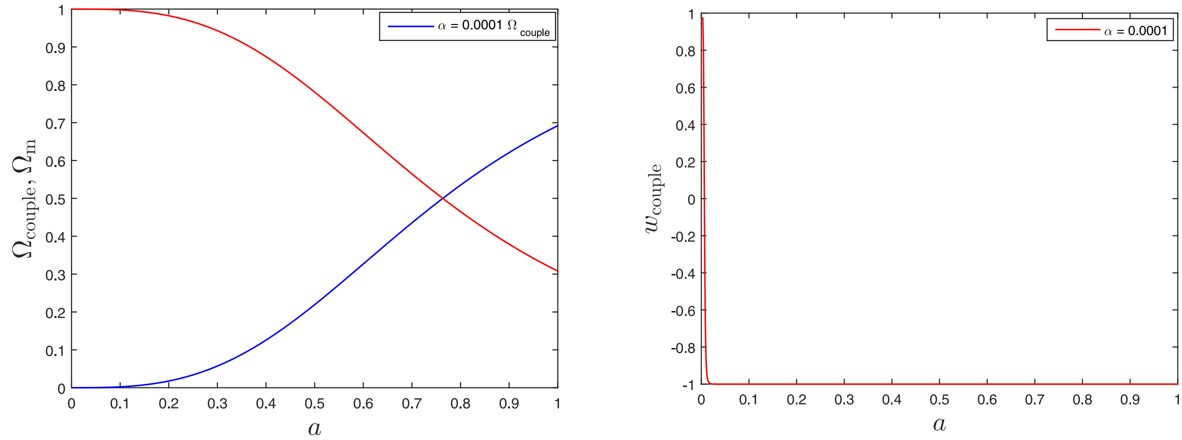

Figure 10.4: Left panel: the evolution of the matter energy density parameter, $\Omega_{\rm m}$, and the neutrinos-dark energy density parameter, $\Omega_{\rm couple}$, for the value of the model parameter, $\alpha = 0.0001$. Right panel: the EoS parameter, $w_{\rm couple}$(a), depending on the value of the scale factor for the value of the model parameter $\alpha = 0.0001$.

of the matter energy density parameter, the energy density parameter for the photons and the energy density parameter for the fluid, which consists of the neutrinos and dark energy.

2. The system of the differential equations, which describes the dynamics of the universe in the MaVaN model, were obtained: i) until the moment of the neutrinos interaction with the scalar field, ii) from the beginning of the neutrinos interaction with the scalar field to the present epoch.

3. We calculated the value of the scale factor and the value of the sum of neutrino masses at the critical point, as well as the value of the sum of neutrino masses at the present epoch depending on the value of the model parameter α of the Ratra-Peebles potential.

4. In our future research, we are going to test this model using various observational data.

Chapter 11

Conclusion

This thesis is devoted to the study of the scalar field ϕCDM models. The detailed description of these investigations is presented below.

I. We investigated the various properties of the Ratra-Peebles ϕCDM model compared to the ΛCDM model:

1. We studied the dynamics of the universe in the Ratra-Peebles ϕCDM model depending on the value of the model parameter α. An increase in the value of the parameter α causes a stronger time dependence of the scalar field, ϕ, its time derivative, $\dot{\phi}$, as well as the EoS parameter, w, and its derivative with respect to the scale factor, dw/da.

2. We found that the Ratra-Peebles ϕCDM model differs from the ΛCDM model in number of characteristics that do not depend on the value of the model parameter, α. These characteristics are generic to the class of the ϕCDM quintessence models of the freezing type:

   a) In the ϕCDM models, the expansion rate of the universe is always greater than the expansion rate in the ΛCDM model.

   b) The domination of the dark energy epoch in the ϕCDM models begins earlier than in the ΛCDM model (provided that the other cosmological model parameters are fixed).

   c) The Ratra-Peebles ϕCDM model and the ΛCDM model differ in their predictions for the growth rate of the matter density fluctuations in the universe: the ϕCDM model predicts a slower growth rate of the matter density fluctuations than in the ΛCDM model.

d) The value of the Linder γ-parametrization in the ϕCDM model increases with an increase in the value of the model parameter α. The value of the Linder γ-parametrization in the ϕCDM model is greater than in the ΛCDM model.

e) We defined the boundaries of the applicability for the Linder γ-parametrization in the Ratra-Peebles model, $z \in (0; 5)$. The applicability of the Linder γ-parametrization is terminated later in the ΛCDM model than in the ϕCDM model.

II. We constrained the Ω_{m} and α model parameters in the Ratra-Peebles ϕCDM scalar field model using various observations:

a) Applying only the observations of the growth rate function, there is a strong degeneracy between the model parameters Ω_{m} and α. It means that with an increase in the value of the parameter Ω_{m}, the larger values of α parameter are allowed. In this case, it is impossible to find a constraint on the value of the parameter α.

b) The degeneracy is eliminated after combining the constraints on the observations of the growth rate function, the constraints on the distance-redshift ratio of the BAO observations and prior distance from CMBR.

c) As a result, we obtained the constraints on the model parameters in the Ratra-Peebles ϕCDM scalar field model: $\Omega_{\mathrm{m}} = 0.30 \pm 0.04$ and $0 \leq \alpha \leq 1.30$ at 1σ confidence level. The best fit value for the model parameter α is $\alpha = 0.00$.

III. We studied the scalar field ϕCDM models: ten quintessence models and seven phantom models:

1. We reconstructed these models using the phenomenological method developed by us. Resulting in, for each potential the following ranges were found: i) the model parameters, ii) the EoS parameters, iii) the initial conditions for differential equations, which describe the dynamics of the universe.

2. Using the MCMC analysis, we obtained the constraints on the scalar field models by comparing the observations for: the expansion rate of the universe, the angular diameter distance and the growth rate function with the corresponding data, generated for the fiducial ΛCDM model.

3. We applied the Bayes statistical criteria to compare the scalar field models. To this end, we calculated the Bayes factor, as well as the AIC and BIC information criteria.

The results of this analysis showed that the DESI data cannot uniquely distinguish between the scalar field models under the assumption and that the ΛCDM model is a true dark energy model.

4. We investigated the scalar field models in the $w_0 - w_a$ phase space of the CPL-ΛCDM contours. We identified the subclasses of the quintessence and the phantom scalar field models, which at the present epoch: i) can be distinguishable from the ΛCDM model, ii) cannot be distinguishable from the ΛCDM model, iii) can be either distinguishable or indistinguishable from the ΛCDM model.

5. Moreover, we found that all the studied models can be divided into two classes: the models that have the attractor solutions and the models whose evolution depends on the initial conditions.

IV. Investigating the MaVaN model:

1. The analysis was carried out and the approximation was found for the possible values of the matter energy density parameter, the energy density parameter for the photons and the energy density parameter for the fluid, which consists of the neutrinos and dark energy.

2. The differential equations, which describe the dynamics of the universe for the MaVaN model, were obtained: i) until the moment of the neutrinos interaction with the scalar field, ii) from the beginning of the neutrinos interaction with the scalar field to the present epoch.

3. The value of the scale factor and the value of the sum of neutrino masses at the critical point, as well as the value of the sum of neutrino masses at the present epoch were calculated depending on the value of the model parameter α in the Ratra-Peebles potential.

Chapter 12

Future Projects

The future projects include:

1. The study of the neutrinos influence on the large-scale structure formation of the universe in the MaVaN model. The investigation of the neutrinos clustering in the MaVaN model in the interaction of the neutrinos with the scalar field.

2. The investigation of the non-flat inflationary ϕCDM scalar field models, Refs. (Ratra & Peebles (1995), Ratra (2017)). Carrying out the Fisher matrix analysis and more advanced Dali matrix analysis to study these models.

3. The exploration of the modified gravity models.

4. The investigation of the large-scale structure of the universe in the modified gravity models.

Bibliography

2dFGRS (2002), 'http://www.mso.anu.edu.au/2dfgrs/'.

Adam, R. et al. (2016), 'Planck intermediate results. XXX. The angular power spectrum of polarized dust emission at intermediate and high Galactic latitudes', *Astron. Astrophys.* **586**, A133.

Ade, P. A. R. et al. (2014*a*), 'BICEP2 II: Experiment and Three-Year Data Set', *Astrophys. J.* **792**(1), 62.

Ade, P. A. R. et al. (2014*b*), 'Planck 2013 results. I. Overview of products and scientific results', *Astron. Astrophys.* **571**, A1.

Ade, P. A. R. et al. (2014*c*), 'Planck 2013 results. XVI. Cosmological parameters', *Astron. Astrophys.* **571**, A16.

Ade, P. A. R. et al. (2016), 'Planck 2015 results. XIII. Cosmological parameters', *Astron. Astrophys.* **594**, A13.

Afshordi, N., Zaldarriaga, M. & Kohri, K. (2005), 'On the stability of dark energy with mass-varying neutrinos', *Phys. Rev.* **D72**, 065024.

Aghamousa, A. et al. (2016), 'The DESI Experiment Part I: Science,Targeting, and Survey Design', **arXiv: 1611.00036**.

Akaike, H. (1974), 'A new look at the statistical model identificatio', *IEEE Transactions on Automatic Control* **19**(06), 716–723.

Albrecht, A. & Skordis, C. (2000), 'Phenomenology of a realistic accelerating universe using only Planck scale physics', *Phys. Rev. Lett.* **84**, 2076–2079.

Alpher, R. A. & Herman, R. C. (1948*a*), 'Evolution of the Universe. Nature', *Nature* **162**.

Alpher, R. A. & Herman, R. C. (1948*b*), 'On the Relative Abundance of the Elements', *Phys.Rev.* **74**.

Amendola, L. (2000), 'Coupled quintessence', *Phys. Rev.* **D62**, 043511.

Amendola, L. et al. (2013), 'Cosmology and fundamental physics with the Euclid satellite', *Living Rev. Rel.* **16**.

Arfken, G. B. (1985), *Mathematical methods for physicists*, Academic Press, San Diego, California.

Arkani-Hamed, N., Dimopoulos, S. & Dvali, G. R. (1998), 'The Hierarchy problem and new dimensions at a millimeter', *Phys. Lett.* **B429**, 263–272.

Armendariz-Picon, C., Damour, T. & Mukhanov, V. F. (1999), 'k - inflation', *Phys. Lett.* **B458**, 209–218.

Armendariz-Picon, C., Mukhanov, V. F. & Steinhardt, P. J. (2000), 'A Dynamical solution to the problem of a small cosmological constant and late time cosmic acceleration', *Phys. Rev. Lett.* **85**, 4438–4441.

Armendariz-Picon, C., Mukhanov, V. F. & Steinhardt, P. J. (2001), 'Essentials of k essence', *Phys. Rev.* **D63**, 103510.

Avsajanishvili, O., Arkhipova, N. A., Samushia, L. & Kahniashvili, T. (2014), 'Growth Rate in the Dynamical Dark Energy Models', *Eur. Phys. J.* **C74**(11), 3127.

Avsajanishvili, O., Huang, Y., Samushia, L. & Kahniashvili, T. (2018), 'The observational constraints on the flat ϕCDM models', *Eur. Phys. J.* **C78**(9), 773.

Avsajanishvili, O., Samushia, L., Arkhipova, N. A. & Kahniashvili, T. (2017), 'Testing Dark Energy Models through Large Scale Structure', *AApTr* **30**(01), 95–114.

Bag, S., Mishra, S. S. & Sahni, V. (2017), 'New tracker models of dark energy', **arXiv:1709.09193**.

Bahamonde, S., Böhmer, C. G., Carloni, S., Copeland, E. J., Fang, W. & Tamanini, N. (2017), 'Dynamical systems applied to cosmology: dark energy and modified gravity', **arXiv:1712.03107**.

Barger, V., Gao, Y. & Marfatia, D. (2007), 'Accelerating cosmologies tested by distance measures', *Phys. Lett.* **B648**, 127–132.

Barreiro, T., Copeland, E. J. & Nunes, N. J. (2000), 'Quintessence arising from exponential potentials', *Phys. Rev.* **D61**, 127301.

Barrow, J. D. & Tipler, F. J. (1988), *The Anthropic Cosmological Principle*, Oxford U. Pr., Oxford.

Begeman, K. G., Broeils, A. H. & Sanders, R. H. (1991), 'Extended rotation curves of spiral galaxies: Dark haloes and modified dynamics', *Mon. Not. Roy. Astron. Soc.* **249**, 523.

Bennett, C. L., Banday, A., Gorski, K. M., Hinshaw, G., Jackson, P., Keegstra, P., Kogut, A., Smoot, G. F., Wilkinson, D. T. & Wright, E. L. (1996), 'Four year COBE DMR cosmic microwave background observations: Maps and basic results', *Astrophys. J.* **464**, L1–L4.

Bento, M. C., Bertolami, O. & Sen, A. A. (2002), 'Generalized Chaplygin gas, accelerated expansion and dark energy matter unification', *Phys. Rev.* **D66**, 043507.

Betoule, M. et al. (2014), 'Improved cosmological constraints from a joint analysis of the SDSS-II and SNLS supernova samples', *Astron. Astrophys.* **568**, A22.

Blumenthal, G. R., Faber, S. M., Primack, J. R. & Rees, M. J. (1984), 'Formation of Galaxies and Large Scale Structure with Cold Dark Matter', *Nature* **311**, 517–525.

Bondi, H. (1947), 'Spherically symmetrical models in general relativity', *Mon. Not. Roy. Astron. Soc.* **107**, 410–425.

Brans, C. & Dicke, R. H. (1961), 'Mach's principle and a relativistic theory of gravitation', *Phys. Rev.* **124**, 925–935.

Brax, P. & Martin, J. (1999), 'Quintessence and supergravity', *Phys. Lett.* **B468**, 40–45.

Brax, P. & Martin, J. (2002), 'Quintessence and the accelerating universe', **arXiv:astro-ph/0210533**.

Brown, A. G. A. et al. (2018), 'Gaia Data Release 2', *Astron. Astrophys.* **616**, A1.

Buchalter, A., Helfand, D. J., Becker, R. H. & White, R. L. (1998), 'Constraining ω_0 with the angular-size redshift relation of double-lobed quasars in the first survey', *Astrophys. J.* **494**, 503.

Cai, Y.-F., Saridakis, E. N., Setare, M. R. & Xia, J.-Q. (2010), 'Quintom Cosmology: Theoretical implications and observations', *Phys. Rept.* **493**, 1–60.

Caldwell, R. R. (2002), 'A Phantom menace?', *Phys. Lett.* **B545**, 23–29.

Caldwell, R. R. & Kamionkowski, M. (2009), 'The Physics of Cosmic Acceleration', *Ann. Rev. Nucl. Part. Sci.* **59**, 397–429.

Caldwell, R. R., Kamionkowski, M. & Weinberg, N. N. (2003), 'Phantom energy and cosmic doomsday', *Phys. Rev. Lett.* **91**, 071301.

Caldwell, R. R. & Linder, E. V. (2005), 'The Limits of quintessence', *Phys. Rev. Lett.* **95**.

Capozziello, S., Carloni, S. & Troisi, A. (2003), 'Quintessence without scalar fields', *Recent Res. Dev. Astron. Astrophys.* **1**, 625.

Carroll, B. W. & Ostlie, D. A. (2007), *An Introduction to modern Astrophysics*, San Francisco, Addison-Wesley.

Carroll, S. M. (2001), 'The Cosmological constant', *Living Rev. Rel.* **4**, 1.

Carroll, S. M. (2004), *Spacetime and Geometry: An introduction to general relativity*, Addison-Wesley, San Francisco.

Carroll, S. M., Duvvuri, V., Trodden, M. & Turner, M. S. (2004), 'Is cosmic speed - up due to new gravitational physics?', *Phys. Rev.* **D70**, 043528.

Carroll, S. M., Press, W. H. & Turner, E. L. (1992), 'The cosmological constant', *Annu. Rev. Astro. Astrophys.* **30**, 499–542.

Casimir, H. B. G. (1948), 'On the Attraction Between Two Perfectly Conducting Plates', *Indag. Math.* **10**, 261–263.

Chang, H.-Y. & Scherrer, R. J. (2016), 'Reviving Quintessence with an Exponential Potential', **arXiv:1608.03291**.

Chevallier, M. & Polarski, D. (2001), 'Accelerating universes with scaling dark matter', *Int. J. Mod. Phys.* **D10**, 213–224.

Chiba, T., De Felice, A. & Tsujikawa, S. (2013), 'Observational constraints on quintessence: thawing, tracker, and scaling models', *Phys. Rev.* **D87**(8), 083505.

Chitov, G. Y., August, T., Natarajan, A. & Kahniashvili, T. (2011), 'Mass Varying Neutrinos, Quintessence, and the Accelerating Expansion of the Universe', *Phys. Rev.* **D83**, 045033.

Coe, D. (2009), 'Fisher Matrices and Confidence Ellipses: A Quick-Start Guide and Software', **arXiv:0906.4123**.

Colless, M. et al. (2003), 'The 2dF Galaxy Redshift Survey: Final data release', **arXiv:astro-ph/0306581**.

Cooray, A., Hu, W., Huterer, D. & Joffre, M. (2001), 'Measuring angular diameter distances through halo clustering', *Astrophys. J.* **557**, L7.

Copeland, E. J., Sami, M. & Tsujikawa, S. (2006*a*), 'Dynamics of dark energy', *Int. J. Mod. Phys.* **D15**, 1753–1936.

Copeland, E. J., Sami, M. & Tsujikawa, S. (2006*b*), 'Dynamics of dark energy', *Int. J. Mod. Phys.* **D15**, 1753–1936.

de Rham, C. & Gabadadze, G. (2010), 'Generalization of the Fierz-Pauli Action', *Phys. Rev.* **D82**, 044020.

de Rham, C., Gabadadze, G. & Tolley, A. J. (2011), 'Resummation of Massive Gravity', *Phys. Rev. Lett.* **106**, 231101.

de Rham, C., Hofmann, S., Khoury, J. & Tolley, A. J. (2008), 'Cascading Gravity and Degravitation', *JCAP* **0802**, 011.

Dodelson, S. (2003), *Modern cosmology*, Academic Press. ISBN, Amsterdam.

Dodelson, S. et al. (2009), 'The Origin of the Universe as Revealed Through the Polarization of the Cosmic Microwave Background', **arXiv:0902.3796**.

Dubrovin, V., Novikov, V. & Fomenko, A. (1979), *Sovremennaia geometria (In Russian)*, Nauka, Moskva.

Durrer, R., Kahniashvili, T. & Yates, A. (1998), 'Microwave background anisotropies from Alfven waves', *Phys. Rev.* **D58**, 123004.

Dutta, S. & Scherrer, R. J. (2009), 'Dark Energy from a Phantom Field Near a Local Potential Minimum', *Phys. Lett.* **B676**, 12–15.

Dvali, G., Gabadadze, G. & Shifman, M. (2003), 'Diluting cosmological constant in infinite volume extra dimensions', *Phys. Rev.* **D67**, 044020.

Dvali, G. R., Gabadadze, G. & Porrati, M. (2000), '4-D gravity on a brane in 5-D Minkowski space', *Phys. Lett.* **B485**, 208–214.

Dvali, G. R., Shafi, Q. & Solganik, S. (2001), D-brane inflation, *in* '4th European Meeting From the Planck Scale to the Electroweak Scale (Planck 2001) La Londe les Maures, Toulon, France, May 11-16, 2001'.

Einstein, A. (1915*a*), 'On the General Theory of Relativity', *Sitzungsber. Preuss. Akad. Wiss. Berlin (Math. Phys.)* **1915**, 778–786.

Einstein, A. (1915*b*), 'The Field Equations of Gravitation', *Sitzungsber. Preuss. Akad. Wiss. Berlin (Math. Phys.)* **1915**, 844–847.

Einstein, A. (1917), 'Cosmological Considerations in the General Theory of Relativity', *Sitzungsber. Preuss. Akad. Wiss. Berlin (Math. Phys.)* **1917**, 142–152.

Eisenstein, D. J. et al. (2005), 'Detection of the Baryon Acoustic Peak in the Large-Scale Correlation Function of SDSS Luminous Red Galaxies', *Astrophys. J.* **633**, 560–574.

Elizalde, E., Nojiri, S. & Odintsov, S. D. (2004), 'Late-time cosmology in (phantom) scalar-tensor theory: Dark energy and the cosmic speed-up', *Phys. Rev.* **D70**, 043539.

Fardon, R., Nelson, A. E. & Weiner, N. (2004), 'Dark energy from mass varying neutrinos', *JCAP* **0410**, 005.

Farooq, M. O. (2013), 'Observational constraints on dark energy cosmological model parameters', *PhD thesis, Kansas State U.,* **arXiv:1309.3710**.

Farrar, G. R. & Peebles, P. J. E. (2004), 'Interacting dark matter and dark energy', *Astrophys. J.* **604**, 1–11.

Ferreira, P. G. & Joyce, M. (1998), 'Cosmology with a primordial scaling field', *Phys. Rev.* **D58**, 023503.

Fierz, M. & Pauli, W. (1939), 'On relativistic wave equations for particles of arbitrary spin in an electromagnetic field', *Proc. Roy. Soc. Lond.* **A173**, 211–232.

Font-Ribera, A., McDonald, P., Mostek, N., Reid, B. A., Seo, H.-J. & Slosar, A. (2014), 'DESI and other dark energy experiments in the era of neutrino mass measurements', *JCAP* **1405**, 023.

Frampton, P. H., Ludwick, K. J. & Scherrer, R. J. (2011), 'The Little Rip', *Phys. Rev.* **D84**, 063003.

Frampton, P. H., Ludwick, K. J. & Scherrer, R. J. (2012), 'Pseudo-rip: Cosmological models intermediate between the cosmological constant and the little rip', *Phys. Rev.* **D85**, 083001.

Freedman, W. L., Madore, B. F., Scowcroft, V., Burns, C., Monson, A., Persson, S. E., Seibert, M. & Rigby, J. (2012), 'Carnegie Hubble Program: A Mid-infrared Calibration of the Hubble Constant', *Astron. Astrophys.* **758**, 024.

Freedman, W. L. et al. (2001), 'Final results from the Hubble Space Telescope key project to measure the Hubble constant', *Astrophys. J.* **553**, 47–72.

Frieman, J. A., Hill, C. T., Stebbins, A. & Waga, I. (1995), 'Cosmology with ultralight pseudo Nambu-Goldstone bosons', *Phys. Rev. Lett.* **75**, 2077–2080.

Frieman, J., Turner, M. & Huterer, D. (2008), 'Dark Energy and the Accelerating Universe', *Ann. Rev. Astron. Astrophys.* **46**, 385–432.

Gabadadze, G. (2007), 'Cargese lectures on brane induced gravity', *Nucl. Phys. Proc. Suppl.* **171**, 88–98.

Gaia (2013), 'http://sci.esa.int/gaia/'.

Galaverni, M., Gubitosi, G., Paci, F. & Finelli, F. (2015), 'Cosmological birefringence constraints from CMB and astrophysical polarization data', *JCAP* **1508**(08), 031.

Gamov, G. (1946), 'Expanding Universe and the Origin of Elements"', *Physical Review* **70**.

Gamov, G. (1956), 'The evolutionary universe', *Scientific American* **195**.

Gawiser, E. & Silk, J. (2000), 'The Cosmic microwave background radiation', *Phys. Rept.* **333**, 245–267.

Giostri, R., Vargas dos Santos, M., Waga, I., Reis, R. R. R., Calvão, M. O. & Lago, B. L. (2012), 'From cosmic deceleration to acceleration: new constraints from SN Ia and BAO/CMB', *JCAP* **3**, 027.

Gmurman, B. (2003), *Teoria veroiatnosti i matematicheskaia statistika (In Russian)*, Vysshaia shkola, Moskva.

Gorbunov, D. S. & Rubakov, V. A. (2011), *Introduction to the theory of the early universe: Cosmological perturbations and inflationary theory*, World Scientific, Hackensack, USA.

Gupta, G., Sen, S. & Sen, A. A. (2012), 'GCG Parametrization for Growth Function and Current Constraints', *JCAP* **1204**, 028.

Hanson, D. et al. (2013), 'Detection of B-mode Polarization in the Cosmic Microwave Background with Data from the South Pole Telescope', *Phys. Rev. Lett.* **111**(14), 141301.

Hassan, S. F. & Rosen, R. A. (2012), 'Bimetric Gravity from Ghost-free Massive Gravity', *JHEP* **02**, 126.

Heitmann, K., Higdon, D., Nakhleh, C. & Habib, S. (2006), 'Cosmic Calibration', *Astrophys. J.* **646**, L1–L4.

Hinshaw, G. et al. (2009), 'Five-Year Wilkinson Microwave Anisotropy Probe (WMAP) Observations: Data Processing, Sky Maps, and Basic Results', *Astrophys. J. Suppl.* **180**, 225–245.

Hinshaw, G. et al. (2013), 'Nine-Year Wilkinson Microwave Anisotropy Probe (WMAP) Observations: Cosmological Parameter Results', *Astrophys. J. Suppl.* **208**, 19.

Howard, R. A. (1971), *Dynamic Probabilistic Systems*, Vol.1, New York: John Wiley and Sons.

Hu, W. & Dodelson, S. (2002), 'Cosmic microwave background anisotropies', *Ann. Rev. Astron. Astrophys.* **40**, 171–216.

Hu, W. & Okamoto, T. (2002), 'Mass reconstruction with cmb polarization', *Astrophys. J.* **574**, 566–574.

Hu, W., Scott, D., Sugiyama, N. & White, M. J. (1995), 'The Effect of physical assumptions on the calculation of microwave background anisotropies', *Phys. Rev.* **D52**, 5498–5515.

Hu, W. T. (1995), Wandering in the Background: A CMB Explorer, PhD thesis.

Hu, W. & White, M. J. (1997), 'CMB anisotropies: Total angular momentum method', *Phys. Rev.* **D56**, 596–615.

Hubble, E. (1929), 'A relation between distance and radial velocity among extra-galactic nebulae', *Proc. Nat. Acad. Sci.* **15**, 168–173.

Jeans, J. H. (1902), 'The Stability of a Spherical Nebula', *Philosophical Transactions of the Royal Society of London* **199**.

Kahniashvili, T. & Ratra, B. (2005), 'Effects of Cosmological Magnetic Helicity on the Cosmic Microwave Background', *Phys. Rev.* **D71**, 103006.

Kamenshchik, A. Yu., Moschella, U. & Pasquier, V. (2001), 'An Alternative to quintessence', *Phys. Lett.* **B511**, 265–268.

Kamionkowski, M. & Kosowsky, A. (1998), 'Detectability of inflationary gravitational waves with microwave background polarization', *Phys. Rev.* **D57**, 685–691.

Kaplinghat, M. & Rajaraman, A. (2007), 'Stable models of super-acceleration', *Phys. Rev.* **D75**, 103504.

Khoury, J. & Wyman, M. (2009), 'N-Body Simulations of DGP and Degravitation Theories', *Phys. Rev.* **D80**, 064023.

Kim, A. G., Linder, E. V., Miquel, R. & Mostek, N. (2004), 'Effects of systematic uncertainties on the supernova determination of cosmologial parameters', *Mon. Not. Roy. Astron. Soc.* **347**, 909–920.

Komatsu, E. et al. (2011), 'Seven-Year Wilkinson Microwave Anisotropy Probe (WMAP) Observations: Cosmological Interpretation', *Astrophys. J. Suppl.* **192**, 18.

Kosowsky, A. (1996), 'Cosmic microwave background polarization', *Annals Phys.* **246**, 49–85.

Kosowsky, A. (1999), 'Introduction to microwave background polarization', *New Astron. Rev.* **43**.

Kosowsky, A. (2001), 'The cosmic microwave background', **arXiv:astro-ph/0102402**.

Kowalski, M. et al. (2008), 'Improved Cosmological Constraints from New, Old and Combined Supernova Datasets', *Astrophys. J.* **686**, 749–778.

Landau, L. & Lifshitz, E. (1971), *The classical theory of fields*, Pergamon Press Ltd., Headington Hill Hall, Oxford.

Leitch, E. M., Carlstrom, J. E., Halverson, N. W., Kovac, J., Pryke, C., Holzapfel, W. L. & Dragovan, M. (2002), 'First season observations with the Degree Angular Scale Interferometer (DASI)', *AIP Conf. Proc.* **616**(1), 65.

Lemaitre, G. (1933), 'The expanding universe', *Annales Soc. Sci. Bruxelles* **A53**, 51.

Lemaître, G. (1927), 'Un Univers homogene de masse constante et de rayon croissant rendant compte de la vitesse radiale des nebuleuses extra-galactiques', *Annales de la Societe Scientifique de Bruxelles* **47**, 49.

Lepora, N. F. (1998), 'Cosmological birefringence and the microwave background', **arXiv:gr-qc/9812077**.

Levi, M. et al. (2013), 'The DESI Experiment, a whitepaper for Snowmass 2013', **arXiv: 1308.0847**.

Lewis, A. (2004), 'CMB anisotropies from primordial inhomogeneous magnetic fields', *Phys. Rev.* **D70**, 043011.

Lifshitz, E. M. (1946), 'On the gravitational stability of the expanding universe', *J. Phys. (USSR)* **16**.

Lima, N. A., Liddle, A. R., Sahlén, M. & Parkinson, D. (2015), 'Reconstructing thawing quintessence with multiple datasets', **arXiv:1501.02678**.

Linder, E. V. (2003), 'Exploring the expansion history of the universe', *Phys. Rev. Lett.* **90**, 091301.

Linder, E. V. (2005), 'Cosmic growth history and expansion history', *Phys. Rev.* **D72**, 043529.

Linder, E. V. (2008), 'The Dynamics of Quintessence, The Quintessence of Dynamics', *Gen. Rel. Grav.* **40**, 329–356.

Linder, E. V. (2015), 'Quintessence's last stand?', *Phys. Rev.* **D91**, 063006.

Linder, E. V. & Cahn, R. N. (2007), 'Parameterized Beyond-Einstein Growth', *Astropart. Phys.* **28**, 481–488.

Lucchin, F. & Matarrese, S. (1985), 'Power-law inflation', *Phys. Rev.* **D32**, 1316–1322.

Ludwick, K. J. (2017), 'The Viability of Phantom Dark Energy: A Brief Review', *Mod. Phys. Lett.* **A32**(28), 1730025.

Martin, J. (2012), 'Everything You Always Wanted To Know About The Cosmological Constant Problem (But Were Afraid To Ask)', *Comptes Rendus Physique* **13**, 566–665.

Mather, J. C., Fixsen, D. J., Shafer, R. A., Mosier, C. & Wilkinson, D. T. (1999), 'Calibrator design for the COBE far infrared absolute spectrophotometer (FIRAS)', *Astrophys. J.* **512**, 511–520.

Mather, J. C. et al. (1994), 'Measurement of the Cosmic Microwave Background spectrum by the COBE FIRAS instrument', *Astrophys. J.* **420**, 439–444.

Mercuri, S. (2009), 'Introduction to Loop Quantum Gravity', *PoS* **ISFTG**, 016.

Mishra, P. & Singh, T. P. (2013), 'Fourth order gravity, scalar-tensor-vector gravity, and galaxy rotation curves', *Phys. Rev.* **D88**(10), 104036.

Misner, C. W., Thorne, K. S. & Wheeler, J. A. (1973), *Gravitation*, W. H. Freeman, San Francisco.

Moffat, J. W. (2006), 'Scalar-tensor-vector gravity theory', *JCAP* **0603**, 004.

Mukhanov, V. (2005), *Physical foundations of cosmology*, Cambridge University Press, The Edinburgh Building, Cambridge.

Nicolis, A., Rattazzi, R. & Trincherini, E. (2009), 'The Galileon as a local modification of gravity', *Phys. Rev.* **D79**, 064036.

Nojiri, S. & Odintsov, S. D. (2003), 'Modified gravity with negative and positive powers of the curvature: Unification of the inflation and of the cosmic acceleration', *Phys. Rev.* **D68**, 123512.

Nojiri, S. & Odintsov, S. D. (2006), 'Introduction to modified gravity and gravitational alternative for dark energy', *eConf* **C0602061**, 06.

Nojiri, S., Odintsov, S. D. & Tsujikawa, S. (2005), 'Properties of singularities in (phantom) dark energy universe', *Phys. Rev.* **D71**, 063004.

Nolta, M. R. et al. (2009), 'Five-Year Wilkinson Microwave Anisotropy Probe (WMAP) Observations: Angular Power Spectra', *Astrophys. J. Suppl.* **180**, 296–305.

Novosyadlyj, B., Sergijenko, O., Durrer, R. & Pelykh, V. (2013), 'Quintessence versus phantom dark energy: the arbitrating power of current and future observations', *JCAP* **1306**, 042.

Okun, L. B. (1988), *Elementary particle physics (In Russian)*, Nauka, Moskva.

Pace, F., Waizmann, J.-C. & Bartelmann, M. (2010), 'Spherical collapse model in dark-energy cosmologies', *MNRAS* **406**, 1865–1874.

Padilla, A. (2015), 'Lectures on the Cosmological Constant Problem', **arXiv:1502.05296**.

Padmanabhan, T. (2003), 'Cosmological constant: The Weight of the vacuum', *Phys. Rept.* **380**, 235–320.

Peebles, P. J. E. (1966), 'Primordial Helium Abundance and the Primordial Fireball. 2', *Astrophys. J.* **146**, 542–552.

Peebles, P. J. E. (1968), 'Recombination of the Primeval Plasma', *Astrophys. J.* **153**, 1.

Peebles, P. J. E. (1994), *Principles of physical cosmology*, Univ. Pr., Princeton, USA.

Peebles, P. J. E. & Ratra, B. (2003), 'The Cosmological constant and dark energy', *Rev. Mod. Phys.* **75**, 559–606.

Penzias, A. A. & Wilson, R. W. (1965), 'A measurement of excess antenna temperature at $\lambda = 7.3$ cm', *Astrophys. J.* **142**.

Percival, W. J., Cole, S., Eisenstein, D. J., Nichol, R. C., Peacock, J. A., Pope, A. C. & Szalay, A. S. (2007), 'Measuring the Baryon Acoustic Oscillation scale using the SDSS and 2dFGRS', *Mon. Not. Roy. Astron. Soc.* **381**, 1053–1066.

Perlmutter, S. et al. (1999), 'Measurements of Omega and Lambda from 42 high redshift supernovae', *Astrophys. J.* **517**, 565–586.

Pogson, N. R. (1857), 'Magnitudes of Thirty-six of the Minor Planets for the first day of each month of the year 1857', *Mon. Not. Roy. Astron. Soc.* **17**.

Polchinski, J. (2007*a*), *String theory. Vol. 1: An introduction to the bosonic string*, Cambridge Monographs on Mathematical Physics, Cambridge University Press.

Polchinski, J. (2007*b*), *String theory. Vol. 2: Superstring theory and beyond*, Cambridge Monographs on Mathematical Physics, Cambridge University Press.

Pouri, A., Basilakos, S. & Plionis, M. (2014), 'Precision growth index using the clustering of cosmic structures and growth data', *JCAP* **1408**, 042.

Rakhi, R. & Indulekha, K. (2009), 'Dark Energy and Tracker Solution: A Review', **arXiv: 0910.5406**.

Ratra, B. (2017), 'Inflation in a closed universe', *Phys. Rev.* **D96**(10), 103534.

Ratra, B. & Peebles, P. J. E. (1988*a*), 'Cosmological Consequences of a Rolling Homogeneous Scalar Field', *Phys. Rev.* **D37**, 3406.

Ratra, B. & Peebles, P. J. E. (1988*b*), 'Cosmology with a time-variable cosmological constant', *Astrophys. J.* **325**, L17–L20.

Ratra, B. & Peebles, P. J. E. (1995), 'Inflation in an open universe', *Phys. Rev.* **D52**, 1837–1894.

Riess, A. G. et al. (1998), 'Observational evidence from supernovae for an accelerating universe and a cosmological constant', *Astron. J.* **116**, 1009–1038.

Riess, A. G. et al. (2007), 'New Hubble Space Telescope Discoveries of Type Ia Supernovae at $z \geq 1$: Narrowing Constraints on the Early Behavior of Dark Energy', *Astrophys. J.* **659**, 98–121.

Rubakov, V. A. (2014), Cosmology, *in* 'Proceedings, 2011 European School of High-Energy Physics (ESHEP 2011): Cheile Gradistei, Romania, September 7-20, 2011', pp. 151–195.

Rubakov, V. A. & Gorbunov, D. S. (2017), *Introduction to the Theory of the Early Universe*, World Scientific, Singapore.

Rubin, V. C., Thonnard, N. & Ford, Jr., W. K. (1980), 'Rotational properties of 21 SC galaxies with a large range of luminosities and radii, from NGC 4605 /R = 4kpc/ to UGC 2885 /R = 122 kpc/', *Astrophys. J.* **238**.

Ryan, J., Chen, Y. & Ratra, B. (2019), 'Baryon acoustic oscillation, Hubble parameter, and angular size measurement constraints on the Hubble constant, dark energy dynamics, and spatial curvature', **arXiv:1902.03196**.

Sachs, R. K. & Wolfe, A. M. (1967), 'Perturbations of a cosmological model and angular variations of the microwave background', *Astrophys. J.* **147**, 73–90.

Sahni, V. & Wang, L.-M. (2000), ‘A New cosmological model of quintessence and dark matter’, *Phys. Rev.* **D62**, 103517.

Samushia, L. (2009), ‘Constraining scalar field dark energy with cosmological observations’, *PhD thesis, Kansas State U.,* **arXiv:0908.4597**.

Scherrer, R. J. (2004), ‘Purely kinetic k-essence as unified dark matter’, *Phys. Rev. Lett.* **93**, 011301.

Scherrer, R. J. & Sen, A. A. (2008*a*), ‘Phantom Dark Energy Models with a Nearly Flat Potential’, *Phys. Rev.* **D78**, 067303.

Scherrer, R. J. & Sen, A. A. (2008*b*), ‘Thawing quintessence with a nearly flat potential’, *Phys. Rev.* **D77**, 083515.

Schimd, C., Tereno, I., Uzan, J.-P., Mellier, Y., van Waerbeke, L., Semboloni, E., Hoekstra, H., Fu, L. & Riazuelo, A. (2007), ‘Tracking quintessence by cosmic shear - constraints from virmos-descart and cfhtls and future prospects’, *Astron. Astrophys.* **463**, 405–421.

Schmidt, B. P. et al. (1998), ‘The High Z supernova search: Measuring cosmic deceleration and global curvature of the universe using type Ia supernovae’, *Astrophys. J.* **507**, 46–63.

Schneider, P. (2006), *Extragalactic Astronomy and Cosmology*, Springer-Verlag Berlin Heidelberg, Bonn, Germany.

Schwarz, G. E. (1978), ‘Estimating the dimension of a model’, *Annals of Statistics* **06**(02), 461–464.

Scott, D. & Smoot, G. F. (2010), ‘Cosmic Microwave Background Mini-review’, **arXiv:1005.0555**.

SDSS (2017), ‘http://www.sdss.org/’.

Shifman, M. (2010), ‘Large Extra Dimensions: Becoming acquainted with an alternative paradigm’, *Int. J. Mod. Phys.* **A25**, 199–225.

Silk, J. (1968), ‘Cosmic black body radiation and galaxy formation’, *Astrophys. J.* **151**, 459–471.

Smoot, G. F. & Scott, D. (1997), ‘The cosmic background radiation’, *Rev. Part. Properties,* **arXiv:astro-ph/9711069**.

Spergel, D. et al. (2015), 'Wide-Field InfrarRed Survey Telescope-Astrophysics Focused Telescope Assets WFIRST-AFTA 2015 Report', **arXiv:1503.03757**.

Steinhardt, P. J., Wang, L.-M. & Zlatev, I. (1999), 'Cosmological tracking solutions', *Phys. Rev.* **D59**, 123504.

Sunyaev, R. A. & Zeldovich, Ya. B. (1970), 'Small scale fluctuations of relic radiation', *Astrophys. Space Sci.* **7**, 3–19.

Suzuki, N. et al. (2012), 'The Hubble Space Telescope Cluster Supernova Survey: V. Improving the Dark Energy Constraints Above $z > 1$ and Building an Early-Type-Hosted Supernova Sample', *Astrophys. J.* **746**, 85.

Taddei, L. & Amendola, L. (2015), 'A cosmological exclusion plot: Towards model-independent constraints on modified gravity from current and future growth rate data', *JCAP* **1502**(02), 001.

Takahashi, R. & Tanimoto, M. (2007), 'Dark energy and neutrino model in SUSY: Remarks on active and sterile neutrinos mixing', *Int. J. Mod. Phys.* **E16**, 1529–1540.

Tolman, R. C. (1934), 'Effect of imhomogeneity on cosmological models', *Proc. Nat. Acad. Sci.* **20**, 169–176.

Tomita, K. (2001), 'A local void and the accelerating universe', *Mon. Not. Roy. Astron. Soc.* **326**, 287.

Tsujikawa, S. (2010), 'Modified gravity models of dark energy', *Lect. Notes Phys.* **800**, 99–145.

Tsujikawa, S. (2011), 'Dark energy: investigation and modeling', **370**(2010), 331–402.

Urena-Lopez, L. A. & Matos, T. (2000), 'A New cosmological tracker solution for quintessence', *Phys. Rev.* **D62**, 081302.

Wang, L.-M. & Steinhardt, P. J. (1998), 'Cluster abundance constraints on quintessence models', *Astrophys. J.* **508**, 483–490.

Weinberg, S. (1972), *Gravitation and Cosmology*, John Wiley and Sons, New York.

Weinberg, S. (1987), 'Anthropic Bound on the Cosmological Constant', *Phys. Rev. Lett.* **59**, 2607.

Weinberg, S. (1989), 'The Cosmological Constant Problem', *Rev. Mod. Phys.* **61**, 1–23.

Weinberg, S. (2000), The Cosmological constant problems, *in* 'Sources and detection of dark matter and dark energy in the universe. Proceedings, 4th International Symposium, DM 2000, Marina del Rey, USA, February 23-25, 2000', pp. 18–26.

Weinberg, S. (2008), *Cosmology*, Oxford Univ. Pr., Oxford, UK.

Wetterich, C. (1988*a*), 'Cosmologies With Variable Newton's 'Constant'', *Nucl. Phys.* **B302**, 645–667.

Wetterich, C. (1988*b*), 'Cosmologies with variable Newton's constant', *Nucl. Phys.* **302**, 645–667.

White, M. J. & Hu, W. (1997), 'The Sachs-Wolfe effect', *Astron. Astrophys.* **321**, 8–9.

Wu, P., Yu, H. W. & Fu, X. (2009), 'A Parametrization for the growth index of linear matter perturbations', *JCAP* **0906**, 019.

Yoo, J. & Watanabe, Y. (2012), 'Theoretical Models of Dark Energy', *Int. J. Mod. Phys.* **D21**, 1230002.

Zeldovich, Y. B. (1968), 'Cosmological constant and the theory of elementary particles', *Uspekhi fizicheskikh nauk* **91**, 209.

Zhao, W. & Li, M. (2014), 'Detecting relic gravitational waves in the CMB: The contamination caused by the cosmological birefringence', *Phys. Lett.* **B737**, 329–334.

Zimdahl, W. & Pavon, D. (2001), 'Interacting quintessence', *Phys. Lett.* **B521**, 133–138.

Zlatev, I., Wang, L.-M. & Steinhardt, P. J. (1999), 'Quintessence, cosmic coincidence, and the cosmological constant', *Phys. Rev. Lett.* **82**, 896–899.